Carbon Formation Inhibition in Solid Oxide Fuel Cells (SOFCs) Using H_2S

by

Asmida Ideris

A thesis
presented to the University of Waterloo
in fulfillment of the
thesis requirement for the degree of
Doctor of Philosophy
in
Chemical Engineering

Waterloo, Ontario, Canada, 2014

AUTHOR'S DECLARATION

I hereby declare that I am the sole author of this thesis. This is a true copy of the thesis, including any required final revisions, as accepted by my examiners.

I understand that my thesis may be made electronically available to the public.

Abstract

Solid oxide fuel cells (SOFCs) are promising devices for power generation due to their high efficiency and clean operation. Another prominent feature of SOFCs is their ability to operate with not only H_2 fuel but also hydrocarbons and syngas. Unlike many other fuel cells, SOFCs also are capable of utilizing CO as fuel. This flexibility with respect to fuel lessens the dependency on pure H_2 and complex fuel processing and has increased the interest in SOFCs as an alternative power source. However, their widespread commercialization is still hindered by high cost and poor long term stability associated with high temperature operation and carbon deposition at the anode when fuelled with hydrocarbons.

The main objective of the research described in this thesis was to introduce and investigate a method to mitigate the effects of carbon formation in Ni-based anodes operating at intermediate temperatures with hydrocarbon fuels (e.g., CH_4). Ni-samaria-doped-ceria (Ni-SDC) anode-supported cells were fabricated and their performance and susceptibility toward carbon deposition were studied when operating galvanostatically with various fuels including CH_4 and CO-CO_2 mixture at intermediate temperatures (550-700ºC). Ni-SDC anode-supported cells operating with CH_4 and CO-CO_2 were strongly affected by the temperature when the cell performance with CH_4 was found to be more stable during operation at 700ºC than at 600ºC. The maximum power density of the cell with CH_4 as fuel was found to be higher than that achieved with H_2 as fuel at 700ºC. Meanwhile, the cell voltage during operation with CO-CO_2 fuel was more stable at 600ºC than at 700°C. Degradation of the performance of the Ni-SDC cells with CH_4 and CO-CO_2 fuels under conditions where carbon formation is thermodynamically favored was found to be relatively small despite the fact that significant amounts of carbon accumulated in the anode. This may due to the fact that carbon deposited predominantly at the surface of the anode closest to the fuel entry point.

Sulphur in the form of H_2S was introduced into the SOFC at ppm level concentrations to evaluate its effect as a potential carbon inhibitor in a cell operating under dry CH_4 at 700ºC. Two methods for exposing the anode to H_2S were investigated: i) continuous introduction throughout

cell operation as part of the gas feed stream and ii) introduction as part of a mixture with H_2 only for a short period of time as a pre-treatment before regular operation with dry CH_4 alone. These studies showed that continuous feeding of H_2S within the dry CH_4 fuel at the level of only a few ppm (10 and 2 ppm) was enough to cause catastrophic failure of the cell within ~20 hrs due to the poisoning effect of H_2S. On the other hand, the introduction of H_2S at a level of 2 ppm in dry H_2 into the cell for 30 minutes as an anode pre-treatment before switching to dry CH_4 was very successful and enabled the SOFC to maintain stable performance for over 100 hours of operation under dry CH_4, with a lower degradation rate than that observed when a cell was not pre-treated with H_2S. This pre-treatment did not affect the methane conversion significantly during the subsequent galvanostatic operation with dry CH_4. The presence of H_2S influenced the type of carbon formed depending on the manner in which the H_2S was introduced into the SOFC. Carbon deposits that formed during operation with dry CH_4 alone after the 30-minute pre-treatment with H_2S were more easily removed than those produced when the fuel contained dry CH_4 alone or H_2S-containing fuel was introduced continuously over the entire run. The introduction of H_2S for a short duration prior to shifting to dry CH_4 suppressed the formation of graphitic carbon at the anode.

The amount of carbon formed on the cells during CH_4 operation was estimated by shifting the gas stream to humidified H_2 while maintaining the applied current unchanged and measuring the quantity of carbon-containing gases evolved. These measurements revealed that less carbon was deposited in a cell that had been pre-treated with H_2S prior to 100 hrs of operation with dry CH_4 compared to a cell that had not been exposed to H_2S. This analysis also showed that the procedure of flowing humidified H_2 into the cell after operation with dry CH_4 while maintaining the same current appeared to remove carbon from the anode and reduce the rate of degradation of the cell voltage.

Acknowledgements

I would like to express my deep appreciation to both of my supervisors, Professor Eric Croiset and Professor Mark Pritzker for their great guidance, help and encouragement. It was a valuable training process for me working with you.

Special thanks to my committee members, Professor Boxin Zhao, Professor Aiping Yu, Professor Zhongchao Tan and Professor Nicolas Abatzoglou for the time you have taken for my dissertation.

I would like to acknowledge Ministry of Higher Education of Malaysia and Universiti Malaysia Pahang for financial support and study leave throughout these years. I also thank NSERC Solid Oxide Fuel Cell Canada Strategic Research Network from the Natural Science and Engineering Research Council (NSERC) for the great opportunities I had through workshops and meetings while studying in this SOFC field.

I appreciate the help from Ms Judy Caron, Ms Rose Guderian and Ms Ingrid Sherrer in the Department of Chemical Engineering for administration work and Mr Bert Habicher and Mr Ralph Dickhout for their technical support.

To my colleagues from SOFC and chemical reaction engineering groups, Dr Mazni Ismail, Dr Weifang Yao, Dr Aiyu Yan, Dr Ashraf Amin, Dr Monrudee Phongaksorn, Dr Noorlisa Harun, thank you for all your assistance and knowledge sharing.

Also I owe my gratitude to all my friends in Waterloo for their support, care and memorable time together.

Finally to my mama, my abah, my brother and sisters, thank you for the endless prayers, understanding and unconditional love you have given me.

Table of Contents

List of Figures

List of Tables

Nomenclature

Raman symbols

a_i	Activity of reactant or product *i*
Ce'_{ce}	Concentration of Ce^{3+} ions
E	Cell potential (V)
E_r	Equilibrium cell potential (V)
E^0	Cell potential at standard condition (V)
E_a	Activation energy
E_B	Binding energy
E_K	Kinetic energy
E_0, I_0	Amplitude of voltage and current
$\tilde{E}, \tilde{I}$	Oscillating voltage and current
F	Faraday's constant (96,487 C mol^{-1})
ΔG	Change in Gibbs free energy (J mol^{-1})
ΔG°	Standard change in Gibbs free energy (J mol^{-1})
$h\nu$	Photon energy
I	Current (A)
i	Current density (A cm^{-2})
i_L	Limiting current density (A cm^{-2})
i_0	Exchange current density (A cm^{-2})
j	Imaginary unit
k	Boltzmann constant (8.617 $\times 10^{-5}$ eV K^{-1})
K_{eq}	Equilibrium constant
ℓ	Thickness
n	Number of electrons
n_i	Mole flow rate of species *i* (mol min^{-1})
P	Power density (mW cm^{-2})
$p_{O_2,an}$	Partial pressures of oxygen at the anode (atm)
$p_{O_2,ca}$	Partial pressures of oxygen at the cathode (atm)
R	Gas constant (8.314 J $mol^{-1}K$)
R_s	Ohmic resistance (Ω cm^2)

R_p	Polarizarion resistance (Ω cm^2)
R_b	Bulk grain resistance (Ω cm^2)
R_{gb}	Grain boundary resistance (Ω cm^2)
R_{el}	Electrode resistance (Ω cm^2)
T	Temperature (K)
t	Time
$V_{\ddot{0}}$	Oxygen vacancy
W_{elec}	Work (J mol^{-1})
$W_{elec,max}$	Maximum work (J mol^{-1})
Z	Impedance (Ω cm^2)
$Re\ Z$	Real part of impedance (Ω cm^2)
$Im\ Z$	Imaginary part of impedance (Ω cm^2)

Greek Symbols

α	Activity of reactant or product
η	Overpotential (V)
η_{act}	Activation overpotential (V)
η_{ohm}	Ohmic overpotential (V)
η_{conc}	Concentration overpotential (V)
$\delta\wp_s$	Entropy change due to irreversible losses (J mol^{-1} K)
v_i	Stoichiometric coefficient of reactant or product *i*
ω	Angular frequency (radian s^{-1})
ϕ	Phase angle
$\mu_{O_2,an}$	Chemical potentials of oxygen at anode
$\mu_{O_2,ca}$	Chemical potentials of oxygen at cathode
σ_e	Electronic conductivity (S cm^{-1})
σ_i	Ionic conductivity (S cm^{-1})

Subscripts

ca	Cathode
el	Electrolyte
an	Anode

Abbreviation

AC	Alternating current
AFC	Alkaline fuel cell
APU	Auxiliary power unit
BSCF	$Ba_{0.5}Sr_{0.5}Co_{0.8}Fe_{0.2}O_{3-\delta}$
BSE	Backscattered electron
CPE	Constant phase elements
CE	Counter electrode
CHP	Combined heat power
CTE	Coefficient of thermal expansion
DFT	Density functional theory
EDX	Energy Dispersive X-ray
EIS	Electrochemical impedance spectroscopy
GDC	Gadolinia-doped ceria
GNP	Glycine-nitrate process
IT-SOFC	Intermediate temperature SOFC
i-V	Current density-voltage
L	Inductor
LGSM	$La_{0.88}Sr_{0.12}Ga_{0.82}Mg_{0.18}O_{3-\delta}$
LSCM	Lanthanum strontium manganese chromite
LSM	Strontium-doped lanthanum manganite
LSCF	Strontium-doped lanthanum cobalt iron oxide
MCFC	Molten carbonate fuel cell
MIEC	Mixed ionic electronic conductor
MS	Mass spectrometry
Ni-SDC	Ni-samaria doped-ceria
Ni-YSZ	Ni-yttria-stabilized zirconia
NiO	Nickel oxide
OCV	Open-circuit voltage
OSC	Oxygen storage capacity
PAFC	Phosphoric acid fuel cell
PEMFC	Proton exchange membrane fuel cell

RE	Reference electrode
S/C	Steam-to-carbon ratio
SDC	Samaria-doped ceria
SE	Secondary electron
SEM	Scanning electron microscopy
SOFC	Solid oxide fuel cell
SMMO	Sr_2MgMoO_6
SSC	Strontium-doped samaria cobalt
TPB	Triple phase boundary
TPH	Temperature-programmed hydrogenation
TPO	Temperature-programmed oxidation
WE	Working electrode
XRD	X-ray diffraction
XPS	X-ray photoelectron spectroscopy
YDC	Yttria-doped ceria
YST	Yittria-stabilized titania
YSZ	Yittria-stabilized zirconia

Chapter 1
Introduction

World-wide energy consumption has dramatically increased over the last two decades due to population and economic growth as well as changes in quality of life. This rapid growth in energy consumption in both industrialized and developing countries has led to an ever increasing dependence on fossil fuels, causing faster depletion of these resources and serious environmental problems (e.g., air pollution and greenhouse gas emissions). To overcome this problem, better use of these energy resources and the development of sustainable and cleaner energy sources are essential.

Fuel cells are efficient energy generation devices that enable clean conversion of chemical energy from fuels into electrical energy. Due to the direct one-step conversion of chemical energy into electrical energy, the efficiency of energy conversion in fuel cells is higher than in conventional combustion turbines. In addition, fuel cells do not generate harmful pollutants such as nitrogen oxides (NO_x), sulphur oxides (SO_x), carbon monoxide (CO) and particulates since combustion does not take place (Li, 2006).

Known as a high temperature fuel cell operating between 600-1000°C, solid oxide fuel cell (SOFC) can operate with electrical energy efficiencies above 50%. A very important feature of SOFC is that it can operate with many types of fuel including H_2, syngas and hydrocarbons. High temperature operation enables direct conversion of hydrocarbons to occur within the SOFC itself, thereby solving the problems associated with having to purify the fuels before introduction into the fuel cell. When H_2 only is used as fuel, SOFCs emit only water and heat with no pollutants (Stambouli and Traversa, 2002). With other fuels such as hydrocarbons (e.g., CH_4) or synthesis gas (syngas), the carbon dioxide (CO_2) content in the SOFC exhaust stream becomes high since it is not diluted with nitrogen. This may offer better efficiency for eventual CO_2 capture (Dijkstra and Jansen, 2002).

SOFC applications include essentially stationary power generation ranging from residential-scale power units (1 to 5 kW) to on-site power plants (100 kW to 1 MW) and larger-scale distributed power plants (2 to 10 MW). In multi-kW power generation, SOFCs are commonly incorporated with combined heat power (CHP) systems which utilize the generated heat to

produce steam and/or provide space heating or domestic hot water. In multi-MW systems, SOFCs can be integrated with gas turbines for further electricity generation using the unreacted portion of the feed stream to the fuel cell. SOFCs are also used for smaller applications such as automobile auxiliary power units (APUs) (5 kW) and portable devices (20-500 W) (Minh, 2004).

Although SOFCs have great potential, technical barriers must be resolved before their widespread commercialization becomes possible. The main challenges are associated with the high costs of the cell component materials and interconnects and the poor long-term performance and stability at the high operating temperatures (i.e., 800-1000°C for high temperature SOFC). Also, when hydrocarbon fuels are used, carbon deposition occurs on the anode and degrades SOFC performance. The accumulation of the carbon in the anode deteriorates performance by impeding the transport of fuel to the active anode sites and in the worst case, by destroying the anode structure.

1.1 Motivation

Intermediate-temperature-SOFCs (IT-SOFCs) which operate from 500 to 700°C have received considerable attention among researchers since they enable much less expensive materials to be used and are more stable due to less thermal degradation than at higher temperatures. However, a decrease in temperature increases the ohmic resistance of the cell operating with the state-of-the-art material (yttria-stabilized zirconia, YSZ). Therefore, the use of materials with better ionic conductivity and a SOFC design aimed at reducing the thickness of the electrolyte is desirable.

Doped ceria (doped-CeO_2) exhibits higher ionic conductivity than YSZ at low operating temperatures. In addition, it has been reported that the presence of ceria in the anode cermet enhances the electrochemical oxidation reaction (Murray *et al.,* 1999). Anode-supported cell design features a thin electrolyte with a thick anode which also serves as the cell support. The thick anode also offers a large number of catalyst sites for chemical and electrochemical reactions to take place when the SOFC is directly fuelled with hydrocarbons. In this work, Ni-samaria doped-ceria (Ni-SDC) anode-supported cells are used. Their performance and the tendency for carbon deposition to occur when hydrocarbon fuels (i.e., CH_4) and CO are used have been examined in this thesis.

Ni-based anodes are highly active for chemical and electrochemical reactions and have high electronic conductivity. However, Ni metal provides a good surface for the formation of carbon and so is prone to carbon deposition when hydrocarbons are fed directly to the anode. Consequently, researchers have made great efforts to improve the carbon tolerance of Ni-based anodes. Most of this work has involved modification of Ni-based anodes during cell fabrication by alloying or impregnating the Ni with metals, noble materials or alkaline earth oxides (Nikolla *et al.,* 2009a; Takeguchi *et al.,* 2003; Asamoto *et al.,* 2009). In this work, we examine the potential to minimize carbon formation by introducing a gas stream containing sulphur in the form of H_2S into the SOFC anode.

Sulphur compounds are well known to be able to poison catalysts and electrodes and thereby terminate electrochemical and chemical reactions. It has been shown that a few ppm of H_2S (e.g. 2-15 ppm at 800 ºC) are sufficient to dramatically degrade the electrochemical performance (Matsuzaki and Yasuda, 2000) and methane reforming activity (Rasmussen and Hagen, 2010) in SOFCs. However, according to DFT calculations by Abild-Pedersen *et al.* (2005), the introduction of the appropriate sulphur-bearing species which has a strong affinity for Ni, can inhibit carbon formation by adsorption onto Ni sites that are active for carbon formation. In a work with methane steam reforming, Rostrup-Nielsen (1984) also reported that the used of 1 ppm H_2S for catalyst pretreatment has eliminated the carbon filaments, leaving only amorphous carbon on the Ni catalyst.

Since sulphur compounds can poison catalysts if present in excess amounts, it is important to determine the range of concentrations at which they can suppress carbon formation, but do not unduly poison the Ni-based anodes. Researchers have focused on the negative effects of sulphur on the reforming activity and electrochemical reactions on Ni-based anodes when SOFC is fuelled directly with CH_4. Yet, very little research so far has focused on the potential positive effect of sulphur to inhibit carbon deposition. For this reason, we focus on this topic in this work.

Briefly, the main objectives in this work were:

- To evaluate the performance of Ni-ceria-based (Ni-SDC) cells and their susceptibility towards carbon deposition when directly fed with hydrocarbons (i.e., CH_4) and CO.
- To investigate the effect of incorporating H_2S into the inlet gas stream on carbon deposition at the SOFC anode when operating Ni-SDC cell with CH_4 fuel.

1.2 Organization of the thesis

This thesis is organized into eight chapters.

Chapter 1 presents a general introduction of the research and discusses the research motivation and objectives of the research. This is followed in Chapter 2 with background on fuel cells and SOFC operation, a review of the types of electrolyte, anode and cathode materials used in SOFCs, discussion of the forms of carbon that deposit in SOFC anodes and describes the previous efforts to minimize carbon deposition in Ni-based anodes. Chapter 3 provides details on the procedures to synthesize the electrolyte and anode materials, fabricate the cell and cell set-up, carry out the electrochemical experiments, analyze gas composition and characterize the anode constituents and morphology. The results of experiments carried out to evaluate the performance and stability of anode-supported Ni-SDC cells operating with different fuels (H_2, CH_4 and CO) at temperatures ranging from 600 to 700°C are presented in Chapter 4. Chapter 5 focuses on carbon deposition in Ni-SDC cells when operating with CH_4 and CO fuels. Chapter 6 describes the results of applying different strategies for introducing H_2S into the Ni-SDC cells operating with dry CH_4 fuel to mitigate the deleterious effects of carbon formation. Based on the results obtained in Chapter 6, a procedure to reduce the extent of carbon deposition during SOFC operation with dry CH_4 fuel that involves pre-treating the anode with a gas stream containing low concentrations of H_2S is explored further in Chapter 7. In particular, the effects of this approach on SOFC performance, outlet gas composition, CH_4 conversion and the amount of carbon deposited are determined. Finally, the thesis closes with conclusions and recommendations for future work in Chapter 8.

Chapter 2
Literature Review

This chapter is divided into three main parts. The first part begins with a background discussion on fuel cells and thermodynamics with specific focus on SOFC operation. As this research is aimed at operating SOFCs at intermediate temperatures, an overview of suitable materials for fuel cell components and cell design are also given. The second part of the chapter covers the topics of internal reforming, direct utilization of hydrocarbon fuels in SOFCs and problems associated with the use of hydrocarbon fuels such as carbon deposition. Included is a review of the forms of carbon that deposit in SOFC anodes. Finally, in the third part of the chapter, efforts to minimize carbon deposition in Ni-based anodes and use H_2S to inhibit carbon formation are discussed.

2.1 Introduction to fuel cells

Fuel cells are very promising devices for energy transfer and power generation. Using the principle of electrochemical conversion, fuel cells produce electricity directly from chemical energy available in their reactants (fuel and oxidant) (O'Hayre *et al.*, 2006). Fuel cells are theoretically more efficient than heat engines and batteries. A heat engine converts the chemical energy into thermal energy and then into mechanical energy before transforming it into electrical energy. This multistep energy conversion tends to lower the overall energy efficiency. Compared to heat engines, fuel cells have potentially higher energy efficiency and are not restricted by Carnot efficiency.

Batteries share the same operational principles as fuel cells where electrical energy is generated directly from reactants through electrochemical reactions. Batteries operate as both energy conversion and energy storage devices. A primary battery undergoes only one discharge cycle in which its chemical reactants are consumed and no attempt is made to recharge it. The maximum amount of energy available depends entirely on the amount of chemical reactants stored within the device. Meanwhile, a secondary battery operates through repeated charge/discharge cycles and requires an external electric power source to regenerate its chemical reactants and thereby recharge its electrical energy. Fuel cells, on the other hand, act solely as

energy conversion units by producing electrical energy as a fuel and oxidant are continuously supplied (Li, 2006).

The conventional pathway of generating electricity involves the thermal combustion of fuel. In a heat engine when hydrogen is used as its fuel, hydrogen reacts with oxygen to produce water and heat:

$$H_2 + \frac{1}{2}O_2 \rightarrow H_2\,O + heat \qquad 2.1$$

The cleavage of the bonds within H_2 and O_2 and the formation of water involve the transfer of electrons between atoms. The resulting energy change associated with these bonds is released as heat which can be converted into intermediate forms of energy and finally into electricity (O'Hayre *et al.,* 2006). In fuel cells, electrons that move from high-energy reactants to low-energy product are directly harvested as electrical energy. This is made possible since the fuel and oxidant reactants and the sites for oxidation and reduction are spatially separated so that the electrons necessary to complete the overall reaction must flow through an external circuit. The electrons produced by the half-cell reaction at the fuel electrode are transferred to the oxidant electrode via the external circuit to complete the reaction. The net reaction in a fuel cell is exactly the same as in a heat engine when the fuel is combusted (O'Hayre *et al.,* 2006). A significant amount of energy in the form of heat is also generated within fuel cells. Thus, the simultaneous utilization of this exhaust heat and electrical energy in a fuel cell-gas turbine can potentially improve the overall efficiency of power generation.

A fuel cell consists of three main components: i) fuel electrode (anode) and ii) oxidant electrode (cathode) separated by iii) an electrolyte. The anode and cathode are connected to an external circuit to provide a pathway for the electrons generated/consumed by the electrochemical reactions. The half-cell reactions at the anode and cathode involve ions and electrons. The ions migrate through the electrolyte, while the electrons are transported between the electrodes through the external circuit in the form of electricity. To achieve a high reaction rate and a large power output, the electrodes are porous to maximize the surface area in contact with the reactants, while the electrolyte is thin to minimize its ionic resistance (Varga, 2007). The electrodes provide sites for the electrochemical reactions and the conductivity required to transport electrons. Meanwhile, the electrolyte acts as an ionic conductor, electronic insulator

and a barrier to separate the reactants. Ions can also flow through the electrodes because the electrodes are composite porous materials containing ionically conducting materials (Li, 2006). During fuel cell operation, gaseous fuel (e.g., hydrogen) is delivered to the anode and gaseous oxidant (i.e., oxygen from air) is supplied to the cathode. By-products can also be formed at the electrodes depending on the fuel. These by-products are also transported out of the electrode into the gas stream (Haile, 2003).

Fuel cells are primarily classified into five major types: alkaline fuel cells (AFCs), phosphoric acid fuel cells (PAFCs), proton exchange membrane fuel cells (PEMFCs), molten carbonate fuel cell (MCFCs) and solid oxide fuel cells (SOFCs). These five major fuel cells operate via different half-cell reactions depending upon the characteristics of the electrolyte. The principal half-cell reactions operating in each fuel cell are given in Table 2-1.

Table 2-1 Half-cell reactions of five major types of fuel cells

Fuel Cells	Anode Reaction	Cathode Reaction
AFC	$H_2 + 2OH^- \rightarrow 2H_2O + 2e^-$	$O_2 + 2H_2O + 4e^- \rightarrow 4OH^-$
PAFC	$H_2 \rightarrow 2H^+ + 2e^-$	$O_2 + 4H^+ + 4e^- \rightarrow 2H_2O$
PEMFC	$H_2 \rightarrow 2H^+ + 2e^-$	$O_2 + 4H^+ + 4e^- \rightarrow 2H_2O$
MCFC	$H_2 + CO_3^{2-} \rightarrow H_2O + CO_2 + 2e^-$ $CO + CO_3^{2-} \rightarrow 2CO_2 + 2e^-$	$O_2 + 2CO_2 + 4e^- \rightarrow 2CO_3^{2-}$
SOFC	$H_2 + O^{2-} \rightarrow H_2O + 2e^-$ $CO + O^{2-} \rightarrow CO_2 + 2e^-$	$O_2 + 4e^- \rightarrow 2O^{2-}$

Among these fuel cells, AFCs were the first developed and successfully operated in space shuttle missions. Attempts to use AFCs for terrestrial applications, however, have been restricted due to the requirement that pure H_2 and O_2 be used. Acid-based PAFCs are available in commercial units that can generate up to 200 kW power. Nevertheless, this type of fuel cell is not yet considered to be commercially mature. PEMFCs and SOFCs have received the most attention in recent years. With membrane electrolyte and low-temperature operations, PEMFCs are ideal for transportation and have been employed in most prototypes for fuel-cell-powered vehicles. The demand for alternative power generation has drawn considerable interest in developing SOFCs. Due to their high operating temperatures, SOFCs are able to utilize

hydrocarbon fuels, making them more flexible with respect to fuel options than the other types. MCFCs which are the other high temperature cells are still in the early stages of development and pre-commercial demonstration (Li, 2006). The operating characteristics of the five types of fuel cells are summarized in Table 2-2.

Table 2-2 Major types of fuel cells (Li, 2006; Demirbas, 2009; Shah, 2007)

Features	Type of fuel cells				
	AFC	PAFC	PEMFC	MCFC	SOFC
Electrolyte	KOH aqueous (immobilized)	H_3PO_4 solution (immobilized)	Polymer membrane	Molten carbonate salt	Ion-conducting ceramic
Electrodes	Pt (Anode/ Cathode)	Pt (Anode/ Cathode)	Pt (Anode/ Cathode)	Ni (Anode/ Cathode)	Ni-YSZ (Anode) $La_{0.8}Sr_{0.2}MnO_3$ (Cathode)
Charge carrier	OH^-	H^+	H^+	CO_3^{2-}	O^{2-}
Operating temperature (^oC)	60-80	160-220	50-80	600-700	600-1000
Fuels	H_2	H_2	H_2, CH_3OH, C_2H_4OH	H_2, CO, CH_4	H_2, CO, CH_4
Efficiency (%)	60-70	40-45	45-60	60-65	55-65
Applications	Transportation, space travel	Stationary power generation, CPH	Transportation, portable equipment, space travel	Stationary power generation, CPH	Stationary power generation, CPH

CHP: Combined heat and power

2.2 SOFC thermodynamics

In a fuel cell, the work W_{elec} or electrical energy output is related to the potential difference between the electrodes called the cell potential, E. The cell potential is defined as the work done by transferring electrons from the electrode at lower potential (anode) to the electrode at higher potential (cathode):

$$E = \frac{W_{elec}}{nF} = \frac{-\Delta G - T\wp_s}{nF} \quad 2.2$$

where n is the number of electrons involved in the electrochemical reactions at the electrodes and F is the Faraday constant (96,487 C mol^{-1}). ΔG is the change in Gibbs free energy of the reaction, T is the temperature of the system and $\wp_s$ is the entropy change due to irreversible losses. The maximum electrical work $W_{elec,max}$ is generated when the irreversible losses are zero. Thus, in this circumstance, Eq. 2.2 shows that $W_{elec,max}$ becomes equal to ΔG which in turn can be related to the cell potential E_r at thermodynamic equilibrium as follows:

$$W_{elec,max} = -\Delta G = nFE_r \quad 2.3$$

When the fuel and oxygen are introduced to a separated anode and cathode, respectively, this leads to an electromotive force that can be related to the chemical potential gradient of oxygen between the two electrodes (Zha *et al.*, 2001). If a fuel cell is viewed as an oxygen concentration cell, the calculation of its equilibrium cell potential can be calculated using the chemical potentials of oxygen at the anode ($\mu_{O_2,an}$) and at the cathode ($\mu_{O_2,ca}$). By combining Eqs. 2.3 and 2.4, the equilibrium cell potential E_r can be directly related to the partial pressures of oxygen at the anode ($p_{O_2,an}$) and at the cathode ($p_{O_2,ca}$). The result is given below in Eq. 2.5:

$$\Delta G = \mu_{O_2,an} - \mu_{O_2,ca} = RTln\left(\frac{p_{O_2,an}}{p_{O_2,ca}}\right) \quad 2.4$$

$$E_r = -\frac{\Delta G}{nF} = -\frac{RT}{nF} ln\left(\frac{p_{O_2,an}}{p_{O_2,ca}}\right) \quad 2.5$$

where R is the gas constant (8.314 J mol^{-1} K).

At the cathode, the reduction of the oxygen is given by:

$$\text{Cathode: } O_{2,ca} + 4e^- \rightleftarrows 2O_{el}^{2-} \quad 2.6$$

Meanwhile at the anode, the oxidation reaction is:

$$\text{Anode: } 2O_{el}^{2-} \rightleftarrows O_{2,an} + 4e^{-} \tag{2.7}$$

If H_2 is the fuel introduced on the anode side, it reacts with $O_{2,an}$ as follows:

$$\text{Anode: } H_{2,an} + \frac{1}{2}O_{2,an} \rightleftarrows H_2O_{,an} \tag{2.8}$$

The subscripts *ca*, *el* and *an* denote the species at the cathode, electrolyte and anode sites, respectively. If the cathode is exposed directly to the air, $p_{O_2,ca}$ is 0.21 atm. Meanwhile $p_{O_2,an}$ is calculated using the equilibrium constant of the fuel oxidation reaction. For the case of H_2 fuel and the reaction given in Eq. 2.8, the partial pressure of oxygen at the anode becomes:

$$p_{O_2,an} = \left(\frac{p_{H_2O}}{K_{eq}p_{H_2}}\right)^2 \tag{2.9}$$

where p_{H_2O}, p_{H_2}, K_{eq} are the partial pressures of H_2O and H_2 at the anode and the equilibrium constant of reaction 2.8, respectively.

At equilibrium, the equilibrium constant K_{eq} is related to the standard Gibbs free energy change ΔG° (Eq. 2.10) where ΔG° is the Gibbs free energy change under standard conditions.

$$K_{eq} = exp\left(-\frac{\Delta G^{\circ}}{RT}\right) \tag{2.10}$$

Combining Eqs. 2.9 and 2.10 with Eq. 2.5 yields an expression for E_r in terms of the standard Gibbs free energy and H_2 and H_2O partial pressures:

$$E_r = -\frac{\Delta G^{\circ}}{2F} - \frac{RT}{2F} ln\left(\frac{p_{H_2O}}{p_{H_2}p_{O_2,ca}{}^{\frac{1}{2}}}\right) \tag{2.11}$$

where $n = 4$. Note that Eq. 2.11 is the Nernst equation for an SOFC when H_2 is the fuel. In the more general situation when any type of fuel is used, E_r can be written as:

$$E_r = E^{\circ} - \frac{RT}{nF} ln\left(\frac{\prod \alpha_{product}^{v_i}}{\prod \alpha_{reactant}^{v_i}}\right) \tag{2.12}$$

where E° is the standard cell potential at temperature T, α is the activity of reactant or product i and v_i is the corresponding stoichiometric coefficient.

2.3 Cell overpotentials

In a practical application, a reasonable amount of the current from a fuel cell generates useful electrical energy in the form of power or power density P (Watt per unit area):

$$P = i.E \tag{2.13}$$

where i is the current density (amp per unit geometrical area) and E (volt) is the operating cell potential. During the operation under a load of current, the operating cell potential E is always lower than the equilibrium cell potential, E_r. The operating cell potential differs from the equilibrium value due to losses associated with kinetic, ohmic and mass transfer effects. These losses are observed as overvoltages or overpotentials that reduce the cell potential from its equilibrium value, i.e.,

$$E = E_r - \eta_{act} - \eta_{ohm} - \eta_{conc} \tag{2.14}$$

where η_{act} is the activation (kinetic) overpotential, η_{ohm} is the ohmic overpotential and η_{conc} is the concentration (mass transfer) overpotential (Li, 2006). The magnitudes of these overpotentials vary with the current drawn by the fuel cell. The more current flowing through the cell, the larger are the magnitudes of the overpotentials and the lower is the resulting cell potential. Once current begins to flow, the cell voltage decreases and each overpotential becomes important in different regions of a current density-potential (i-V) curve. Figure 2-1 shows a typical i-V curve in which the cell voltage is plotted versus the current density. Activation overpotential is the dominant loss at small current density while the other overpotential losses are less important. Activation overpotential also occurs at higher current density, but ohmic overpotential becomes more significant at intermediate currents and concentration overpotential becomes operative at high current densities.

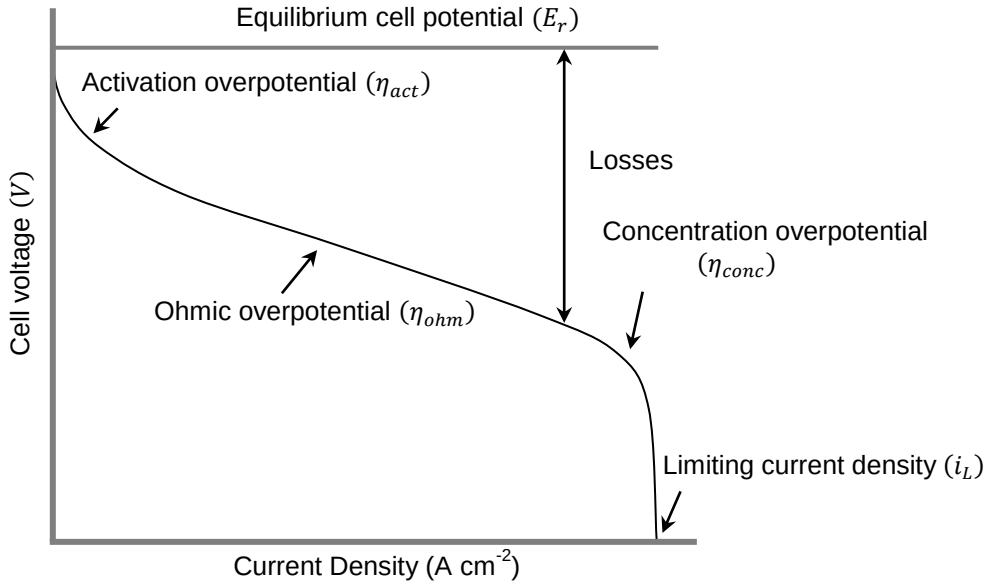

Figure 2-1 A typical current density-voltage (i-V) curve of a fuel cell

Activation overpotential

The activation overpotential, η_{act} is caused by limitations associated with the electrode kinetics of the electrochemical reactions and so is strongly affected by the nature of the electrode-electrolyte interface (Virkar *et al.*, 2000). The relationship between the current density i and the activation overpotential η_{act} is given by the well-known Butler-Volmer equation:

$$i = i_0 \left[\exp\left(\frac{\alpha n F \eta_{act}}{RT}\right) - \exp\left(-\frac{(1-\alpha) n F \eta_{act}}{RT}\right) \right] \qquad 2.15$$

where i_0 is an exchange current density (ampere per unit geometrical area) and α is the transfer coefficient ($0< \alpha<1$). The magnitude of i_0 is a measure of facility of the electrochemical reaction. The higher the value of i_0, the faster is the inherent kinetics of the electrochemical reaction (Chan *et al.*, 2001). The value of i_0 can be obtained from a plot of the Tafel equation, which is a simplified version of the Butler-Volmer equation that arises when η_{act} is large ($\eta_{act} > 0.05$ V) (Li, 2006):

$$\eta_{act} = \frac{RT}{\alpha n F} \ln\left(\frac{i}{i_0}\right) \qquad (\eta_{act} > 0.05 \text{ V}) \qquad 2.16$$

Ohmic overpotential

The ohmic overpotential, η_{ohm} accounts for the resistance to transport ions through the electrolyte and electrons through the electrodes and current collectors and the contact resistance between the cell components (Aguiar *et al.,* 2004). Since some ionic transport also takes place through the porous electrodes, the ohmic overpotential also accounts for the resistance to transport of ions through the electrodes. The dominant resistance, however, comes from the electrolyte where the effect can be reduced by decreasing the electrolyte thickness and improving its ionic conductivity (Chan *et al.,* 2001). The ohmic overpotential can be expressed in terms of Ohm's law whereby it increases linearly with the current density i:

$$\eta_{ohm} = iR_{ohm} \tag{2.17}$$

where R_{ohm} is the ohmic resistance (Ω cm^2).

Concentration overpotential

Concentration overpotential, η_{conc} results from the limitations in the mass transfer of reactants and products to and from the porous electrodes. It is strongly affected by the electrode microstructure, namely porosity, pore size and tortuosity (Virkar *et al.,* 2000). This overpotential arises when the feed rate of a reactant and/or the removal rate of a product from the electrode cannot keep pace with the rate of the electrochemical reactions. Reactant gases must diffuse through the pores to reach reaction sites. When current is being drawn from the cell and a reactant gas at the electrode surface is consumed more rapidly than it can be replaced by transport from the bulk gas stream, its partial pressure at the reaction sites will be lower than it is in the bulk gas stream (Chan *et al.,* 2001). As more current is drawn, the gas in the vicinity of the reaction sites becomes increasingly depleted. If the point is reached where the gas concentration at the electrode surfaces becomes low enough, the cell voltage rapidly drops to zero and the cell reaches its limiting current density, i_L. Under the assumption that the current density is high and the rate of reactant transport is the rate limiting, η_{conc} can be calculated using the equation below (Li, 2006):

$$\eta_{conc} = \frac{RT}{nF} \ln\left(\frac{i_L}{i_L - i}\right) \tag{2.18}$$

2.4 Solid oxide fuel cell operation and component materials

Ideally operated for stationary power generation with an output of 100 kW to 250 kW, SOFCs are expected to have an electrical efficiency of 50%. Incorporation of these systems with gas turbines for co-generation can increase the efficiency up to 70% (Singhal, 2000). Although the utilization of SOFCs for transportation is limited due to its high temperature operation, SOFCs can provide energy for a wide range of power applications: portable and small power systems, combined power heat (CPH) and SOFC-gas turbine systems (Minh, 2004). Operation at high temperatures tends to reduce kinetic problems associated with the electrochemical reactions and thereby allows the use of low cost catalysts (e.g. Ni) and accommodates the direct utilization of hydrocarbon fuels. Methane (the main component of natural gas) has been the main hydrocarbon fuel employed in SOFCs (Murray *et al.*, 1999). Other than methane, fuels such as liquid methanol (Sahibzada *et al.*, 2000), ethanol (Ye *et al.*, 2007) and biogas also have been directly used (Shiratori *et al.*, 2008). Furthermore, unlike other fuel cells that are intolerant to CO, SOFCs are capable of using CO as fuel and so are not highly dependent on pure H_2 and complex fuel processing. This flexibility has become the main reason for continual interest among researchers in SOFC development.

2.4.1 SOFC operation

The electrochemical reactions in an SOFC occur at the interface between the electrode and electrolyte, known as the triple phase boundary (TPB). At these sites, the gas phase, anode (or cathode) and electrolyte meet each other. At the cathode-electrolyte interface, oxygen ions (O^{2-}) are formed by the electrochemical reduction of O_2 from the gas stream via the half-cell reaction:

$$\frac{1}{2}O_2 + 2e^- \rightarrow O^{2-} \qquad 2.19$$

Ideally, the dense solid electrolyte with high ionic conductivity and negligible electronic conductivity does not permit the passage of the oxidant gas molecules or electrons but only the migration of O^{2-} to the anode. The O^{2-} ions move through the electrolyte via a vacancy hopping mechanism towards the anode-electrolyte interface. At the anode-electrolyte interface, the ions participate in an electrochemical reaction with the fuel to produce electrons. When H_2 is the fuel, for example, it reacts with the O^{2-} as follows to generate water and electrons:

$$H_2 + O^{2-} \rightarrow H_2O + 2e^- \quad (2.20)$$

The electrons then, in turn, flow back to the cathode through the external circuit as electricity. The overall reaction in an SOFC when H_2 is the only fuel is:

$$H_2 + \frac{1}{2} O_2 \rightarrow H_2O \quad (2.21)$$

The final products of this process depend on the fuels used. A fuel with a mixture of H_2 and CO, for example, will produce H_2O and CO_2. These reaction products will flow back to the fuel channel through the anode pores. The operating principle of an SOFC is illustrated in Figure 2-2.

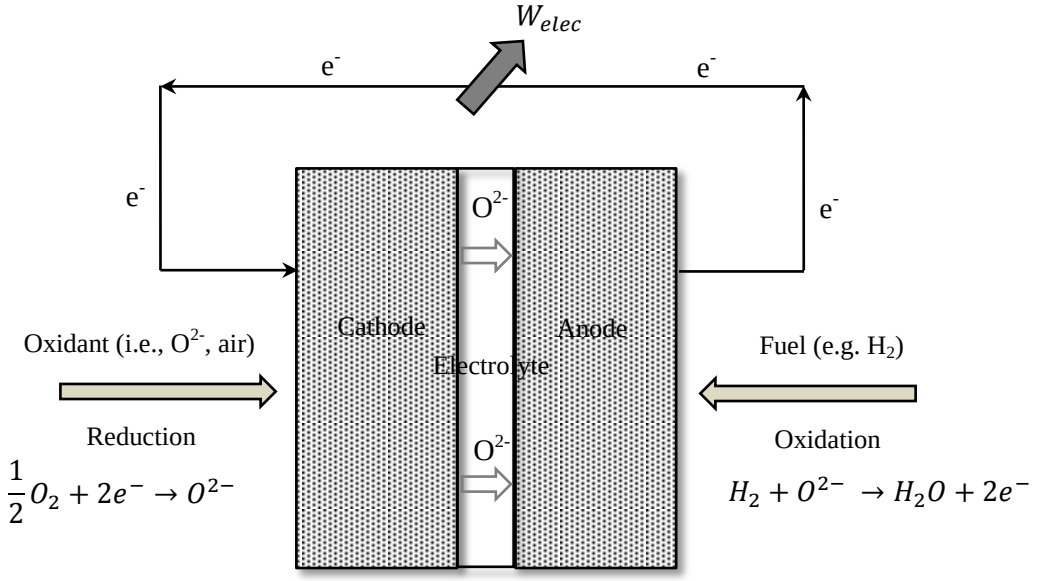

Figure 2-2 Schematic diagram showing SOFC operation

2.4.2 SOFC materials

Over several decades, numerous studies have led to some materials being selected as standard materials for SOFC components. Yttria-stabilized zirconia (Y_2O_3-stabilized ZrO_2 denoted as YSZ) is known as a standard SOFC electrolyte. Since its discovery in 1899 and utilization as the solid electrolyte in the first SOFC in 1937, YSZ has been successfully applied in most SOFC laboratories and demonstration units (Minh, 1993). The state-of-the-art materials for the SOFC anode and cathode are nickel-YSZ (Ni−YSZ) cermet and strontium-doped lanthanum manganate (Sr-doped $LaMnO_3$, LSM), respectively (Sammes *et al.*, 2006).

Material selection for each SOFC component depends on its function and the conditions it will face. For example, the SOFC electrolyte must be an oxygen ion conductor. The oxygen ions move through the crystal lattice of the electrolyte from one site to another by thermally-activated hopping into vacant oxygen sites. The oxygen ion conductivity is highly dependent on temperature (Skinner and Kilner, 2003). The SOFC electrolyte must have the following important properties (Minh and Takahashi, 1995):

- chemically, morphologically and dimensionally stable in the combined reducing and oxidizing atmospheres
- high ionic conductivity and negligible electronic conductivity
- non-reactivity with electrode materials during operation and fabrication
- thermal expansion that matches that of the electrodes
- high density to prevent gas leakage of oxidant and fuel

The SOFC anode promotes the electrochemical oxidation of fuels. It must allow for the diffusion of the fuel and exhaust gases to and from the anode-electrolyte interface and also permit the conduction of generated electrons to the external circuit. For these reasons, the SOFC anode should have excellent electrocatalytic activity towards fuel oxidation, high electronic conductivity, chemical stability in a reducing environment, coefficient of thermal expansion (CTE) close to that of the other cell components and sufficient porosity for fuel and product gas transport (Jiang and Chan, 2004). At the SOFC cathode, O_2 is reduced to O^{2-} ions. This requires cathode material that is highly stable under oxidizing environments and electronically conductive. Analogous to the anode, cathode also should have a sufficient porosity to facilitate

the transport of molecular oxygen from the oxidant feed channel to the cathode-electrolyte interface and a CTE that matches that of the electrolyte (Singhal, 2000).

Known as an excellent electrolyte, YSZ can withstand the wide range of oxygen partial pressures from $1-10^{-22}$ atm and has high ionic conductivity at elevated temperatures (0.16 S cm^{-1} at 1000°C and 0.03 S cm^{-1} at 800°C) (Yamamoto, 2000). Conventional SOFCs operate at high operating temperatures (850-1000°C) to ensure that the oxygen ion conductivity in the solid electrolyte is high. Nevertheless, it would be cost effective and make SOFCs more commercially viable if their operating temperatures could be reduced. This would enable much less expensive materials to be used since a broader choice of non-electrochemical SOFC components, e.g., interconnect and cell housing, becomes available. In addition, high temperature problems such as densification of electrodes and crack formation due to thermal stress can be avoided (Xia *et al.,* 2002).

An improvement of cell chemical and mechanical stabilities with cost-effective operation is possible at temperatures below 800°C (Huijsmans *et al.,* 1998). Therefore, many efforts have been made towards intermediate-temperature-SOFCs (IT-SOFCs), operating in the 500-700°C temperature range. Lower temperatures, however, cause a significant reduction in YSZ conductivity and consequently increase the ohmic losses in the electrolyte. Therefore, the use of electrolytes with higher ionic conductivity at lower temperatures is necessary and consequently ceria doped with rare earth oxides such as samaria (SDC), gadolinia (GDC) and yttria (YDC) have become the main electrolyte materials for intermediate-temperature SOFCs (Ralph *et al.,* 2001). Another option to improve the ionic conductivity at low temperatures is to reduce the electrolyte thickness using an anode-supported cell geometry (Kim *et al.,* 2005).

Electrolyte material

Pure ceria (CeO_2) has a negligible ionic conductivity. However, doping oxides of metals with lower valence into pure ceria introduces oxygen vacancies into its fluorite crystal structure in order to maintain charge neutrality when the Ce^{4+} host is replaced by Sm^{3+} or Gd^{3+}. Since oxygen ions can readily move through the ceria lattice via these oxygen vacancies, doped-ceria exhibits excellent oxygen ion conductivity. Using the Kröger-Vink notation, vacancy formation

can be described as a reaction in which one oxygen vacancy unit is produced in the ceria host lattice with addition of each samaria (Sm_2O_3):

$$Sm_2O_3 \xrightarrow{CeO_2} 2Sm'_{Ce} + V_{\ddot{O}} + 3O_O \qquad 2.22$$

where Sm'_{Ce} is Sm on the Ce crystal site that leaves the lattice negatively charged relative to the undoped oxide, $V_{\ddot{O}}$ is an oxygen vacancy and O_O is a neutral oxygen. When a small amount of samaria is added to CeO_2, a solid solution of $(CeO_2)_{1-x}(SmO_{1.5})_x$ is formed with an ionic conductivity two orders of magnitude higher than that of pure ceria at 800-1000°C (Yahiro *et al.*,1988). The ionic conductivity in materials such as doped ceria depends on temperature, oxygen partial pressure in the gas environment, type and concentration of dopant, microstructure and processing conditions (Hui *et al.,* 2007). The ionic conductivity increases with dopant level due to the formation of more oxygen vacancies up to an optimum concentration, but then decreases with any further increase. At higher dopant level, stronger dopant-oxygen vacancy interactions tend to reduce the mobility of vacancies and the ionic conductivity (Xia, 2009).

Researchers report differing findings regarding whether samaria-doped ceria or gadolinia-doped ceria has the higher conductivity. Yahiro *et al.* (1988) found that SDC with dopant concentration x=0.2 ($Ce_{0.8}Sm_{0.2}O_{1.9}$) exhibits an ionic conductivity of 0.095 S cm^{-1} at 800°C, 1.7 times higher than the value of 0.055 S cm^{-1} for GDC ($Ce_{0.8}Gd_{0.2}O_{1.9}$) with the same dopant composition. Eguchi *et al.* (1992) from the same group confirmed that the ionic conductivity is the highest at the optimum dopant ionic radius, which corresponds to that of Sm^{3+}. The optimum ionic radius of the dopant in one most closely matches that of the host Ce^{4+} (Inaba and Tagawa, 1996). On the other hand, Steele (2000) compared the conductivities of GDC and SDC over the temperature range of 500-700°C and found that GDC ($Ce_{0.9}Gd_{0.1}O_{1.95}$) has a higher conductivity of 0.0095 S cm^{-1} than the value of 0.0033 S cm^{-1} for SDC ($Ce_{0.9}Sm_{0.1}O_{1.95}$) at 500°C. It is worth noting that the dopant concentration of x=0.1 in this work differed from that of the previous work. Mogensen *et al.* (2000) attributed the differences in the reported conductivities of SDC and GDC to the methods of fabrication which affects grain boundary conductivity of each sample. Later, Zha *et al.* (2003) reported no significant difference in the ionic conductivities of SDC and GDC when measured over the temperature range of 400-850°C. Although they found that the conductivity reached its maximum at a dopant concentration x=0.15 in both electrolytes, they suggested that other electrochemical and mechanical properties such as the ionic

transference number, thermal expansion constant (CTE) and compatibility with other components should be considered in selecting the best electrolyte material. In summary, doped-ceria has better conductivity at lower temperatures than does YSZ. The conductivities of SDC and GDC at 700°C are very similar to that of YSZ at 1000°C (Zha *et al.*, 2003). At identical temperatures, the conductivity of doped-ceria is about one-order of magnitude larger than that of YSZ, making doped-ceria a promising candidate for SOFC electrolyte at intermediate temperatures (Zhu and Deevi, 2003). For example, the ionic conductivities of pure ceria, SDC, GDC and YSZ at 800°C are listed in Table 2-3 (Eguchi, 1997).

Table 2-3 Ionic conductivities of ceria-based and YSZ electrolytes at 800°C (Eguchi, 1997)

Materials	Ionic conductivity ($\sigma \times 10^{-2}$), S cm^{-1}
CeO_2	0.03
$Ce_{0.8}Sm_{0.2}O_{1.9}$ (SDC)	9.45
$Ce_{0.8}Gd_{0.2}O_{1.9}$ (GDC)	5.53
$(ZrO)_{0.92}(Y_2O_3)_{0.08}$ (YSZ)	3.01

The main limitation in using doped-ceria electrolytes, however, concerns their chemical stability at the low oxygen partial pressures on the anode side which causes some Ce^{4+} to be reduced to Ce^{3+}. Doped-ceria, although primarily an ionic conductor, also exhibits some electronic conductivity. A lower open circuit voltage (OCV) is expected for doped-ceria electrolyte compared to the Nernst voltage E_r due to this electronic conduction. Since the cell voltage is a direct measure of fuel efficiency, this internal shorting also lowers the energy efficiency (Zhang *et al.*, 2007). In the worst case, this short circuit effect may expand the lattice and cause its mechanical integrity to degrade to some extent (Kharton *et al.*, 2004). It should be noted, however, that the electronic conductivity of doped-ceria may be reduced and become less of a problem when current is flowing through a cell (Doshi *et al.*, 1999). Other than the oxygen partial pressure, the electronic conductivity of the electrolyte is also affected by temperature. A rise in temperature triggers a dramatic increase in the electronic conductivity of doped-ceria. For this reason, Zhu and Deevi (2003) suggested that doped-ceria would only be useful as an SOFC electrolyte at temperatures below 800°C. Matsui *et al.* (2005) reported that the suppression of

electronic conduction is possible by reducing the operating temperature and increasing oxygen partial pressure by introducing fuel in a humidified state into the cell.

The utilization of ceria in industrial catalysis as a promoter or main catalyst has been well reported. Trovarelli *et al.* (1999) have described the usages of ceria for 1) catalytic treatment of SO_x generated from fluid catalytic cracking units and exhaust gases (CO, NO and hydrocarbons) from combustion engines, 2) catalytic wet oxidation for removal of organics present in wastewater and 3) dehydrogenation of ethyl benzene to styrene. Laosiripojana's group has utilized ceria in reforming of methane (Laosiripojana and Assambumrungat, 2005) and higher hydrocarbons (Laosiripojana and Assambumrungat, 2006a; Laosiripojana *et al.,* 2006; Laosiripojana and Assambumrungat, 2006b). Its properties such as reduction/oxidation (redox) behavior, high oxygen storage capacity, interaction with supported metal can also be easily modified to make it a very promising catalyst (Laosiripojana and Assambumrungat, 2006a). When ceria is used as a promoter for CH_4 reforming, a gas-solid reaction occurs between CH_4 and CeO_2 at high temperatures in addition to the reactions on the Ni surface that produce CO and H_2. Moreover, the reduced state of ceria, CeO_{2-n}, can react with CO_2 and H_2O to produce more CO and H_2 and regenerate CeO_2. Redox reactions between CH_4 and lattice oxygen which take place on the CeO_2 surface improve the reforming activity and increase the resistance towards carbon deposition (Laosiripojana *et al.,* 2005). The high resistance to carbon deposition is also attributed to the high oxygen storage capacity (OSC) of ceria (Laosiripojana and Assambumrungat, 2006a).

In SOFC applications, ceria is very well known as an oxidation catalyst that can increase the activity for anodic oxidation of hydrogen and hydrocarbons. In general, finely dispersed ceria is more active than doped ceria as an oxidation catalyst (Atkinson *et al.,* 2004). However, Zhao and Gorte (2004) reported that the rates of oxidation of methane on ceria and samaria-doped ceria were very similar.

Anode material

Pure Ni has an electronic conductivity of 2.0×10^4 S cm^{-1} at 1000°C and is an excellent catalyst for C-H breaking and fuel oxidation. The electrochemical activity of Ni-based anodes in SOFC depends strongly on the triple-phase boundary (TPB) where Ni, gas and the electrolyte phase meet (Jiang and Chan, 2004). The main drawback with the use of Ni, however, is that it catalyzes carbon formation when hydrocarbons are used as fuel. Consequently, numerous studies focused on developing Ni-free anodes for use with hydrocarbon fuels have been reported.

Gorte *et al.* introduced the use of Cu-based anodes based on the idea that Cu does not catalyze carbon formation and has high electronic conductivity. They found that Cu-YSZ anodes performed poorly due to the negligible activity of Cu for the oxidation of hydrogen and hydrocarbons. However, by incorporating ceria into this Cu-YSZ anode, this group was able to operate the cell using various hydrocarbon fuels and maintain stable conditions without any carbon deposition. They suggested that ceria plays a catalytic role in the composite anode and that the addition of an oxide such as ceria is crucial for the acceptable performance of a Cu-based anode (Gorte *et al.,* 2002; McIntosh *et al.,* 2002; Gorte and Vohs, 2003).

Other Ni-free anodes examined to minimize carbon deposition in SOFCs are perovskites. Tao and Irvine (2003) employed LSCM ($(La_{0.75}Sr_{0.25})Cr_{0.5}Mn_{0.5}O_{3-\delta}$) in a CH_4-fuelled SOFC at 900°C and found this anode to have good catalytic activity for electrochemical oxidation of CH_4, while maintaining good stability in both reducing and oxidizing conditions. Among the promising materials from titania-based oxides, $Sr_{0.88}Y_{0.08}TiO_{3-\delta}$ (YST) was found to be very stable and maintain good electronic conductivity in a reducing environment (Jiang and Chan, 2004). He *et al.* (2004) introduced ceria into YST-YSZ anodes to enhance their catalytic activity. The cells exhibited excellent OCVs in the presence of H_2 and CH_4, indicating a good CTE match between YST and YSZ, but generated moderate power densities. A double perovskite, Sr_2MgMoO_6 (SMMO), was also studied and successfully used with methane and sulphur-containing fuels to give good performance (Huang *et al.,* 2006).

Although these perovskites displayed an excellent resistance to carbon deposition when operated in SOFC with hydrocarbons, they still have problems with performance or chemical stability. LSCM and YST, for example, have low electronic conductivities so that their electrical performance is much inferior to that of Ni-based anodes (Sun and Stimming, 2007). Despite

showing reasonable performance with hydrocarbons, SMMO was observed to react with most of the commercially available SOFC electrolytes (i.e. YSZ, GDC and LGSM) at high temperatures. The SMMO-electrolyte interactions produced new phases that caused an increase of the ohmic and polarization resistances (Marrero-López *et al.*, 2010). On the other hand, Ni is an excellent electronic conductor and is thermally and chemically compatible with the electrolytes. Ni-based anodes have good electrochemical catalytic activity for hydrogen and hydrocarbons, ease of fabrication and are relatively inexpensive. Due to these desirable properties, Ni remains the preferable choice for SOFC anodes and so various efforts have been made to improve the carbon tolerance of Ni-based anodes.

Considering that Ni is already a good oxidation catalyst, the addition of doped-ceria to Ni would be expected to enhance fuel oxidation within an SOFC anode. Wang *et al.* (2003) observed Ni-SDC anodes to exhibit high catalytic activity, low polarization and stable performance in SOFCs for 30 hrs under OCV conditions while treating dry CH_4 feed. They found Ni-SDC to have lower polarization than Ni-YSZ and proposed that Ni-SDC is a better anodic electrocatalyst due to the mixed conductivity of SDC. Under reducing condition at the anode, lattice oxygen anions are released from the SDC. Accompanying the release of lattice oxide ions are the liberation of two electrons. The oxide ions participated in the electrochemical oxidation of CH_4 while the liberated electrons were rapidly transferred to the current collector through the conductive network between Ni and SDC. Iida *et al.* (2007) have measured the carbon deposition rate for several anode materials by gravimetric technique and found that the Ni-SDC has the highest carbon deposition rate. SOFC operation under a current load however showed more stable operation in Ni-SDC compared to the Ni-YSZ. The deposited carbon formed over Ni-SDC can be effectively removed with a supply of current. Iida *et al.* (2007) stated that the oxygen potential at the anode during the carbon deposition is very low causing the reduction of ceria. The reaction of reduced ceria with electrochemical products, H_2O or CO_2 incorporates oxygen in the lattice. The lattice oxygen will subsequently eliminate the carbon, making the removal of carbon proceeds more rapid for Ni-SDC than for Ni-YSZ.

Cathode material

The traditional cathode material, LSM, has good electronic conductivity (~ 300 S cm^{-1} at 900°C) and low ionic conductivity. However, its electrical properties are not sufficient for SOFC operation at temperatures below 800°C (Sun *et al.,* 2009). $Sm_{0.5}Sr_{0.5}CoO_3$ (SSC), $La_{0.6}Sr_{0.4}Co_{0.2}Fe_{0.8}O_{3-\delta}$ (LSCF) and $Ba_{0.5}Sr_{0.5}Co_{0.8}Fe_{0.2}O_{3-\delta}$ (BSCF) have been the most studied materials as cathode alternatives for use in SOFCs at low temperatures. As mixed ionic-electronic conductors, they exhibit lower cathodic polarization resistance and higher ionic conductivity compared to LSM. The polarization resistance of LSM-GDC with YSZ electrolyte was reported to be 0.65 Ω cm^2 at 650°C (Xia *et al.,* 2003). A LSCF-GDC cathode with GDC electrolyte exhibited lower polarization resistances of 0.33 Ω cm^2 and 0.1 Ω cm^2 at 600 and 700°C, respectively (Murray *et al.,* 2002). A lower value of 0.18 Ω cm^2 at 600°C was obtained when an SSC-SDC cathode with SDC electrolyte was tested (Xia *et al.,* 2002). Remarkably low values of 0.051-0.071 Ω cm^2 at 600°C were obtained for BSCF cathode materials (Shao and Haile, 2004).

Since the cathode-electrolyte interfacial resistance is the biggest contributor to the total cell resistance (Xia and Liu, 2002), replacement of LSM with a material having better catalytic activity and conductivity at low temperatures is necessary to maintain high power densities. Except for BSCF, these materials also have greater electronic conductivities than LSM at low temperatures. LSCF and SSC exhibit electronic conductivities about two and ten times, respectively, higher than LSM at 600°C. The electronic conductivities for the LSM, SSC, LSCF and BSCF at 600°C are shown in Table 2-4.

Table 2-4 Electronic conductivities of LSM, SSC, LSCF and BSCF at 600°C (Rembelski *et al.,* 2012)

Materials	Electronic conductivity, S cm^{-1}
LSM	~180
SSC	~1000
LSCF	~300-400
BSCF	~30

SSC was chosen in this work due to its high electrochemical activity and electrical conductivity. The electrochemical performance of SSC also can be improved by the addition of doped-ceria which tends to suppress SSC particle growth, maintain good porosity within the cathode structure and increase the TPB area (Zhang *et al*., 2006). A few studies have reported the excellent performance of Ni−SDC cells with SDC electrolyte using SSC-SDC cathode. The optimum SDC content in the SSC−SDC cathode composite was found to be 25-30 wt.% (Xia *et al.*, 2002; Zhang *et al*., 2006; Wang *et al*., 2008a).

2.4.3 SOFC designs

Two main types of cell configuration in SOFCs are tubular and planar designs. In tubular SOFC, the cylindrical cell is more resistant to the thermal stress damage to its structure. Another advantage of tubular SOFCs is that they do not require gas-tight sealing. Compared to tubular SOFCs, the planar design is easier to fabricate and uses less material, making it cheaper to manufacture. A planar SOFC is comprised of flat plates which are rectangular or circular in shape. They appear to be more attractive due to better performance when measured on the basis of active cell surface area. This is attributed to the smaller ohmic resistance associated with the transport of the oxide ions and electrons. The main concerns with the planar design, however, are the strict requirements that the thermal expansion coefficients of the components match each other and that seals be gas-tight (Li, 2006).

Cell support plays the important role of providing the mechanical strength to the whole device. Cathode-supported structures are normally used in tubular cells, while electrolyte- and anode-supported structures are more common in planar cells. In an electrolyte-supported cell, relatively strong structural support is provided by a dense and thick electrolyte, while the anode is generally thin (~50 μm). On the other hand, an anode-supported cell contains a thin electrolyte supported by ~ 1 mm thick anode.

The breakdown in connectivity in any of the three phases at the TPB will hinder the reactions at the anode and cathode (Gorte and Vohs, 2003). It has been estimated that the electrochemical reactions in the anode at the TPB occur a distance not more than 10 μm from the electrolyte (Gorte and Vohs, 2003). The factors affecting the active area in the composite anode are its microstructure (solid grain size, pore size, porosity) and composition (Deng and Petric, 2005; Ai

et al., 2008). The effective reaction zone can also be enlarged by use of mixed ionic-electronic conductor (MIEC) oxide such as doped-ceria in the anode. Fukunaga *et al.* (2007) showed that an effective thickness of Ni-SDC anodes was 110 μm, but can be increased above this level if the anode structure is further optimized. The region in an anode that contains the entire TPB is commonly known as an anode functional layer and the optimization of this region improve the charge-transfer processes. In an electrolyte-supported cell, an entire thin anode can be considered to be a functional layer, while in an anode-supported cell, portions of the anode that do not contain a TPB function as a support layer or so-called conduction layer.

During lower temperature operation, electrolyte-supported cells tend to experience large ohmic polarization due to the high resistance to oxide ion transport through the thick electrolyte. Since ohmic loss is one of the dominant factors affecting cell performance, reduction of the electrolyte thickness is desirable and so anode-supported cells are preferable in the development of SOFCs for operation at low- and intermediate temperatures (Huijsmans, 2001). The technical challenges in anode-supported design are primarily to construct a thin electrolyte without any defects (e.g. cracks, pinholes) and form a dense and gas-tight electrolyte that adheres to the porous anode substrate. These features prevent the cross-over of gases through the electrolyte (Basu *et al.,* 2008). Also, the effect of concentration polarization becomes important in the anode-supported cells due to limitations of reactant gas transport to the anodic reaction sites through the thick porous anode (Kim *et al.,* 1999). While a finer-grained microstructure is necessary to reduce the effective charge-transfer resistance, the anode has to be porous enough to facilitate the diffusion of gaseous species (Tanner *et al.,* 1997). On the other hand, excessive porosity will significantly reduce the mechanical strength of the anode (Yu *et al.,* 2007). Since the anode functions as a support in this type of cell, maintenance of adequate mechanical strength is very important.

2.5 Internal reforming in SOFCs

Other than the anode-electrolyte interface area which active for the electrochemical reactions, the remainder of the anode in anode-supported cells serves non-electrochemical purposes. It functions as an electronic conductor to carry electrons from the charge-transfer region to the current collector and as a structural backbone for the cell. In addition, the remaining anode may serve as catalytic sites for heterogeneous chemical reactions when the SOFC is fuelled with hydrocarbons. Ni contained in an SOFC anode support is known as an excellent reforming catalyst (Belyaev *et al.,* 1995) and is active for thermal decomposition of hydrocarbons (Kishimoto *et al.,* 2006). The catalytic activity of Ni allows SOFCs to internally reform hydrocarbons and use CO as a fuel, both of which give SOFC its fuel flexibility.

Within the anode structure, the hydrocarbons are reformed by reacting with steam. This process is catalyzed by Ni and produces H_2 and CO which are then readily oxidized by the electrochemical reactions. Steam reforming of methane, which is the main component of natural gas, occurs by the reaction:

$$CH_4 + H_2O \rightarrow 3H_2 + CO \tag{2.23}$$

which has a standard enthalpy $\Delta H^0_{298} = 206\ kJ\ mol^{-1}$.

The Ni anode also catalyzes the water-gas shift reaction ($\Delta H^0_{298} = -41\ kJ\ mol^{-1}$) to form more H_2 fuel:

$$CO + H_2O \rightarrow H_2 + CO_2 \tag{2.24}$$

Internal steam reforming is made possible due to the elevated SOFC operating temperatures. Heat generated in the cell by the electrochemical reactions is directly used for the endothermic reforming reaction. The main concern with the process, however, is the large temperature gradient within the anode originating from the endothermic steam reforming occurring at the outer region and the exothermic electrochemical reaction at the inner region of the anode. This large temperature gradient may cause thermal stress within the cell structure. Another problem with internal steam reforming is that the fuel must also contain water which dilutes the fuel, lowers the cell voltage and reduces the electrochemical efficiency (Mogensen and Kammer, 2003).

2.6 Direct hydrocarbon utilization in SOFCs

Another important application of anode-supported cells is direct utilization of hydrocarbons. In direct conversion, hydrocarbon fuel is fed directly into the anode compartment without processing the fuel and significant mixing with H_2O or CO_2 (Mogensen and Kammer, 2003). Direct use of hydrocarbons in SOFCs has high thermodynamic efficiency and reduces the thermal gradient within the cell when steam reforming occurs.

Mogensen and Kammer (2003) defined the direct conversion of hydrocarbons as either the direct electrochemical oxidation of the fuel or the electrochemical oxidation of the decomposition products from the hydrocarbon fuel. When referring specifically to direct oxidation, all steps in the reaction must be electrochemical steps. Therefore, any process that involves decomposition or cracking of the hydrocarbon on the anode surface followed by the electrochemical oxidation of the cracking products is not classified as being direct oxidation. McIntosh and Gorte (2004) stated that it is unlikely that the electrochemical oxidation of hydrocarbons could occur without heterogeneous chemical reactions involving the scission of C-H and C-C bonds on the anode compartment. Mogensen and Kammer (2003) also suggested that both direct chemical oxidation and oxidation of cracking products can occur in parallel. In addition, the direct oxidation might not only involve with total oxidation but also partial oxidation reactions.

CH_4 may be electrochemically oxidized at the TPB, but also decompose within other regions of the anode support. Buccheri and Hill (2012) have listed the chemical and electrochemical reactions that may possibly occur at the anode when fuelled with CH_4. The anode may contain a maximum of six species according to their thermodynamic stabilities: deposited carbon (C), H_2, CO, CO_2, H_2O and residual CH_4. One possible chemical reaction within the anode is methane decomposition, also known as methane cracking (Eq. 2.25), which produces H_2 and carbon deposit:

$$CH_4 \rightarrow C + 2H_2 \qquad 2.25$$

In addition, steam reforming (Eq. 2.23) and water-gas shift reaction (Eq. 2.24) may also possibly occur with the participation of H_2O produced electrochemically at the TBP region. Species such as C, H_2, CO and CH_4 may be anodically oxidized by reaction with O^{2-} via the following electrochemical reactions:

$$C + O^{2-} \rightarrow CO + 2e^{-} \quad (2.26)$$

$$H_2 + O^{2-} \rightarrow H_2O + 2e^{-} \quad (2.27)$$

$$CO + O^{2-} \rightarrow CO_2 + 2e^{-} \quad (2.28)$$

$$CH_4 + 4O^{2-} \rightarrow 2H_2O + CO_2 + 8e^{-} \quad (2.29)$$

$$CH_4 + 2O^{2-} \rightarrow 2H_2 + CO + 2e^{-} \quad (2.30)$$

The primary problem with direct hydrocarbon oxidation is the faster cell degradation due to carbon deposition on the anode surface. With direct feed of hydrocarbons, Ni actively catalyzes the carbon formation. Also, it is not possible to entirely prevent carbon deposition in the presence of high oxide ion concentration when current is flowing. The O^{2-} flux can only remove carbon in a region near the TPB and has no influence on the situation at the Ni cermet in the anode support region (McIntosh and Gorte, 2004). Anode-supported cells exhibit better OCV and larger limiting current densities than electrolyte-supported cells when methane fuel is being used. The conduction layer enhances the catalytic activity for decomposition and/or reforming reactions within the thicker anode and improves the performance. However, this cell design is more harmed by carbon deposition than electrolyte-supported cells due to higher degradation rates in the presence of methane (Buccheri *et al.,* 2011).

2.7 Carbon deposition in SOFCs

Carbon deposition is a major problem for SOFCs operating with hydrocarbon fuels. Surface carbon deactivates the SOFC anode by blocking the access of reactants to reaction sites (Maček *et al.,* 2007), while the growing carbon filaments can lead to Ni loss due to metal dusting (Toh *et al.,* 2003). In addition, the deposition of carbon may lead to volume expansion within the anode and fracture the anode structure (Kim *et al.,* 2002). In SOFCs, Ni-based anode catalysts are not only excellent for reforming and electrochemical reactions but also can initiate the formation of carbon when hydrocarbons such as methane are directly utilized used as fuel. This occurs through decomposition or cracking (Eq. 2.25) whereby CH_4 dissociates on the Ni surface and

loses its hydrogen atoms in sequence to produce CH_x intermediates and form atomic carbon. The dissociative adsorption reactions for methane decomposition are (Trimm, 1999):

$$CH_4 \rightarrow CH_x + \frac{(4-x)}{2} H_2 \quad 2.31$$

$$CH_x \rightarrow C + \frac{x}{2} H_2 \quad 2.32$$

Methane decomposition initiates the deposition of carbon at high temperatures. The rate of methane decomposition increases with temperature and leads to an increase of carbon deposition on the catalyst surface, even more so at temperatures higher than 700˚C (Murray *et al.*, 1999). Another pathway for the formation of carbon is the disproportionation of CO in the system through the Boudouard reaction:

$$2CO \rightarrow C + CO_2 \quad 2.33$$

Since this reaction is highly exothermic, its equilibrium is shifted to the right as the temperature is reduced and so contributes to more carbon deposition. In fact, most of the carbon formed during low-temperature SOFC operation is associated with this reaction (Wang *et al.*, 2008b).

From a thermodynamic analysis, the regime where carbon is unstable can be determined and the amount of steam needed to avoid carbon deposition for a particular fuel can be calculated. For example, a steam-to-carbon ratio (S/C) of 1.5 was found to be sufficient to prevent carbon deposition for methane fuel over the temperature range 100-1000°C (Sasaki and Teraoka, 2003). Nonetheless, thermodynamic calculations only reflect the expected equilibrium conditions and do not account for the impact of reaction kinetics. Experiments have shown that carbon can form under conditions where it is predicted to be thermodynamically unstable (Kim *et al.*, 2006). Thus, kinetics play a very important role in controlling carbon deposition and must be considered when determining the conditions for stable operation without carbon deposition (Offer *et al.*, 2009).

The extent of carbon deposition is governed by a balance between carbon formation and carbon removal. Obviously, carbon accumulation occurs when the rate of carbon formation exceeds the rate of carbon removal (Trimm, 1999). The main processes by which carbon forms are methane decomposition (Eq. 2.25) and the Boudouard reaction (Eq. 2.33). Carbon can be electrochemically oxidized and removed by reaction Eq. 2.26. The interaction of carbon with

H_2O and/or CO_2 produced from the electrochemical reactions at the anode also help to remove it. he presence of significant amounts of CO_2 and H_2O in the vicinity of the anode can remove carbon by reversal of the Boudouard reaction (Eq. 2.34) and gasification via reaction 2.35:

$$C + CO_2 \rightarrow 2CO \quad 2.34$$

$$C + H_2O \rightarrow CO + H_2 \quad 2.35$$

2.7.1 Type of carbons

The morphology and the reactivity of the carbon deposited at the anode of SOFCs are varied depending on the fuels, anode materials and the operating conditions. Sehested (2006) indicated three kinds of carbon morphology produced within the hydrocarbon environments: 1) pyrolytic carbon 2) whisker carbon and 3) encapsulating carbon. At high temperatures, carbon deposition mechanisms involve with the reactions in a gas phase or the reactions over solid surface of catalyst.

Pyrolytic carbon is known as gas-phase carbon formed in non-catalytic free-radical, gas-phase condensation reactions. This carbonaceous compound is formed by the exposure of hydrocarbons heavier than methane to high temperatures. Pyrolytic carbon deposits on the external surface of solids rather than on the internal surfaces of porous solids. Hence, its formation does not cause pitting of the surfaces to which the hydrocarbon is exposed (McIntosh and Gorte, 2004).

The C-H bonds in methane are much stronger than the C-C bonds in higher hydrocarbons. Thus, higher temperatures are needed to pyrolyze CH_4 than that required for larger alkanes. Therefore, in the case of carbon deposition from methane, it is most likely that the carbon is formed by surface reactions (He and Hill, 2007). Although carbon formation on Ni catalyst surfaces has been well investigated, not all aspects are fully understood yet (Trimm, 1999). It is believed that methane dissociates on the surface of Ni and produces highly reactive monatomic carbon that can be easily removed by the carbon removal reactions. However, if an excess of carbon forms and/or carbon removal reactions are slow, it can polymerize to a less reactive form. Once present as a polymer, carbon is much more difficult to remove and so will accumulate on the surface of catalyst or dissolve into the bulk of the nickel particles (Trimm, 1999). The dissolution of carbon into the Ni catalyst causes the formation of carbon whiskers or filaments through a dissolution-precipitation mechanism. According to this mechanism, dissolved carbon

diffuses through the Ni particles to their grain boundaries where it precipitates as a thin fiber at the Ni rear side. These carbon fibers tend to press against the Ni particles as their filament tips grow. This stress causes lifting and separation of the Ni particles from the anode support which can eventually lead to fracture and even catastrophic failure or fragmentation of the catalyst (Snoeck *et al.,* 1997).

Kan and Lee (2010a) found whisker carbon or known as carbon filaments on a Ni-GDC anode when investigating the effect of introducing Fe into an anode-supported cell operating with dry methane fuel at 650°C. This caused a slight decrease in cell voltage although operation remained stable for 50 hr. A similar type of carbon deposit was found on a Ni-YSZ anode by the same group when operating with a humidified methane fuel at 650°C (Kan and Lee, 2010b). They proposed that the carbon initially deposits in an amorphous form in both cases, but it transforms into a crystalline structure as it accumulates after a prolonged exposure at high temperature. It is the crystallized filament form of carbon that appears to cause cell degradation. The transformation of carbon filaments into a strongly bound structure at high temperature over time was also reported by Finnerty and Ormerod (2000). Chen *et al.* (2011) also confirmed that the carbon morphology and its effect on the degradation of Ni-based anode supported cells are strongly affected by the operating temperature.

At high temperatures, the dissolution of carbon filaments into Ni particles has also been observed. He and Hill (2007) reported filamentous carbon to be the dominant form found on Ni-YSZ pellet at temperatures up to 600°C. When the temperature was increased above 750°C, the amount of carbon deposit formed significantly increased although most was observed to dissolve into the bulk of the Ni particles and cause a significant expansion of the Ni-YSZ structure. However, when oxidation of this dissolved carbon began to occur, the Ni-YSZ structure collapsed entirely. Nikooyeh *et al.* (2008) reported the formation of carbon filaments on Ni-YSZ cermet at 800°C when hydrogen was present in the methane feed stream. This carbon was subsequently removed fully by temperature-programmed hydrogenation (TPH) without damage to the Ni-YSZ structure. In the absence of hydrogen, carbon dissolved into Ni particles and irreversibly changed the Ni structure. In this case, the removal of carbon by TPH led to the appearance of numerous cracks on the Ni particle surfaces.

Encapsulating carbon originates either from polymeric carbon or gas-phase carbon. Encapsulating carbon may consist of a thin hydrogenated carbon (CH_x) film or a few layers of graphite covering the nickel particles. This type of carbon remains on the surface of Ni, encapsulates the surface and results in the loss of activity and deactivation of the catalyst (Sehested, 2006). Carbon deposits formed on the surface can contain fairly ordered structures, possibly formed via dehydrogenation, surface migration and growth (Trimm, 1999).

Granular and encapsulating carbons are the types of carbon responsible for blockage of anode active sites, causing fuel shortage and degradation of cell performance in most SOFC operations. Alzate-Restrepo and Hill (2008) reported the formation of granular-type carbon when operating Ni-YSZ anode in SOFC with dry methane fuel at 800°C. Under current load when the electrode is polarized they suggested that the dehydrogenation of methane becomes slower and the adsorbed CH_x species do not completely dehydrogenate. These species do not diffuse through the Ni particles and instead remained on the anode surface as a granular-type of carbon deposit. Similarly, a significant amount of carbon has been observed on the surface of both Ni-YSZ and Ni-SDC anodes operating with humidified methane fuel at 850°C. The blockage of the anode by this carbon was responsible for the deterioration of cell performance and led to an increase of gas-phase diffusion resistance (Yun *et al.,* 2012). Sumi *et al.* (2010) found a large amount of encapsulating carbon on a Ni-YSZ anode surface in a SOFC operating with methane at a S/C ratio of 0.5 and 1000°C. The encapsulating carbon covered the Ni-YSZ surface and deactivated the anode by decreasing its catalytic activity and inhibiting gas diffusion.

Carbon deposits also can be characterized in terms of its reactivity with oxygen through temperature-programmed oxidation (TPO). TPO has been a useful technique that for determining the amount and type of carbon deposited on SOFC anodes. The type of carbon formed on the catalyst surface and the reactivity of the deposits are determined from measuring the temperature at which it is oxidized to CO_2. Finnerty *et al.* (1998) have categorized carbon found on Ni-YSZ surfaces using the terminology of type I, type II and type III according to TPO profiles. Type I carbon can be removed from the Ni-anode at a temperature of ~ 597°C, type II is removed just above 627°C and type III can only be removed above 727°C. Type III is the most strongly bound-type of carbon believed to have a graphitic structure. Meanwhile, type I is the most reactive carbon and type II carbon is formed from type I over time, possibly due to ageing processes. Guo *et al.* (2007) have classified carbon deposited on Ni-based catalysts into Cα, Cβ

and Cγ based on the temperature where the CO_2 peaks appear in TPO profiles. Peak Cα is observed at temperatures below 250°C, Cβ at temperatures in the range 250-600°C and Cγ above 600°C. The forms of carbon Cα and Cβ detected at low temperatures on the TPO profile are reactive, while Cγ appearing at higher temperatures is inert. It is reported that Cα and Cβ are amorphous or polyaromatic carbon and Cγ is graphite-like carbon.

2.8 Carbon inhibition

When hydrocarbon fuels are being used, carbon deposition on Ni is almost unavoidable. Therefore, carbon deposition must be minimized to extend the useful lifetimes of Ni-based anodes when operating with hydrocarbons. Thus, considerable effort has been expended to modify Ni cermets to take advantage of their good properties and reduce the deposition problem. One approach has been to use alloys or impregnate Ni-based anodes with metals such as Cu (Kim *et al.*, 2002; Park *et al.*, 2009), Sn (Nikolla *et al.*, 2009a; Kan *et al.*, 2009; Singh and Hill, 2012) and Au (Niakolas *et al.*, 2010).

Since Cu does not catalyze the formation of carbon filaments, alloying Ni with Cu has reduced the amount of carbon deposited on anode surfaces (Kim *et al.*, 2002). Unfortunately, CuO_x and Cu melt at temperatures below that needed for electrolyte sintering impede the application of Cu-based anodes in SOFCs. Also, Cu ions tend to migrate into the YSZ electrolyte during high-temperature calcination. This complicates matters by requiring fabrication methods in which Cu is added in a separate step that does not involve high-temperature processing (Gorte and Vohs, 2003).

From DFT calculations, Nikolla *et al.* (2009b) proposed that the ability of Sn to disrupt carbon formation is due to its displacement of Ni atoms at the step sites of Ni particles. Sn neutralizes the active step sites which serve as the nucleation centers for carbon and moves the dominant pathways to the more abundant, yet less active, terrace sites. The same group found that the introduction of Sn did not affect the electrochemical activity and electronic conductivity of the anode. They also proposed that the addition of Sn to Ni anodes improves their carbon tolerance by their ability to catalyze the oxidation of the C atoms rather than forming C-C bonds (Nikolla *et al.*, 2009a). The opposite effect, however, was observed by Singh and Hill (2012) who reported that the addition of Sn did not improve the electrochemical reaction rate or carbon

tolerance on Ni-based anodes. In fact, the presence of large amounts of Sn was believed to hinder the carbon removal reactions.

The carbon tolerance of bimetallic Au-Ni anodes was studied by Neophytides's group. The presence of Au allowed stable operation with no obvious carbon deposition even at high methane concentration ($CH_4/H_2O>3$). This group suggested that the Au-Ni alloy surface retards the sequential dehydrogenation of CH_x species that produces carbon. Instead, the oxidation of CH_x to the oxyhydrogenated species CH_xO which subsequently decomposed to CO and H_2 was observed (Gavrielatos *et al.,* 2008; Niakolas *et al.,* 2010).

The use of noble metals such as Ru, Pt and Pd has also been considered for carbon inhibition. Small additions of Ru, Pt and Pd have been found to improve the electrochemical activity of Ni-based anodes and suppress carbon deposition. Takeguchi *et al.* (2003) added Ru and Pt when operating SOFC under internal reforming conditions and suggested that the steam reforming of methane becomes rapid due to the effective gasification of the carbonaceous specious. Very little carbon deposited and enough hydrogen was formed to improve the cell performance. Based on their study on the use of a Pd-Ni anode with a dry methane fuel, Nabae *et al.* (2006) suggested that although the anode enhanced the methane decomposition to H_2 and C, the deposited carbon so formed was smoothly gasified by the H_2O produced electrochemically.

Alkaline earth oxides (CaO, MgO, SrO and BaO) have also been investigated for their capabilities to minimize carbon formation. CaO and SrO were effective in suppressing carbon deposition on Ni-YSZ anodes, while MgO was found to promote carbon deposition (Takeguchi *et al.,* 2002). A slight decrease in the power density was observed with the addition of alkaline oxides which was attributed to the electronic insulation from the oxides. A similar trend was reported after the incorporation of CaO, SrO and MgO into Ni-SDC anodes by Asamoto *et al.*(2009), with the exception of MgO that was found not to affect carbon deposition. Another promising alkaline metal oxide for carbon removal is BaO. BaO nanostructures are believed to promote the water-mediated carbon removal reactions on Ni anodes. The formation of nanosized BaO islands on the anode surface by vapor deposition successfully sustained the Ni-YSZ performance for 100 hrs under C_3H_8 with no degradation (Yang *et al.,* 2011).

2.8.1 H_2S as carbon inhibitor

Another substance well known to have a harmful effect on SOFC operation is sulphur. Sulphur is commonly added to natural gas as an odorant in various forms such as thiophene, mercaptan, dimetyl sulphide or H_2S (Pacific Gas and Electric Company, 2014). Sulphur poisons SOFC anodes and leads to degradation of the electrochemical performance (Sasaki *et al.,* 2006) and reduced methane conversion (Rasmussen and Hagen, 2010). On the other hand, sulphur has been reported to have a positive effect by inhibiting carbon formation. In a review on coke minimization, Trimm *et al.* (1999) stated that a controlled amount of sulphur on the Ni surface is an effective way to reduce the extent of carbon deposition.

In an early effort to inhibit carbon formation by adding sulphur to the gas stream, Rostrup-Nielsen (1984) used H_2S for methane steam reforming. Rostrup-Nielsen suggested that carbon deposition on a Ni-based catalyst can be controlled by the adsorption of sulphur on its surface. Carbon filaments were entirely eliminated and only amorphous carbon remained on the Ni surface at a critical sulphur coverage that depended upon the temperature and partial pressure of H_2S. The mechanism proposed to explain this effect involved a concept known as *ensemble size control* by which the size of Ni ensemble sites responsible for methane reforming or carbon formation is controlled by the occupancy of sulphur. Carbon deposition is reduced by minimizing the size of these sites and thereby interfering with the reactions that form carbon. Compared to the reforming reaction, carbon formation was more affected by the sulphur. It was also suggested that a larger number of active sites is needed for carbon formation than for methane reforming. As carbon formation proceeds from methane decomposition to the dissolution of adsorbed carbon in Ni particles and finally to carbon precipitation, the size of the ensemble sites increases. With occupancy of sulphur, the ensemble sites for dissolution of adsorbed carbon are blocked and the dissolution of carbon into Ni is retarded. Meanwhile, enough sulphur-free Ni ensembles remain for the adsorbed carbon to react with steam. Hence, carbon filament formation is suppressed while methane reforming proceeds at a slower rate.

Kuhn *et al.* (2008) investigated the influence of H_2S on the catalytic activity of Ni-YSZ cermet during methane steam reforming. The cermet was exposed to H_2S at 700°C before being cooled down and fuel gases were introduced. They discovered that the effect of sulphur on methane reforming and carbon formation depends strongly on temperature. At low temperature (<525°C)

under H_2S flow, the activity for methane conversion exhibited only a small decrease although carbon deposition was effectively inhibited. However, at temperatures above 700°C, both methane reforming and carbon formation were deactivated. It appeared that H_2S inhibited the methane decomposition that caused carbon formation but also reduced the activity for methane reforming at these higher temperatures.

Since sulphur compounds adsorb very strongly on Ni, it is necessary to introduce only tolerable quantities of sulphur to prevent total deactivation of the catalyst. For example, 1 ppm of H_2S used by Rostrup-Nielsen (1984) was sufficient to render the formation of carbon filaments, while 50 ppm H_2S employed by Kuhn *et al.* (2008) likely deactivated methane reforming. Therefore, the amount of H_2S in the system should be controlled to a level that inhibits carbon formation but still permits methane activity on a sufficient number of active sites.

The effect of sulphur on hydrocarbon reforming and carbon formation was also studied theoretically using DFT calculation. Bengaard *et al.* (2002) proposed the presence of two kinds of active sites on the Ni surface that are involved in methane reforming and carbon formation: steps and terraces. Due to the different binding energies of these two sites to sulphur, sulphur atoms preferentially bind to step sites rather than terrace sites. Calculations demonstrated that carbon formation begins with its nucleation at steps and then proceeds with growth over the nearby terrace sites. Thus, the adsorption of sulphur species on Ni step sites should block the sites for carbon formation. Whereas Rostrup-Nielsen (1984) proposed that carbon inhibition by sulphur occurs due to an insufficient number of sites in the ensemble for carbon dissolution, Bengaard *et al.* (2002) suggested that sulphur inhibits carbon formation due to a competition for step sites on the basis of DFT. They also suggested that the unoccupied terrace sites may dominate methane reforming after sulphur introduction by providing a stable but lower rate for this process.

Abild-Pedersen *et al.* (2005) used DFT calculations to calculate the energy barriers for methane decomposition on Ni step sites. They found that although step sites are highly active, the reaction does not occur exclusively on steps. While the steps can be blocked to eliminate carbon formation, methane activation is still possible on the terrace sites with a moderate decrease in its rate. Galea *et al.* (2007) later computed the energy barriers for the various stages of methane decomposition. They found that sulphur blocking inactivates the step sites for

methane decomposition and forces adsorption to occur on the terrace sites lying between the steps. Comparison of the energies for methane decomposition on sulphur-blocked step sites and free terrace sites revealed a much higher barrier for the reaction on the blocked step sites, indicating that the reaction on terrace sites is dominant. Based on these DFT analyses, carbon formation inhibition on the Ni surfaces is possible by the blocking of step sites by active species such as sulphur. At the same time, methane activation can occur on terraces with a moderate reduction in reforming rate.

Grgicak *et al.* (2008) examined the effect of H_2S on carbon deposition in SOFC in the presence of dry methane fuel. This group used much higher concentrations of H_2S (i.e. 10% v/v) than previous researchers studying steam reforming. In the presence of dry CH_4 fuel with no H_2S, a significant amount of carbon confirmed to be graphite deposited on both Ni-YSZ and Co-YSZ anodes. This carbon caused a full degradation and disengagement of the anode from their electrolytes. When the H_2S was introduced into the fuel, the cell performance initially decreased, but then began to improve and eventually stabilize. The group suggested that the initial disruption when H_2S was introduced into the system may have been caused by the initial blocking of the actives sites due to sulphur adsorption on the metal surface. The slight recovery of the catalytic activity after a prolonged supply of H_2S was attributed to the conversion of the adsorbed sulphur into metal sulphide compounds believed to have a good resistance towards carbon formation.

Recently, the introduction of H_2S into a reformate stream was reported to significantly prolong the operating life of an SOFC stack consisting of Ni-YSZ anodes to over 3,000 hrs (Mukerjee *et al.,* 2013). The controlled addition of H_2S (0.5 to 2.5 ppm) to the reformate stream (28% H_2, 30% CO, 6% H_2O) effectively retarded the formation of carbon and prevented the coarsening of the granular microstructure of the Ni-YSZ anode, while not degrading the power output from the stack.

Grgicak *et al.* (2008) suggested that the stable anode performance in the presence of dry methane and H_2S could be attributed to metal sulphide formation. Thermodynamic analysis by Wang and Liu (2007), however, showed that only a sulphur-adsorbed Ni intermediate should be present during most SOFC operations at 650-800°C, if operating at H_2S concentrations below than 1000 ppm. They suggested that sulphidization which leads to metal sulphide formation

would not likely occur at the high temperatures during SOFC operation. Their finding was supported by the *in situ* Raman spectroscopy analysis of Cheng and Liu (2007). At SOFC operating temperatures (>500°C), no metal sulphides were observed even when a high H_2S concentration of 100 ppm was introduced into the system. The presence of metal sulphides was only detected at 300°C after the Ni-YSZ anode was cooled slowly.

2.9 Summary

To summarize, the literature review that has been presented can be summarized as follows:

- SOFCs can operate with high energy efficiency and have much greater flexibility than other fuel cell types with regard to the fuels that can be used and the direct utilization of hydrocarbons.
- In order to reduce the cost and solve the mechanical problems related to high temperature operation, it would be desirable to operating SOFS at lower temperatures. Thus, the materials chosen for intermediate-temperature SOFC operation in this study are:

  electrolyte: samaria-doped ceria (SDC)
  anode: nickel-samaria-doped ceria (Ni-SDC)
  cathode: samaria-doped strontium cobalt oxide- samaria-doped ceria (SSC-SDC)
- Carbon deposition is the main problem in SOFCs when operating with direct hydrocarbon fuels. Rapid degradation in the cell performance has been attributed to the deposition of various types of carbon on the anode.
- Carbon deposition on Ni-based anodes must be controlled when operating with hydrocarbon fuels. Many studies on carbon inhibition have been reported; carbon minimization is possible by retarding the carbon-producing mechanisms and/or improving the carbon removal reactions.
- Sulphur has been reported to inhibit carbon deposition. Nonetheless, its poisoning effect on electrodes and catastrophic effects on SOFC cell performance is also well known. Thus, further research is needed into the role of sulphur as a carbon inhibitor in SOFCs and determination of the optimum amount that should be added into hydrocarbon fuels.

Chapter 3
Experimental Method

This chapter describes the procedures followed in testing the Ni-SDC cells fed with carbon-containing fuels in the SOFC test station. The chapter begins with discussions of the synthesis of fresh anode and electrolyte powders using the glycine-nitrate process (GNP) and then cell fabrication. Next, the steps for cell setup and the electrochemical techniques to determine the cell performance and stability are described. The chapter also explains the utilization of micro-GC and mass spectrometry (MS) for the outlet gas analysis. Finally, the chapter closes with descriptions of the conductivity measurements and techniques to characterize the anode before and after the electrochemical tests.

3.1 SDC and NiO powder synthesis

The powder materials for use in the anode and electrolyte were nickel oxide (NiO) and samaria-doped ceria (SDC – $Ce_{0.8}Sm_{0.2}O_{1.9}$) and were synthesized using the glycine-nitrate process. It is a self-combustion method for powder synthesis that occurs at flame temperatures of 1100 to 1450 ^{o}C with a large amount of product gases. GNP is an inexpensive technique that produces fine electrolyte powders with high relative density and excellent conductivity after sintering (Peng *et al.,* 2004). It yields homogenous nano-sized powders with low carbon residue through a very rapid combustion reaction (Chick *et al.,* 1990). GNP was chosen for this work particularly since it can generate SDC powder that has a highly porous, foam-like structure with very low fill density. This morphology is desirable for the successful fabrication of a thin and pin-hole free electrolyte film via the dry-pressing technique (Xia and Liu, 2001). In this work, the SDC powder was pressed onto the anode material. Both were then co-sintered at relatively high temperature to ensure that the resulting electrolyte layer is dense enough to prevent fuel-oxidant crossover between electrodes.

According to Chick *et al.* (1990), the structure of the loose powder generated by glycine-nitrate combustion is related to the volume of the three main gases released (N_2, CO_2 and H_2O). The overall combustion reactions for the SDC and NiO when all glycine fuel is stoichiometrically oxidized by nitrates are given by Eqs. 3.1 and 3.2, respectively.

$$\frac{1}{5}Sm(NO_3)_3 + \frac{4}{5}Ce(NO_3)_3 + \frac{5}{3}NH_2CH_2COOH + \frac{1}{5}O_2 \rightarrow Sm_{0.2}Ce_{0.8}O_{1.9} + \frac{7}{3}N_2 + \frac{10}{3}CO_2 + \frac{25}{6}H_2O \quad 3.1$$

$$Ni(NO_3)_2 + \frac{20}{9}NH_2CH_2COOH + \frac{5}{2}O_2 \rightarrow NiO + \frac{19}{9}N_2 + \frac{40}{9}CO_2 + \frac{50}{9}H_2O \quad 3.2$$

To obtain SDC powder with a stoichiometric proportion of $Ce_{0.8}Sm_{0.2}O_{1.9}$, cerium (III) nitrate hexahydrate, $Ce(NO_3)_3{\cdot}6H_2O$ (Alfa Aesar, USA) and samarium (III) nitrate hexahydrate, $Sm(NO_3)_3{\cdot}6H_2O$ (Alfa Aesar, USA) were dissolved in 250 mL of distilled water with a metal mole ratio of Ce^{3+}:Sm^{3+}= 4:1. GNP involves a quick, simultaneous combustion whereby glycine and metal nitrates act as fuel and oxidizers, respectively. The ratio for glycine-to-nitrate (G/N) used in this preparation corresponded to a fuel-lean composition. Glycine (NH_2CH_2COOH) (Alfa Aesar, USA) was added into the precursor solution at a G/N of 0.53:1, which is smaller than the stoichiometric value of 1.67:1. This ratio is similar to that used by Chick *et al.* (1990), who found that it resulted in the highest flame temperature of 1450ºC. The higher the flame temperature, the more rapid and complete is the combustion and the finer and more crystalline is the powder. A solution of nickel (III) nitrate hexahydrate, $Ni(NO_3)_2{\cdot}6H_2O$ (Alfa Aesar, USA) on the other hand was used as the precursor for NiO. This time, a fuel-rich composition with a G/N ratio of 3:1 was used for NiO preparation based on the work of Jung *et al*. (2005) who reported that a more crystalline Ni phase was produced under fuel-rich conditions. They suggested the use of a fuel content ~ 2-times more than the stoichiometric composition for NiO synthesis through GNP.

Before combustion, the solution of glycine and nitrates was stirred and heated at 90ºC overnight using a digital hot-plate stirrer (VWR, USA) to obtain a solution in a viscous gel form. The combustion reaction was carried out inside a fume cupboard in a compartment made of aluminum sheets. The gel was heated on an electric stove (Salton Canada, Canada) until it reached its ignition temperature and erupted into flame. This self-initiated combustion produced a very fine pale-yellow ash of SDC and a dark brown, foam-like structure of NiO ash. The ashes were then calcined inside a bench-top furnace (Barnstead Themolyne, USA) to remove any remaining carbon residues and to form powder with a well-crystallized structure. The NiO ash

was calcined at 850ºC for 4 hrs and turned a dark green colour after the calcination. Meanwhile, the SDC was calcined at 800ºC for 2 hrs but retained its pale-yellow color. The SDC ash after combustion and NiO after calcination are shown in Figure 3-1a and b, respectively.

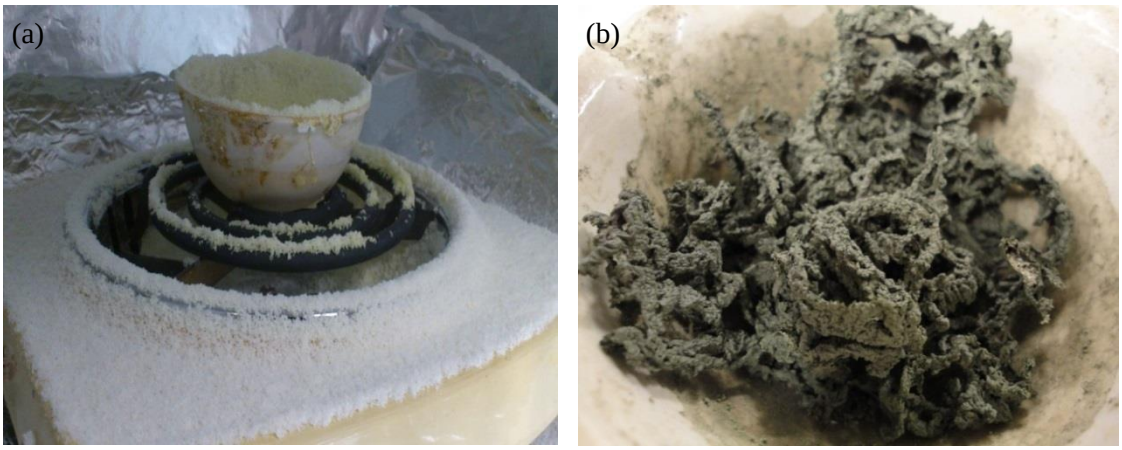

Figure 3-1 a) SDC ash after combustion; b) NiO ash after calcination

3.2 Button cell fabrication

The button cell used in this work consisted of samaria-doped ceria (SDC), nickel oxide-samaria-doped ceria (NiO-SDC) and samaria-doped strontium cobalt oxide-samaria-doped ceria (SSC-SDC) as its electrolyte, anode and cathode, respectively. The NiO-SDC cermet had a composition of 55 wt.% NiO and 45 wt.% SDC. The NiO and SDC were mixed by wet ball-milling at 75 rpm for 24 hrs in an ethanol solution using a jar mill (US Stoneware, USA) with zirconia grinding balls. 5 wt.% polyvinyl-butyral (PVB) (Scientific Polymer Products Inc., USA) was added as a binder and 5 wt.% of di-octyl phthalate (DOP) (Sigma-Aldrich, USA) was used as a plasticizer. During the wet-milling of the anode, a 5:45 weight ratio of solid:total suspension was used. The composition of the anode slurry during the wet-milling is given in Table 3-1. After the wet-milling, the slurry was heated at 115ºC and a powder of NiO-SDC was obtained after drying. The powder was then ground using a pestle and sieved to generate particles finer than 354 µm.

Table 3-1 Anode slurry composition during wet-milling

Materials	Cermet (wt.%)	Anode composition (wt.%)	Suspension (wt.%)
NiO	55	90	5
SDC	45		
Polyvinyl-butyral (PVB)	-	5	
Di-octyl phthalate (DOP)		5	
Ethanol		-	45

For cathode preparation, a commercially available samaria-doped strontium cobalt oxide ($Sm_{0.5}Sr_{0.5}CoO_3$, SSC) (Praxair Specialty Ceramics, USA) was mixed with the SDC powder at a weight ratio of SSC:SDC=70:30. α-terpeniol, isopropanol (Sigma-Aldrich, USA) and ethyl cellulose (Sigma-Aldrich, USA) were added into the SSC-SDC powders to act as solvent, liquid carrier and binder, respectively. The concentrations of α-terpeniol, isopropanol and ethyl cellulose in the suspension were maintained at 32.5, 10 and 2.5 wt.%, respectively. The mixture was ball-milled for 48 hrs at 75 rpm to form a cathode ink. The composition of the SSC/SDC cathode ink is shown in Table 3-2.

Table 3-2 Cathode ink composition

Materials	Cathode (wt.%)	Ink (wt.%)
SSC	70	55
SDC	30	
α-terpeniol	-	32.5
Isopropanol		10
Ethyl cellulose		2.5

Anode-supported cells were fabricated by uniaxial dry-pressing. 1.0 (± 0.001) g of NiO-SDC powder was weighed and pressed in a stainless steel mold at 160 MPa for 1 min using a hydraulic presser (Carver, USA) to obtain a circular disk of the anode substrate. Then 0.033 (± 0.0005) g of SDC powder was then carefully distributed over the anode substrate and co-pressed at 220 MPa for another 1 min. The co-pressed anode-electrolyte bilayer was then sintered in a high-temperature furnace (CM Furnaces Inc., USA) at 1330ºC for 5 hrs to produce an anode-supported NiO-SDC|SDC bi-layer with a thin film electrolyte. The sintered NiO-SDC|SDC bi-layer was ~ 17 mm in diameter. In order to accommodate the diameter of the alumina tube

holding the cell in the SOFC test station, the bi-layer was polished to a 15 mm diameter using wet sand paper affixed to a roll grinder (Buehler, USA).

The SSC-SDC ink was then applied to the middle of the NiO-SDC|SDC bi-layer at the electrolyte surface through a 6 mm diameter hole cut in 6 layers of Scotch® tape. The thickness of the cathode was controlled by the number of tape layers and its surface was made flat by leveling the ink over the hole. Based on a diameter of 6 mm, a geometric area of 0.283 cm^2 for the cathode was used in the subsequent electrochemical characterization in this work. The cell with the painted cathode then went through another sintering step at 1000ºC for 2 hrs. The temperature profiles followed during the sintering of the NiO-SDC|SDC bilayer and of the SSC-SDC to the NiO-SDC|SDC bi-layer are given in Appendix A. Within the sintering procedures for the anode-electrolyte and cathode, the specimens were initially heated at 400 ºC for 30 min to ensure that all binders were burned-off over the firing. Photographs of the sintered NiO-SDC|SDC bilayer and NiO-SDC|SDC|SSC-SDC cell are presented in Figure 3-2a and b, respectively.

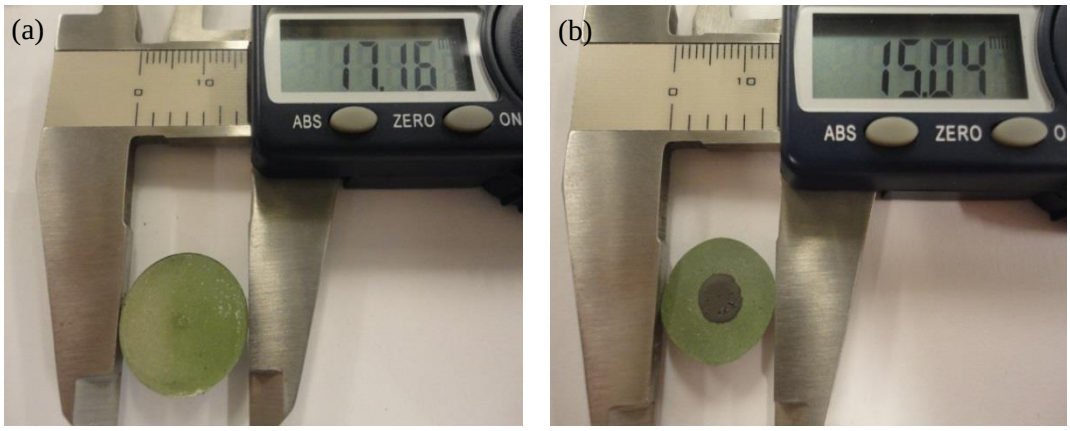

Figure 3-2 a) Sintered NiO-SDC|SDC bi-layer b) NiO-SDC|SDC|SSC-SDC cell

3.3 SOFC testing

3.3.1 Cell setup

The NiO-SDC|SDC|SSC-SDC cell is mounted on a vertical alumina tube with the same outer diameter (15 mm). Inside the alumina tube is a parallel quartz tube with a smaller outer diameter of 6 mm. The purpose of the alumina tube is to hold the cell during the testing, while the quartz tube supplied the fuel gases to the cell. Fuel flows through the quartz tube to the anode surface. Once the fuel gases pass through the anode and the electrochemical reactions have occurred, the resulting gases leave through a space between the quartz tube and the alumina tube to the outlet stream. The current collector for the anode consists of an Ag wire with 0.25 mm O.D. (Alfa Aesar, USA) connected to Ag gauze with 50 mesh size (Alfa Aesar, USA) that is seated on top of one end of quartz tube. The Ag mesh is used to increase the contact area with the electrode. A small force is applied by a spring located at the other end of the quartz tube to maintain good contact between the anode and current collector. A similar current collector and arrangement are used on the cathode side. Air supply is introduced to the cathode surface through a quartz tube and the outlet gas is discharged directly into the environment. The Ag current collectors at the anode and cathode sides are connected to their corresponding terminals of the potentiostat/impedance analyzer. A schematic diagram of the cell set-up inside the furnace is shown in Figure 3-3a.

A ceramic sealant (Aremco Product Inc., USA) is employed to seal the cell onto the alumina tube (Figure 3-3b). The method to apply this sealant proceeds as follows. The ceramic sealant was a mixture of ceramic paste (Ceramabond 552-VFG) and thinner (Ceramabond 552-T) at a weight ratio of 92:8. A quartz tube (12 mm O.D. and 45 cm long) was used temporarily to hold the cell in place while the sealant was carefully applied between the alumina tube and the cell. The sealant was then left to harden at room temperature for one day. On the next day, the cell was heated according to the sealant heating procedure; to 93ºC for 2 hrs and then to 260ºC for another 2 hrs. This heating step was carried out at 1.6ºC min^{-1} under 10 mL min^{-1} of N_2 flow.

The next step was to reduce NiO in the NiO-SDC cermet into its active Ni metal form. The reduction was carried out at 600ºC under a humidified H_2/bal. N_2 while increasing the H_2 concentration gradually for every hour from 10% H_2-90% N_2 to 100% H_2 over duration of 6 hrs. The cell's open circuit voltage (OCV) was monitored throughout the reduction process. In order

to ensure that the cell had stabilized after this pretreatment, it was held overnight under a humidified 10% H_2-90% N_2 at 600ºC before the electrochemical testing. After stabilization, the temperature was then adjusted according to the desired operating condition and the gas feed rate was gradually increased to 80 mL min^{-1} of humidified H_2 after the operating temperature was reached. Air was supplied to the cathode surface at a fixed flow rate of 86 mL min^{-1}.

An initial electrochemical test (open circuit voltage, DC potentiodynamic and impedance analysis) was conducted with humidified H_2 fed to the anode side to ensure that the cell had been properly fabricated and could achieve acceptable SOFC performance. Finally, the desired fuel was introduced into the system by slowly changing the fuel from humidified H_2 to carbon-containing fuel (dry CH_4 or CO-CO_2 mixture) under a galvanostatic mode at 0.1 A cm^{-2} or 0.35 A cm^{-2}. Stability tests were also conducted using galvanostatic mode of operation at the same current densities. H_2S was introduced into the cells either continuously as part of fuel gas mixtures with CH_4 or for short intervals as mixtures with H_2.

The experimental procedure involves in this work were time-consuming where it took 3 consecutive days from sealing procedure before the cell is ready for any electrochemical testing. The overall steps required for cell preparation before the start of the electrochemical experiments are shown schematically in Figure 3-4.

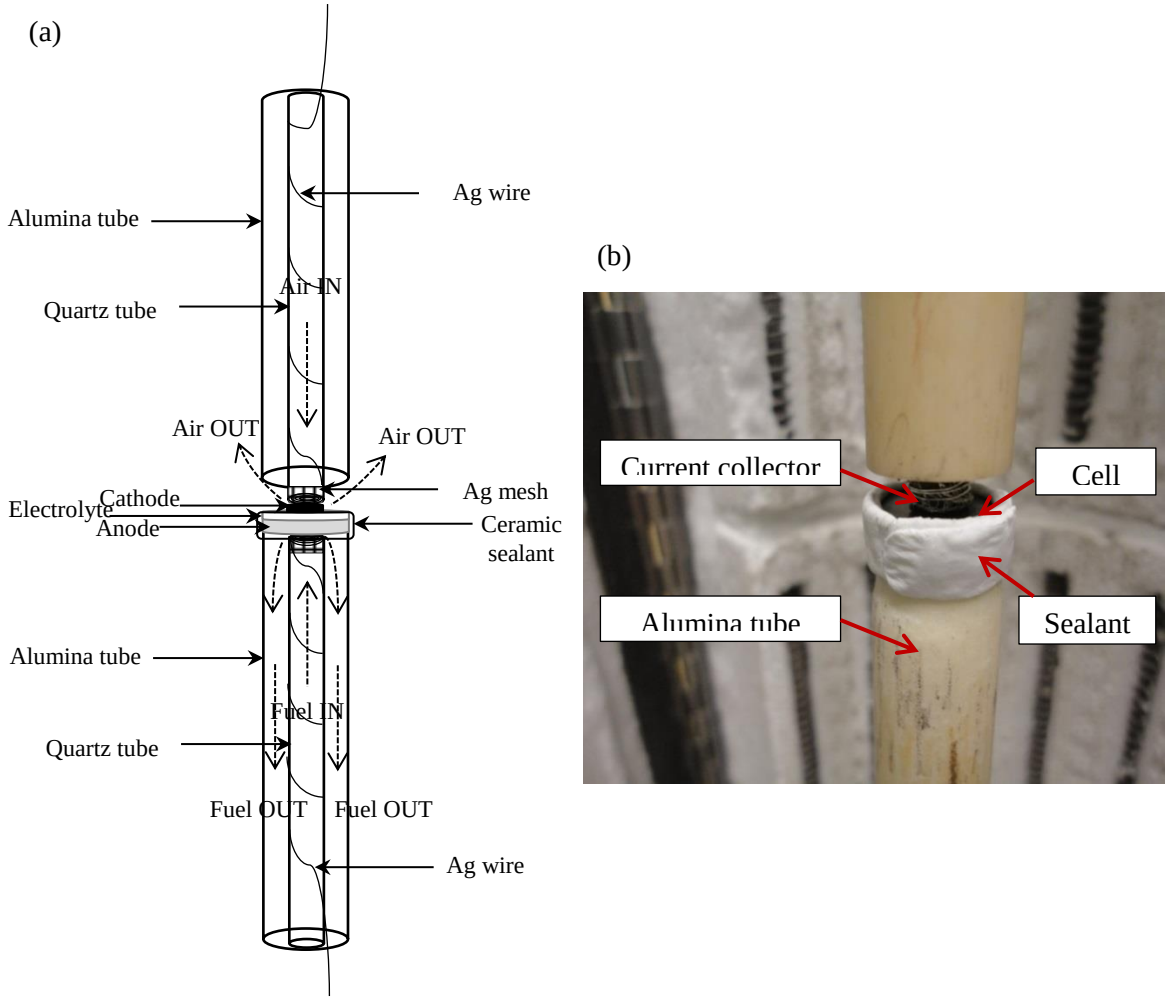

Figure 3-3 a) Cell set-up b) Button cell is sealed on the alumina tube

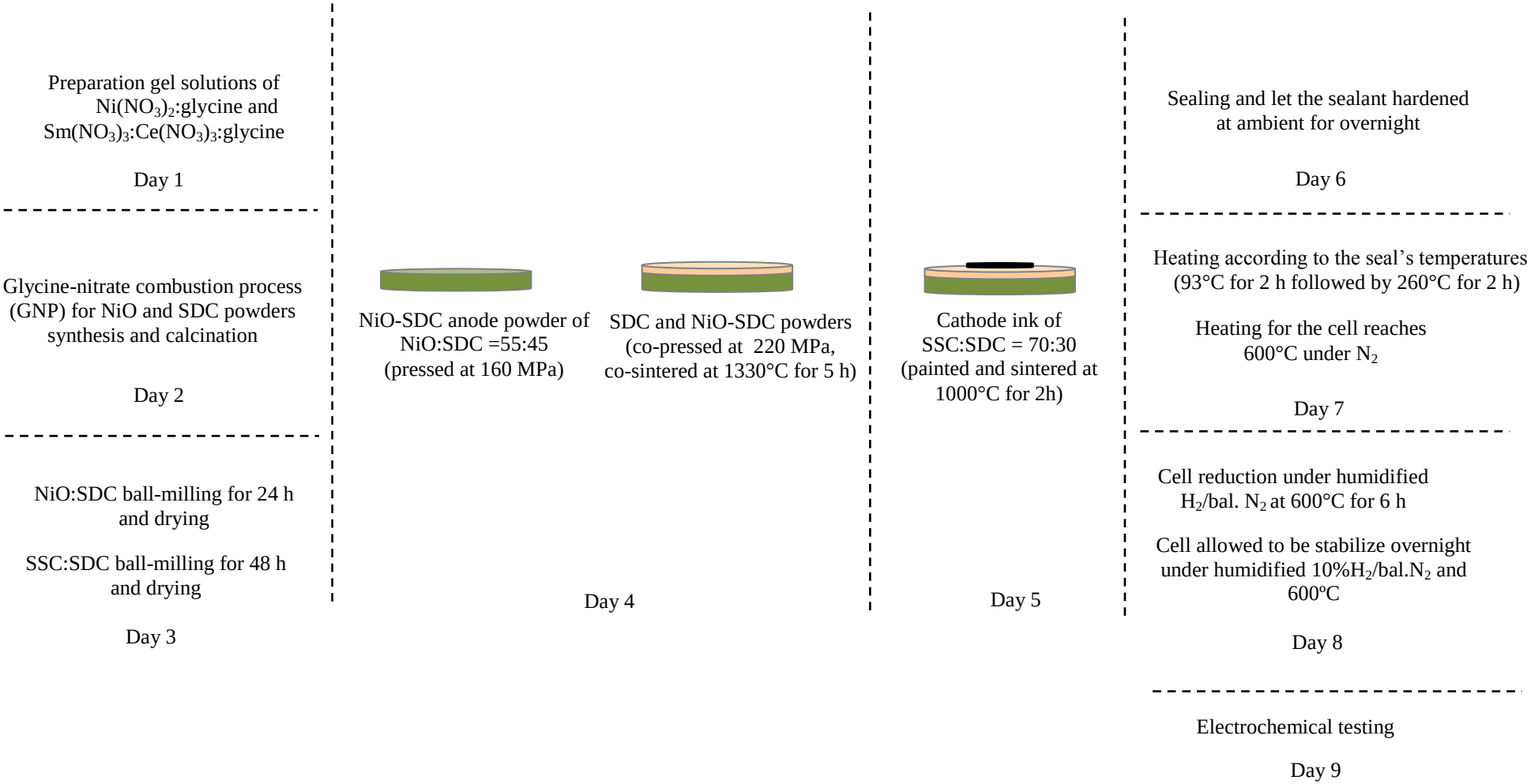

Figure 3-4 Overall steps of cell preparation prior to electrochemical testing

3.3.2 SOFC test station set-up

The electrochemical measurements were conducted in a SOFC test station shown schematically in Figure 3-5. The test station consists of a gas controlling system, bubbler for gas humidification, button cell, furnace, electrochemical measurement equipment and outlet gas analysis instruments. The compositions of the various fuel gases were adjusted using a series of mass flow controllers (Bronkhorst, USA) connected to a FieldPoint device linked to the LabVIEW Version 7.0 (National Instruments, USA). The flow rates of the SOFC fuels were controlled through LabVIEW software while air as oxidant set by a manual rotameter.

All gases were commercially available from Praxair Inc. (USA). The feed gases to the anode side were comprised of H_2 (Grade 5.0), N_2 (Grade 4.8), Ar (Grade 5.0), CH_4 (Grade 2.0), CO_2 (Grade 3.0), CO (Grade 2.5) and certified gas mixtures of 40 ppm H_2S in H_2 and 20 ppm H_2S in CH_4. A total fuel gas flow rate of 80 mL min^{-1} was used in the experiments involving H_2 and CO-CO_2, while a flow rate of 40 mL min^{-1} was used when dry CH_4 was introduced into the cell. The fuel gases were either dry or humidified to 3% H_2O by bubbling dry fuel through a water column at 25ºC.

A button cell was placed on a alumina tube (McDanel Advance Ceramic Technologies, USA) inside a vertical tubular furnace (Carbolite, UK). During the experiment, the fuel flowed upward along the tube to the anode surface and was discharged by flowing downward from the tube to the outlet stream connected to a water trap. The outlet gas composition was analyzed using an online micro-gas chromatograph (Agilent, USA) or OmniStar^{TM} mass spectrometry (Pfeiffer Vacuum, Germany) before being vented to fume hood. The electrochemical experiments were conducted using various gas fuels and the resulting cell performance and stability were monitored by a PC attached to a potentiostat/galvanostat coupled with an impedance analyzer (Solartron Analytical, UK).

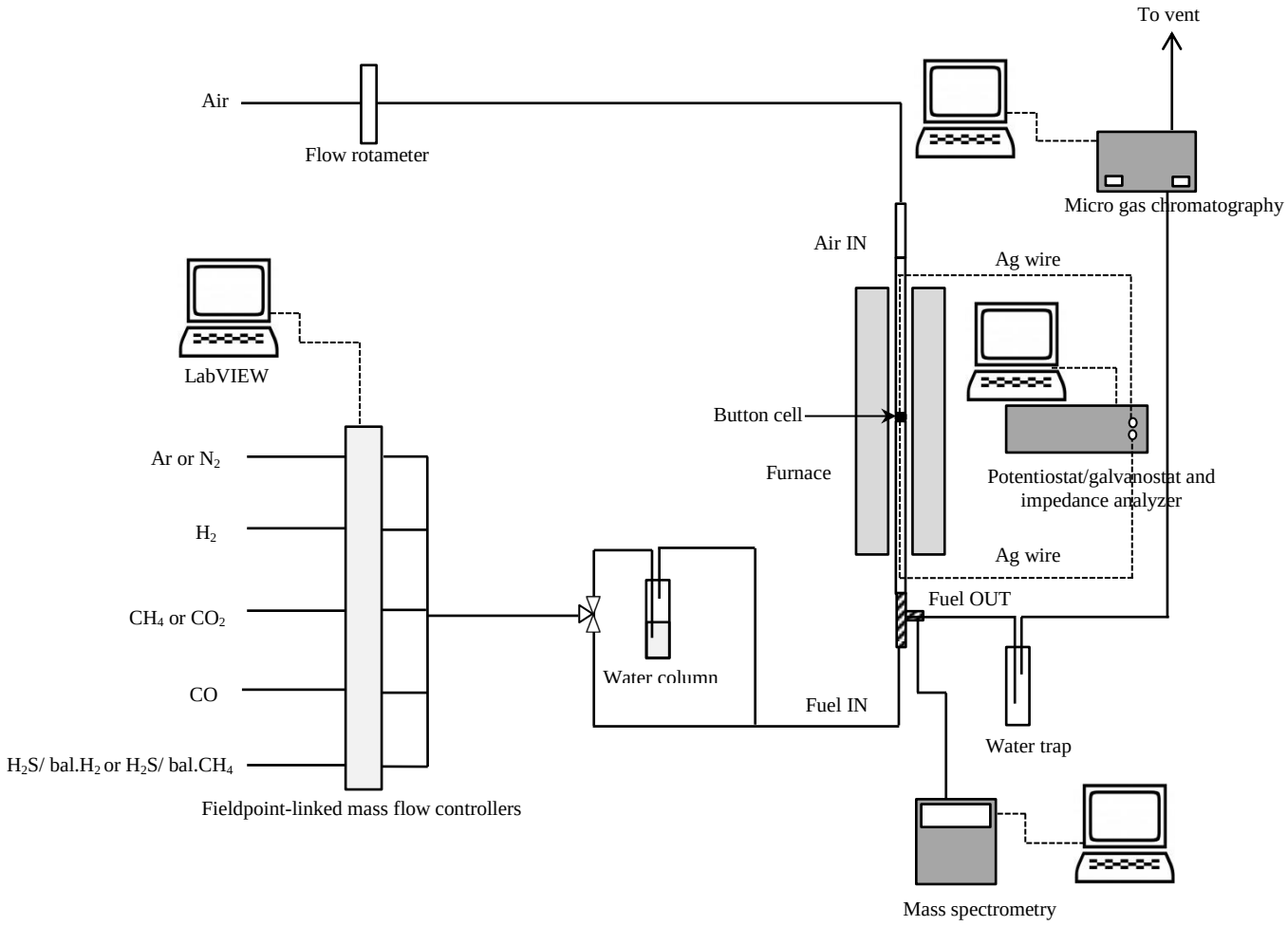

Figure 3-5 A schematic diagram of SOFC test station

3.3.3 Electrochemical experiments

In this work, the cell electrochemical performance was analyzed by measuring its open circuit voltage and conducting DC potentiodynamic, galvanostatic and electrochemical impedance spectroscopy experiments. The open circuit voltage and DC potentiodynamic and galvanostatic experiments were carried out using a Solartron Electrochemical Interface model 1287 potentiostat/galvanostat, while a Solartron Impedance Analyzer model 1260 was used for impedance measurements. The model 1287 potentiostat/galvanostat has 4 terminals for connection to a working electrode (WE), counter electrode (CE) and two reference electrodes (RE1 and RE2).

A standard two-electrode configuration was used to characterize the electrochemical behavior of the cell in this study. In a two-electrode configuration, the potential difference between the anode and cathode is measured to give the cell voltage. This is the simplest cell setup since a reference electrode is not required, but interpretation of the resulting data can be complicated by the fact that they reflect events occurring at the anode, cathode and electrolyte simultaneously. With no reference electrode, the RE1 terminal is shorted directly to the WE terminal and connected to the working electrode, while the RE2 and CE terminals are shorted together and connected to the counter electrode. Similarly, impedance analysis using the two-electrode system measures the impedance of the overall cell instead of that of an individual electrode. The use of a three-electrode configuration enables the behavior of a single electrode to be isolated from that of the remainder of the cell. With this arrangement, a differentiation between the behavior of the anode and cathode can be made. Unfortunately, the cell geometry used in this work (i.e., anode-supported cell) complicates the use of a three-electrode system due to difficulties in positioning the reference electrode on an anode-supported cell. In an impedance study by McIntosh *et al*. (2003) using a three-electrode system for an anode-supported cell, the response of the cathode obtained after locating the reference electrode in the electrolyte could not be distinguished from that of the total cell obtained through a two-electrode measurement.

Open circuit voltage experiment

The open circuit voltage (OCV), the cell voltage at zero current, was measured under humidified H_2 conditions for at least 10 min to ensure a stable value was obtained before any electrochemical testing with carbon-containing fuels was conducted. This initial measurement was crucial to ensure that a particular cell has a decent OCV value.

Galvanostatic and potentiodynamic experiments

Potentiodynamic experiments were conducted to determine the cell voltage (V) over a range of cell current densities (i). The experiments were performed by applying a potential difference across the cell that increased linearly with time at a rate of 5 mV s^{-1}. Cell performance was further analyzed by calculating the power density ($P = i.V$) and presented in i-V curves. Meanwhile, cell stability tests were conducted by monitoring the cell voltage as function of time at a given applied current (i.e. galvanostatic mode). In this work, current density of 0.1 or 0.35 A cm^{-2} was employed for the galvanostatic experiments based on a geometric area of 0.283 cm^2 (cathode area).

The rate of cell degradation (or improvement) was calculated using an equation:

$$Cell\ degradation\ (or\ improvement) rate\ , mV\ hr^{-1} = \frac{(V_{final} - V_{stable})}{t_{final} - t_{stable}} \qquad 3.3$$

where V_{final} is the cell voltage at the end of the experiment at t_{final}. V_{stable} is the cell voltage obtained at the time t_{stable} when the cell reaches its steady voltage during the experiment. The selected time for t_{stable} varied depending on the duration of the experiment. For 6, 10 and 100 hrs experiments, t_{stable} was set to 1, 2 and 30 hrs, respectively. The potentiodynamic and galvanostatic experiments were carried out using CorrWare software (Scribner Associates Inc., USA) and the resulting i-V and cell voltage data were gathered and evaluated using CorrView software (Scribner Associates Inc., USA).

Electrochemical impedance spectroscopy (EIS)

Electrochemical impedance spectroscopy (EIS) is a useful tool to characterize the behavior of an operating SOFC cell. Known as an alternating current (AC) technique, the measurement can be conducted with or without a direct current (DC) signal superimposed on an AC signal. Although a small perturbation of either the potential or current can be applied, the former alternative is most commonly used in the case of fuel cells. In this case, the applied potential has the following sinusoidal form:

$$\tilde{E} = E_0 \sin \omega t \qquad 3.4$$

where $\tilde{E}$ is the oscillating potential, E_0 is the amplitude of the input signal, ω is the angular frequency ($\omega = 2\pi f$) and t is time. The response of the system to this perturbation is a sinusoidal current with the same frequency, but shifted with time according to a phase angle ϕ, as follows:

$$\tilde{I} = I_0(\sin \omega t + \phi) \qquad 3.5$$

where $\tilde{I}$ is the oscillating current and I_0 is the amplitude of the output current signal. Analogous to the resistance-current-potential relationship in a DC circuit, the relationship between the applied sinusoidal potential and its resulting current is known as the impedance Z. Thus an expression for impedance is given by the ratio between the sinusoidal potential and current:

$$Z = \frac{\tilde{E}}{\tilde{I}} \qquad 3.6$$

The impedance can be expressed as a complex number and converted from the time domain to the frequency domain (Huang *et al.* 2007). When expressed in complex notation, Z is:

$$Z = |Z| \exp j\,\phi = |Z| \cos\,(\phi) + j|Z| \sin(\phi) = Z' + jZ'' \qquad 3.7$$

where j is the imaginary unit ($\sqrt{-1}$), while Z' and Z" are the real and imaginary parts of the impedance:

$$Z' = Re(Z) = |Z| \cos\,(\phi) \qquad 3.8$$

$$Z'' = Im(Z) = |Z| \sin(\phi) \quad 3.9$$

The impedance spectra are commonly presented as a Nyquist plot where $-Im\ Z$ is plotted versus $Re\ Z$ over a range of frequencies. A schematic diagram of a Nyquist plot of an electrochemical system featuring two frequency-dependent semicircles is given in Figure 3-6. The intercept on the real axis at the high- frequency end of the spectra corresponds to the pure ohmic resistance R_s in the cell. Although the value accounts for losses associated with both ionic and electronic transport within the electrodes, the main source of R_s is usually ionic transport within the electrolyte. Meanwhile, the difference between the intercepts at the low and high frequency ends of the spectra yields the polarization resistance $R_p = R_1+R_2$ related to electrode processes (Jasinski *et al.*, 2004).

An electrical circuit model involving a combination of inductor (L), resistor (R), capacitor (C) and/or constant phase elements (CPE) is typically fit statistically to the impedance spectra. An equivalent circuit often used to fit the impedance spectra obtained from operating SOFC cells is shown in Figure 3-7. Inductance (L) is often observed at the high frequency end below the real-impedance axis. This effect has been attributed to the inductance of the connecting wire and the internal inductance of the measuring instrument (Azad and Irvine, 2011). In SOFC systems, a CPE is usually selected over a simple capacitance to fit the data to compensate for inhomogeneities associated with the roughness of porous electrodes (Pajkossy, 2005). The experimental data from the impedance experiments of this work were modeled and fitted according to the equivalent circuit shown in Figure 3-7 and used to characterize the changes to the state of the cell during the course of operation.

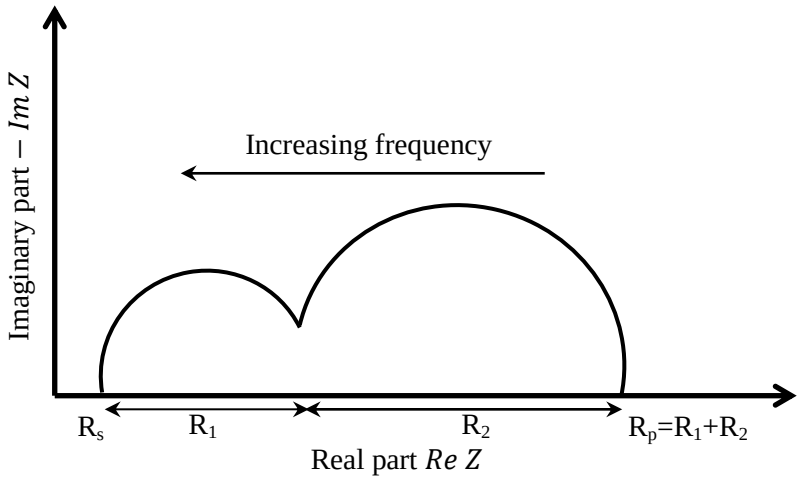

Figure 3-6 A Nyquist plot of a typical electrochemical system

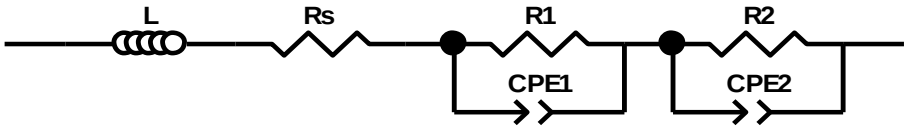

Figure 3-7 Equivalent circuit model used in this electrochemical work

The impedance measurements in this study were conducted on the full cell between the anode to cathode using a two-electrode configuration. Thus, the polarization resistance R_p obtained from the measurement combines the effects of both anode and cathode processes. Measurements were conducted using a zero DC bias (i.e. OCV condition) and at DC current (0.1 A cm^{-2} or 0.35 A cm^{-2}). The impedance spectra were generated using ZPlot software (Scribner Associates Inc., USA). The frequencies of the input potentials were varied over the range from 0.1 to 10^5 Hz during the EIS measurements on each sample. Finally, the impedance data were analyzed through the equivalent circuit model using ZView software (Scribner Associates Inc., USA).

3.3.4 Gas outlet analysis

In this work, analysis of the outlet gas from the SOFC for one experimental condition was conducted using micro-gas chromatography (Agilent model 3000A) and for another set of experiments using mass spectrometry (MS) (OmniStar^{TM} model GSD 320). The micro-GC was employed for on-line analysis of the outlet gas composition during experiments to assess cell stability under dry CH_4 while the MS was used to determine the gas composition while flowing humidified H_2 gas under galvanostatic mode on the cell after the stability tests. The micro-GC equipped with Molecular Sieve and Plot U columns, both operated with TCD detectors using Ar and He as carriers, respectively, was used to measure the amounts of CH_4, H_2, CO and CO_2 in the discharge from the anode gas chamber. However, it was not possible to determine the amount of H_2O present using micro-GC. A known amount of N_2 (10 mL) was introduced as an internal standard into the outlet stream before entering the micro-GC to avoid measurement error due to reactions that change the gas volume. 2000 µL of gas sample was injected into the instrument every 15 min. The gases were identified from the retention times of the various peaks and the concentration of each gas was obtained from a calibration factor relating the area of its peak to its concentration. The gas analysis via micro-GC was managed using the Agilent Cerity software (Agilent, USA).

The MS operates with a C-SEM/Faraday detector with two gas-tight filaments for its ionization source. Operating at 1000 mbar sample pressure, the instrument uses a stainless steel capillary heated to 200ºC. The MS signals given by the ion current intensities for H_2 (m/e=2), CH_4 (m/e=16), CO (m/e=28) and CO_2 (m/e=44) were continuously monitored and the measured data were generated every 50 milliseconds. The signals were initially calibrated with gas mixtures of known concentration and gas analysis by MS through Quadera® software (Pfeiffer Vacuum, Germany). The outlet gas from the SOFC setup was measured immediately by the MS by connecting the instrument directly to the outlet from the furnace. A heating tape (Omega Engineering Inc., Canada) was wrapped around the gas line leading to the MS to ensure that water entering the instrument remained in vapor form. A variable

autotransformer (Staco Energy Products Co., USA) and a type-K thermocouple (Omega Engineering Inc., Canada) were used to maintain the gas line temperature at ~140ºC.

3.3.5 Quantification of carbon

Amount of carbon deposited after some of the cell stability tests was determined according to amount carbon-containing gases produced while contacting the cell with humidified H_2. After the stability test, the fuel gas was switched to Ar and the cell purged with 40 mL min^{-1} of this inert gas. Gas analysis using MS during the gasification procedure was started while the cell was being purged to ensure that no trace of the gases from the electrochemical reactions remained in the outlet gas line. After 30 min of purging, the inlet gas was then switched to 80 mL min^{-1} of 3%-humidified H_2 for 1 hr at 700ºC at a constant current of 0.35 A cm^{-2}. The amount of carbon deposit in the cell formed during the previous stability test was measured from the amount of CO, CO_2 and CH_4 in the effluent gas.

3.4 Material characterization

3.4.1 Conductivity measurement

In this work, the ionic conductivity of the SDC electrolyte at various temperatures from 500 to 800 ºC was also measured. EIS has been widely employed by researchers to measure the electrical conductivities of solid materials due to its ability to separate the contributions to the electrical behavior of the grain, namely the bulk conductivity and grain boundary conductivity (Zhan *et al.*, 2001). In general, an impedance spectrum obtained during a conductivity measurement consists of distinct arcs at high, intermediate and low frequencies that can be attributed to responses in the bulk grain, grain boundary and electrode, respectively. As the temperature increased, individual polarizations were reduced and the arcs shifted to higher frequencies (Christie and Barkel, 1996) and in most occasions the arc at

high frequency did not appear at all over the frequency range selected for the testing (Bu *et al.*, 2013; Zhou *et al.* 2012).

In this study, conductivity measurements of SDCs were carried out using two-probe impedance spectroscopy. Approximately 0.700 g of a calcined SDC powder was pressed in a stainless steel mold at 220 MPa for 1 min and then sintered in a high-temperature furnace at 1330ºC for 5 hrs. The thickness of the dense disk after the sintering was measured. An Ag paste (ESL ElectroScience, USA) was then applied onto both sides of the disk by painting it through a hole cut into Scotch® tape layers. The Ag paste was positioned so that it was aligned in the middle of the disk. The paste was then baked for 1 hr at 700ºC. Similar to the other electrochemical tests, the current collectors used were an Ag wire and Ag mesh and the disk was fixed with a ceramic sealant to an alumina tube in the test apparatus. The measurement was conducted in air from 500 to 800ºC at 50ºC intervals over the frequency range from 0.1 to 10^5 Hz. Curve fitting of impedance data for each temperature was performed using an equivalent circuit via ZView.

3.4.2 Temperature- programmed oxidation (TPO)

The presence of carbon deposited on the anode surface after the cell stability tests in the presence of carbon-containing fuels was analyzed using temperature-programmed oxidation (TPO). TPO is an essential technique used in catalytic studies to identify and determine the quantity of carbon deposited on catalyst surfaces. In this work, the analysis was conducted in a CATLAB microreactor equipped with a mass spectrometry model QIC-20 (Hiden Analytical Ltd., UK). TPO was only used to determine the nature of the deposited carbon, depending on the temperature at which the CO_2 from carbon oxidation evolved. It is important to note that the amount of CO_2 from the TPO would not reflect the total amount of deposited carbon on the anode surface since the analysis was only conducted for a small part of the cell. A broken sample of the cell with known weight was initially placed in the CATLAB reaction chamber. A gas stream containing He with 5% O_2 and 1.5% Ar was then

introduced at a flow rate of 90 mL min^{-1}. The reaction temperature was then increased from room temperature to 850ºC at a linear rate of 10 ºC min^{-1} and the CO_2 generated in the exit gas was monitored by mass spectrometry.

3.4.3 Scanning electron microscopy (SEM) and Energy dispersive x-ray (EDX)

The anode microstructure and the morphology of the carbon deposits after electrochemical testing were examined using model LEO 1530 scanning electron microscope (SEM) equipped with an energy dispersive x-ray analyzer (EDX). The EDX was employed to analyze the elemental composition of the material. All SEM-EDX analysis was used to examine cell cross-sections particularly on the anode part. Prior to the analysis, a small fragment of the cell was mounted on a 70º pre-tilt stub holder (Ted Pella Inc., USA) using carbon conductive tape (Ted Pella Inc., USA) and then sputtered with gold to ensure that a ~10 nm thick layer was produced. SEM images of varying magnifications were taken using 10 and 20 kV energy beams using both secondary electron (SE) and backscattered electron (BSE) detection modes. The BSE mode distinguishes areas of different chemical composition so that elements with high atomic number appear brighter than lighter elements. EDX analysis was performed by focusing on a particular spot or area or by scanning along a particular line over the sample cross-section. The analysis was conducted in the Waterloo Advanced Technology Lab (WATLab) in the Chemistry Department.

3.4.4 X-ray photoelectron spectroscopy (XPS)

X-ray photoelectron spectroscopy (XPS) is a surface-sensitive technique used to analyze the surface chemistry of a material. In this work, the analysis was employed to characterize the chemical state of elements present on the surface of the cell cross-section before and after electrochemical testing. In XPS spectra, peaks for the various elements present appear at the binding energies of the ejected electrons. During XPS analysis, photoelectron is injected

from a core level by an X-ray photo of energy hν. The energy of the emitted electrons is the analyzed by electron spectrometer in a form of kinetic energy (E_K). The binding energy of the electron (E_B) is quantified and presented by the instrument according to relationship between the XPS parameters:

$$E_B = h\nu - E_K - W \quad 3.10$$

where $h\nu$ is the photon energy, E_K is the kinetic energy of the electron and W is the spectrometer work function. XPS analysis captures the composition within a region very close to the material surface within a 1-10 nm depth (Watts, 2003). For the analysis in this study, the narrow XPS scans in the sulphur (S 2p), nickel (Ni 2p) and carbon (C 1s) were carried out. The identification of the chemical states in each region was assigned according to the binding energy (eV) of the various peaks appearing in the spectrum.

The XPS analysis was performed using a Thermo ESCALab 250 unit (VG Scientific, UK) configured with a monochromatic Al Kα (hν = 1486.6 eV) x-ray source at a power of 150 W with the base pressure in the analytical chamber maintained below 3.0 $\times 10^{-10}$ bar. Data were collected with pass energy of 20 eV for the core-shell spectra and 50 eV for the survey spectra. The take-off angle, defined as the angle between the substrate normal and the detector, was fixed at 0 degree. Curve fitting and deconvolution of these scans were done using CasaXPS version 2.3 (Casa Software Ltd, UK).

3.4.5 X-ray diffraction (XRD)

X-ray diffraction (XRD) was used to identify the crystalline phases in the SDC, NiO and NiO-SDC samples prepared in this work. The measurements were conducted using a Bruker D8 Focus x-ray diffractometer (Bruker, Germany) available in the Analytical Lab of the Chemical Engineering Department. Powder samples were introduced and evenly dispersed within the sample holder. A glass slide was used to level the sample with the top of the cup and obtain a well-dispersed sample with a smooth surface. Solid samples were fixed to the

middle of the sample holder cup with a piece of double-sided tape. The analysis was performed using CuKα radiation (λ= 1.5425 Å) at a 40 kV potential and 40 mA current. Each sample was scanned over a range of 2θ angles from 20-90º at a rate of 0.05º per second. The data obtained were analyzed using EVA software (Bruker, Germany) for phase identification and generate XRD patterns for freshly-prepared, calcined, ball-milled sintered and reduced materials.

3.5 Summary

In conclusion, the experimental procedure in this work involves material preparation, cell fabrication, electrochemical testing, deposited carbon quantification and anode surface characterizations before and after experiments. The overall procedure starting from the cell setup is summarized below in Figure 3-8.

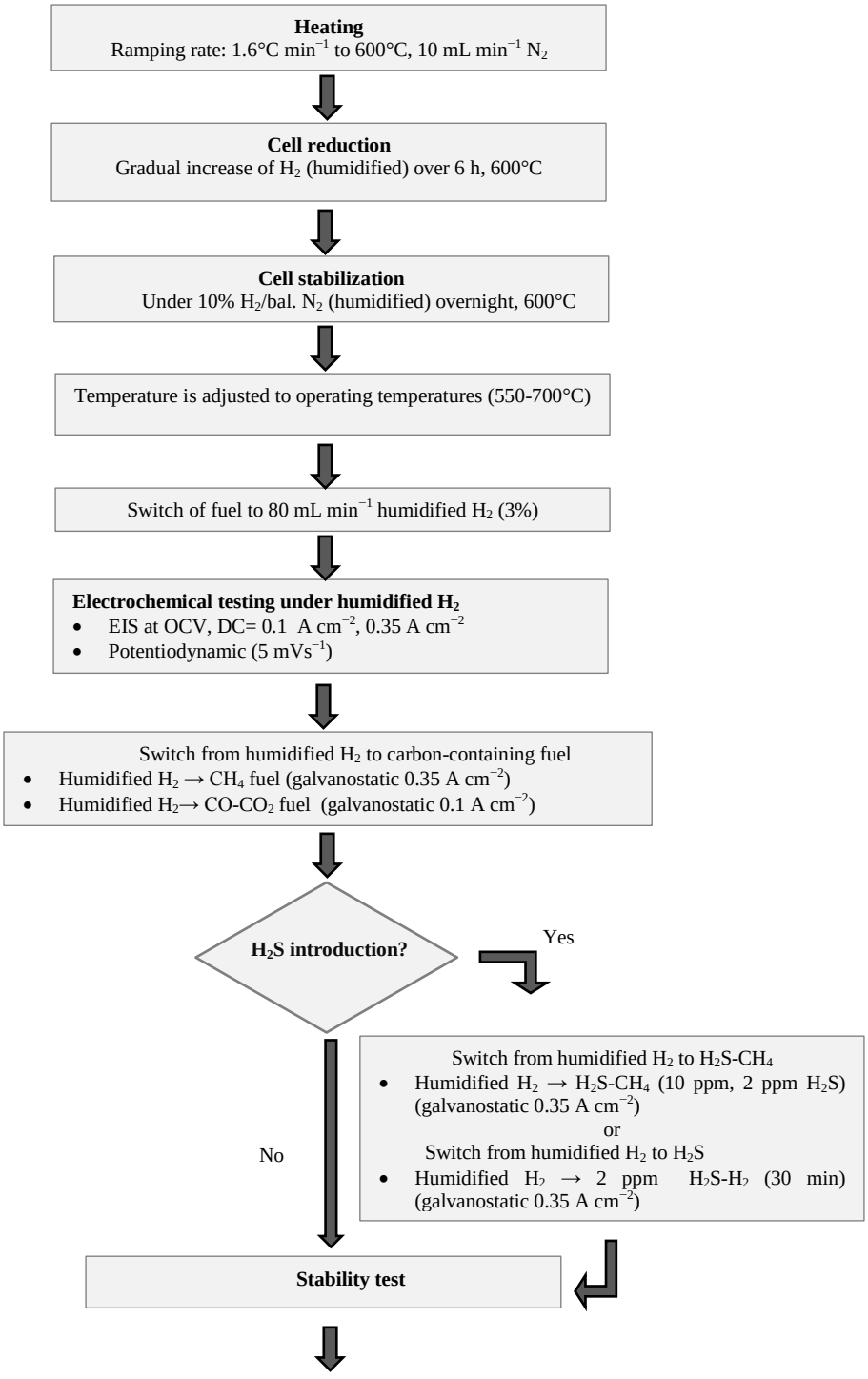

Procedure for experimental procedure in this work (cont.')

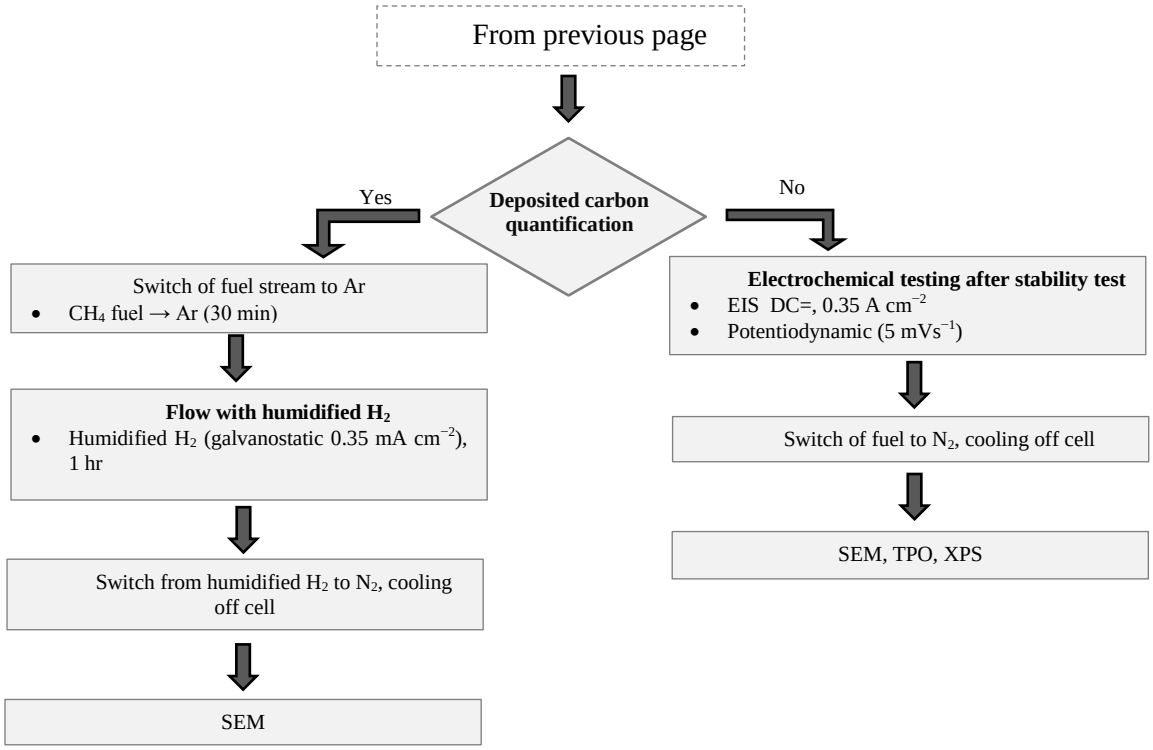

Figure 3-8 Procedure for experimental procedure in this wok

Chapter 4

Ni-SDC anode-supported cells: Performance in H_2, CH_4 and CO-CO_2

4.1 Introduction

Traditional solid oxide fuel cells (SOFCs) consisting of state-of-the-art material, YSZ are normally operated at high operating temperatures (800-1000°C). Elevated temperature operation, however, results in high cost and problems in material selection and component degradation. Therefore, reducing the operating temperature is crucial in order to improve long term reliability of SOFC. Numerous studies have been conducted using doped-ceria-based material for intermediate temperature SOFCs (IT-SOFCs). Doped-ceria exhibits superior ionic conductivity as an electrolyte in low operating temperatures (Eguchi, 1997). Plus, the presence of ceria in the anode cermet is known to improve the oxidation reaction (McIntosh *et al.*, 2002). In this study, Ni-samaria doped-ceria (Ni-SDC) anode-supported cells have been fabricated using a dry-pressing technique. The performance of the cell at intermediate temperatures (600-700°C) has been extensively evaluated under various types of fuel (H_2, CH_4, CO-CO_2).

4.2 Experimental Procedure

Cell fabrication and set-up procedure for Ni-SDC anode-supported cells were described briefly in sections 3.2 and 3.3.1, respectively. After the cell reduction step at 600°C, the temperature was adjusted according to the desired operating condition in this work (600-700°C). The Ni-SDC cell was then evaluated under humidified H_2 and carbon-containing fuels; humidified CH_4, dry CH_4, or CO-CO_2. The flow rates of H_2 and CO-CO_2 gases at the anode was at a total 80 mL min^{-1} (STP) while the flow rate of CH_4 gas is 40 mL min^{-1}. The flow rate of CH_4 was half of the flow rate of H_2 to maintain a constant total molar flow rate of hydrogen. Meanwhile, air flow rate at the cathode was at 86 mL min^{-1} (STP).

The electrochemical performance of the cell was evaluated under potentiodynamic, galvanostatic and impedance modes using the Electrochemical Interface 1287 and Impedance Analyzer 1260 (Solartron Analytical, UK). Cell stability test was carried out with humidified H_2, humidified CH_4 and CO-CO_2 under galvanostatic mode at 0.1 A cm^{-2} and the impedance analysis was carried out before and after the stability test. Impedance measurements were performed at DC condition (0.1 A cm^{-2}) at a frequency range of 0.1 to 10^5 Hz.

Conductivity test was carried out to determine the ionic conductivity of the SDC electrolyte. The SDC disc was obtained by pressing the SDC powder and sintered it at 1330°C for 5 hrs. Silver paste was applied at both sides of the disc and fired at 700ºC for 1 hr. The measurement was performed in air in the temperature range of 500-800°C for every 50°C interval using two-probe impedance spectroscopy. The frequency range through the analysis was fixed at 0.1 to 10^5 Hz.

The phase identification of the raw powders, anode substrate and electrolyte film were examined through XRD by Bruker D8 Focus (Bruker, Germany) using CuKα radiation (λ= 1.5425 Å). The as-prepared, calcined, sintered, ball-milled and reduced samples were scanned at 40 kV potential and 40 mA current over a range of 2θ angles from 20-85º. The microstructure and the elemental composition of the fresh Ni-SDC cell were characterized using SEM (LEO 1530) equipped with an energy dispersive X-ray (EDX).

4.3 Results and Discussions

4.3.1 XRD

The XRD patterns for NiO, SDC and NiO-SDC are shown in Figure 4-1. Two phases coexist in the as-prepared NiO with additional phase of metallic Ni found in the sample (Figure 4-1a). One possible reason for the presence of metallic Ni may be due to the localized reducing environment, induced by the remaining glycine during the late stages of the combustion (Prasad *et al.*, 2008). However, the Ni peaks disappeared after powder calcination at 850°C

for 4 hrs, leaving all peaks indexed only to a single NiO phase. The calcined sample was a pure NiO with all main peaks; (111), (200), (220) and (311) corresponding to the fluorite-type cubic structure. The NiO peaks become stronger indicating an increase in the crystalline structure after the calcination.

Similarly in Figure 4-1b, the peaks from the as-prepared, calcined and sintered of SDC indicate a cubic fluorite structure for SDC. There was no peak referring to either Sm or CeO_2 phase, showing that Sm and Ce ions were homogenously formed into a single phase of SDC. After the sample was sintered at 1330°C for 5 hrs, the resulting SDC film was very well-crystallized, as demonstrated by the sharp and narrow diffraction peaks.

Much higher intensity of the peaks was observed for the sintered NiO-SDC compared to the ball-milled NiO-SDC (Figure 4-1c). All peaks in these two NiO-SDC samples were only ascribed to either NiO or SDC suggesting there was no chemical interaction between NiO and SDC, thus no undesired phase was formed during the cell processing. Later, after the cell reduction, the sample presented strong peaks including some belonging to metallic Ni. This indicates that most of the NiO phase in the NiO-SDC anode cermet has been successfully reduced into its Ni active form during the reduction.

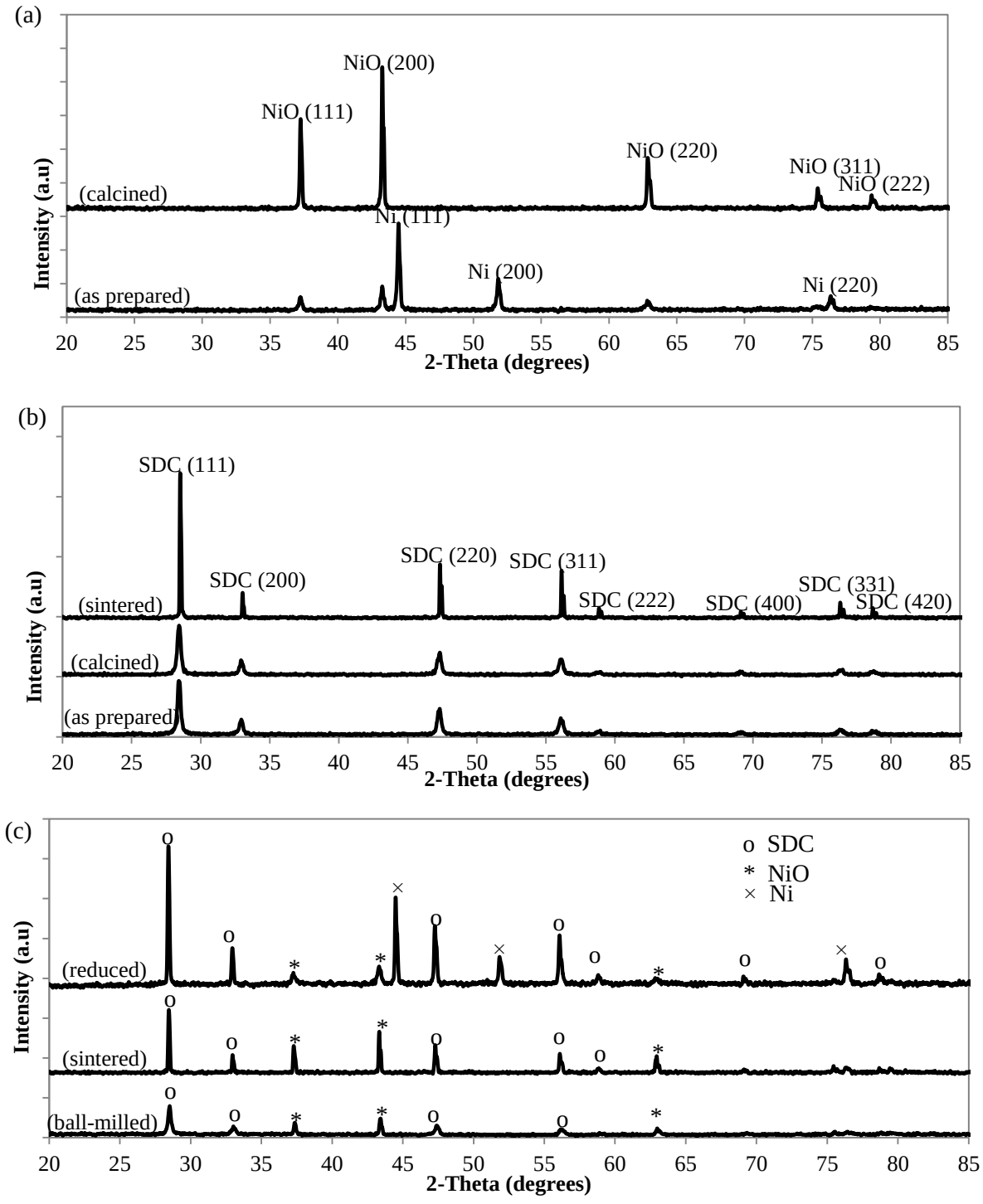

Figure 4-1 XRD patterns for a) NiO b) SDC and c) NiO-SDC

4.3.2 Conductivity

Impedance spectra have been widely used to measure the ionic conductivity of solid materials. In general, an impedance spectrum of an ionic conductor consists of several independent semicircular arcs from high frequency to low frequency corresponding to the bulk, grain boundary and electrode contributions. However, not all arcs from these contributions can be observed, depending on the nature of the sample and the measurement conditions. In this work, for example, only one well-defined arc was observed from each impedance plot of the SDC disc tested within the temperature range of 500-800°C (Figure 4-2a and b). The first and second semicircles of the plot, which typically occur in the high frequency region, were not visible, indicating that both bulk and grain boundary resistances (R_b and R_{gb}) were frequency independent. The observed semicircle was only for the low frequencies, which can be attributed to the electrode resistance (R_{el}). A similar trend was observed by a few researchers when testing the conductivity for SDC and GDC electrolytes at temperatures higher than 500°C (Ding *et al.*, 2010; Öksüzömer *et al.*, 2013). Fuentes and Baker (2008) have described the phenomena of this single arc as the effect on the spectra of inductances generated within the experimental apparatus.

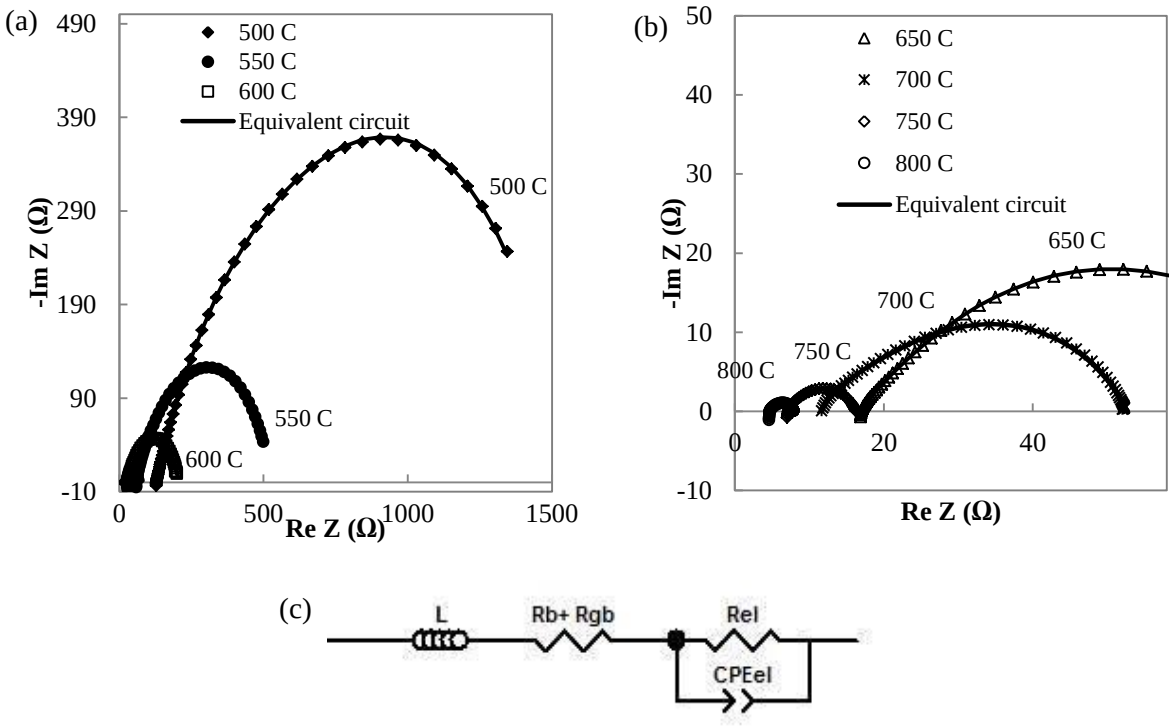

Figure 4-2 Impedance spectra for SDC pellet measured at temperatures a) 500-600°C and b) 650-800°C c) Equivalent circuit for ionic conductivity measurement

The ionic conductivity σ is determined using equation Eq. 4.1 where R is the total resistance, calculated from $R = R_b + R_{gb}$. Meanwhile, ℓ and A are the thickness of the SDC disc and the electrode area, respectively:

$$\sigma = \frac{\ell}{AR} \qquad 4.1$$

In this work, the bulk resistance, R_b and the grain boundary resistance, R_{gb} could not be separated and the values for $(R_b + R_{gb})$ and the electrode resistance, R_{el} were estimated by fitting the plots according to the equivalent circuit shown in Figure 4-2c.

The ionic conductivities measured for the SDC electrolyte at 500- 800ºC are listed in Table 4-1. Obviously the ionic conductivity increases when increasing the temperature, with a maximum value of 0.063 S cm^{-1} at 800ºC. There is a bit of disparities regarding conductivities values in the literature, but overall, the ionic conductivities of the SDC prepared in this work were somewhat lower than the values attained by other researchers. Peng *et al.* (2004) found that the ionic conductivity of the SDC produced using the similar GNP process was 0.082 S cm^{-1} at 800ºC. Approximately 0.075 S cm^{-1} at 800ºC was observed in Liu *et al.* (2013)'s work through the same preparation method. Tian *et al.* (2011) have studied the effect of the sintering temperature on the SDC from GNP. They have obtained the highest conductivity at 1300ºC sintering temperature, approximately the same temperature used for sintering in this work (1330ºC). Their maximum conductivity was 0.0154 S cm^{-1} at 600ºC, which is higher than the value of 0.010 S cm^{-1} obtained in the present study.

Temperature dependence of the conductivity is plotted according to Eq. 4.2 (Hui *et al.*, 2007):

$$\sigma T = A\, exp\left(\frac{-E_a}{kT}\right) \qquad 4.2$$

where T is absolute temperature, A is the pre-exponential constant, E_a is the activation energy and k is the Boltzmann constant (8.617×10^{-5} eV K^{-1}). The plot is shown in Figure 4-3. E_a was calculated from the slope of the plot of ln σT versus 1000/T giving a value of E_a= 0.86 eV. The value of the E_a obtained is within the range of activation energies of SDC electrolyte produced from various fabrication methods (0.66-0.93 eV) (Ding *et al.*, 2010).

Table 4-1 Ionic conductivities of SDC electrolyte

Temperature (ºC)	Conductivity (S cm^{-1})
800	0.063
750	0.042
700	0.026
650	0.017
600	0.010
550	0.005
500	0.002

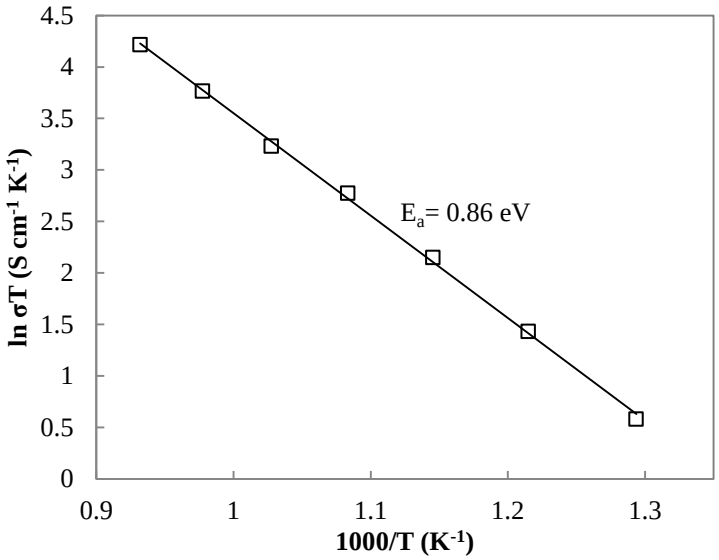

Figure 4-3 Linearized plot of ionic conductivities of SDC electrolyte

4.3.3 Cell dimension and composition

A dry-pressing technique was employed to fabricate the Ni-SDC anode-supported cells. Figure 4-4 shows the SEM micrographs of the cross-sectional area of fresh Ni-SDC cell taken after reduction under humidified H_2. Figure 4-4a shows that the electrolyte is well adhered to both the anode and cathode substrates without any noticeable cracks. This suggests a good quality of SDC film formed on the substrate. The electrolyte is uniform over the cell structure and having a thickness of approximately 31 µm. Being the support layer of the cell, the anode exhibited a thickest of about 600 µm. Meanwhile the cathode layer thickness is around 160 µm (Figure 4-4b).

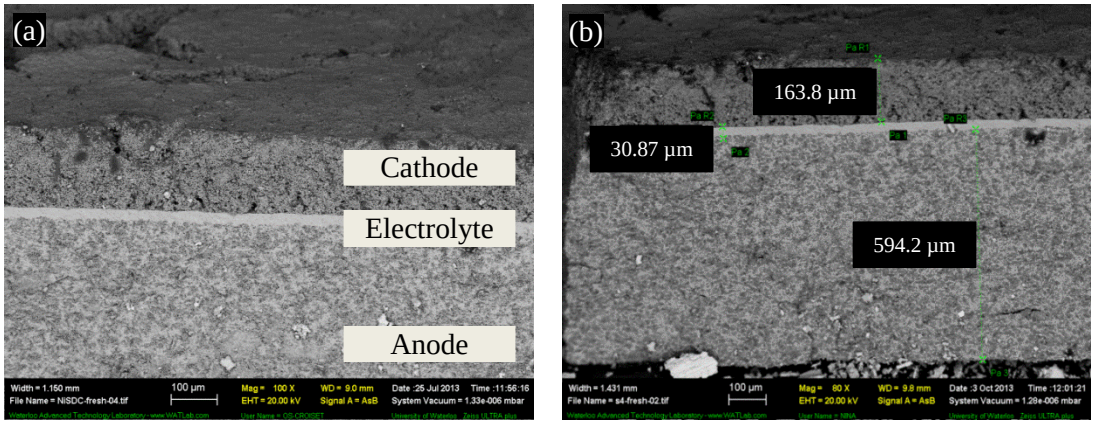

Figure 4-4 SEM images of Ni-SDC|SDC|SSC-SDC cell cross-section a) Cell components b) Cell dimensions

A dense structure of the SDC layer is clearly shown in Figure 4-5a. An EDX scanning of Area 2 (electrolyte), given in Figure 4-5c, verified that Ce, Sm, and O are the primary elements of the electrolyte. A detected amount of Al in the composition is most likely due to contamination from the aluminum compartment employed during the GNP combustion. There was also a trace of Au detected which originated from the gold-coating procedure.

At the cathode region, multiple pores with various pore sizes were observed on the surface implying cathode with a porous structure. The EDX mapping of a selected area on the

cathode vicinity (Area 1) (Figure 4-5b) provides an elemental composition of mainly Sm, Ce, Co, Sr, and O which is representative of the composite of samaria-doped strontium cobalt oxide and samaria-doped ceria (SSC-SDC).

An EDX analysis for the anode region (Area 3) (Figure 4-5d) indicates the mapping of Ni, Sm, Ce and O which reflects the anode composition of Ni and samaria-doped ceria (Ni-SDC). The anode structure consists of a uniform distribution of Ni phase within a framework of SDC. Both linked and isolated Ni phases were observed in the anode region, surrounded by the SDC network. A good connection was found established between the SDC network and the SDC electrolyte.

(a)

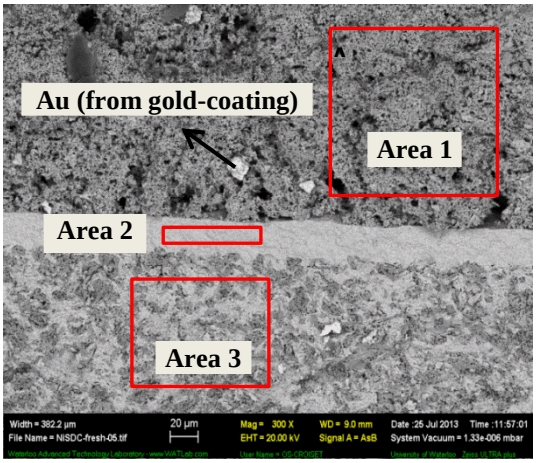

(b)

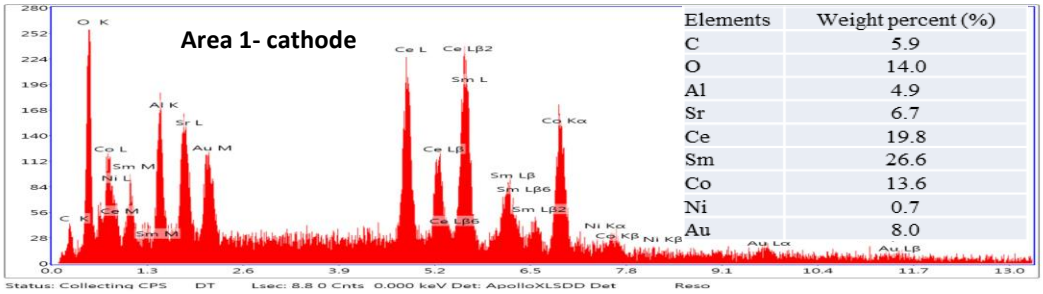

Elements	Weight percent (%)
C	5.9
O	14.0
Al	4.9
Sr	6.7
Ce	19.8
Sm	26.6
Co	13.6
Ni	0.7
Au	8.0

(c)

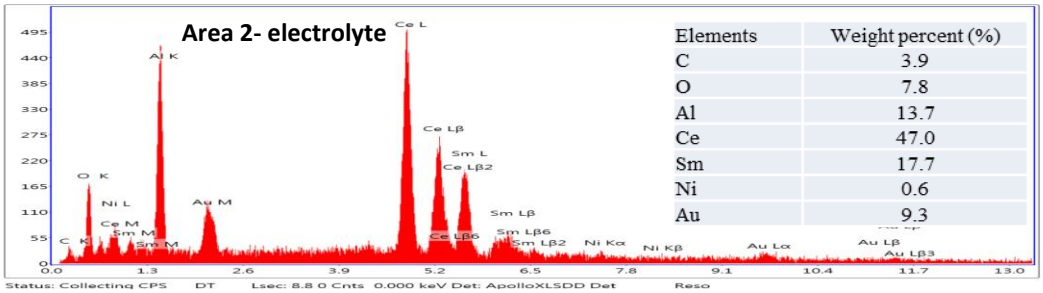

Elements	Weight percent (%)
C	3.9
O	7.8
Al	13.7
Ce	47.0
Sm	17.7
Ni	0.6
Au	9.3

(d)

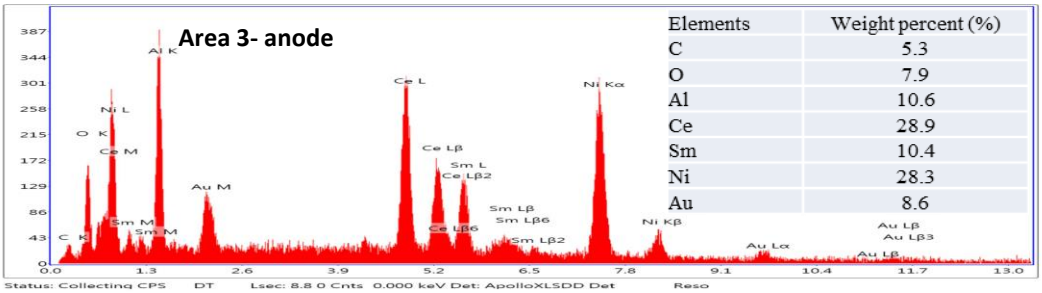

Elements	Weight percent (%)
C	5.3
O	7.9
Al	10.6
Ce	28.9
Sm	10.4
Ni	28.3
Au	8.6

Figure 4-5 a) Cross-section of Ni-SDC|SDC|SSC-SDC cell and EDX mappings for b) cathode, c) electrolyte and d) anode regions

4.3.4 Open circuit voltage in H_2 and CO-CO_2 feeds

The equilibrium cell potential can be determined using the Nernst equation shown in Eq. 4.3. $p_{O_2,an}$ and $p_{O_2,ca}$ are the partial pressures of oxygen at the anode and the cathode, respectively. F is the Faraday constant (96,487 C mol^{-1}), R is gas constant (8.314 J mol^{-1} K) and T is temperature (K).

$$E_r = -\frac{RT}{4F} ln \left(\frac{p_{O_2,an}}{p_{O_2,ca}}\right) \quad 4.3$$

The Nernst equation, however, does not provide an accurate estimation for OCV when a fuel cell operates with mixed ionic-electronic conductors, such as doped-ceria electrolyte. Besides the ionic conduction, doped-ceria also exhibits an electronic conduction, which effect is stronger at high reducing condition. Reducing environment, which promotes the partial reduction of Ce^{4+} into Ce^{3+}, causes a rise in electronic conduction inside the doped ceria material (Mogensen, 2000). Known as an electronic carrier, Ce^{3+}, which is formed uniformly within the ceria fluorite structure, is responsible for the electron transport. The electronic conductivity, σ_e can then be expressed as:

$$\sigma_e = [Ce'_{ce}]e\mu \quad 4.4$$

where $[Ce'_{ce}]$ is the concentration of Ce^{3+} ions, e is the charge of the electron and μ is the mobility. Due to this mixed-ionic conduction behavior, the OCV of doped-ceria electrolyte will be lower than the Nernst cell potential.

Therefore, an electronic conduction factor should be considered when calculating the theoretical OCV for a doped-ceria electrolyte. The calculation of theoretical OCV takes into account the effect of the electronic conductivity within the doped-ceria electrolyte according to Eq. 4.5 (Matsui *et al.*, 2005a):

$$E_r = \frac{RT}{4F} \int_{\ln p_{O_2,an}}^{\ln p_{O_2,ca}} \frac{\sigma_i}{\sigma_i + \sigma_e} d \ln p_{O_2} \quad 4.5$$

where σ_i is the ionic conductivity which is dependent entirely on the temperature. Meanwhile the electronic conductivity, σ_e is a function of local oxygen partial pressure, p_{O_2}:

$$\sigma_e = \sigma_e^0 p_{O_2}{}^{\left(-\frac{1}{4}\right)} \quad 4.6$$

At zero electronic conductivity ($\sigma_e = 0$), the Eq. 4.5 reduces back into its former Nernst equation. Therefore, under conditions where the electronic conduction is suppressed, for example at relatively low temperatures and highly humidified fuel (high $p_{O_2,an}$), the measured OCVs will be closed to that predicted by the Nernst equation (Matsui *et al.*, 2005a).

By applying Eq. 4.5, the theoretical OCV for a system operating with SDC can be better estimated. In this work, the predicted OCVs for ceria-based electrolyte have been calculated using the SDC electrolyte parameters under humidified H_2 obtained from Matsui *et al.* (2005b) (Table 4-2). The calculations for both Nernst potential and theoretical OCV for SDC are given in Appendix B.

Table 4-2 Electrolyte properties from Matsui *et al.,* (2005b)

Temperature (K)	σ_i (S cm^{-1})	σ_e^0 (S cm^{-1})
1073	0.101	7.16×10^{-6}
973	0.0471	5.01×10^{-7}
873	0.0176	1.78×10^{-8}
773	0.00532	2.51×10^{-10}

The OCVs for Ni-SDC cells have been measured in humidified H_2 and 40% CO-CO_2 at different temperatures. The values obtained from the experiments, as well as those calculated from the Nernst potential (Eq. 4.3) and from the theoretical OCVs for ceria-based electrolyte (Eq. 4.5) are compared in Figure 4-6 and Figure 4-7 for humidified H_2 and 40% CO-CO_2, respectively. The humidified H_2 fed at the anode contained of 97% H_2+3% H_2O and 40% CO-CO_2 mixture composed of 40% CO and 60% CO_2. Meanwhile 21% O_2 in air was used at the cathode. The thermodynamic properties for both reactants and oxidant were obtained from Smith's Introduction to Chemical Thermodynamics (5th edition) (Smith, 1996).

From Figure 4-6, the cell showed a large discrepancy of the experimental OCVs from the Nernst potential and this is believed due to the electronic conduction. The prediction of OCV

using the theoretical OCVs from Eq. 4.5 provides a better evaluation for the the ceria-based electrolyte cell. However, experimentally observed OCVs were still lower than the theoretical OCVs-SDC by approximately ~12%. The reason for this can be due to the improper sealing (Zhang *et al.,* 2004) or physical defects on the electrolyte (Moon *et al.,* 2004). A wider difference between the experimental and theoretical values was observed at low temperature (550ºC). This may due to the effect of electrode polarization with temperature. When operating the cell at low temperatures, the electrode polarization increases, resulting in loss of the cell voltage even at OCV condition (Zhang *et al.,* 2007). Nonetheless, the OCVs measured from this study are close to the OCVs obtained by other researchers on the Ni-SDC anode-supported cells. The OCVs attained in this work and by other researchers are compared in Table 4-3.

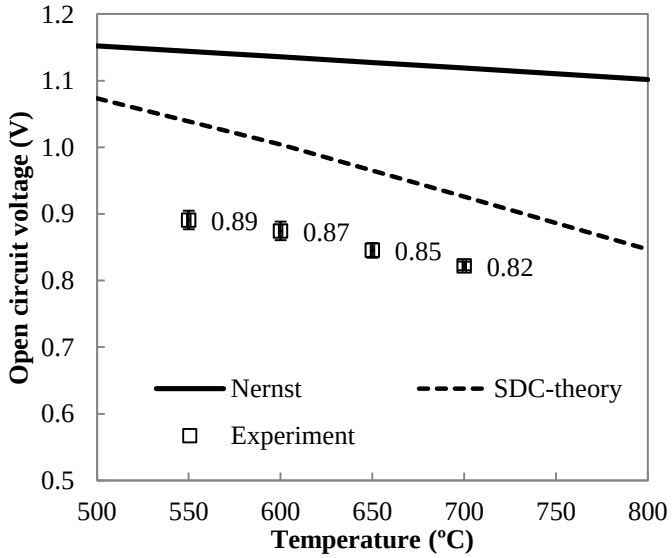

Figure 4-6 OCVs from Nernst equation, theoretical SDC and experimental work for humidified H_2

Table 4-3 OCVs of Ni-SDC|SDC|SSC-SDC cell under humidified H_2

Temperature (ºC)	Open circuit voltage (V)				
	Yin *et al.*, (2004)	Zhang *et al.*, (2006)	Wang *et al.*, (2008a)	Yang *et al.*, (2012)	This study
450	0.94	0.98	0.95	0.95	-
500	0.92	0.95	-	0.93	-
550	0.89	0.92	-	0.90	0.89
600	0.88	0.88	-	0.85	0.87
650	0.87	0.85	0.82	0.82	0.85
700	-	-	-	-	0.82

Meanwhile, the experimental OCVs obtained for 40% CO-CO_2 show a smaller discrepancy to the theoretical OCVs compared to that for humidified H_2 (Figure 4-7). The experimental values were lower than the theoretical OCVs for the SDC by only ~5%.

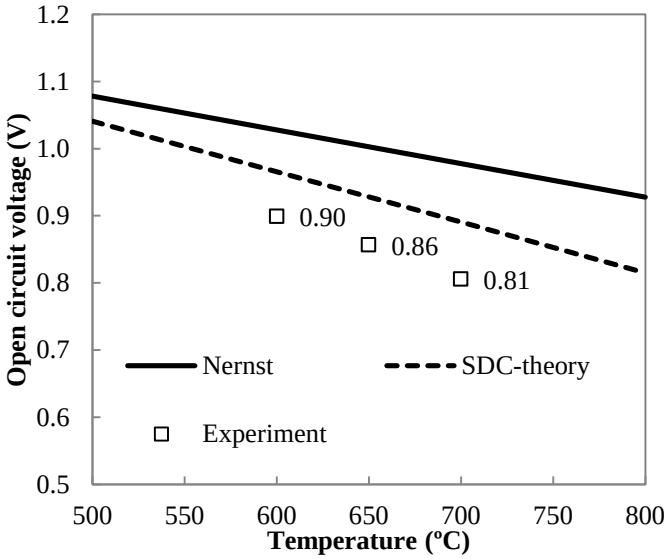

Figure 4-7 OCVs from Nernst equation, theoretical SDC and experimental work for 40%CO/60%CO_2

4.3.5 Performance in H_2, CH_4 and CO-CO_2

The Ni-SDC cells were tested with various fuels from humidified H_2 to carbon-containing feeds; humidified CH_4, dry CH_4, and mixtures of CO-CO_2. The cells were evaluated from 600 to 700ºC, a temperature range for an intermediate-temperature SOFC. The OCVs, maximum power densities and limiting current densities obtained for Ni-SDC measured in this work are summarized in Table 4.4. The i-V curves and the corresponding power densities for Ni-SDC under humidified H_2, humidified CH_4 and dry CH_4 are shown in Figure 4-8.

The maximum power densities obtained using Ni-SDC anode-supported cells in this work (e.g. 376 mW cm^{-2} at 600ºC under humidified H_2 (Figure 4-8a)) is comparable to the published results for the cell using a similar cathode material, SSC-SDC. Xia *et al.* (2001) who worked on a cell with an electrolyte thickness similar to that used in the present work (30 µm), but deposited through screen-printing, obtained a power density of 397 mW cm^{-2} at 600ºC under humidified H_2. Nonetheless, a power density of 400 mW cm^{-2} was obtained by Ding *et al.* (2008) using a cell with an electrolyte thickness of 70 µm fabricated using dry-pressing and co-sintering. Later, Yang *et al.* (2012) have successfully produced a dense SDC electrolyte of thickness ~15 µm using spin coating. A relatively higher power density (438 mW cm^{-2}) was attained in their work under humidified H_2 at 600ºC. The cell performance is influenced by various factors for example electrolyte thickness, component compositions as well as fabrication methods. For instance, thinner electrolyte film (~15 µm) and the use of active cathode material (such as BSCF) will lead to better cell performance (Ai *et al*., 2006). Maximum power densities of 553 and 663 mW cm^{-2} were found under humidified H_2 at 650 and 700ºC, respectively. The performance found at these temperatures also comparable with the results in the literature.

Obviously, the highest power densities were achieved at the highest temperature tested here, that is 700ºC. It is interesting to note that the maximum power density was slightly better with CH_4 than for H_2 (Figure 4-8a-b and c). The maximum power densities at 700ºC are 663, 721 and 697 mW cm^{-2} for humidified H_2, humidified CH_4 and dry CH_4, respectively.

The limiting current densities were also higher in CH_4 (~3.0 A cm^{-2}) compared to H_2 (~2.0 A cm^{-2}). This better performance in CH_4 fuel may be attributed to the high catalytic activity of Ni-SDC anode towards CH_4 oxidation (Murray *et al.*, 1999). It is suggested that the ability of ceria to store and transfer the oxygen ions enhances the rate of methane oxidation. Wang *et al.* (2003) found that the rate of methane oxidation on the surface of Ni-SDC anode is even higher than the O^{2-} supply rate to the actives sites. They also recommended that the high activity and stability of Ni-SDC in CH_4 is due to the ability of SDC to release the lattice oxygen ions under reducing environment. The released lattice oxygen ions were then participated in the electrochemical oxidation of CH_4. A better performance on the cell under CH_4 than the H_2 fuel was also found similar at 650ºC. Meanwhile at 600ºC, the humidified H_2 exhibited a better performance compared to CH_4. Maximum power density of 376 mW cm^{-2} was achieved at 600ºC compared to 370 mW cm^{-2} and 356 mW cm^{-2} for humidified CH_4 and dry CH_4, respectively.

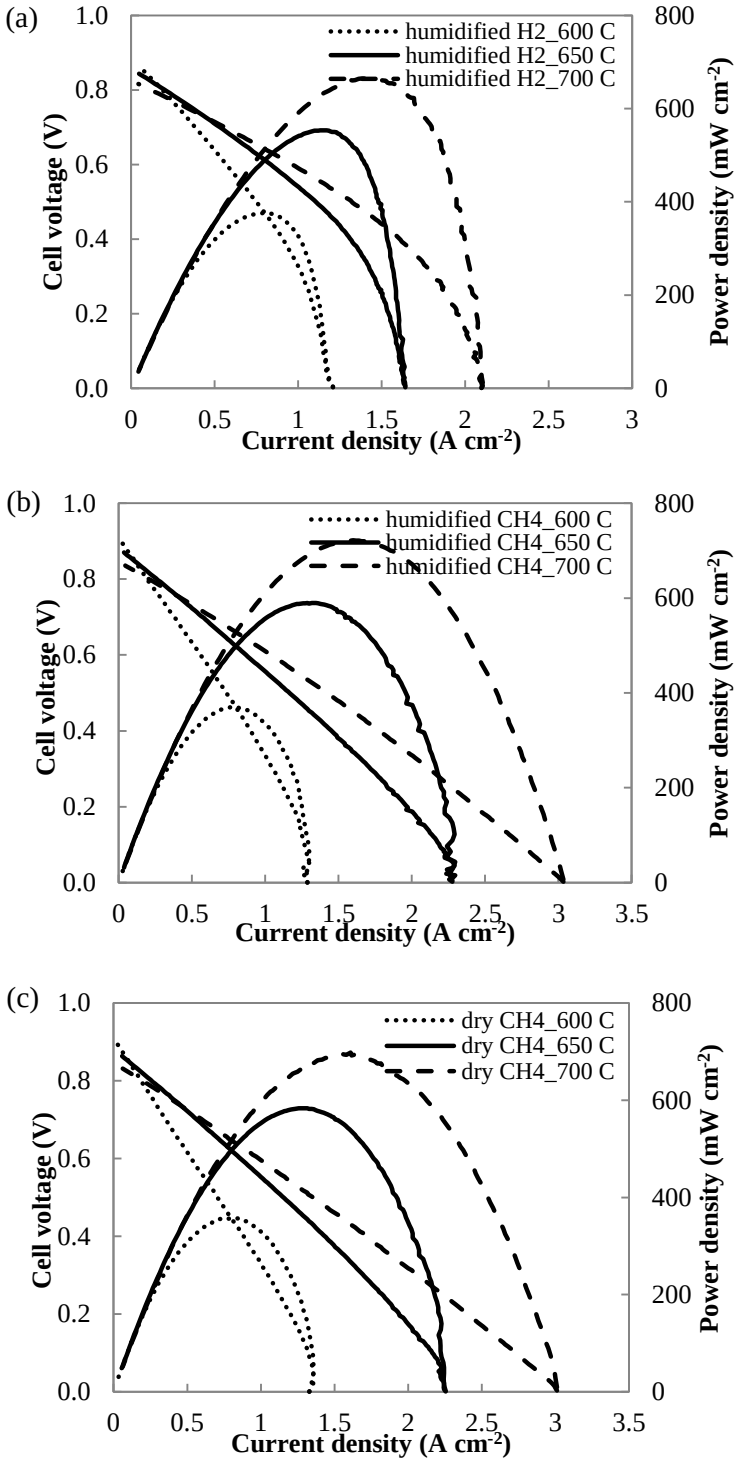

Figure 4-8 i-V curves under a) humidified H_2 b) humidified CH_4 and c) dry CH_4 at various temperatures

Although seldom being directly fed into SOFC due to its toxicity, CO can enter as a synthesis gas component and also an important intermediate during direct utilization of CH_4. Thus, the electrochemical activity of Ni-SDC with CO-containing fuel was also assessed (Figure 4-9). In this work, carbon deposition inside the gas delivery tube has become the main concern while operating with CO due to possibility of the Boudouard reaction ($2CO \rightarrow C + CO_2$). Carbon formation through the Boudouard reaction is thermodynamically favorable at lower temperatures. At temperatures below 500ºC, carbon formation will occur unless the ratio of CO/CO_2 is kept very low (Murray *et al.,* 1999). In order to avoid the accumulation of carbon in the delivery tube, the CO concentration used in this work was only limited to 20-40%, representing less favourable conditions toward the Boudouard reaction. The concentrations were selected based on equilibrium compositions calculated for $CO\text{-}CO_2$ mixtures (Appendix C). In addition, heating tape was applied to ensure rapid heating of the CO gas feed.

Only 239 mW cm^{-2} was achieved with the 40% $CO\text{-}CO_2$ mixture at 600ºC, about 1.5 times lower than what was obtained with H_2 and CH_4 at the same temperature. However, it has to be considered that the concentrations of CO used in this work (20 and 40 %) were much lower than that used for H_2 and CH_4 (100%). Nevertheless, the power density obtained (239 mW cm^{-2}) was higher than that reported by Su *et al.* (2010) at similar temperature (180 mW cm^{-2}) using pure CO. The maximum power densities for 40% $CO\text{-}CO_2$ were within a range of 239-270 mW cm^{-2}. Meanwhile, cell working with 20% $CO\text{-}CO_2$ provided maximum power densities of 50-88 mW cm^{-2}. The highest power density achieved by CO was 270 mW cm^{-2}, obtained at 650ºC with 40%CO. Li *et al.* (2010) have found a limiting current density of 0.39 A cm^{-2} at 800ºC with 20% $CO\text{-}CO_2$ using Ni-YSZ cell. A higher limiting current density (0.59 A cm^{-2} with 20% CO) was found in the present study, even at lower operating temperature, 700ºC.

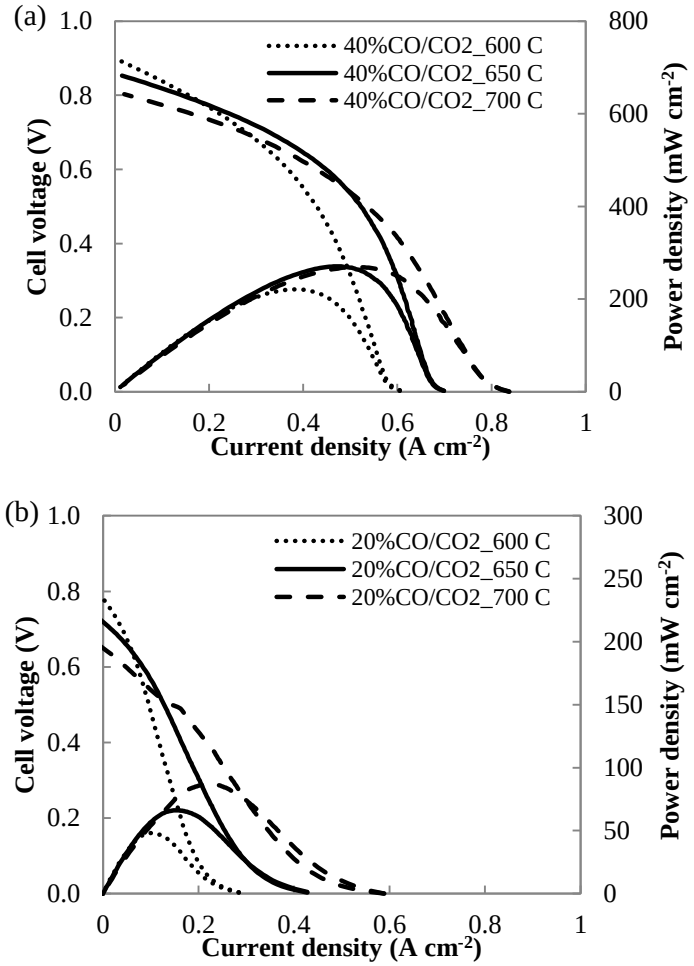

Figure 4-9 i-V curves under a) 40% CO-CO_2 b) 20% CO-CO_2 at various temperatures

Table 4-4 Open circuit voltage (OCV), maximum power density and limiting current density of Ni-SDC|SDC|SSC-SDC cell under various fuels and temperatures

Fuels	Temperature (ºC)	OCV (V)	Max. power density (mW cm^{-2})	Limiting current density (A cm^{-2})
Humidified H_2	700	0.82	663	2.09
	650	0.84	553	1.64
	600	0.85	376	1.21
Humidified CH_4	700	0.83	721	3.04
	650	0.87	589	2.28
	600	0.90	370	1.29
Dry CH_4	700	0.83	697	3.01
	650	0.86	583	2.25
	600	0.89	356	1.33
40% CO-CO_2	700	0.81	268	0.84
	650	0.86	270	0.69
	600	0.89	239	0.60
20% CO-CO_2	700	0.73	88	0.59
	650	0.77	66	0.43
	600	0.83	50	0.28

4.3.6 Cell stability

The stability of Ni-SDC cells under H_2, CH_4 and CO fuels was tested under galvanostatic mode at a constant current density (0.1 A cm^{-2}). The current density was chosen based on i-V curves of each fuel in section 4.3.5 to allow the cell operates at least at ~0.6-0.7 V cell voltage. The stability tests were conducted at 600 and 700ºC where cell voltages were monitored over time. Humidified CH_4 and 20% CO-CO_2 mixture were selected instead of dry CH_4 and 40% CO-CO_2 in order to reduce the risk of carbon deposition on the anode. Stability tests for H_2 and CH_4 were performed for 10 hrs while experiment with CO was limited to for 6 hrs only to avoid the accumulation of carbon inside the gas delivery tube.

Figure 4-10 shows that there was no clear drop in the performance of the cell with all fuels. Cell voltages were stable at 0.78-0.79 V for H_2, 0.74 V for CH_4 and 0.65-0.64 V for CO. A slight improvement of 0.06 mV hr^{-1} was observed in the cell operating with CH_4 and small cell degradation occurred under H_2 (1.12 mV hr^{-1}) and CO-CO_2 (2.34 mV hr^{-1}).

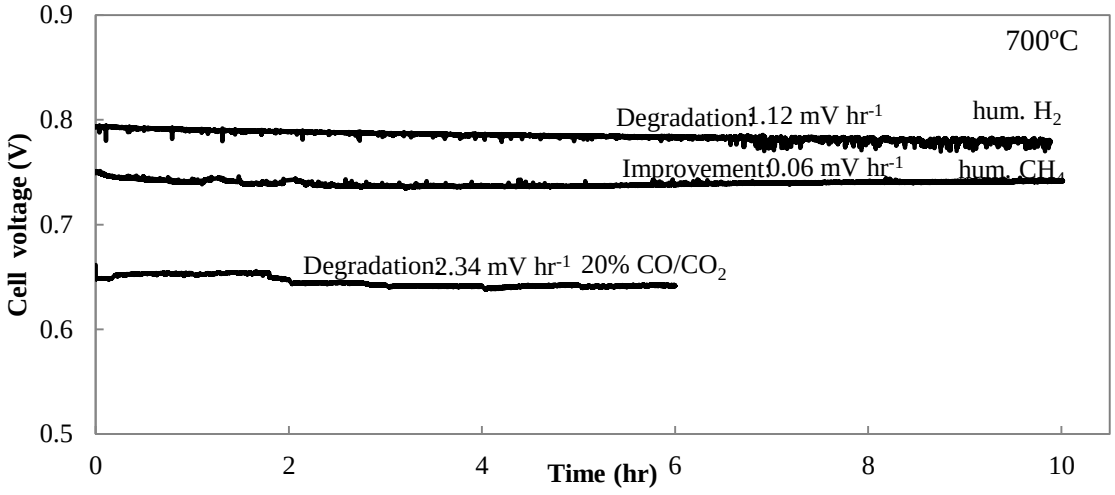

Figure 4-10 Cell voltage versus time at constant current density of 0.1 A cm^{-2} at 700ºC

A similar set of galvanostatic experiments carried out at a lower operating temperature (600ºC) is shown in Figure 4-11. Cell operating with H_2 shows a stable cell performance with a degradation rate (0.63 mV hr^{-1}) smaller than that obtained at 700ºC (1.12 mV hr^{-1}). Cell with CH_4 however showed a significant degradation rate of 5.36 mV hr^{-1} rather than an improvement at 700ºC. This is suggests that the cell performance with CH_4 was more stable during operation at 700ºC than at 600ºC. Meanwhile, the cell voltage for CO improved over time at 600ºC, contrary to what happened at 700ºC. Figure 4-10 and Figure 4-11 demonstrate the important effect of temperature on cell stability for Ni-SDC operating with CH_4 and CO.

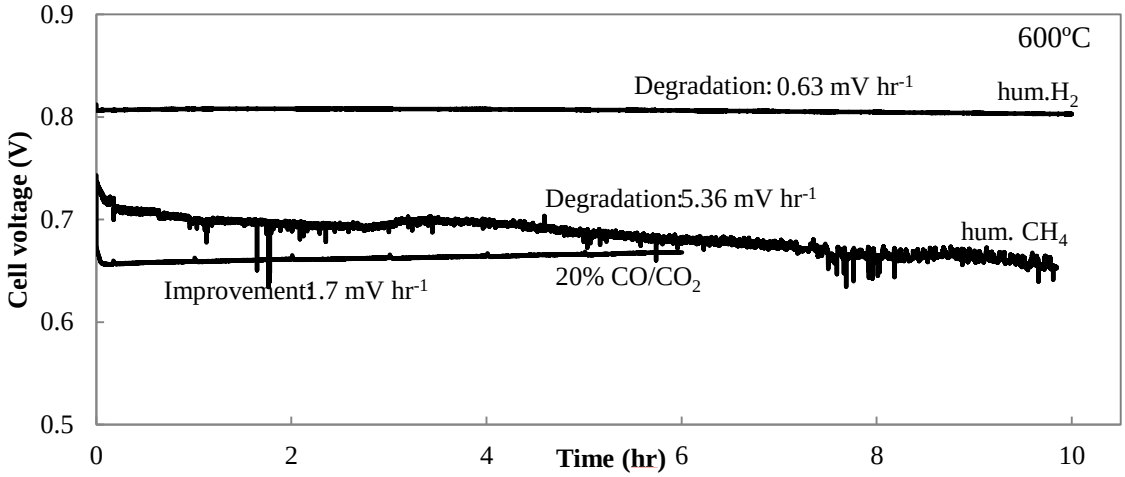

Figure 4-11 Cell voltage versus time at constant current density of 0.1 A cm^{-2} at 600ºC

Electrochemical impedance of the cell was analyzed before and after the stability tests at 700 and 600ºC. The analysis was performed using two-electrode configuration under a DC-biased condition at 0.1 A cm^{-2}. Each spectrum is fitted using a standard equivalent circuit shown in Figure 4-12a. The intercept on the real axis at the high- frequency end of the spectra corresponds to the ohmic resistance in the cell, R_s. Meanwhile, the difference between the two intercepts at the real axis yields the polarization resistance ($R_p=R_1+R_2$) which is related to the electrode processes. Since the air flow rate employed at the cathode side in all cells remained constant, changes in R_p can be directly related to changes in the feed at the anode. The values for R_s and R_p from both 700 and 600ºC experiments are tabulated in Table 4-5. In overall, the values of Rs and Rp obtained in this works are comparable with the values reported by other researchers using Ni-SDC anode-supported cells (Yin *et al.*, 2007; Wang *et al.*, 2008; Ai *et al.*, 2011).

Figure 4-12b-d show the impedance spectra for the cells operating with H_2, CH_4 and CO-CO_2 mixture at 700 ºC. There was no obvious change on the impedance spectra for H_2 and CH_4 before and after the stability tests. The value of R_s for H_2 did not vary while there was a small increase in R_p from 0.043 to 0.071 Ω cm^2 (Figure 4-12b). On the other hand, CH_4

showed no difference in the R_s but a reduction in the R_p from 0.086 to 0.064 Ω cm^2 after the 10 hrs stability test (Figure 4-12c). Kim *et al.* (2002) have ascribed the decrease of resistances after operation with CH_4 to the formation of carbon within the anode region. The addition of carbon at moderate levels has formed a connection between the isolated metal particles in the anode and made the particles electronically linked to the outside circuit. Thus, more anode surface is involved for the electrochemical reaction and as a result, has reduced the ohmic and polarization resistances. On the other hand, the change in impedance spectra after the stability test under CO fuel was significant (Figure 4-12d). R_s has increased from 0.19 to 0.23 Ω cm^2 and R_p has doubled from 0.26 to 0.59 Ω cm^2.

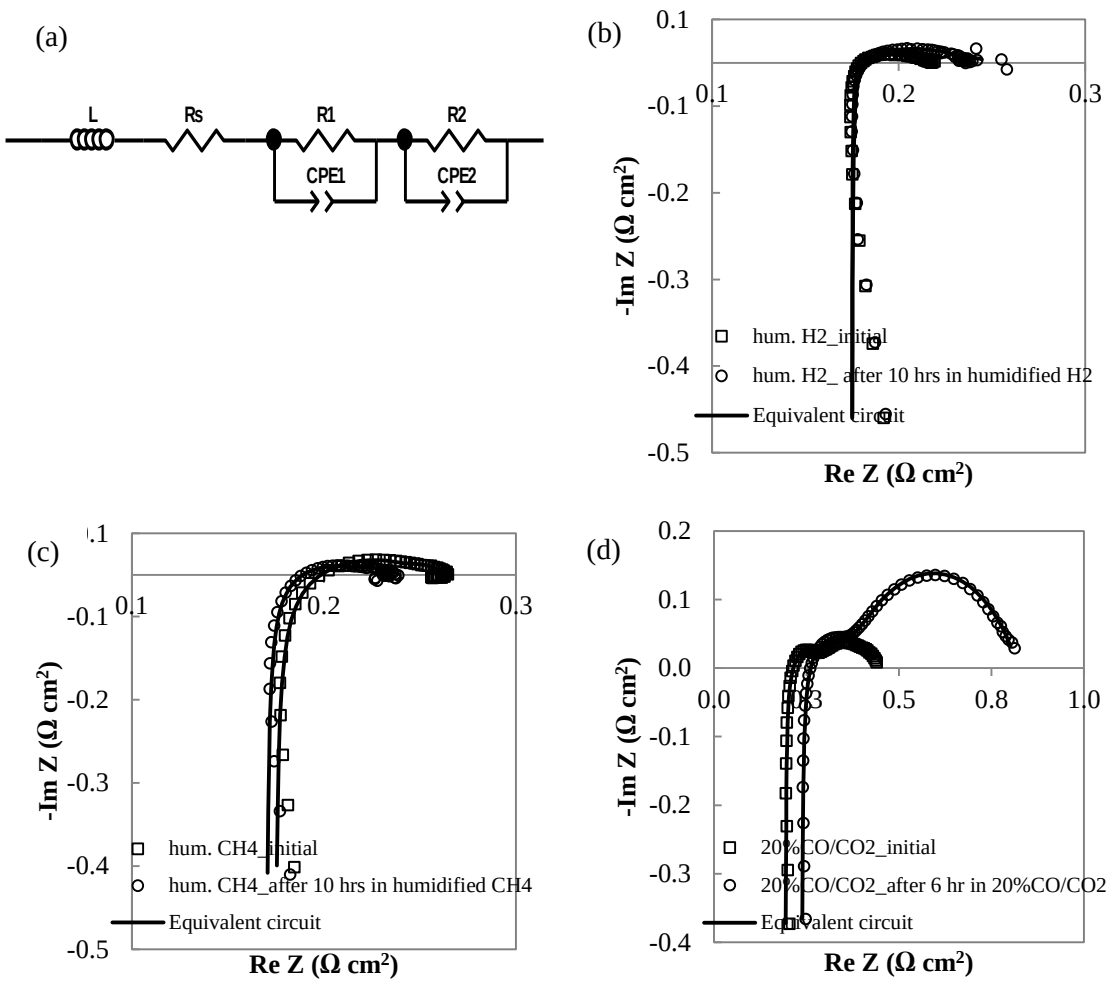

Figure 4-12 a) Equivalent circuit. Electrochemical impedance spectra before and after stability test for b) humidified H_2, c) humidified CH_4 and d) 20%CO/CO_2 at 700ºC

Table 4-5 R_s and R_p before and after stability test at 700 and 600ºC

Conditions	700ºC		600ºC	
	R_s (Ω cm^2)	R_p (Ω cm^2)	R_s (Ω cm^2)	R_p (Ω cm^2)
Initial humidified H_2	0.18	0.043	0.25	0.24
After 10 hrs in humidified H_2	0.17	0.071	0.24	0.30
Initial humidified CH_4	0.17	0.086	0.23	0.36
After 10 hrs in humidified CH_4	0.17	0.064	0.30	0.50
Initial 20%CO-CO_2	0.19	0.26	0.34	0.35
After 6 hrs in 20%CO-CO_2	0.23	0.59	0.33	0.36

The impedance spectra before and after stability test at 600ºC is presented by Figure 4-13. There was no significant change in R_s for the cell measured before and after the stability test in humidified H_2 at 600ºC, similar to results found at 700ºC. A slight increase was observed on the $R_{p.}$ In CH_4 fuel, there was an increase in both R_s and R_p, as illustrated by the impedance spectra, clearly reflects higher cell performance degradation over time at 600ºC than at 700ºC. Meanwhile, the decent performance in CO at 600ºC can be related to the constant resistance in both R_s and R_p.

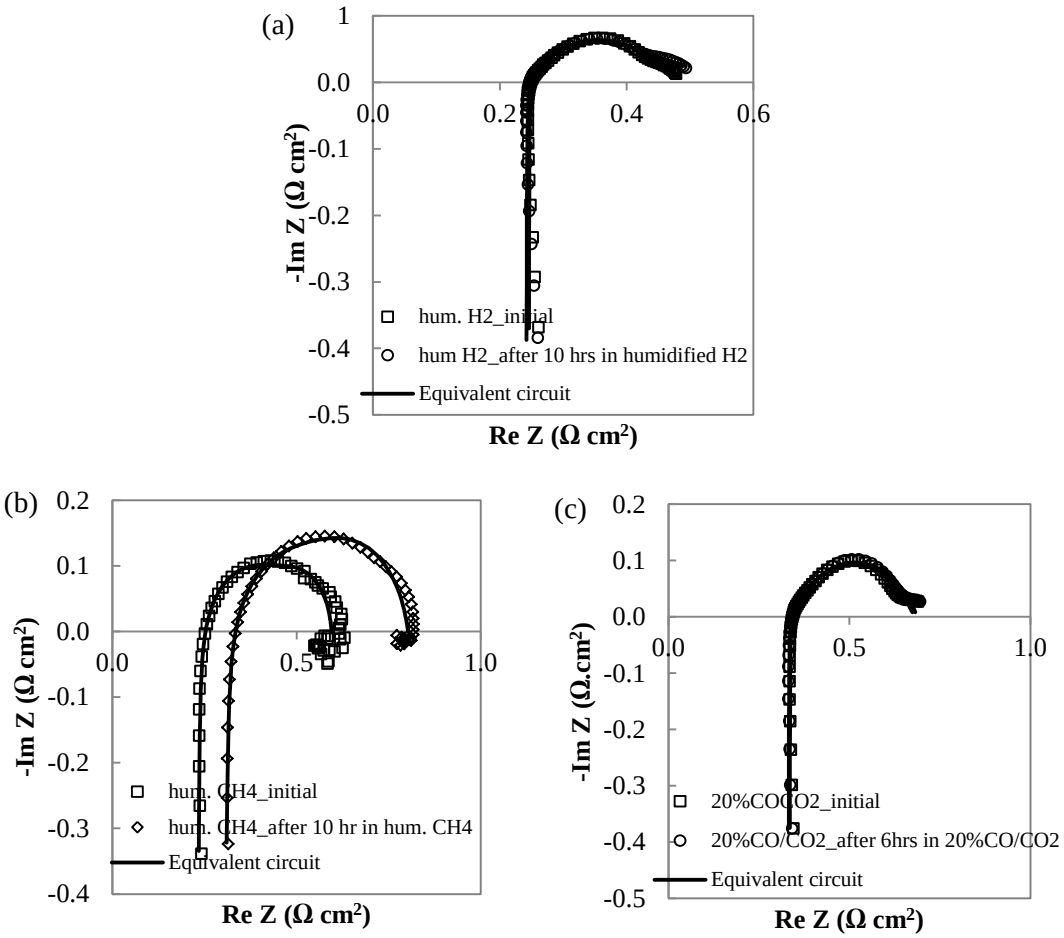

Figure 4-13 Electrochemical impedance spectra before and after stability test for a) humidified H_2, b) humidified CH_4 and c) 20%CO-CO_2 at 600ºC

4.4 Summary

In this study, Ni-SDC anode-supported cells were fabricated in-house and the cell performance was tested under H_2 and carbon-containing fuels: CH_4 and CO-CO_2 mixture. The findings from this work can be summarized as below:

- Ni-SDC anode-supported cells have been successfully fabricated using dry-pressing technique. Single cell composed of a thin electrolyte (~31 µm) adhered well to the porous anode and cathode of ~600 µm and ~160 µm in thickness, respectively.
- The theoretical OCVs were calculated using a modified Nernst equation to consider the effect from mixed ionic-electronic conductivity for ceria-based electrolyte. Experimental OCVs obtained by the cells with humidified H_2 were lower than the theoretical OCVs by 12%. Meanwhile, the difference between the experimental and theoretical OCVs for the cells operating with 40% CO-CO_2 was only 5%.
- The highest maximum powder densities of 663, 721, 697 mW cm^{-2} were achieved for humidified H_2 humidified CH_4 and dry CH_4 at 700ºC, respectively. Better overall performance at both 700°C and 650°C was observed for the cell in CH_4 than the H_2. On the other hand, the use of humidified H_2 yielded the best performance at 600ºC compared to CH_4. Much lower power densities were observed with CO fuel than H_2 and CH_4. However, it should be considered that CO concentrations used in this study were only 20-40%. Nevertheless, the maximum power density and limiting current density achieved in CO-CO_2 were found to be better than that reported in previous works.
- Stable performance with no significant cell drop was found for all cells tested at 600 and 700ºC under H_2, CH_4 and CO-CO_2. The cell was found to exhibit higher voltage and be more stable using CH_4 at 700ºC than at 600ºC. However, a larger degradation in cell performance was observed with CH_4 at 600ºC. The opposite trend was found for operation with CO: the cell performance showed better stability at 600 than at 700°C. The temperature, even over the range 600-700°C, has a strong effect on the stability of the cell performance for CH_4 and CO-CO_2.

Chapter 5

Carbon deposition on Ni-SDC anode-supported cells in presence of CH_4 and CO

5.1 Introduction

Fuel flexibility is one of the most important advantages of SOFCs over other fuel cells. SOFC can operate with a direct supply of hydrocarbons and is also capable of utilizing CO as fuel. Hydrocarbons can be fed directly into the anode compartment without additional processing or significant mixing with steam. Among the hydrocarbon fuels, CH_4 has attracted much attention for SOFCs since it is the main constituent of natural gas. CO, on the other hand, enters as a component of the reformate gas generated from hydrocarbon processing. The common problem associated with these two fuels, however, is the faster degradation in SOFC performance due to carbon deposition at the anode. Despite having excellent electrochemical activity, Ni-based anodes also catalyze carbon formation on their surface.

Carbon is generally formed from the decomposition of CH_4 (Eq. 2.25) and via the Boudouard reaction (Eq. 2.33) when CO is fed into the system. During SOFC operation under current load, H_2 from Eq. 2.27 and carbon produced from Eqs. 2.25 and 2.33 can be electrochemically oxidized into H_2O and CO. When CH_4 is fed into the system, methane total oxidation (Eq. 2.29) and partial oxidation (Eq. 2.30) reactions may occur. H_2O produced electrochemically can interact with CH_4 and CO and lead to the steam reforming reaction (Eq. 2.23) and water-gas shift reaction (Eq. 2.24). When CO is available in the system either through the feed or resulting from oxidation of carbon, partial oxidation of CH_4 or methane steam reforming, CO oxidation into CO_2 (Eq. 2.28) is expected.

It has been reported that the ability of doped-ceria to better avoid carbon deposition than other oxides is due to the reaction of its lattice oxygen with the surface carbon (Huang *et al.*, 2005). One interesting feature with ceria-based material is that, as the material is reduced under reducing condition producing electrons, formation of oxygen vacancy is formed within the lattice structure. Formation of vacancy will increase the transfer of oxide ions and this

ionic conductivity is expected to reduce carbon deposition rate in Ni-SDC anode. Also, surface oxygen becomes available when the electrochemical products H_2O or CO_2 dissociate over the reduced ceria. This surface oxygen can readily react with carbon and thereby remove it from the surface (Iida *et al.*, 2007). Wang *et al.* (2003) reported that the release of lattice oxygen of SDC is also possible during OCV condition (no current load) within reducing atmosphere. These oxide ions then further participated in the electrochemical oxidation reactions.

Previously in Chapter 4, performance of Ni-SDC anode-supported cells has been evaluated under H_2, CH_4 and CO at various operating temperatures. In this study, stability of the cell was further monitored with CH_4 and CO fuels under conditions which carbon deposition is favoured.

5.2 Experimental Procedure

Stability tests have been conducted at current densities of 0.35 A cm^{-2} and 0.1 A cm^{-2} in the presence of dry CH_4 and CO, respectively. For the experiments conducted with dry CH_4 feed, pure gas was fed into the cell at a rate of 40 mL min^{-1}. In the case of CO, a mixture containing 40% CO and 60% CO_2 was fed into the cell at a total flow rate of 80 mL min^{-1}. For comparison, a test under similar conditions was carried out on a cell operating with humidified H_2 (3% H_2O) as fuel.

Electrochemical impedance spectroscopy (EIS) was performed during the course of the stability tests using the galvanostatic mode at a DC current density of 0.35 A cm^{-2} when the feed stream consisted of dry CH_4 and 0.1 A cm^{-2} when the feed contained CO. The frequency range for the EIS was from 0.1 to 10^5 Hz. An equivalent circuit was then used to fit the impedance spectra to obtain numerical values of the effective ohmic resistance, R_s and polarization resistance, R_p. Following the stability experiments, sections of the anode were examined using SEM (LEO 1530). The presence of carbon deposit on the anode was also monitored using the energy dispersive X-ray analysis (EDXA).

The equilibrium composition expected within the anode compartment after with dry CH_4 and CO-CO_2 was computed using the HSC Chemistry 5.1 software package (Outokumpu, Finland). In this analysis, the amount of each product is obtained by minimization of the Gibbs free energy for the system. The thermodynamic calculations were based on inlet gas feeds that match the experimental conditions of the stability tests described in the preceding paragraph. Under a current load, the flux of oxygen ions delivered to the anode from the cathode side is governed by the applied current according to Faraday's law:

$$n_{O_2} = \frac{I}{zF} \qquad 5.1$$

where n_{O_2} is the flow of oxygen supplied (mol s^{-1}). $z = 4$ is the number of electrons involved in the oxygen reduction reaction ($O_2 + 4e^- \rightarrow 2O^{2-}$), I is current (A) and F is the Faraday constant (96,487 s A mol^{-1}).

5.3 Results and Discussions

5.3.1 Equilibrium composition

Figure 5-1 shows the equilibrium composition as a function of temperature in a SOFC operated with dry CH_4 and 40%CO-60%CO_2. From the analysis using dry CH_4 as feed (Figure 5-1a), the amount of H_2 produced is almost twice that of C indicating that both H_2 and C originated from methane decomposition (Eq. 2.25). CH_4 is more stable at low temperature, but it increasingly decomposes to H_2 and C as the temperature is raised. The methane conversion, $x$$CH_4$ reaches ~92.6% at 800ºC. Under the condition applied (dry CH_4, 0.35 A cm^{-2}), C deposition is predicted to occur regardless of the temperature. The amount of carbon formed increases with increasing temperature and the amount of C formed no longer changes when the temperature is increased above 600°C. The flux of oxygen ions produced at a current density of 0.35 A cm^{-2} yields only relatively small amounts of CO, CO_2 and H_2O of less than 10 mol%. H_2O production is favoured to a small extent at lower temperature,

while the amount of CO increases slightly as the temperature rises. However, the amount of CO_2 produced always remains insignificant under these conditions.

Figure 5-1b shows the results of the corresponding calculations when a feed stream containing a 40%CO-60%CO_2 mixture is introduced and the SOFC operates at a current density of 0.1 A cm^{-2}. The CO conversion, *x*CO and the amount of C formed drop sharply as the temperature is raised and become virtually non-existent at temperatures above 640ºC. This trend is expected given the exothermic nature of the Boudouard reaction (Eq. 2.33). Thus, no carbon should be deposited at temperatures above 640ºC when equilibrium is reached.

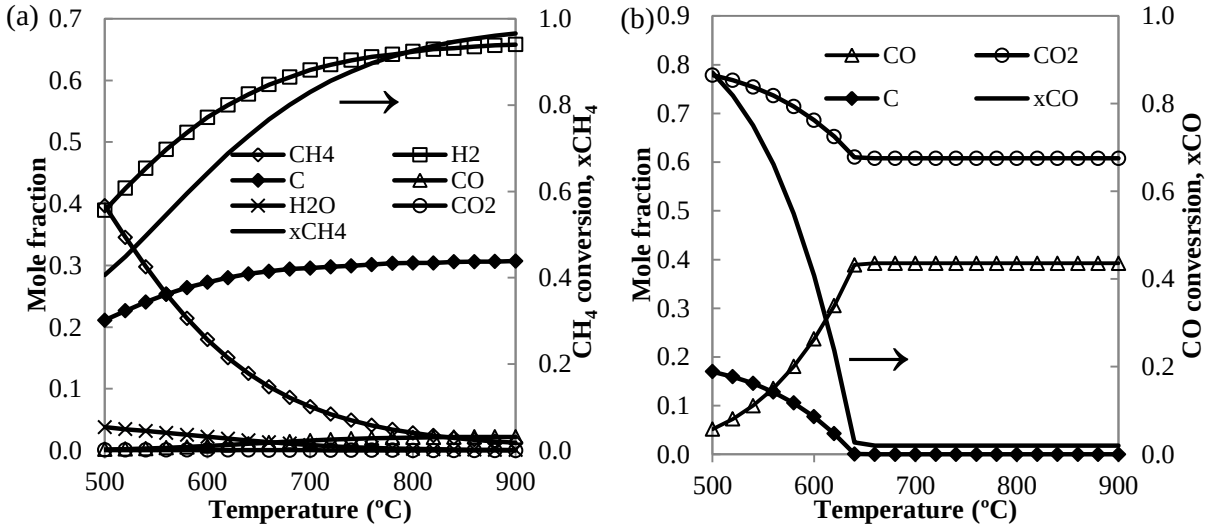

Figure 5-1 Equilibrium composition as a function of temperature for SOFC operating with the following feed streams: a) dry CH_4 (0.35 A cm^{-2}) and b) 40%CO-60%CO_2 (0.1 A cm^{-2})

5.3.2 Ni-SDC under CH_4 and CO

Experimental stability tests have been carried out to investigate the carbon deposition behavior in Ni-SDC anode-supported cells operating with a fuel stream containing dry CH_4 and another stream containing a 40%CO-60%CO_2 mixture. These experiments were carried out under conditions where carbon formation is thermodynamically favoured (700ºC for dry CH_4 and 550ºC for 40%CO-60%CO_2 mixture).

The cell performance was operated for 100 hrs in dry CH_4 to obtain the time course of the cell voltage shown in Figure 5-2. The cell voltage remained stable at approximately 0.75 V for the first 20 hrs before the performance started to gradually decrease over the remainder of the experiment at a rate of 1.33 mV hr^{-1}. The tiny spikes observed continually are caused by the disruption of the galvanostatic mode required to carry out the impedance measurements. These interruptions however have no effect on the overall measurement and behaviour of the system. The gradual degradation trend was maintained until 100 hrs.

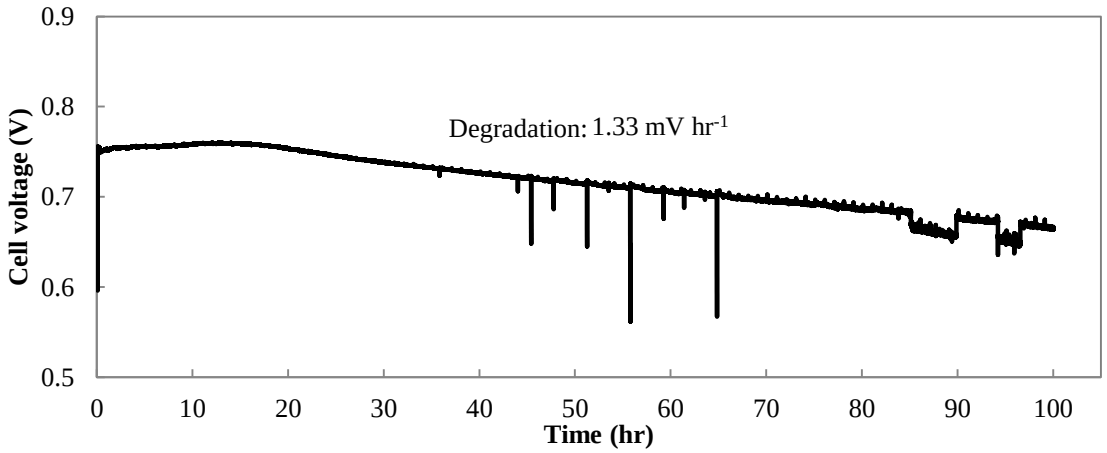

Figure 5-2 Variation of cell voltage over 100 hrs of SOFC operation at 700ºC with dry CH_4 at a current density of 0.35 A cm^{-2}

The corresponding values of R_s and R_p obtained from impedance analysis are plotted against time in Figure 5-3. No significant change in R_s was observed other than a slight increase between 30 and 50 hrs of operation, suggesting that the ohmic resistance of the cell remained almost constant with CH_4 exposure. The polarization resistance R_p, on the other hand, decreased during the first hour and then increased steadily from 0.052 to 0.104 Ω cm^2, indicating that the electrode process of the Ni-SDC cell deteriorated over time.

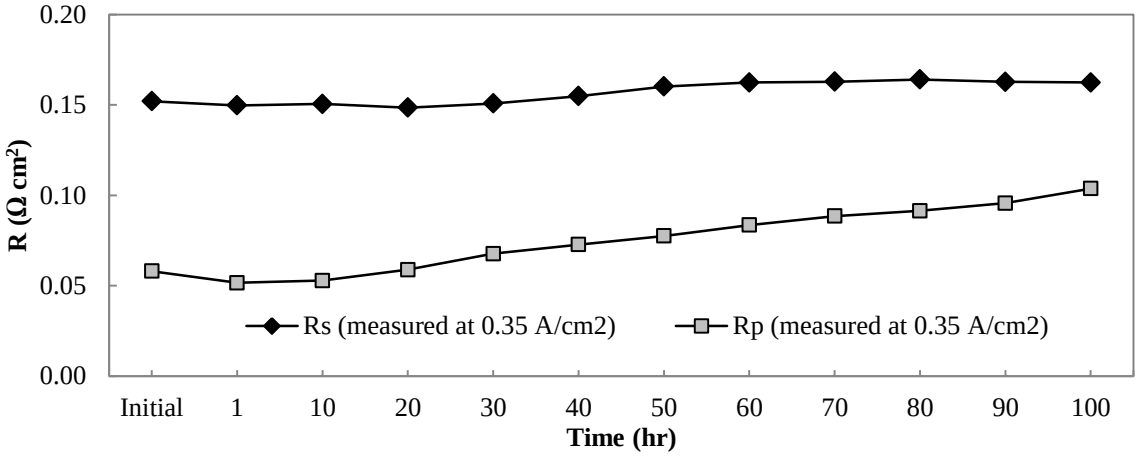

Figure 5-3 Variation of R_s and R_p over 100 hrs of SOFC operation at 700ºC with dry CH_4 at a current density of 0.35 A cm^{-2}

In order to determine whether carbon deposition caused the degradation in cell performance after CH_4 exposure, the performance was compared with the cell voltage monitored when the feed stream contained humidified H_2 only. The variation of the cell voltage over 75 hrs of operation with humidified H_2 is presented in Figure 5-4. The voltage remained stable between 0.72 V and 0.74 V over most of the experimental run with a degradation rate of 0.33 mV hr^{-1} that was smaller than that obtained in the presence of dry CH_4 (i.e., 1.33 mV hr^{-1}). Over the first 30 hrs of operation, the cell voltages measured in the presence of humidified H_2 and dry CH_4 were comparable to each other. However, as the time progressed, the cell operating with humidified H_2 maintained its cell voltage while the other using dry CH_4 began to decline. This difference in behaviour is consistent with what would

be expected if carbon were accumulating on the anode during the long exposure to dry CH_4. The deposited carbon on the Ni-SDC anode might have blocked the pores at the anode and increased the resistance for transport of the gas to reaction sites. Another possible effect of carbon is that it could have reduced the number of available Ni active sites for electro-oxidation at the electrolyte-anode interface or covered the sites for CH_4 decomposition over the entire anode.

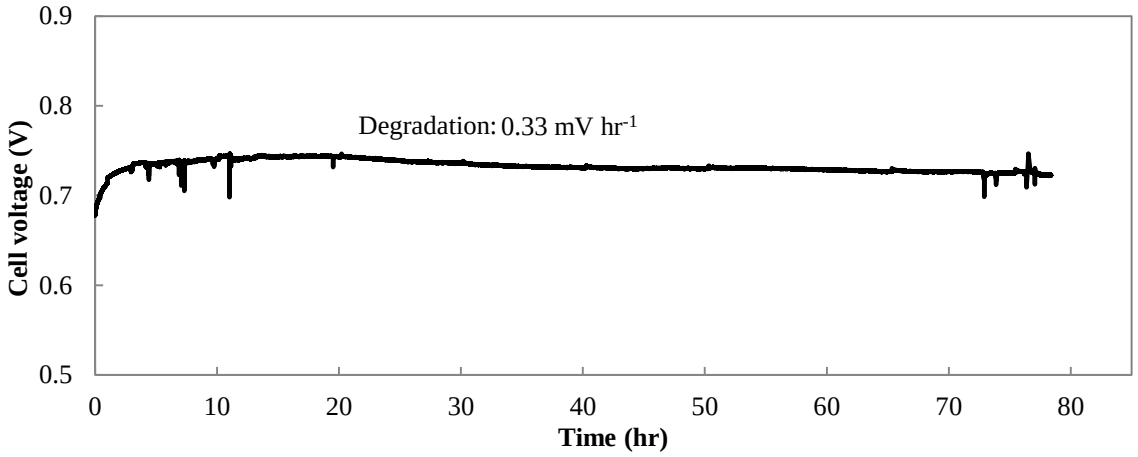

Figure 5-4 Variation of cell voltage over 75 hrs of SOFC operation at 700ºC with humidified H_2 at a current density of 0.35 A cm^{-2}

The variation of R_s and R_p of the cell when operating with humidified H_2 was also measured for comparison. As shown in Figure 5-5, both quantities remained almost unchanged over the 75-hour period. R_s increased very slightly from 0.154 to 0.165 Ω cm^2, but on the whole was unaffected by the nature of the gas (humidified H_2 or dry CH_4). Meanwhile, the R_p for dry CH_4 was only slightly higher than the R_p from the humidified H_2. Thus, although carbon may have deposited on the anode, the electrochemical processes involving the Ni-SDC anode remained active in generating electrical energy for at least 100 hrs operation.

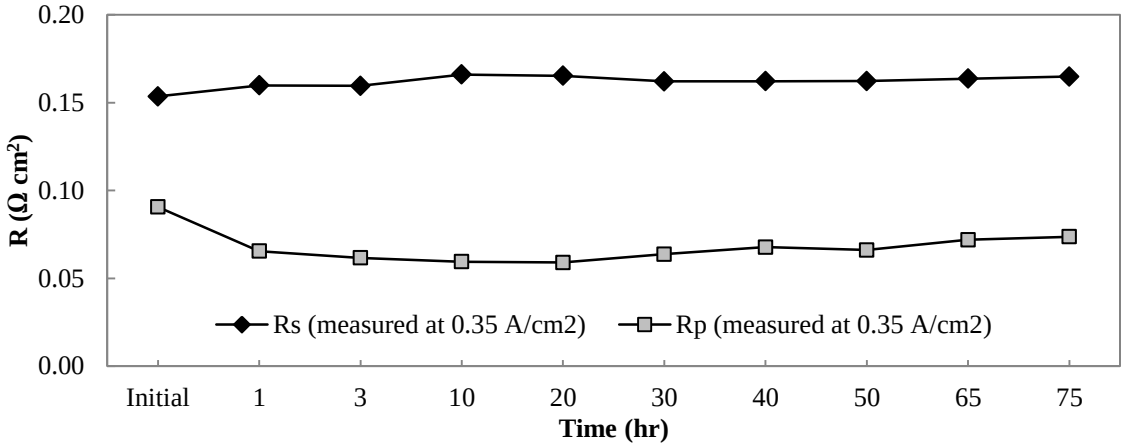

Figure 5-5 Variation of R_s and R_p over 75 hrs of SOFC operation at 700ºC with humidified H_2 at a current density of 0.35 A cm^{-2}

The variation of the cell voltage over time during operation of the Ni-SDC cell at 0.1 A cm^{-2} and 550ºC with the 40%CO-60%CO_2 feed is shown in Figure 5-6. As with the runs using dry CH_4, the spikes on the plot arose due to the disturbances to the system when the impedance was measured. Carbon deposited inside the gas delivery tube has become the main concern while operating with CO due to possibility of the Boudouard reaction. Thus, the operation for CO-CO_2 mixture was only limited for 6 hours only. Over the operation, the cell voltage decreased from 0.75 to 0.72 V. The degradation rate of 4.5 mV hr^{-1} was much higher than that observed when operating with the humidified H_2 and dry CH_4 feed streams. Since carbon was also found to accumulate on the tube leading to the anode when CO was employed, it is possible that higher rate of carbon formation through Boudouard reaction compared to that of methane decomposition has caused higher degradation under CO fuel.

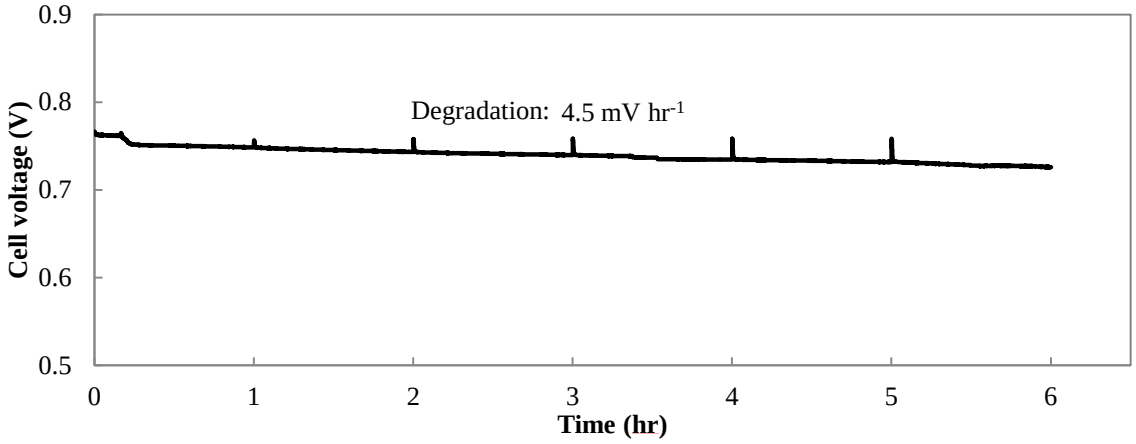

Figure 5-6 Variation of cell voltage over 6 hrs of SOFC operation at 550 ºC with 40%CO-60%CO_2 at a current density of 0.1 A cm^{-2}

The values of R_p and R_s measured during the operation with 40% CO-60%CO_2 are presented in Figure 5-7. In both cases, much higher resistances were obtained than in the previous cases, no doubt due in part to the lower operating temperature. It should also be noted that the relative magnitudes of R_p and R_s obtained in the presence of the CO-CO_2 mixture differed from that observed in the presence of humidified H_2 and dry CH_4. The electrode polarization R_p was smaller than R_s in the case of dry CH_4 and humidified H_2, whereas the opposite trend was obtained in the CO-CO_2 mixture. This difference suggests that the electrochemical oxidation of CO in the Ni-SDC cell proceeded with more difficulty than that of dry CH_4. Similar to that observed in humidified H_2 and dry CH_4, R_s remained virtually constant over most of the experimental run with the CO-CO_2, except for a small increase during the final hour. On the other hand, R_p increased by 25% over the 6-hr operation, suggesting a continuous deterioration of the cell performance, perhaps due to the accumulation of carbon deposited at the anode.

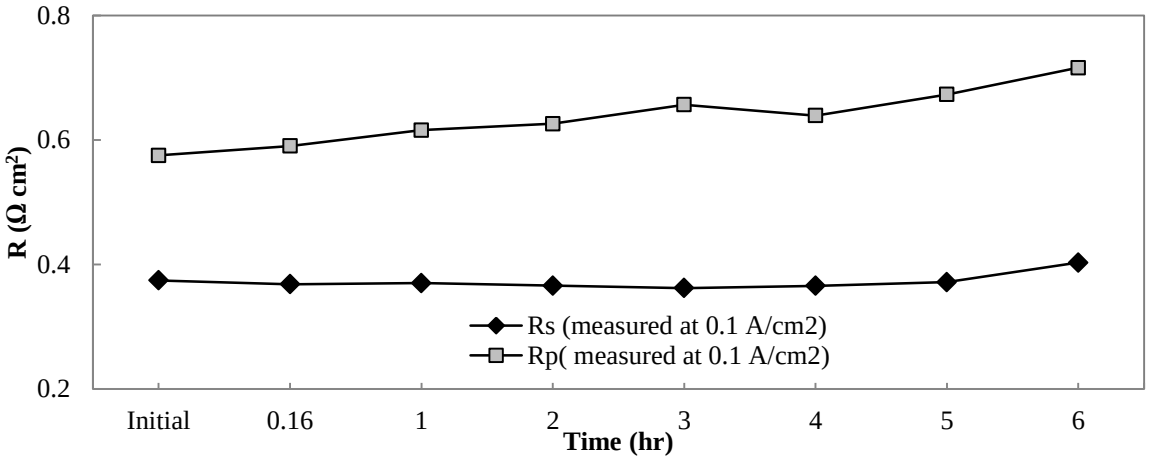

Figure 5-7 Variation of R_s and R_p over 6 hrs of SOFC operation at 550ºC with 40%CO-60%CO_2 at a current density of 0.1 A cm^{-2}

After the stability tests, the Ni-SDC cells were examined using SEM equipped with EDX. The micrographs of different sections of the anode (electrolyte-anode interface, middle of the anode and near the fuel entry location) obtained after operation with dry CH_4 and 40%CO-60%CO_2 are presented in Figure 5-8d-f and Figure 5-8g-i, respectively. The anodes were compared with one from fresh Ni-SDC (Figure 5-8a-c). The grey regions of the anode are ascribed to the SDC phase while the darker spots correspond to Ni. In spent anodes, dark regions are observed in the section near to the fuel entry point (Figures 5-8f and 5-8i), but not at the electrolyte-anode interface and the middle part of the anode. These dark features are suggested to be carbon deposits which have accumulated throughout the stability tests. Essentially, no deposit was observed at the electrolyte-anode interface and in the middle of the anode in both cases.

Carbon formed after exposure to the CO-CO_2 mixture appears to form as a carbon layer covering the whole network between Ni and SDC (Figure 5-8i). Meanwhile, the carbon generated in the anode that had operated with dry CH_4 appears to have deposited only on the Ni particles of the anode and separated the particles from the existing Ni-SDC network within the anode Figure 5-8f). This carbon deposition effect can be clearly distinguished

when the two anodes were compared to the fresh Ni-SDC (Figure 5-8c). The electrolyte-anode interface and the middle of the anode sections after both dry CH_4 and CO (Figures 5-8d-e and Figures 5-8g-h) however were not affected by carbon deposition and retained their original structures.

Fresh Ni-SDC

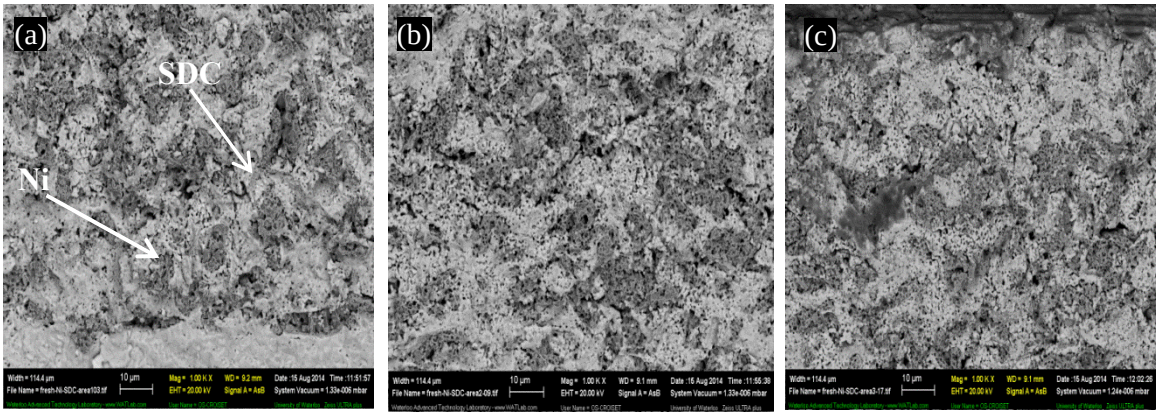

Dry CH_4

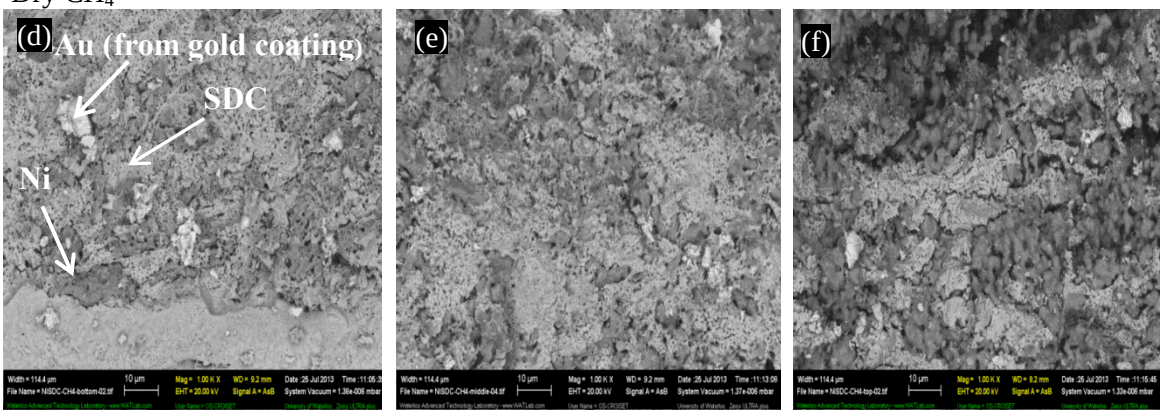

40% CO-60%CO_2

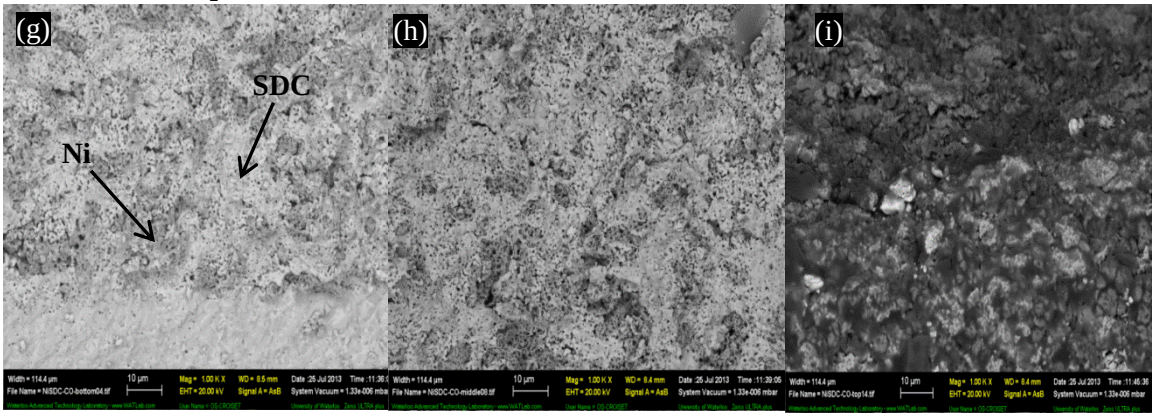

Figure 5-8 SEM micrographs of anode from anode-supported cells of (a, b, c) fresh Ni-SDC and after operation with (d, e, f) dry CH_4 and (g, h, i) 40%CO-60%CO_2 feed streams. Left: electrolyte-anode interface. Centre: middle section. Right: near to fuel entry side

EDX analysis was performed on selected areas of the Ni-SDC anodes after stability tests with dry CH_4 and CO-CO_2. The SEM micrographs of cross-sections from the two anodes after operation with dry CH_4 and CO-CO_2 and elemental analysis of different regions from these cross-sections are presented in Figure 5-10 and Figure 5-11, respectively. The elemental analysis was carried out near the electrolyte-anode interface (Area 1), the middle of the anode (Area 2) and near to the fuel entry side (Area 3). For comparison, the same characterization was also conducted for the fresh Ni-SDC (Figure 5-9). Carbon was detected in the EDX spectra of the two anodes after dry CH_4 and CO-CO_2 operations, but mostly in the anode section close to the fuel entry side (Area 3). The carbon weight percentage in the middle sections and the anode-electrolyte interface was found to be 6-7%, but 15% on the fuel entry side after operation with dry CH_4 and 34% on the fuel entry side after operation with CO. Small carbon contamination peak always appear on spectra of each sample. Since carbon detected for the fresh Ni-SDC was around 4-5%, the amount detected at the middle section and the anode-electrolyte interface for the cells with dry CH_4 and CO (6-7%) was considered to be insignificant. Thus, it is suggested that relatively very low amount of carbon has deposited near to the electrolyte-anode interface (Area 1) and in the middle of the anode (Area 2). Carbon from the exposure to dry CH_4 and CO was mostly deposited at the anode section close to the fuel entry side. In addition, carbon formation is believed to be responsible for the degradation of the upper surface of both anodes. Nevertheless, the carbon deposition occurred in this work has less impact on the bulk of the anode structure and thus allowed the cell to operate under carbon-containing fuels without a catastrophic failure.

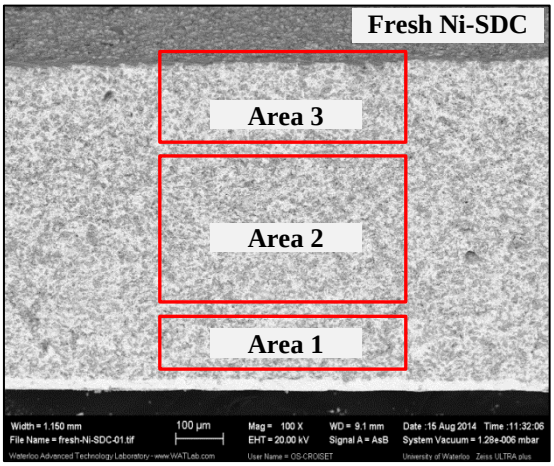

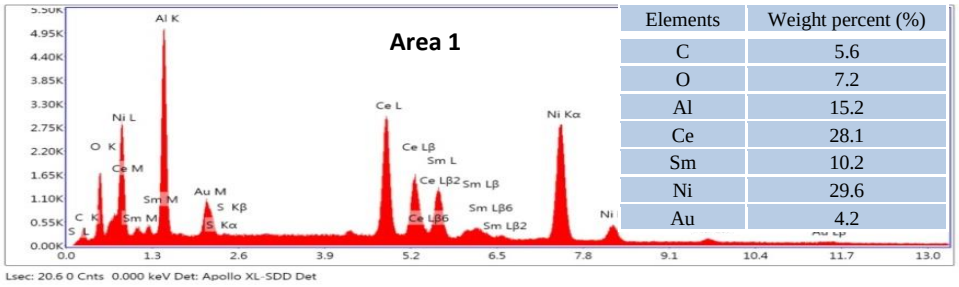

Elements	Weight percent (%)
C	5.6
O	7.2
Al	15.2
Ce	28.1
Sm	10.2
Ni	29.6
Au	4.2

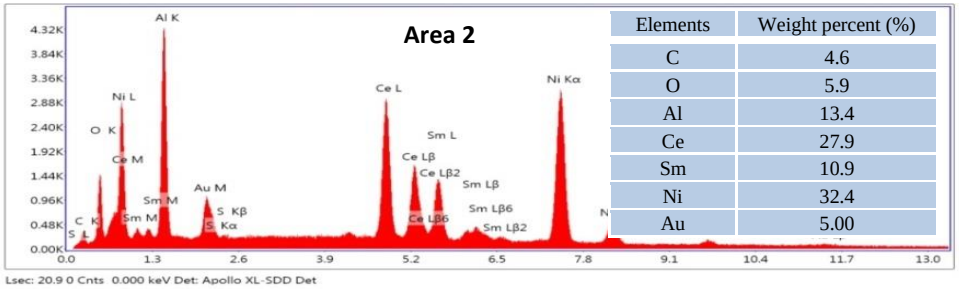

Elements	Weight percent (%)
C	4.6
O	5.9
Al	13.4
Ce	27.9
Sm	10.9
Ni	32.4
Au	5.00

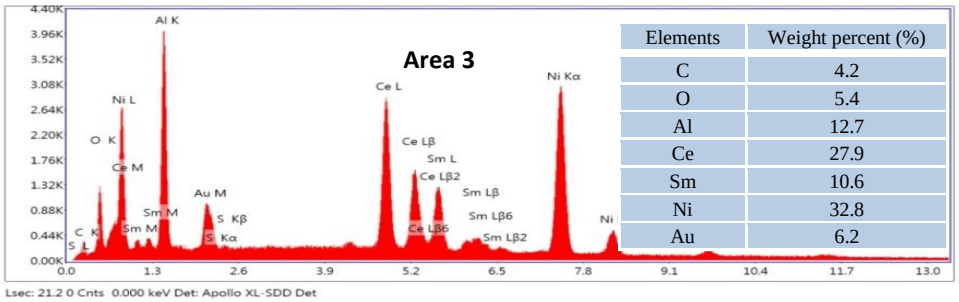

Elements	Weight percent (%)
C	4.2
O	5.4
Al	12.7
Ce	27.9
Sm	10.6
Ni	32.8
Au	6.2

Figure 5-9 SEM micrograph and EDX mapping in the labelled regions of cross-sections taken from fresh Ni-SDC

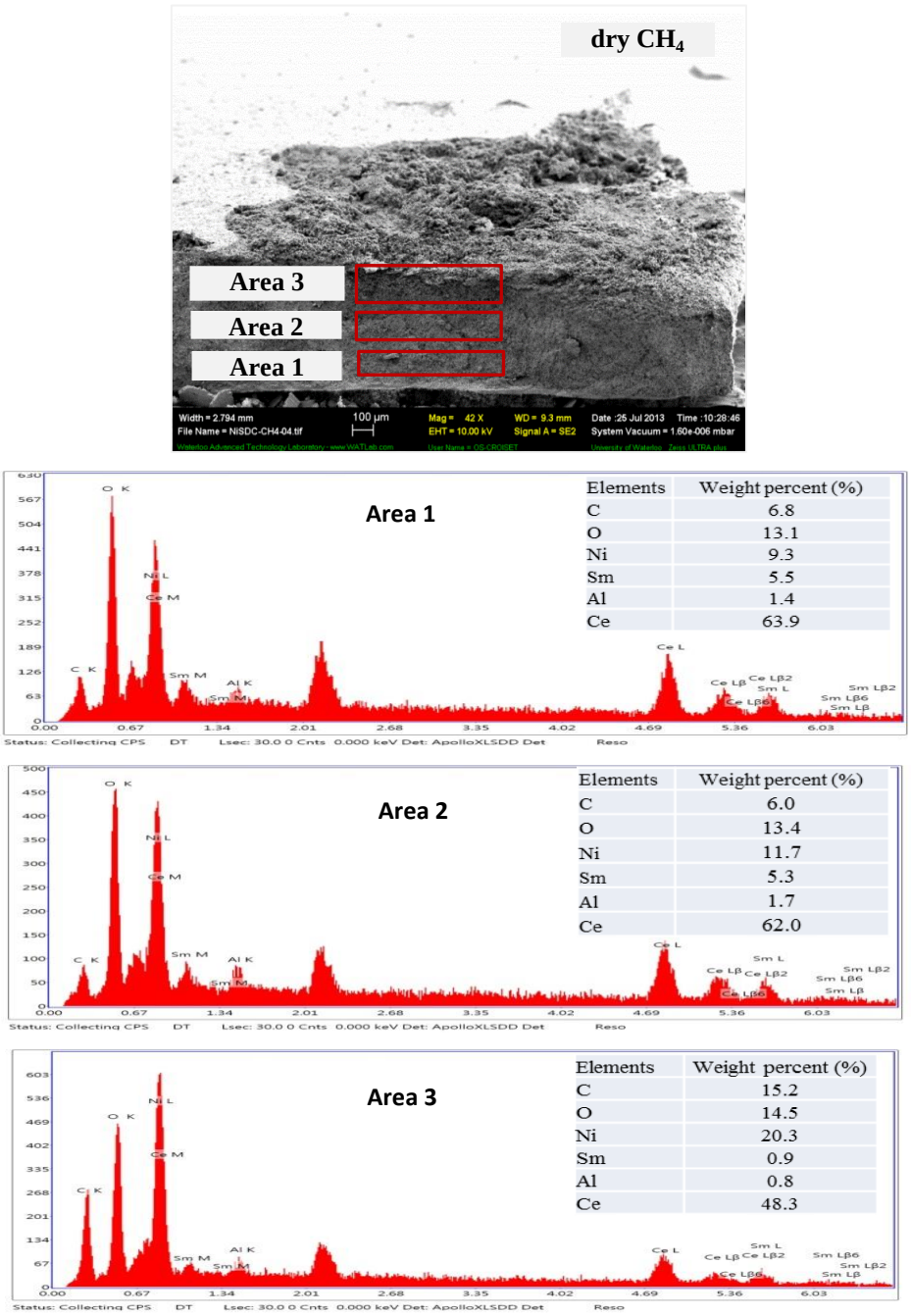

Figure 5-10 SEM micrograph and EDX mapping in the labelled regions of cross-sections taken from the cell after operation with dry CH_4

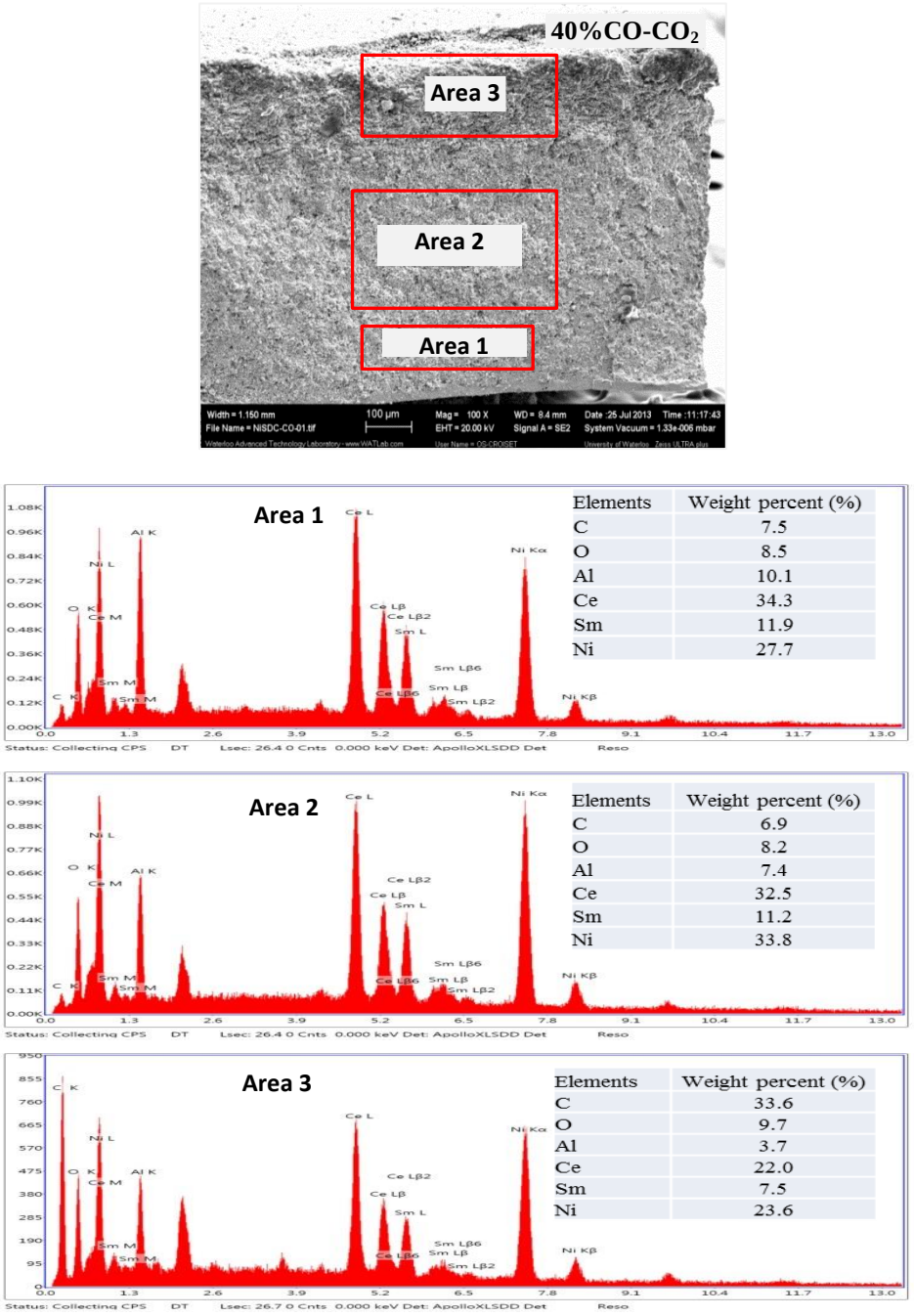

Figure 5-11 SEM micrograph and EDX mapping in the labelled regions of cross-sections taken from the cell after operation with 40%CO-CO_2

Further EDX scanning of the carbon content was performed along a line from the electrolyte-anode interface toward the fuel entry side, as indicated in Figure 5-12. The distance of 0 signifies the point at the electrolyte-anode interface. As shown in Figure 5-12, the results of this analysis confirms the previous observation that carbon deposited in the Ni-SDC cells after the stability tests with both dry CH_4 and 40%CO-60%CO_2 was detected primarily in the anode section near the fuel entry side. Sumi *et al.* (2011) conducted similar analysis of the anode segment after galvanostatic tests with CH_4 and CO fuels on Ni-YSZ anode-supported cells. Carbon deposited only near the fuel entry side when CO was used as fuel, but formed everywhere within the thick anode when CH_4 was the fuel. They proposed that the Boudouard reaction which is the main process by which carbon forms from CO proceeded only near the anode surface, whereas CH_4 decomposition which can produce carbon in the presence of CH_4 could take place throughout the entire anode layer. They also concluded that methane cracking proceeded more slowly than the Boudouard reaction. In another study on the operation of a Ni-YSZ anode-supported cell with CH_4 fuel, Buccheri *et al.* (2011) also found that carbon formed over the entire anode layer, i.e., near the electrolyte-anode interface (functional layer) and the remainder of the anode (conduction layer). They proposed that the conduction layer catalyzed carbon formation and that carbon formation caused breakdown of the structure of the layer.

A possible explanation for the less detrimental effect of carbon formation in the current study is that carbon only deposited near the anode surface exposed to the fuel. Since most of the anode region including the electrolyte-anode interface were free from carbon and remained intact, electro-catalytic processes at the anode could continue without a large drop in cell performance. The smaller area over which carbon forms could be due to the presence of SDC within the anode instead of YSZ. Within the reducing condition in SOFC, ceria is reduced followed by the formation of oxygen vacancies within the lattice which increase the transfer of oxygen ions within the anode. Lattice oxygen from the bulk SDC can effectively react with CH_4 (or CO) or quickly oxidize some carbon formed in the anode layer. Yun *et al.* (2012) have suggested that with the SDC available at the anode, whether through the

additional SDC layer or SDC bulk phase, carbon accumulation can be reduced by its subsequent oxidation ($C + O^{2-} \rightarrow CO + 2e^-$) by oxygen ions within the anode. Thus, the SDC in the Ni-SDC anode cermet may have promoted carbon removal within the anode and reduce the risk of cell failure due to carbon deposition.

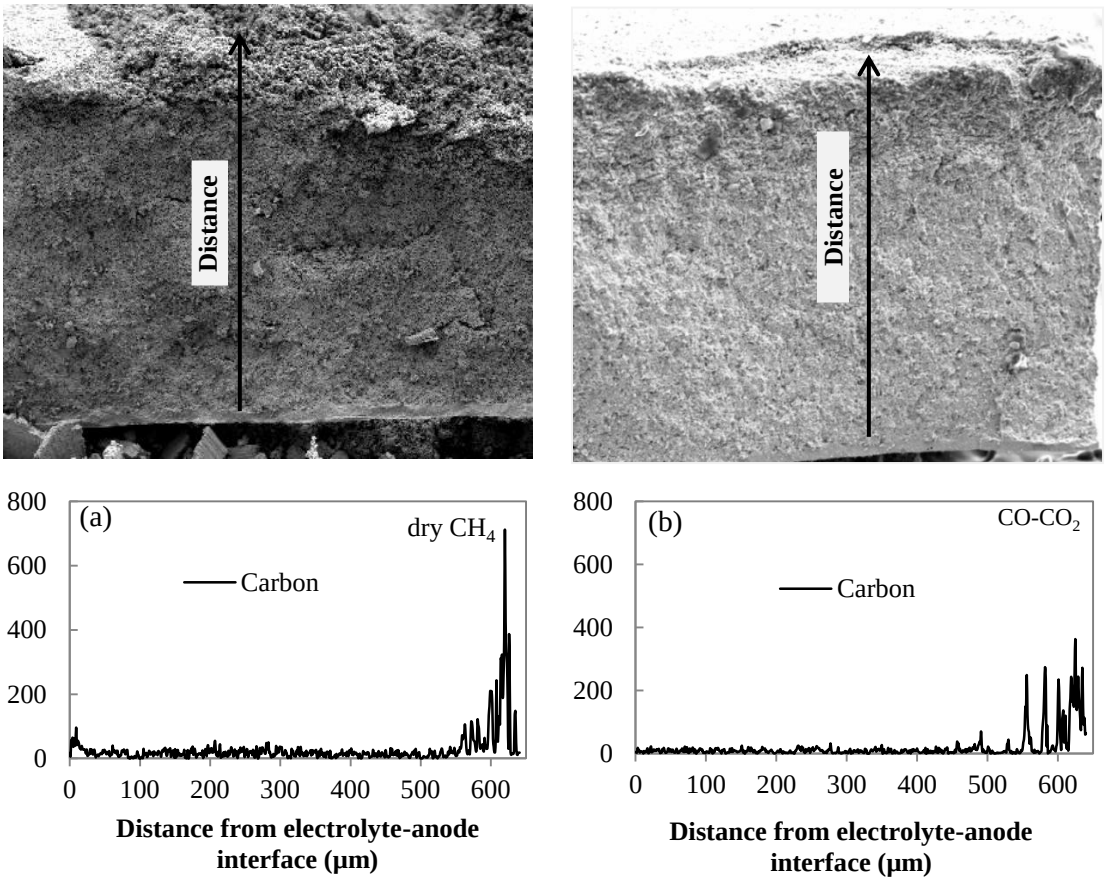

Figure 5-12 EDX scans of carbon content over the labelled line from the electrolyte-anode interface to the fuel entry side of Ni-SDC anode-supported cells after operation with a) dry CH_4 and b) 40%CO-60%CO_2

5.4 Summary

Carbon deposition study has been conducted on Ni-SDC anode supported cells operating with fuels containing dry CH_4 and a 40%CO-60%CO_2 mixture. The results obtained from this work are summarized as follows:

- From thermodynamic analysis, carbon formation during operation with dry CH_4 fuel at 0.35 A cm^{-2} is predicted to occur within the range of temperatures studied (500-900ºC). The predicted amount of carbon deposited at equilibrium increases with temperature up to a temperature of ~600°C, after which this amount does not change much with temperature. Meanwhile, when the cell operates with a 40%CO-60%CO_2 fuel at 0.1 A cm^{-2}, carbon formation at equilibrium is predicted to occur only at temperatures below 640ºC.

- Under dry CH_4, the cell voltage was stable during the first 20 hrs before beginning to gradually decrease at rate of 1.33 mV hr^{-1}. The cell degradation during operation with the CO-CO_2 fuel was faster at a rate of 4.5 mV hr^{-1}.The long-term cell degradation in both cases was related to the accumulation of carbon in the anode.

- Carbon formed in the Ni-SDC cells after the stability tests with both the dry CH_4 and 40%CO-60%CO_2 fuels was only detected in the anode section close to the fuel entry point. Little evidence of carbon formation at the electrolyte-anode interface and the middle part of the anode was observed.

- Although carbon was clearly found to deposit on the anode, the drop in the cell performance was relatively small. One possible explanation is that the presence of SDC helps promote carbon removal within the Ni-SDC anode.

Chapter 6
H_2S in CH_4-based fuel operation: Effect on cell performance and carbon deposition

6.1 Introduction

The use of hydrocarbon-based fuels often leads to faster degradation in SOFC performance due to carbon deposition (Finnerty *et al.,* 1998; Alzate-Restrepo and Hill, 2008; Sumi *et al.*, 2010). Ni-based anodes which are known for their high electrochemical activity and high electronic conductivity also tend to catalyze the decomposition of hydrocarbons and carbon formation. Hydrocarbons (e.g. CH_4) dissociate through catalytic surface reactions on Ni to produce carbon and H_2. Obviously, if the rate at which carbon forms exceeds the rate at which it is removed, carbon will begin to accumulate within the anode. This can cause deactivation by blocking the access of reactants to anodic reaction sites (Maček *et al.*, 2007) or loss of Ni sites due to growing carbon filaments (Toh *et al.,* 2003) and can even cause the fracture of the anode structure due to excessive volume expansion (Kim *et al.,* 2002).

Since Ni is still an attractive candidate for SOFC anodes, researchers have made great efforts to improve its carbon tolerance by modifying the surface properties of the Ni cermet. Some have considered alloying or impregnating the Ni anode with metals such as Cu (Park *et al.,* 2009), Sn (Nikolla *et al.,* 2009) or Au (Niakolas *et al.,* 2010). A few researchers have added small amounts of noble metals such as Ru, Pt and Pd (Takeguchi *et al.,* 2003; Nabae *et al.,* 2006) to the Ni anode, while others have incorporated alkaline earth oxides CaO, SrO, MgO and LaO (Takeguchi *et al.,* 2002; Asamoto *et al.,* 2000; Yan *et al.,* 2012).

Another approach to suppress carbon deposition is through passivation of the Ni surface by sulphur. It has been reported that the presence of sulphur can lower the formation of carbon on Ni catalysts (Rostrup-Nielsen, 1984; Oudghini-Hassani *et al.,* 2007) and Ni-based anodes (Grgicak *et al.,* 2008). Rostrup-Nielsen (1984) suggested that carbon deposition can be limited by the adsorption of sulphur by limiting the size of Ni ensemble sites responsible for carbon formation. Bengaard *et al.* (2002) proposed the presence of two kinds of active sites

on Ni surface: steps and terraces. Their DFT calculations showed that sulphur atoms preferentially bind to step sites rather than terrace sites. Since the nucleation of carbon begins at the steps, the adsorption of sulphur on Ni step sites inhibits carbon formation. Rostrup-Nielsen (1984) used 1 ppm H_2S to treat the catalyst before performing the methane steam reforming at 850ºC and reported that the formation of carbon filaments was entirely eliminated, leaving only amorphous carbon on the Ni surface. Grgicak *et al.* (2008) has conducted experiments on an SOFC operating with Ni-YSZ and Co-YSZ anodes. They found that the addition of 10% v/v H_2S to dry methane fuel inhibited carbon deposition and improved cell performance through the formation of metal sulphides.

Nonetheless, sulphur species such as H_2S are also very well-known to poison SOFCs by severely deactivating Ni-based anodes. Sulphur has a strong affinity to Ni and only a few ppm of H_2S (e.g. 2-15 ppm at 800 ºC) are sufficient to dramatically degrade the electrochemical performance of SOFCs (Matsuzaki and Yasuda, 2000). It has been reported that the poisoning effect of sulphur on the Ni-based anodes occurs mainly in two sequential stages: an initial stage leading to fast and drastic performance degradation, followed by a second stage where the effect is slower but longer lasting. This poisoning behavior has been shown to be similar regardless whether H_2S is present in either H_2- or CH_4- containing fuels (Zha *et al.*, 2007; Sasaki *et al*., 2007). Most researchers agree that the initial rapid cell drop arises due to sulphur adsorption onto the nickel surface. The subsequent slower degradation has been attributed to a number of different phenomena – surface reconstruction of nickel (Zha *et al*., 2007), migration and depletion of nickel at the anode (Lussier *et al.,* 2008), formation of nickel sulphides NiS_x (Trembly *et al.,* 2006) or the change in anode structure due to the melting of the nickel sulphides (Ishikura *et al*., 2007).

Therefore, it is necessary to introduce only the appropriate quantity of sulphur to a level that prevents significant deactivation of the catalyst, yet is sufficient to inhibit carbon deposition. In this work, the incorporation of H_2S into dry CH_4 fuel is investigated and its effect on carbon deposition on a Ni-based anode in an SOFC is examined.

6.2 Experimental Procedure

One way of introducing the H_2S is by continuously flowing the gas as a part of the fuel stream. H_2S initially mixed with dry CH_4 at a concentration of 20 ppm was diluted to the desired amount by mixing with another stream containing pure dry CH_4. Before this fuel stream was introduced, a gas mixture containing humidified H_2 and N_2 was fed into the cell to reduce the NiO of the anode cermet into its active form, Ni. The reduction was done for 6 hrs at 600ºC while gradually increasing the H_2 concentration for every 1 hour until it reached 100%. The temperature was then increased to 700ºC and the galvanostatic test was began under humidified H_2 for 6-12 minutes before switching the gas composition into a dry CH_4-H_2S fuel mixture. The mixture was fed into the SOFC inlet at relatively low H_2S concentrations (10 and 2 ppm) at a flow rate of 40 mL min^{-1} and the resulting electrochemical activity of the cell was monitored. The stability of Ni-SDC anode-supported cells at 700ºC was assessed while operating in galvanostatic mode at 0.35 A cm^{-2} for an extended period of time. Periodically, these runs were interrupted to characterize the cell using electrochemical impedance spectroscopy in the galvanostatic mode with a base DC current density of 0.35 A cm^{-2} over a frequency range of 0.1 Hz to 1MHz. In another experiment, H_2S was introduced into the cell differently by feeding it only for a short interval. To do this, a mixture of 40 ppm H_2S in H_2 was diluted with pure H_2 to obtain a 2 ppm H_2S/H_2 stream and then introduced into the cell for only 30 min under galvanostatic conditions (0.35 A cm^{-2}) at 700ºC. At the end of 30 min, no more H_2S was fed into the cell and the fuel stream was switched to dry CH_4 alone.

Carbon deposited on the cells was characterized using temperature program oxidation (TPO). A broken piece from the cell was taken for this analysis which was conducted in a CATLAB microreactor equipped with a mass spectrometry model QIC-20 (Hiden Analytical Ltd., UK). A gas stream containing He with 5% O_2 and 1.5% Ar was then introduced at a flow rate of 90 mL min^{-1}. The reaction temperature was then increased from room temperature to 850ºC at a linear rate of 10ºC min^{-1} and CO_2 generated in the exit gas was monitored by mass spectrometry. Cross-sections of the Ni-SDC anodes after the stability

tests were examined using scanning electron microscopy (SEM, LEO 1530) equipped with an EDX (LEO, Germany).

Finally, XPS analysis was employed to identify the elements present in the surface regions of some of the samples and their oxidation states. XPS was performed using a Thermo ESCALab 250 unit (VG Scientific, UK) configured with a monochromatic Al Kα ($h\nu$ = 1486.6 eV) x-ray source at a power of 150 W with the base pressure in the analytical chamber maintained below 3.0×10^{-10} bar. The region analyzed by XPS was a circular spot ~0.5 mm in size covering almost the entire anode cross-sectional area and located a few microns from the electrolyte. Wide survey scans were first done to identify the different elements present. This was followed by narrow scans for sulphur (S 2p), nickel (Ni 2p) and carbon (C 1s). Curve fitting and deconvolution of these scans were done using CasaXPS version 2.3 (Casa Software Ltd, UK).

6.3 Results and Discussions

6.3.1 Continuous introduction of H_2S within CH_4 gas feed

The variation of the cell voltage with time for the cell continually exposed to a fuel stream containing 10 ppm H_2S in CH_4 is presented in Figure 6-1a. A constant cell voltage of approximately 0.79 V was maintained over the first 12 hours or so before beginning to drop sharply and reaching close to zero by about 16 hours. At this point, the testing was terminated. The degradation rate when the cell voltage largely degraded at 12 to 16 hrs was 151.3 mV hr^{-1}.

This experiment was followed by another using a fuel containing 2 ppm H_2S in CH_4 under otherwise identical conditions. At this lower H_2S level, the cell was able to maintain its electrochemical activity longer than that observed at the higher concentration although the cell degradation was still very severe (Figure 6-1b). The cell failed well before it had reached 100 hrs of operation. The decline started fairly gradually after about 25 hours of operation,

but then began to increase more quickly after ~ 40 hours until it reached 0.15 V after 53 hrs. The degradation rate with 2 ppm H_2S measured from 25 to 53 hrs was 21.1 mV hr^{-1}. The difference in the cell performance shown in Figure 6-1 at these two H_2S concentrations also indicates that the behaviour of the system is very sensitive to the H_2S level even when it is changed by only a few ppm.

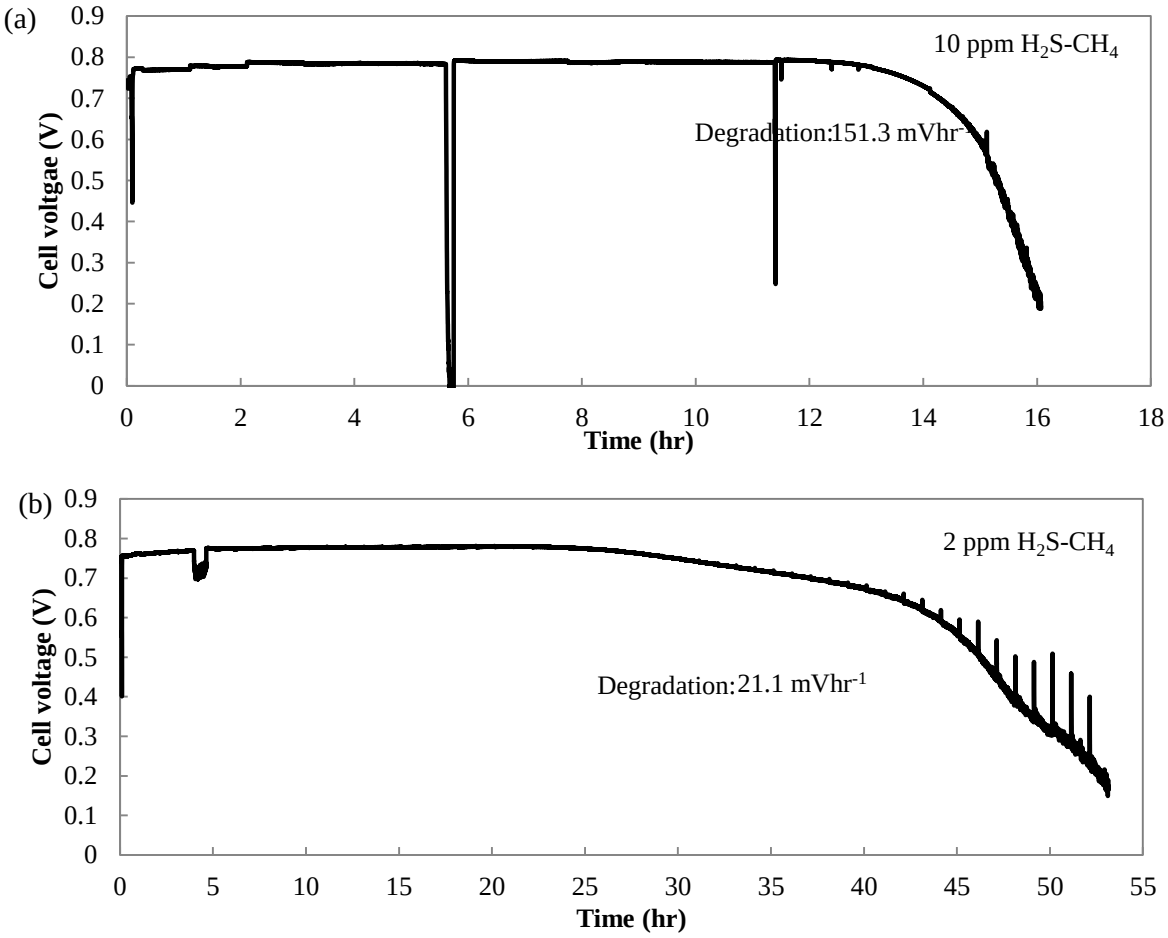

Figure 6-1 Variation of SOFC cell voltage during operation at 0.35A cm^{-2} and 700ºC with a continuous fuel stream containing a) 10 ppm H_2S in dry CH_4 and b) 2 ppm H_2S in dry CH_4

EIS analysis for the cells operating with the mixtures of dry CH_4 and H_2S was performed at a DC current density of 0.35 A cm^{-2}. Impedance spectra obtained at the first hour and at the end of stability test for each cell are given in Figure 6-2. The intercept on the real axis at the high- frequency end of the spectra corresponds to the ohmic resistance in the cell, R_s. Meanwhile, the difference between the two intercepts at the real axis yields the polarization resistance, R_p. No significant difference in the R_s between the first hour of exposure and at the end of stability test for both H_2S concentrations was observed. The R_p on the other hand, increased significantly for both cells after the stability test suggesting that the electrode processes have been strongly affected by the continuous exposure of H_2S in the dry CH_4.

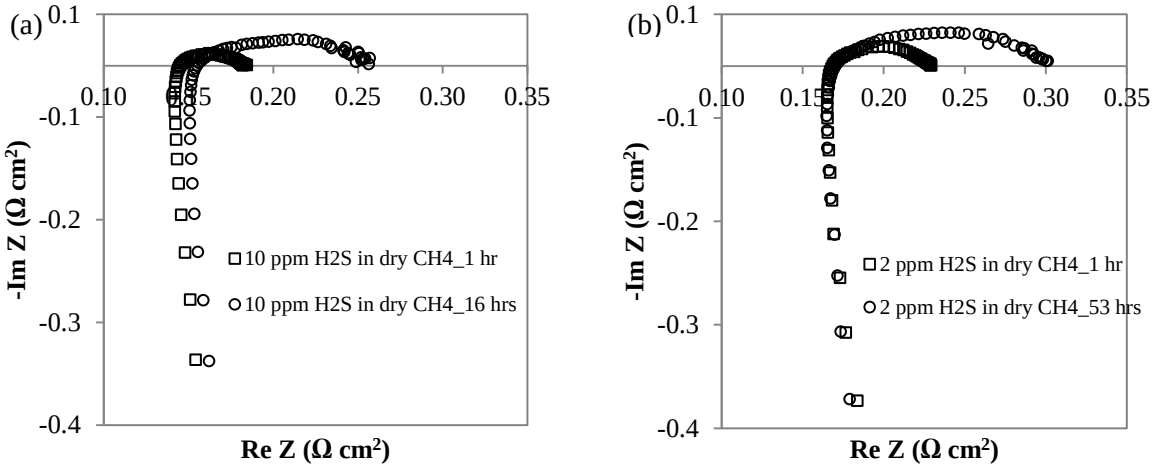

Figure 6-2 Impedance spectra for Ni-SDC cell at 1st hour and at the end of operation under 0.35 A cm^{-2} and 700ºC with fuel stream containing a) 10 ppm H_2S in dry CH_4 and b) 2 ppm H_2S in dry CH_4

The R_s and R_p throughout the galvanostatic tests were obtained by fitting the impedance spectra using a standard equivalent circuit (refer Figure 4.12a) and the variation of the values is presented in Figure 6-3. It is noteworthy from Figure 6-3 that the variation in R_p follows similar trends at the two H_2S levels. It remains stable close to 0.05 Ω cm^2 during an initial operation period (i.e., up to ~ 12 and ~ 25 hours at 10 ppm and 2 ppm H_2S, respectively).

Thereafter, R_p begins to rise linearly with time before catastrophic failure of the cell occurs. In the presence of 10 ppm H_2S, it increased by over 200% from 0.033 to 0.104 Ω cm^2 over the operation period from 12 to 16 hrs (Figure 6-3a). A similar large rise of R_p from 0.059 Ω.cm^2 to 0.138 Ω cm^2 between 25 hours and 53 hours of operation was observed in 2 ppm H_2S (Figure 6-3b). Based on the results obtained at these two H_2S concentrations, it appears that a continual rise in R_p may be an indicator of imminent collapse of the cell. Meanwhile, R_s did not change much except a very small increase for 10 ppm H_2S at the end of the test, probably due to the disruption in connectivity as the cell structure disintegrates.

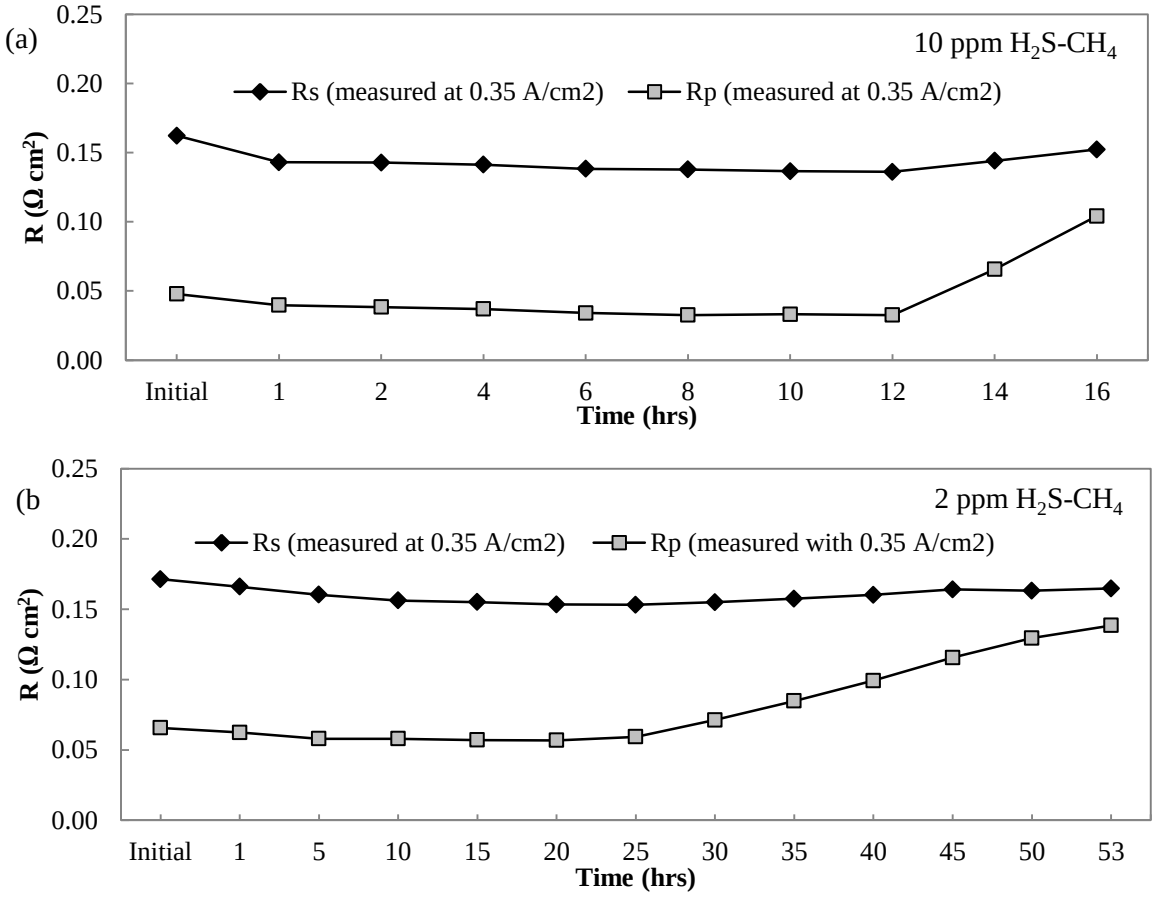

Figure 6-3 Variation of the R_s and R_p values of an SOFC during operation at 0.35A cm^{-2} and 700ºC with a continuous fuel stream containing a) 10 ppm H_2S in dry CH_4 and b) 2 ppm H_2S in dry CH_4

SEM micrographs of the anode cross-section in the middle section and near the fuel entry point in the Ni-SDC cells that had operated with the dry CH_4-based fuels containing 10 ppm H_2S and 2 ppm H_2S are presented in Figure 6-4a-b and Figure 6-4c-d, respectively. SEM pictures for a fresh Ni-SDC is given in Figure 6-4e-f. For samples exposed to H_2S in CH_4, the images obtained in the middle and near the fuel entry point are different from each other. Clear evidence of the presence of carbon, which appears as the black substance, is present in the sections near the fuel entry point (Figure 6-4b and 6-4d) in both cases, but not in the middle segments (Figure 6-4a and 6-4c). Similar behaviour was observed in the anode examined after an exposure of 100 hrs to dry CH_4 (in the absence of H_2S), as shown previously (see section 5.3.2). It should be recalled from previous findings in the absence of H_2S that the build-up of carbon near the fuel entry side does not necessarily lead to a large drop in cell performance. However, from what is observed when the fuel was mixed with the H_2S, the cells suffered catastrophic failure after only 16 hrs and 53 hrs. Thus, it appears that the substantial degradation in the cell performance is due more to the poisoning effect of H_2S than to the build-up of carbon.

10 ppm H_2S in dry CH_4

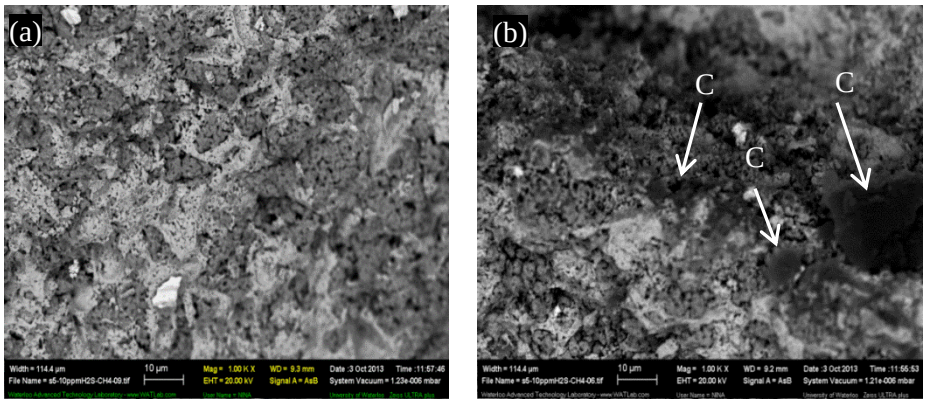

2 ppm H_2S in dry CH_4

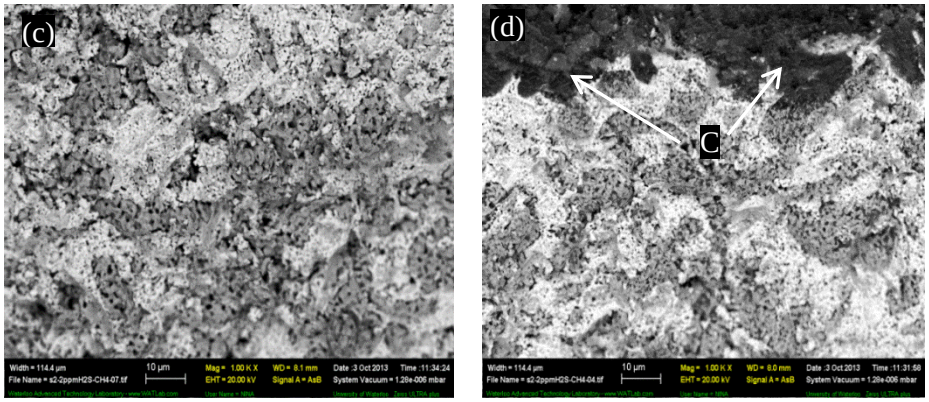

Fresh Ni-SDC

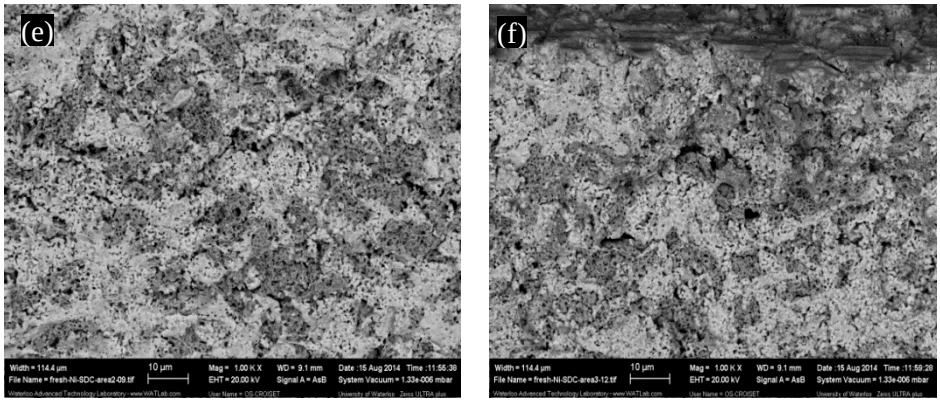

Figure 6-4 SEM micrographs of the Ni-SDC anode after operation with a dry CH_4-based fuel containing (a, b) 10 ppm H_2S and (c, d) 2 ppm H_2S at 0.35 A cm^{-2} and 700ºC. (e, f) Fresh Ni-SDC. Left: middle section. Right: section near fuel entry side

SEM micrographs and the results of EDX elemental analysis over the entire cross-section of the anodes after exposure to 10 ppm H_2S in dry CH_4 and 2 ppm H_2S in dry CH_4 are shown in Figure 6-5. These samples were obtained at the end of the stability tests of 16 and 53 hrs, respectively. Some delamination is observed at the surface of the anode close to the fuel entry side after contact with 10 ppm H_2S in dry CH_4 (Figure 6-5a). The anode surface exposed to 2 ppm H_2S in CH_4 showed no signs of delamination, although it is covered by the carbon deposit (Figure 6-5b). EDX elemental analysis was conducted along the lines leading from the electrolyte- anode interface to the fuel entry side indicated by the arrows in Figure 6-5a and Figure 6-5b. The results of this analysis presented in Figure 6-5c and Figure 6-5d confirmed that a significant amount of carbon had formed, but that it was confined almost exclusively to the section near the fuel entry point at both H_2S concentrations. However, at the same time, no evidence for the presence of sulphur over the cross-section of the anodes was found. Furthermore, the EDX scans for sulphur in these samples were not measurably different from that of a fresh Ni-SDC anode not previously exposed to any fuel, as shown in Figure 6-5e. Considering that EDX analysis normally probes a depth below 1-3 microns, it is reasonable to conclude that bulk nickel sulphide which should be detectable does not form in these anodes. Presumably, the concentration of H_2S is too low in these experiments to be detected by EDX.

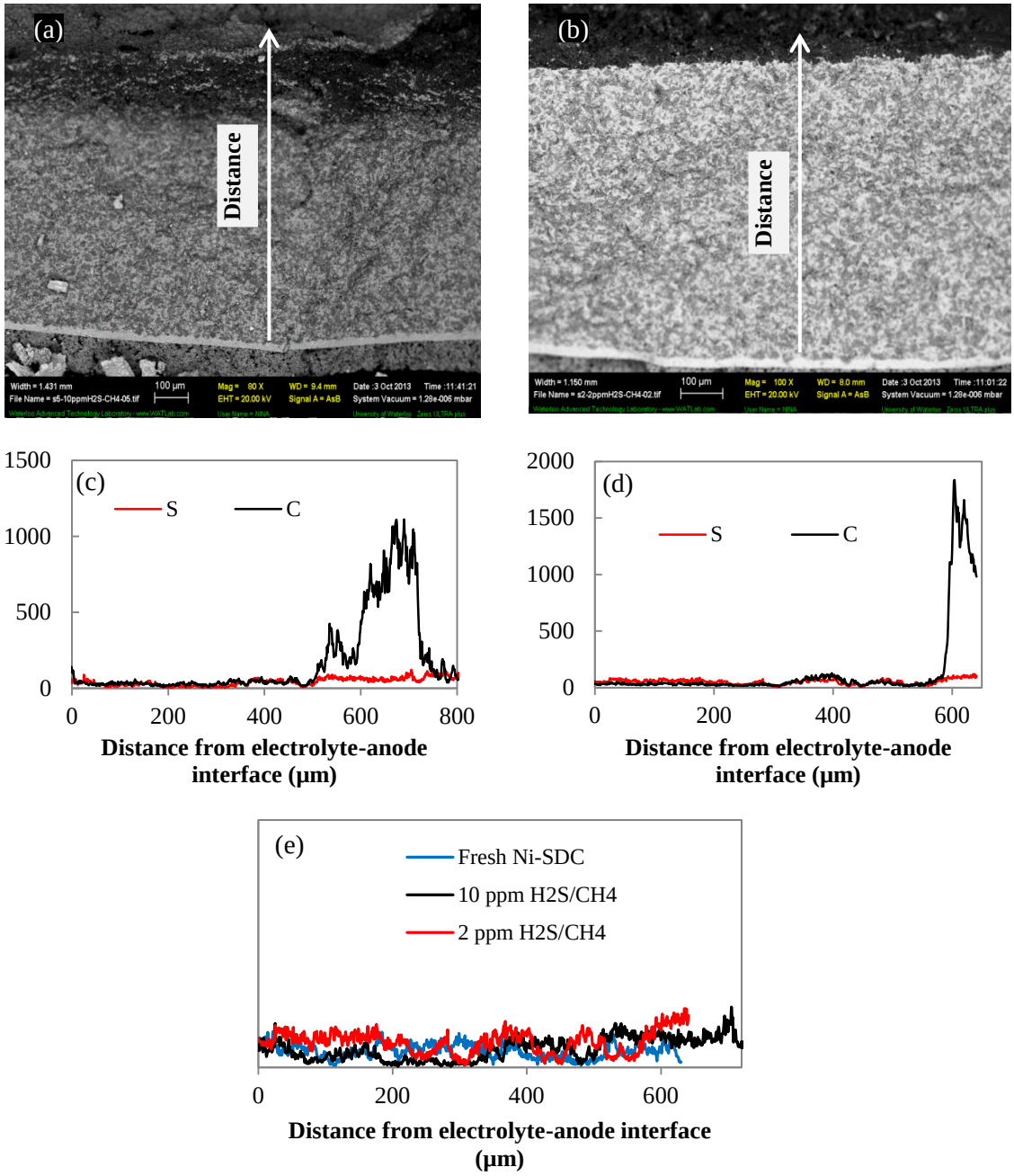

Figure 6-5 SEM micrograph of cross-section and EDX elemental analysis along the indicated line of Ni-SDC anode operating with (a, c) 10 ppm H_2S in dry CH_4 and (b, d) 2 ppm H_2S in dry CH_4 at 0.35 A cm^{-2} and 700ºC. e) EDX line scans for sulphur in fresh Ni-SDC and Ni-SDC anodes exposed to 10 ppm and 2 ppm H_2S

The performance drop with the continuous introduction of H_2S is consistent with the significant increase of R_p (Figure 6-2). Anode sections at the electrolyte-anode interface of the Ni-SDC cells after exposure to dry CH_4, 10 ppm H_2S in dry CH_4 and 2 ppm H_2S in dry CH_4 were monitored with SEM to yield the micrographs presented in Figure 6-6. The fuels that contain H_2S appear to cause a significant change to the structure of the Ni-containing phase in the Ni-SDC anode. For the most part, the Ni-containing grains in the sample exposed to dry CH_4 alone are distributed homogenously throughout the Ni-SDC network (Figure 6-6a). After contact with the H_2S-CH_4 fuels, on the other hand, the surfaces of the Ni-bearing grains appear to have become rougher and these grains have tended to cluster together (Figure 6-6b and c). Presumably, this change in morphology is due to some interaction of the Ni-bearing grains with H_2S. This modification of the Ni-bearing grains in electrochemically active regions could be the cause of the increase of electrode resistance associated with the charge transfer and/or diffusion processes. The change in structure also suggests that H_2S penetrated all the way through the anode to its base at the electrode-electrolyte interface. It appears that the build-up of carbon at the fuel-entry side of the anode did not block the fuel gases from penetrating deeply into the anode.

Zhang *et al*. (2010) have proposed that the roughening of the Ni-bearing grains in Ni-based anodes is related to the formation of nickel sulphide (NiS_x) due to the direct interaction with H_2S. Subsequent decomposition of this nickel sulphide after reaction with H_2 present within the fuel or produced by reactions with the fuel could lead to the change of the structure and agglomeration of the Ni-bearing grains observed in Figure 6-6. However, according to the thermodynamic analysis conducted by Wang and Liu (2007), the formation of a bulk sulphide such as Ni_3S_2 is not favorable at H_2S concentrations below 1000 ppm and at temperatures of 650-800°C used for SOFC operation. Thus, the formation of bulk nickel sulphides would not be expected under the experimental conditions employed in the current study. Therefore, it is much more likely that the extent of the interaction involves the reconstruction or modification of the surfaces of the Ni-bearing grains by adsorbed sulphur, as described by Zha *et al.* (2007). Meanwhile, based on the SEM images in Figure 6-6, very

little alteration of the SDC phase occurred in the presence of H_2S. The structure of the SDC after exposure to the H_2S-containing fuels remained similar to that observed after contact with dry CH_4 alone, consistent with what would be expected if little interaction between H_2S and SDC had occurred.

The inclusion of H_2S within the fuel does not appear to deter carbon deposition since a considerable amount of carbon was found on the anode surface. Abild-Pedersen *et al.* (2005) from DFT calculation stated that both sulphur and carbon are preferred to absorb on the step sites of Ni rather than the terrace sites. Thus, it is possible that the simultaneous penetration of H_2S and CH_4 into the anode enabled the competition for the adsorption of sulphur and carbon on the available Ni sites. Beyond the negative outcome due to its poisoning effect on SOFC performance (Figure 6-1a and Figure 6-1b), it is not obvious from the results obtained so far that H_2S inhibited carbon deposition when it was introduced with the fuel continuously throughout the entire SOFC run. Thus, we re-visited the manner in which H_2S was fed into the system.

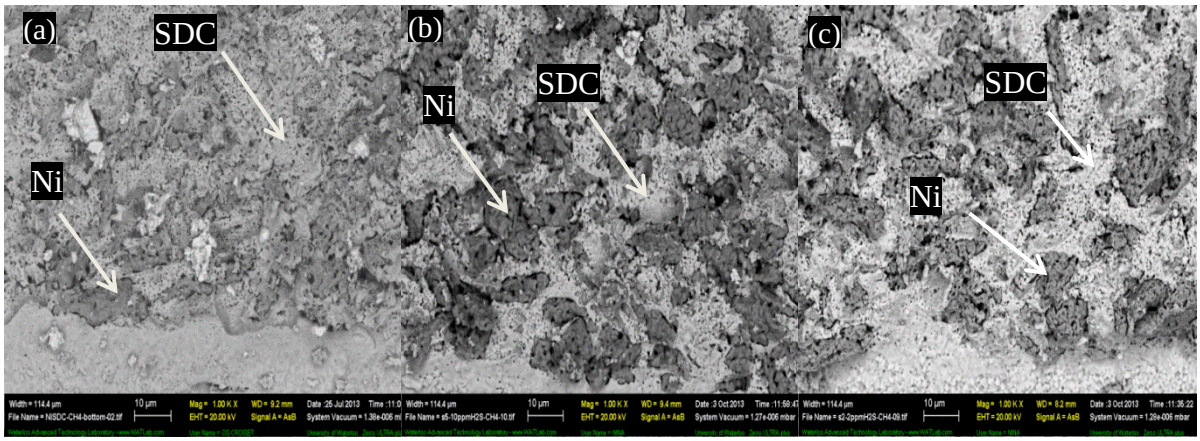

Figure 6-6 SEM micrographs of regions close to the electrolyte-anode interface in Ni-SDC cells operating with the following fuels: a) dry CH_4 b) 10 ppm H_2S in dry CH_4 and c) 2 ppm H_2S in dry CH_4 at 0.35 A cm^{-2} and 700ºC

6.3.2 Introduction of H_2S at short interval followed by CH_4 operation

The transport of H_2S through the anode toward the electrolyte followed by its adsorption onto electrochemically active Ni sites is the key factor that causes the cell voltage to drop sharply (Zha *et al.*, 2007). The adsorption of sulphur in the anode functional layer effectively blocks active sites from otherwise participating in the electrochemical reactions that generate current and so can quickly deteriorate the electrochemical activity at the triple phase boundary (TPB) region.

Figure 6-7 shows the variation in cell voltage over 1 hour of operation depending on the fuel used after the first 0.1 hour. The fuel fed into the cell consisted of humidified H_2 alone and then was switched to either dry CH_4 alone (Figure 6-7a) or a mixture of 10 ppm H_2S in dry CH_4 (Figure 6-7b) for the duration of the run. A comparison of the results indicates that the presence of 10 ppm H_2S did not harm the cell performance at least over the first hour of operation, consistent with the behaviour observed previously in Figure 6-1. In both cases shown in Figure 6-7, the only significant drop in cell voltage occurred at ~0.1 hr when the fuel was switched from humidified H_2 to dry CH_4 or the H_2S-CH_4 mixture, but almost instantaneously the cell voltage recovered completely and in fact rose above the level prior to the change in fuel.

The observation of a delay in the poisoning by H_2S is reasonable when one considers that anode-supported cells were being used in this study. Due to the larger anode size, it would take longer for all nickel sites to be saturated with sulphur than it would in an electrolyte-supported cell. The adsorption of sulphur would first occur on the surface on the fuel entry side, proceed into the conduction layer and eventually reach the active functional layer. Meanwhile, the oxygen ions transported through the electrolyte from the cathode at a rate corresponding to the current density of 0.35 A cm^{-2} would be available to facilitate the oxidative desorption of sulphur, particularly in the active functional layer. The time required for these various processes to occur would delay the dramatic drop in performance ultimately observed when the H_2S-containing fuel was introduced into the system.

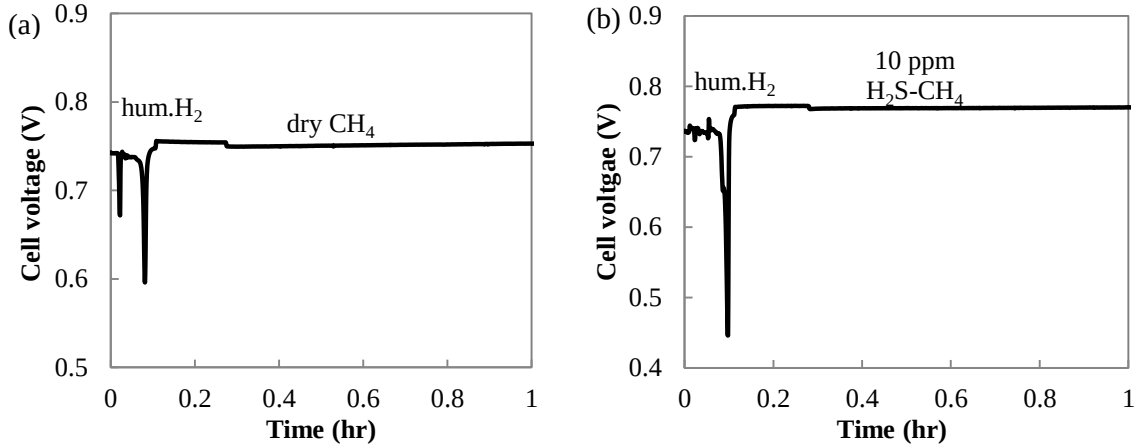

Figure 6-7 Variation of SOFC cell voltage during the first hour of operation at 0.35A cm^{-2} and 700ºC with humidified H_2 fuel for the first 0.1 hour followed by a switch to a) dry CH_4 and b) 10 ppm H_2S in dry CH_4

Taken together, these considerations indicated that a key factor determining whether H_2S would have a poisoning effect would be the cumulative amount of the gas introduced into the cell. In order to take advantage of the potential beneficial effects of H_2S on SOFC performance while minimizing the possibility of poisoning, we investigated the following feeding scheme for the fuel gases. Humidified H_2 was introduced into the cell for the first 0.2 hour before switching to 2 ppm H_2S in dry H_2 for 30 minutes and then finally to dry CH_4 for the remainder of the run, all the while operating at a current density of 0.35 A cm^{-2}.

As shown in Figure 6-8a, the cell did not experience any degradation while the H_2S-H_2 mixture was flowing into the anode. This observation differs from that of Zha *et al.* (2007) who reported a sharp drop in cell performance with the introduction of 2 ppm H_2S into Ni-YSZ cells and the subsequent gradual decline as H_2S was continually added. There were several aspects which varied between Zha's study and this work including the cell design, operating temperature and cell performances (0.7 V at 0.2 A cm^{-2} from Zha's cell versus 0.75 V at 0.35 A cm^{-2} from this work). Yet, the reason for difference effect in sulphur poisoning

behavior on the two cells is unclear and it is interesting to further investigate if that is also due to the variation in electrolyte material in the anode cermet (YSZ versus SDC).

The degradation rate (0.63 mV hr^{-1}) of the cell voltage over 100 hours of operation with dry CH_4 after exposure to H_2S (2 ppm) for 30 minutes (Figure 6-8b) was smaller than that obtained during operation with dry CH_4 without any previous exposure to H_2S (1.33 mV hr^{-1}), as shown in Figure 5.2. This supports that the introduction of H_2S can help maintain good SOFC performance due to the inhibition of carbon formation in the Ni anode (Grgicak *et al.*, 2008). The experimental results presented here suggest that the order in which the gases were fed into the cell was important and that it was necessary to add H_2S prior to the introduction of the carbon-containing gas for a beneficial effect to be derived. To know for sure, it was necessary to conduct additional analysis to directly determine whether carbon formation in the anode was actually influenced by the presence of H_2S which is discussed in sections 6.3.3 and 6.3.4.

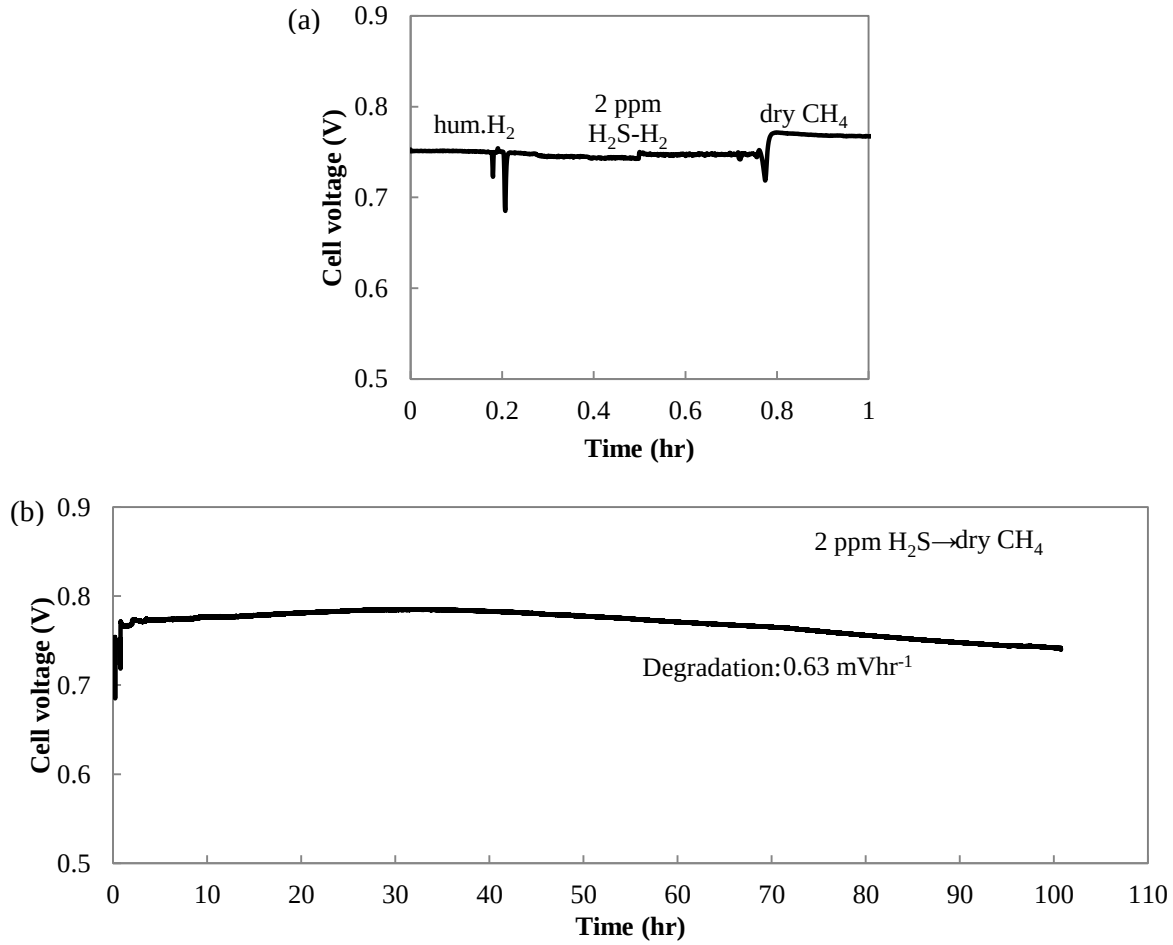

Figure 6-8 Variation of cell voltage over (a) 1st hour and (b) 100 hours of operation at 0.35A cm^{-2} and 700ºC when fuel gases are introduced according to the following scheme: humidified H_2 for 0.2 hour → 2 ppm H_2S in H_2 for 0.5 hour → dry CH_4

SEM micrographs for the Ni-SDC being exposed to 2 ppm H_2S in H_2 for 30 min followed by dry CH_4 for 100 hrs are presented in Figure 6-9. Carbon was observed on the anode indicated by the black substance deposited on some parts of the section near the fuel entry point. This shows that carbon was still deposited on the anode regardless which method was used to introduce H_2S into the system.

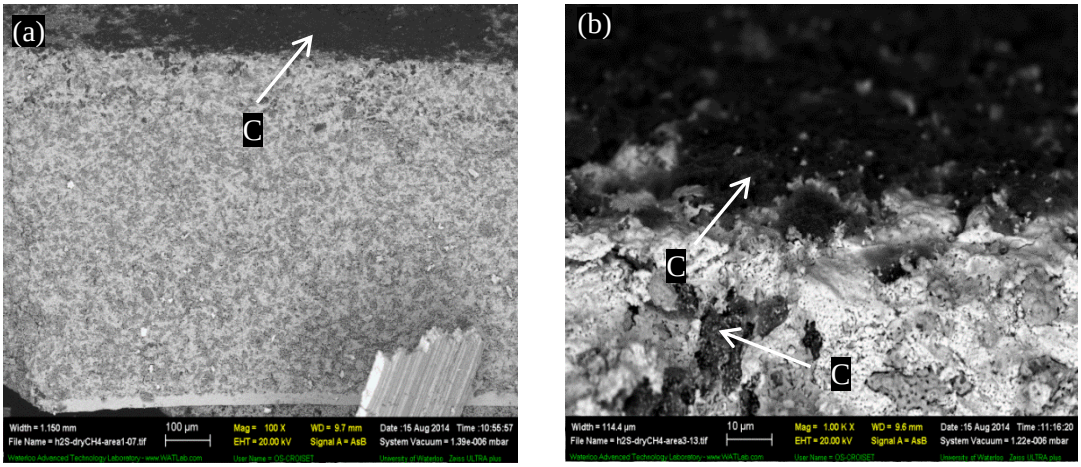

Figure 6-9 SEM micrographs for Ni-SDC cell operating with 2 ppm H_2S in H_2 for 0.5 hour followed by 100 hrs dry CH_4. (a) Whole anode cross-section b) section near fuel entry side

6.3.3 Temperature-programmed oxidation (TPO)

After SOFC operation with the fuels both in the presence and absence of H_2S, the anodes were analyzed using temperature-programmed oxidation (TPO) in order to characterize the nature of the carbon formed. During TPO analysis, carbon accumulated on the anode is oxidized to produce CO_2. It provides information on the chemical stability of carbon based on the temperature at which it is oxidized to CO_2. Due to the difficulty of maintaining the cell intact after removing it from the SOFC setup, we could only carry out the analysis on a fragment of the anode taken from each cell. Therefore, it was not possible to determine the total amount of carbon that had deposited in the anodes using this technique. The anodes analyzed were the same as those yielded the performances depicted in Figure 5.2 in Chapter 5, Figure 6-1a, Figure 6-1b and Figure 6-8. Figure 6-10 presents the TPO profiles obtained for these anodes. Each profile exhibited a single peak centred at the temperature at which CO_2 was generated from oxidation of the carbon deposit. The peaks for the anodes exposed to dry CH_4 alone, 10 ppm H_2S in dry CH_4 and 2 ppm H_2S in dry CH_4 over the entire course of SOFC operation appeared at 560, 545 and 568ºC, respectively. On the other hand, the CO_2 peak for the cell which had contacted with 2 ppm H_2S in H_2 for 30 minutes and then dry CH_4

alone for close to 100 hours was observed at a lower burn-off temperature of ~ 480ºC. This indicated that the carbon formed on this anode was more weakly bound to the surface and more easily removed than the carbon deposited when the fuel contained dry CH_4 alone or when H_2S-containing fuel was introduced for the entire run. According to the terminology on the type of carbon given by Guo *et al.* (2007), it is likely that the carbon formed on the anode after exposure to 2 ppm H_2S in H_2 for 30 minutes and then dry CH_4 alone can be categorized as C_β which is poly-aromatic in nature. Meanwhile, the other carbons accumulated after being exposed to dry CH_4, 10 ppm H_2S-CH_4 and 2 ppm H_2S-CH_4 for extended periods of time were presumably a combination of C_β and a less reactive form C_γ. C_γ is a graphite-like carbon which normally decomposes at 600°C and above. Overall, the TPO analysis suggested that the presence of H_2S did influence the type of carbon formed by the reaction of CH_4 at the anode and the effect was strongly dependent on the manner and duration over which H_2S was introduced into the anode.

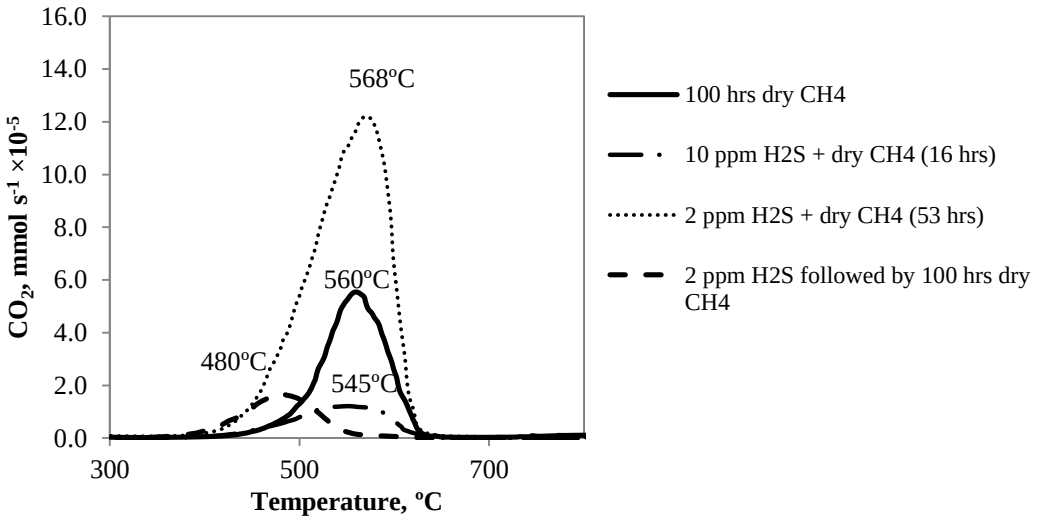

Figure 6-10 TPO profiles of anodes after exposure to various fuel streams for different durations

6.3.4 X-ray photoelectron spectroscopy (XPS)

Further details regarding the surface of the anode cross-sections were explored using XPS. XPS scans were conducted on the various anodes discussed in this chapter and also on a fresh Ni-SDC sample that had not previously contacted any fuel. As shown in Figure 6-11, the spectra for S 2p do not provide any convincing evidence for the presence of sulphur in any of the anodes. A slight elevation of the baseline at a binding energy of ~ 163.2 eV is observed in the anode that had contacted 10 ppm H_2S in dry CH_4 for 16 hours. Signals at binding energies within the range 163.2 and 163.8 eV has been previously reported in studies on the interaction of sulphur on Ni surfaces (Struis *et al*., 2009) or nickel sulphides (Kuhn *et al.*, 2008). It is possible that the very weak signals in Figure 6-11 could be due to the fact that the sulphur was mostly covered by the large amount of carbon that deposited in these samples. To investigate this possibility, we conducted an additional experiment in which an initially fresh anode was exposed to 2 ppm H_2S in H_2 for 30 minutes and then immediately removed for XPS analysis without any contact to a carbon-bearing fuel. The scan for this sample exhibited a slight rise in the baseline at ~ 163.8 eV (see second spectrum from the bottom in Figure 6-11) that did not appear in the scan for the anode that had contacted 2 ppm H_2S in H_2 for 30 minutes and then dry CH_4 for close to 100 hours (see second spectrum from the top in Figure 6-11). However, given that the differences are so slight, nothing obvious can be concluded from these S 2p scans. Perhaps we could have obtained more definitive results regarding the interaction of H_2S with the anode by conducting experiments at higher H_2S concentrations, but this would have poisoned the cells and caused their rapid failure.

The Ni 2p region was also examined for evidence of any interaction between nickel and sulphur (Figure 6-12). Due to differences in the spins of the Ni 2p electrons and the interaction (called spin-orbit coupling) between these spins and the magnetic field generated by their orbits around the nucleus, a splitting of the atomic energy levels of these electrons into $2p_{1/2}$ and $2p_{3/2}$ states occurs. Thus, the XPS signal for the Ni 2p electrons includes separate peaks for these Ni $2p_{3/2}$ and Ni $2p_{1/2}$ states (Watts, 2003). The Ni $2p_{3/2}$ and $2p_{1/2}$ peaks appear at ~854 eV and 873 eV, respectively, in the scans of the various anode samples

shown in Figure 6-12. In addition, other effects lead to multiplet splitting of the Ni $2p_{3/2}$ peaks, while the photoionization of core electrons can cause satellite peaks to appear. The splitting of the signal at ~855 eV in the scans for all of the anode samples in Figure 6-12 can be attributed to multiplet splitting of Ni $2p_{3/2}$. The peak at ~861 eV in all the samples is a satellite of the main Ni $2p_{3/2}$ peak at 853-854 eV and was previously shown to be characteristic of NiO samples (Biesinger *et al.,* 2008). Since the anodes used in the current study were in the reduced form, the presence of NiO could be attributed to the interaction of the Ni substrate with oxide ions coming from the cathode during SOFC operation or oxide remaining after the reduction process of the anodes (see section 3.3.1). Alternatively, some NiO could have formed by oxidation of the substrate in ambient air at room temperature after SOFC operation.

However, from Ni $2p_{3/2}$ peaks at 854.2 eV (2 ppm H_2S-H_2) and 853.9 eV (10 ppm H_2S-CH_4), the sulphur trace should not be from Ni_3S_2 which Ni $2p_{3/2}$ is presented by 856.1 eV (Kuhn *et al.,* 2008). Also, if another nickel sulphide such as NiS had formed, one would have expected a peak in the Ni $2p_{3/2}$ region at 853-854 eV is accompanied by a peak in the S 2p region at 161-162 eV (Legrand *et al.,* 1998) which was not the case. Thus, once again, these scans provide no strong evidence that nickel sulphide formed from the contact of H_2S with the Ni anodes. The only change observed was in the scan obtained on the anode exposed to 2 ppm H_2S in H_2 for 30 minutes that was not subsequently contacted with a carbon-bearing fuel. As shown in Figure 6-12, the spectrum for this sample exhibited a small shift of its main Ni $2p_{3/2}$ peak to a higher binding energy of ~ 854.2 eV. Referring the corresponding signal from S 2p of the same sample (~ 163.8 eV) which can be associated to the interaction of sulphur on Ni surfaces (Struis *et al*., 2009), the binding energy of ~ 854.2 eV from the anode exposed to 2 ppm H_2S in H_2 for 30 minutes could arise due to the adsorption of a sulphur species on Ni. Thus, if anything, the S 2p and Ni 2p scans presented here suggest that their interaction involved the adsorption of sulphur on the Ni substrate.

Another small elevation in the S 2p baseline was observed at 169.7 eV in the anode exposed to 10 ppm H_2S in CH_4 for 16 hours (Figure 6-11). Peaks in this range are

characteristic of oxidized forms of sulphur, i.e, sulphate species (Xu *et al.*, 2011). Presumably, this originated from the interaction of adsorbed sulphur with oxide ions from the cathode or with ambient air at room temperature after SOFC operation.

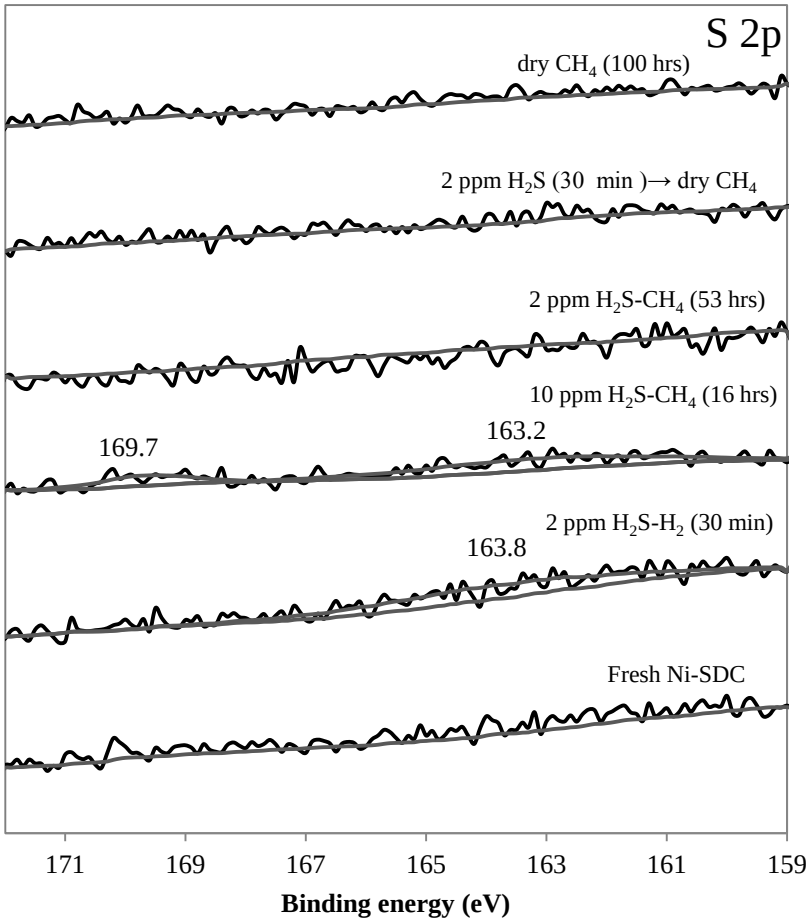

Figure 6-11 XPS scans in S 2p region of anode cross-sections after exposure to the various fuels

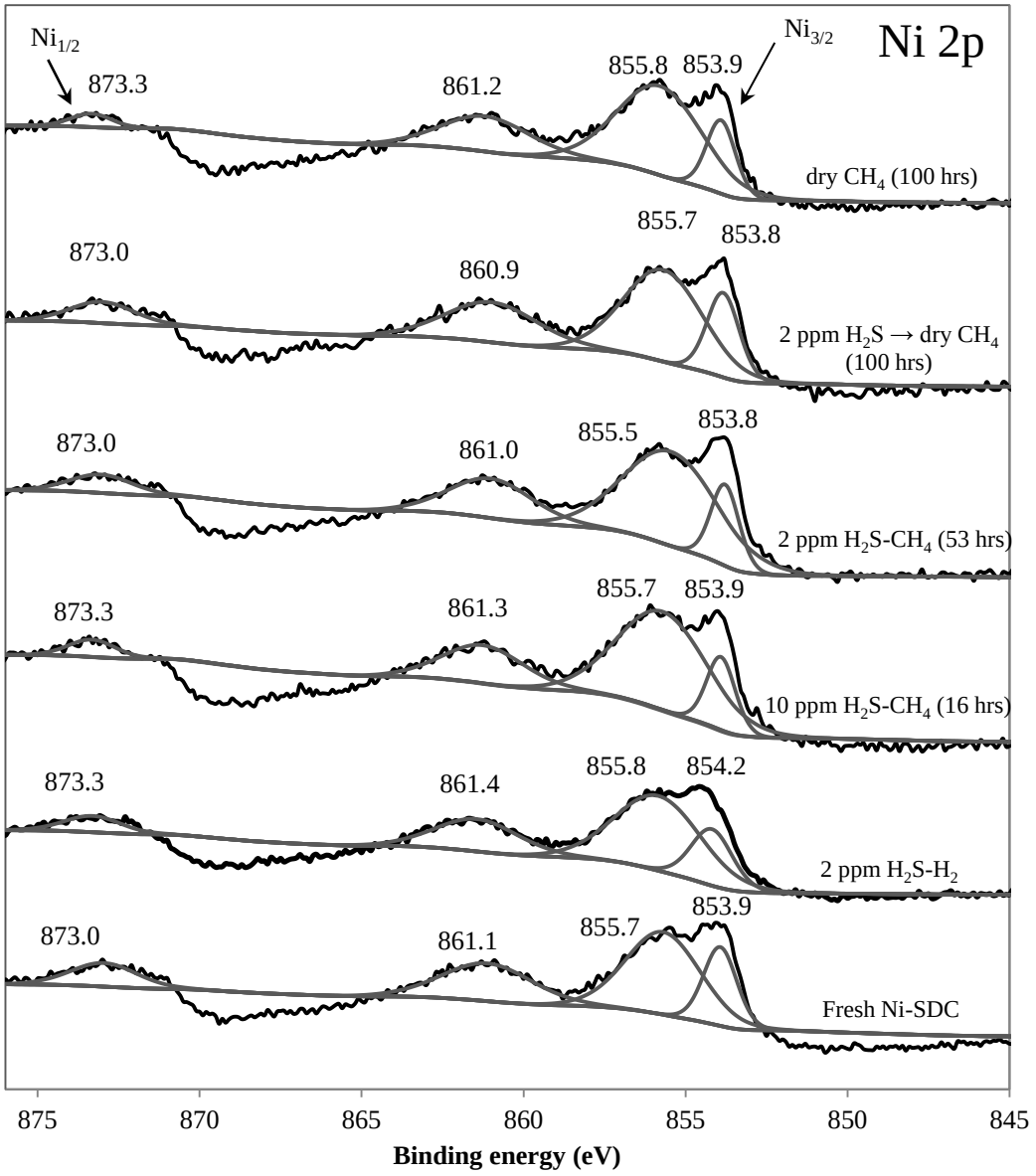

Figure 6-12 XPS scans in Ni 2p region for anode cross-sections after exposure to the various fuels

Compared to the XPS spectra for S 2p and Ni 2p regions, C 1s spectra provided a clearer picture of the effect of sulphur on the anode. Samples always exhibit a C 1s peak even if they have not been purposely exposed to carbon-containing species. This peak arises due the formation of a thin surface layer of carbonaceous material, often known as adventitious

carbon, due to even the smallest exposure to the atmosphere (www.xpsfitting.com, 2013). This carbon is generally comprised of relatively short-chain and perhaps polymeric hydrocarbon species bound by both single and double bonds to oxygen and is not graphitic in nature. Its presence on insulating surfaces provides for a convenient charge reference by setting the main line of the C 1s spectrum to values ranging from 285.0 eV to 284.5. As shown in Figure 6-13, a major peak at ~285.9 eV appeared in the scan of each anode sample, including fresh Ni-SDC and the one exposed to 2 ppm H_2S in H_2 but not dry CH_4, and is attributed to adventitious carbon but with a shift upward by ~1 eV than its normal range (285.0 eV to 284.5). Comparison of the scans for fresh Ni-SDC and the one exposed to 2 ppm H_2S in H_2 but not dry CH_4, with the others indicated that the exposure of the anodes to fuel caused the peak position for adventitious carbon to shift more toward higher binding energy where the most prominent shift was observed for the dry CH_4.

The scans of the anodes that had contacted a fuel containing H_2S in CH_4 or 2 ppm H_2S followed by dry CH_4 show a strong peak at ~284.5 eV. Such a peak was assigned to graphitic-like carbon in a previous study (Rodriguez *et al*., 2001). A similar graphitic form of carbon was found on the anode contacted with dry CH_4 alone, but not H_2S, but at a somewhat higher binding energy (285.1 eV). Most importantly, the size of this peak relative to the other C 1s peaks was smallest for the anode which had been exposed to H_2S only for 30 minutes prior to the switch to dry CH_4 for ~ 100 hours, suggesting that this mode of operation led to the least amount of graphitic carbon being formed. It should be recalled that this cell also exhibited the best long-term performance of all those tested in this study. Thus, it appears that the key to this success was the reduction of the amount of graphitic carbon formed. This result confirmed the finding from the TPO analysis (Figure 6-10) that the treatment of the anode with H_2S reduced the amount of graphitic carbon formed during operation with dry CH_4, making it easier to remove. Another peak observed in all samples was found at high binding energies between 289-290 eV and is attributed to a heavily oxidized form of carbon with C=O bonds (Resofszki *et al.*, 2003).

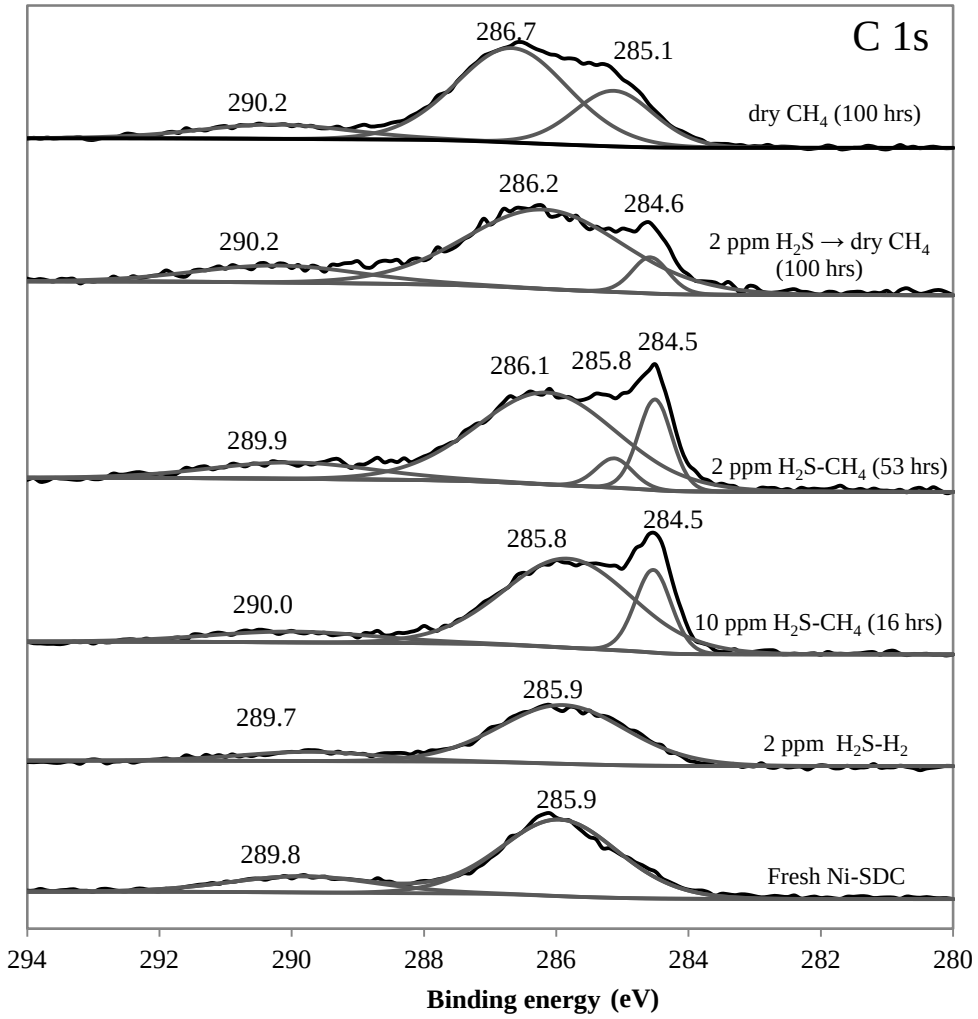

Figure 6-13 XPS spectra for C 1s region for anode cross-sections exposed to various fuels

6.4 Summary

In summary, the main findings in this chapter are:

- The continuous long-term feeding of 10 and 2 ppm H_2S within the CH_4 fuel caused the performance of the Ni-based cell to fail catastrophically, reaching close to zero voltage at 16 and 53 hours, respectively due to the poisoning effect of H_2S.
- Although the long-term exposure of the anode to H_2S eventually led to poisoning, no significant cell degradation was observed immediately after H_2S was introduced. Long-term degradation was attributed to the modification of the Ni phase in active regions of the anode by H_2S.
- The introduction of H_2S (2 ppm) for only a short interval (30 minutes) followed by a switch to dry CH_4 alone was found to be successful in maintaining good SOFC performance of the Ni-based cell for over 100 hours of operation. In fact, the introduction of H_2S in this way enhanced the stability of the cell performance over the 100 hours relative to that observed if the anode was not contacted with H_2S prior to operation with dry CH_4.
- Exposure to H_2S appeared to influence the type of carbon deposited on the anode depending on the manner in which it was incorporated into the SOFC. Carbon deposits that formed on the anodes during operation with dry CH_4 alone after they had been contacted with H_2S for only 30 minutes appeared easier to be removed.
- The introduction of H_2S through the anode compartment for only a short duration prior to shifting to dry CH_4 was found to suppress the formation of graphitic carbon on the anode.
- No evidence for the formation of nickel sulphide was obtained from XPS examination.

Chapter 7

H_2S in CH_4-based fuel operation: Carbon quantification

7.1 Introduction

In this work, effect of H_2S was further analyzed by monitoring the gas outlet compositions from the operation of dry CH_4 after treating the cell with H_2S. The result was compared to that of the cell without H_2S pretreatment. Finally, a quantitative determination of carbon was attempted to examine the effect of H_2S on the amount of carbon deposited on the cell.

7.2 Experimental Procedure

The effect of H_2S was examined by feeding dry CH_4 alone into the Ni-SDC anode-supported cell and monitoring its performance over a duration of 100 hrs at a fixed current density of 0.35 A cm^{-2} after pre-treating with 2 ppm H_2S in H_2 for 30 min at the same current. The H_2S/H_2 mixture was supplied to the anode at a total flow rate of 80 mL min^{-1}, while dry CH_4 was fed at a rate of 40 mL min^{-1}. Meanwhile, the air flow rate at the cathode was fixed at 86 mL min^{-1}. EIS was performed before and after galvanostatic operation under humidified H_2 at a DC current density of 0.35 A cm^{-1} over the frequency range from 0.1 Hz to 1MHz. This was followed by potentiodynamic scans at 5 mV s^{-1} which were also conducted under the humidified H_2.

The gas outlet composition during the galvanostatic operation with dry CH_4 was analyzed using a micro-GC Agilent model 3000A (Agilent Technologies, USA). On-line analysis of the gas outlet was conducted for CH_4, H_2, CO and CO_2 with a known amount of N_2 (10 mL) added into the outlet stream as an internal standard. An automated injection of 2000 μL of gas sample was carried out every 15 min.

At the end of the 100 hours of operation, the fuel was switched to humidified H_2 (3% H_2O) with the current density remaining at 0.35 A cm^{-2}. The analysis of the gas composition continued while humidified H_2 was introduced. The analysis was carried out using a mass spectrometry (MS) OmniStar™ model GSD 320 (Pfeiffer Vacuum, Germany) attached to the

SOFC product stream. The transfer line of the SOFC outlet leading to the MS was heated to ~140ºC to ensure that water entering the instrument remained in vapor form. The MS signals for H_2 (*m/e*=2), CH_4 (*m/e*=16), CO (*m/e*=28) and CO_2 (*m/e*=44) from the effluent gas were observed and the measured data were generated every 50 milliseconds.

The morphology of carbon was analyzed by examining the anode section of the cells using SEM (LEO 1530) equipped with energy dispersive X-ray analysis (EDXA).

7.3 Results and Discussions

7.3.1 Cell performance and gas outlet analysis

The performance of Ni-SDC operating with dry CH_4 after 30 min of H_2S treatment was compared with that of the cell operating with dry CH_4 without having been exposed to H_2S beforehand (Figure 7-1). When not pre-treated with H_2S, the cell exhibited a gradual increase in voltage over the first 30 hrs to 0.76 V before leveling off and then starting to decay at a rate of 1.05 mV hr^{-1} after 50 hrs. In comparison, the cell voltage after H_2S pre-treatment remained relatively stable at ~ 0.77 V over the entire operation with a smaller degradation rate of 0.33 mV hr^{-1}. This result suggests that the short exposure to the low level of H_2S enhanced cell stability over the subsequent 100 hr operation with dry CH_4. The degradation in performance of the cell untreated with H_2S can be attributed to the deterioration resulting from the accumulation of carbon on the anode surface.

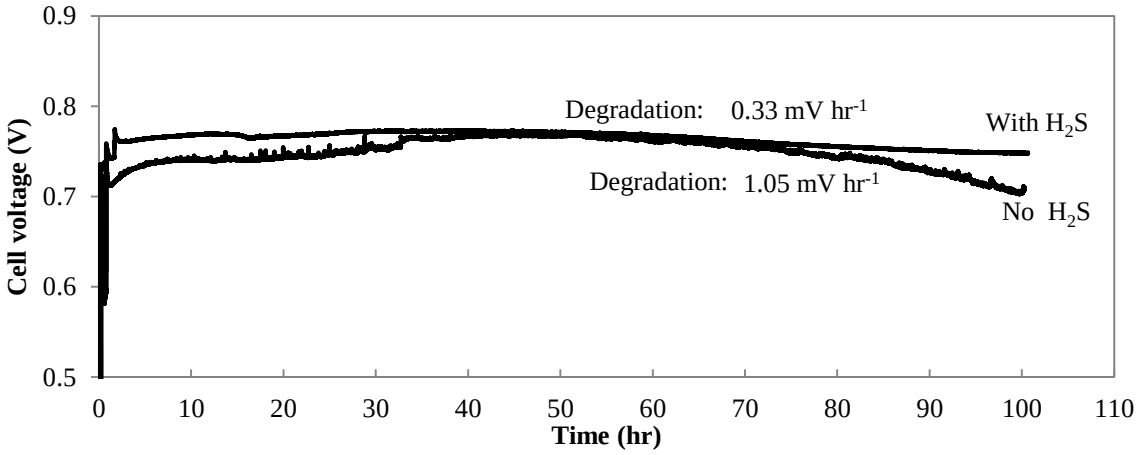

Figure 7-1 Variation of cell voltage over 100 hrs of SOFC operation at 700 ºC with dry CH_4 at a current density of 0.35 A cm^{-2} with and without H_2S pre-treatment

EIS analysis was performed to determine R_s and R_p of the cell in its initial condition and after operation with dry CH_4. The initial characterization was carried out under humidified H_2 at 0.35 A cm^{-2} before dry CH_4 was introduced into the cell. After the galvanostatic operation under dry CH_4, the fuel was switched back to humidified H_2 at which point impedance analysis and potentiodynamic measurements to obtain i-V curves were conducted.

R_s and R_p values were obtained by fitting the electrochemical impedance spectra using an equivalent circuit model. The values obtained before and after 100 hours of galvanostatic operation are presented in Figure 7-2. Essentially no change in R_s was observed for the cell that did not receive the H_2S treatment (Figure 7-2a) and only a small decrease from 0.15 to 0.14 $\Omega.cm^2$ was observed for the one initially exposed to H_2S (Figure 7-2b). Similarly, R_p remained essentially unaffected in both cases. Kim *et al.* (2002) investigated a Cu-Ni alloy anode in dry CH_4 for 168 hrs and reported that R_s decreased significantly with time. They suggested that carbon formed in the anode improved the electronic conductivity within the anode. The decrease of R_s in their work, however, was much higher than that observed here. The difference in these two results is most likely due to the fact that the previous study was conducted in an electrolyte-supported cell where carbon likely formed throughout the entire anode including the electrolyte-anode interface. On the other hand, with the anode-supported

cell used in the current study, the effect on R_s was less since carbon formed after the exposure to CH_4 was only found deposited near the anode surface at the fuel entry point (Chapters 5 and 6).

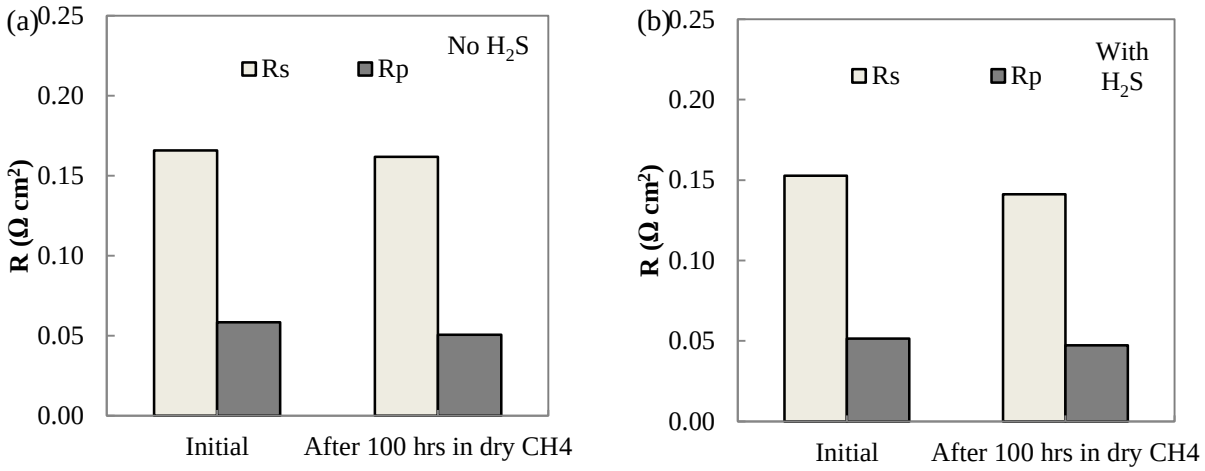

Figure 7-2 R_s and R_p measured from EIS at DC current density of 0.35 A cm^{-2} in humidified H_2 before and after 100 hrs of operation in dry CH_4 for cells a) without H_2S and b) with H_2S pre-treatment

The i-V curves measured under humidified H_2 for the cells before and after 100 hrs of operation with dry CH_4 are shown in Figure 7-3. When the cell did not receive H_2S pre-treatment, the maximum power density for the cell was reduced slightly from its initial performance of 715 mW cm^{-2} to 692 mW cm^{-2} although some improvement occurred at higher current densities (Figure 7-3a). More significantly, the cell that had been pre-treated with H_2S and then undergone 100 hours of operation exhibited a 24% increase in the maximum power density from 657 to 863 mW cm^{-2} and a large improvement in performance at high current densities relative to its initial state (Figure 7-3b). The limiting current density for this cell was enhanced almost two-fold from 1.83 to 3.57 A cm^{-2}. In order to verify this effect, this set of experiments was repeated. The resulting i-V curves before and after 100 hours of operation are presented in Appendix D. Although the cells in this run exhibited

lower initial performance than that those shown in Figure 7-3, the cell performance after 100 hours of operation showed a similar larger improvement. These results show that this approach of pre-treating the anode with a H_2 gas stream containing a low level of H_2S may be a very effective way of improving cell performance with a fuel containing dry CH_4.

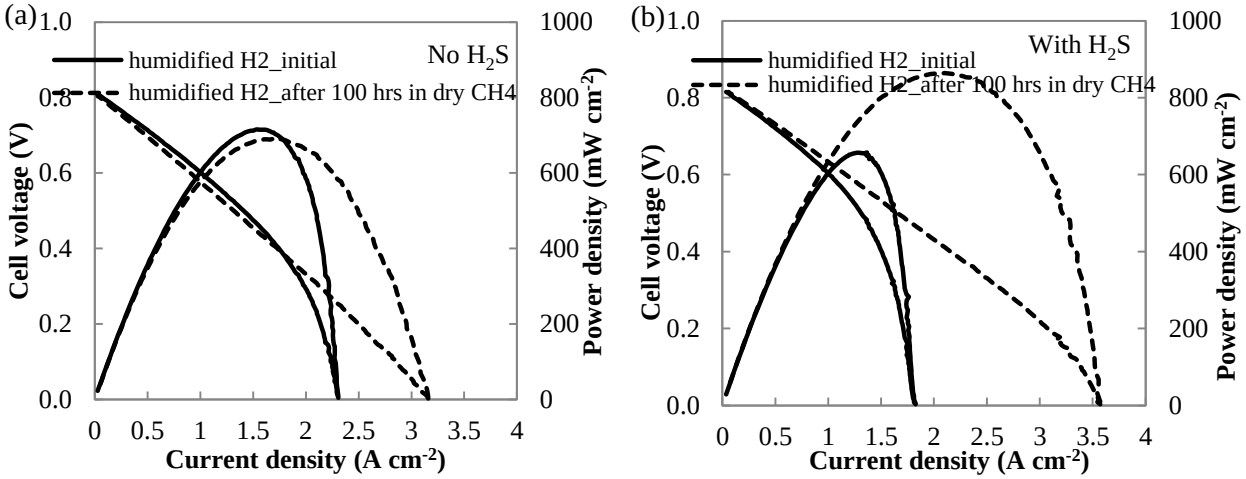

Figure 7-3 i-V and power density-current density curves measured under humidified H_2 before and after 100 hrs operation with dry CH_4 at 700ºC for cells a) without H_2S and b) with H_2S pre-treatment

From the on-line gas analysis conducted throughout these galvanostatic runs, the amount of each gas generated (in μmol s^{-1}) was determined from the concentration of the individual gases as measured by micro-GC and the total molar flow rate fed to the anode (40 mL min^{-1}). Since the presence of water vapour in the gas stream would interfere with the GC measurements of the other constituents, H_2O was condensed in a trap at the SOFC outlet before reaching the micro-GC. Nevertheless, the H_2O content in the discharge stream could be determined from its molar flow rate ($\dot{n}(H_2O)_{out}$) leaving the cell, as calculated from the following hydrogen mole balance:

$$\dot{n}(H_2O)_{out} = 2[\dot{n}(CH_4)_{in} - \dot{n}(CH_4)_{out}] - \dot{n}(H_2)_{out} \quad 7.1$$

where $\dot{n}(CH_4)_{in}$ is the inlet molar flow rate of CH_4 and $\dot{n}(CH_4)_{out}$ and $\dot{n}(H_2)_{out}$ are the outlet molar flow rates of CH_4 and H_2, respectively. Methane conversion during the operation was computed from the inlet and outlet molar flow rates of CH_4:

$$xCH_4 = \frac{\dot{n}(CH_4)_{in} - \dot{n}(CH_4)_{out}}{\dot{n}(CH_4)_{in}} \quad 7.2$$

The molar flow rates of the outlet gases during operation with dry CH_4 in the cell with no H_2S pre-treatment are presented in Figure 7-4a, while the corresponding results obtained in the cell that had been pre-treated with H_2S are shown in Figure 7-4b. When CH_4 is directly fed into the anode, various chemical and electrochemical reactions may take place simultaneously on the electrode. However, determination of the reaction pathways involved is not an easy task. Researchers agree that the reaction products depend highly on the current density applied. Yet, they have varied upon suggesting which chemical or electrochemical reactions are contributing for particular products (Liu and Barnett, 2003; Lin *et al.*, 2005; You *et al.*, 2007; Buccheri and Hill, 2012).

H_2 in the outlet gas (Figure 7-4a and Figure 7-4b) can be formed by the partial oxidation of CH_4 (Eq. 2.30), decomposition of CH_4 (Eq. 2.25) and steam reforming (Eq. 2.23). CO also can be formed via the same routes (partial oxidation of CH_4 and steam reforming) and the oxidation of carbon (Eq. 2.26) originating from the decomposition of CH_4. Meanwhile, the presence of CO_2 can be attributed to the electrochemical reaction of CO (Eq. 2.28), water-gas shift reaction (Eq. 2.24) or total oxidation of CH_4 (Eq. 2.29).

As shown in Figure 7-4, H_2 and CO compositions were smaller for the cell that had received H_2S pre-treatment than the one that had not. On the other hand, the amount of CO_2 present was very small and not significantly different in the two cells. The generation rate of H_2 from the cell without exposure to H_2S reached the highest amount of 6.2 µmol s^{-1} at 60 hrs of operation. Meanwhile, the maximum H_2 production rate when the cell received H_2S pre-treatment was 4.8 µmol s^{-1} at approximately the same operation time. The maximum rate of CO generation was 2.2 µmol s^{-1} and 2.9 µmol s^{-1} from the cell with and without exposure to H_2S, respectively. Methane conversion in the cell initially treated with H_2S was slightly

lower than in the one without pre-treatment (Figure 7-4a and Figure 7-4b). As a consequence, the gas outlet from the cell that had been exposed to H_2S contained less H_2 and CO.

The highest methane conversion achieved in the cell not exposed to H_2S was approximately 20% compared to ~17% for the cell with H_2S pre-treatment. The value was not significant indicates the pretreatment with H_2S did not have an effect on the overall cell activity. As a result, a good electrochemical performance and stability were still achieved, as shown in Figure 7-1b.

The ratio $\frac{\dot{n}(H_2)}{\dot{n}(CO)}$ was calculated by taking the average on the value over the operation found to be ~2.1 and ~2.3 for the cell without and with H_2S pretreatment, respectively. For the H_2 and CO to be produced exclusively by the partial oxidation of CH_4, a stoichiometric ratio of 2 is expected. This implies that at least some decomposition of CH_4 has occurred in both cells to produce some extra H_2 in addition to carbon and yield $\frac{\dot{n}(H_2)}{\dot{n}(CO)}$ greater than 2. If the carbon is not further removed by reacting with O^{2-}, H_2O or H_2, the amount will accumulate at the anode surface.

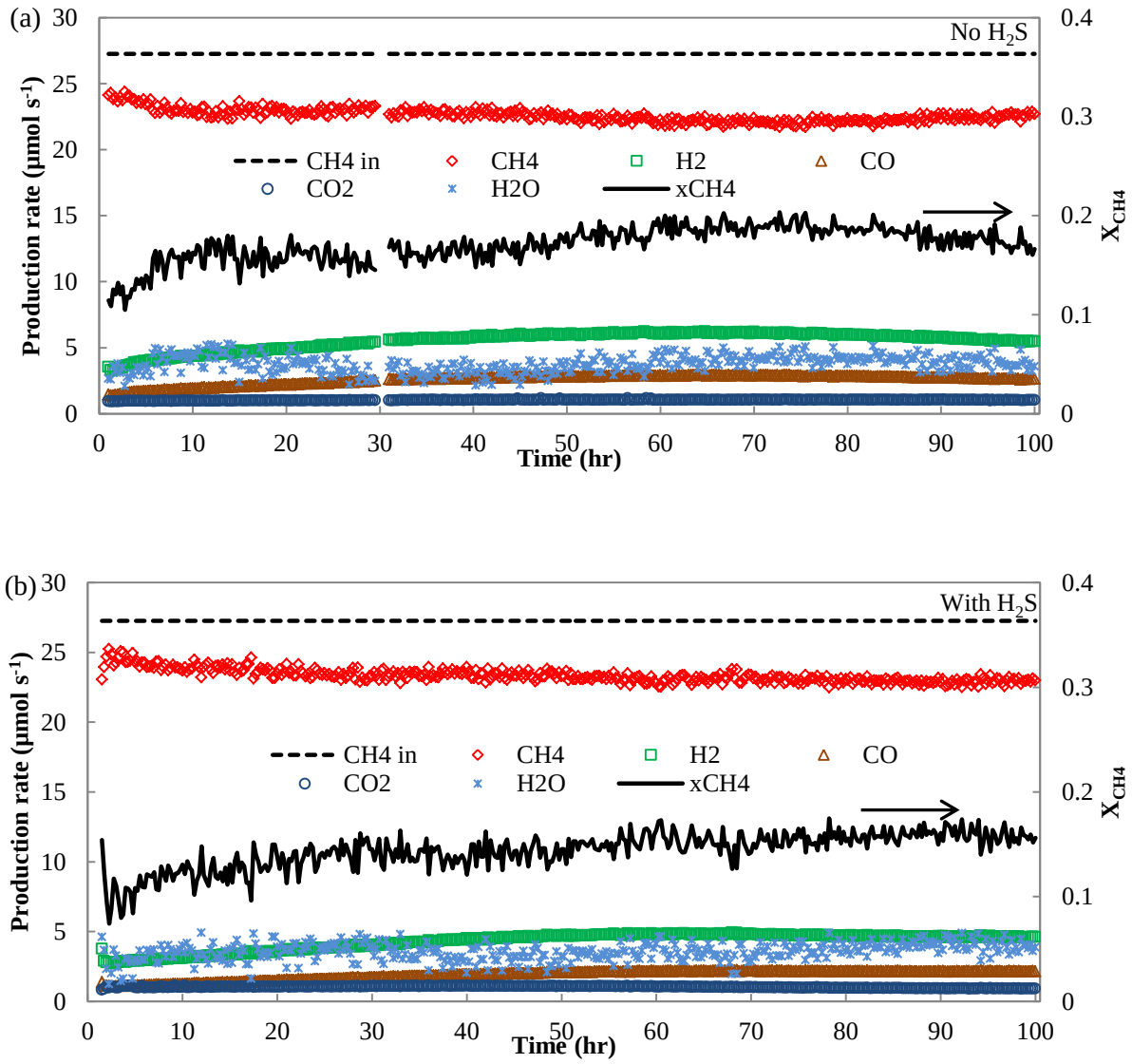

Figure 7-4 Gas outlet compositions during 100 hrs galvanostatic run using dry CH_4 alone at 0.35 A cm^{-2} and 700ºC for cells a) without H_2S and b) with H_2S pre-treatment

The results of the carbon balance for both galvanostatic experiments are shown in Figure 7-5. The balance was calculated as the ratio of the molar flow rates of all carbonaceous species in the outlet gas to the molar flow rate $\dot{n}(CH_4)_{in}$ of CH_4 entering the anode, i.e.:

$$Carbon\ balance = \frac{[\dot{n}(CH_4)_{out} + \dot{n}(CO)_{out} + \dot{n}(CO_2)_{out}]}{\dot{n}(CH_4)_{in}} \times 100 \quad 7.3$$

where $\dot{n}(CO)_{out}$ and $\dot{n}(CO_2)_{out}$ are the outlet molar flow rates for CO and CO_2, respectively. As shown in Figure 7-5, the carbon balance for both tests accounts for about 96% of the amount introduced into the cell. The deviation from 100% reflects the small amount of solid carbon formed during the galvanostatic tests. Not much difference in the carbon balance is observed whether or not the cell had been treated with H_2S. Therefore, it was not possible to relate the small reduction of methane conversion observed in the cell that had been treated with H_2S (Figure 7-4b) to the decrease in carbon formation (i.e., decomposition reaction of CH_4) at the anode.

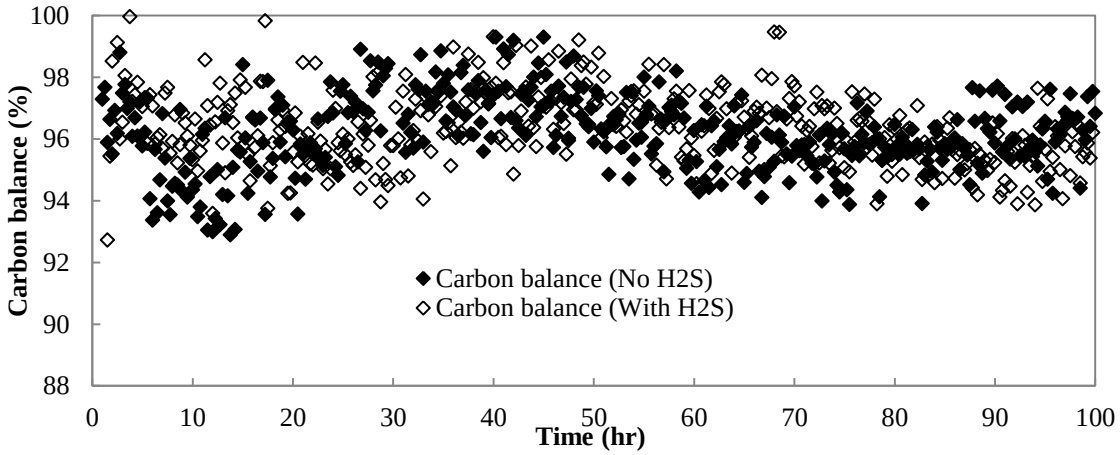

Figure 7-5 Carbon balance during 100 hrs of galvanostatic operation with dry CH_4 for cells with and without H_2S pre-treatment at 0.35A cm^{-2} and 700ºC

At the end of the 100 hours of operation with dry CH_4, the gas feed to the anode was switched to humidified H_2 for ~ 30 minutes while maintaining the current density at 0.35 A cm^{-2} and the composition of the gas stream being discharged was monitored using mass spectrometry (MS). The amount of each gas is reported in terms of its molar flow rate (μmol s^{-1}) according to the gas concentration analyzed through MS and the flow rate of humidified H_2 fed to the anode (80 mL min^{-1}). The molar flow rates of H_2, CO, CO_2 and CH_4 over a 30 minute period are presented in Figure 7-6. Dry CH_4 is still being introduced into the cell at t=0 and the switch-over to humidified H_2 is obvious from the sudden change in gas composition. Figure 7-6a shows the unreacted amount of H_2 discharged from the cell that had been exposed to H_2S and the one that had not. The dashed line is referred to the molar flow rate of H_2 entered into the anode. The period over which the H_2 molar flow rate increases before reaching the stable plateau corresponds to the time during which some of the gas was consumed after being introduced into the anode. Meanwhile, the small decrease in the amount of H_2 observed at t ~ 20-25 min occurred when the potentiodynamic analysis was carried out for the cells.

A substantial amount of CO was observed once the humidified H_2 was fed into the anode (Figure 7-6b). Since the H_2 fuel did not contain any carbonaceous species, the CO produced originated from the solid carbon previously deposited on the anode. With a current density of 0.35 A cm^{-2} flowing, the oxide ions generated at the cathode could react with the deposited carbon to produce CO. As discussed previously, carbon was only found to accumulate in the anode surface region next to the fuel inlet, away from the electrolyte-anode interface where most the electrochemical reactions took place. Nonetheless, the SDC phase in Ni-SDC anode might help extending the oxide ions within the entire anode region and assist carbon oxidation. Alzate-Restrepo and Hill (2008) stated that although oxide ions may be able to spill over beyond the electrolyte-anode interface region, it is likely that only produced H_2O from electrochemical oxidation reacts with the deposited carbon as the water migrates through the anode to the gas phase. Thus, CO could also be generated by the reaction of carbon with H_2O formed through the electrochemical oxidation of H_2 or contained within the

fuel (3% H_2O). A comparison of the two plots in Figure 7-6b reveals that more CO was generated from the cell that had not been pre-treated with H_2S than the cell that had received this treatment. Such a trend is consistent with what would be expected if more carbon deposited on the anode that had not been exposed to H_2S.

CO_2 was also generated but in a smaller amount than CO (Figure 7-6c). The reactions that lead to this gas could be the oxidation of CO or the reaction of CO with water. As with CO, a lower amount of CO_2 was produced in the cell pre-treated with H_2S. Surprisingly, a small peak for CH_4 was also observed when the switch-over to humidified H_2 took place (Figure 7-6d). The most probable reaction by which CH_4 could form involves the interaction between H_2 in the fuel and surface carbon, i.e. reverse of CH_4 decomposition. Nikooyeh *et al.* (2008) suggested that sufficiently high H_2 content is the key factor for effective removal of deposited carbon on a catalyst surface. They demonstrated that CH_4 production from the reaction of H_2 with a carbon deposit using 80% H_2 at 627-727ºC was not limited by equilibrium. Much higher H_2 concentration (100% H_2) was employed in our study and formation of CH_4 was clearly observed during the potentiodynamic analysis under humidified H_2 in both cells whether or not they had been exposed to H_2S.

The improvement of cell performance under humidified H_2 shown by the i-V curves in Figure 7-3 may have arisen due to the consumption of deposited carbon. Li *et al.* (2011) reported that the performance of anode-supported cells containing carbon deposits could be improved by the electrochemical oxidation of this carbon. Furthermore, it appears from our study that even better performance and stability can be achieved if the cell is pre-treated with H_2S, possibly because this makes carbon more easily removable from the anode than when it is not pre-treated. Therefore, during cell operation (galvanostatic), it is assumed that the carbon has been quickly consumed by various carbon removal reactions (reactions with O^{2-}, H_2O or H_2) that regenerate fuels (CO, CH_4) and thus improve cell performance. As a result, the amount of carbon deposited on the anode surface for the cell with H_2S treatment is also lowered and does not accumulate to the extent that the anode is damaged.

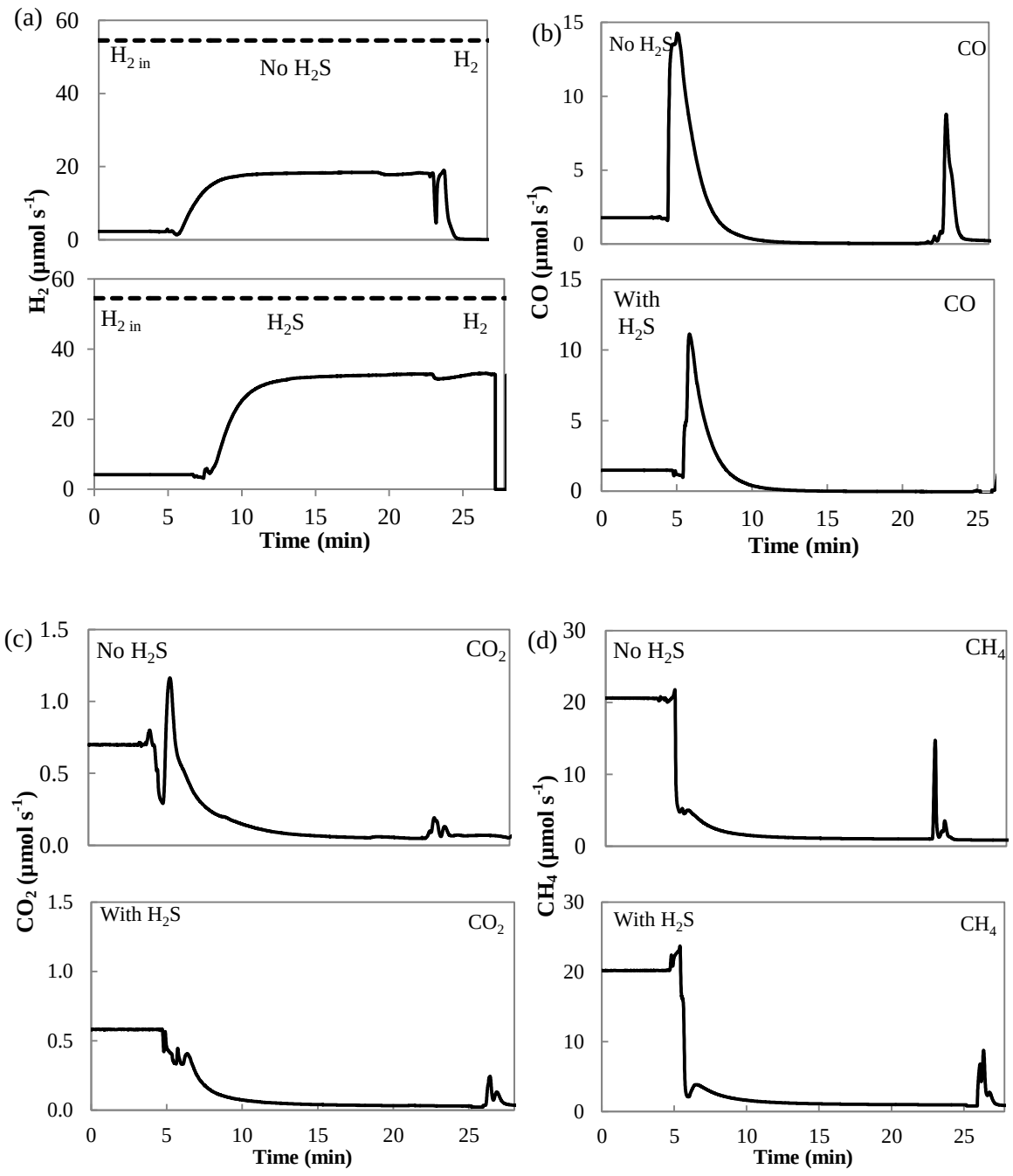

Figure 7-6 a) H_2, b) CO, c) CO_2 and d) CH_4 production while flowing humidified H_2 into the cells after 100 hrs of operation with dry CH_4 at 0.35A cm^{-2} and 700ºC

After exposure to dry CH_4 and humidified H_2, the anode sections were examined using SEM to yield the micrographs presented in Figure 7-7. Carbon deposits were confirmed by EDX elemental analysis to be present on the anode whether or not the cell was treated with H_2S. This demonstrated that the flow of humidified H_2 under galvanostatic conditions did not entirely remove the carbon formed on the anode surfaces of both cells. Some isolated particles identified by EDX analysis to be Ni appeared on the surface of carbon deposits in the sample from the cell that did not receive H_2S pre-treatment (Figure 7-7a). This suggests carbon may have promoted the detachment of Ni particles from its bulk structure which would have contributed to the cell degradation observed in Figure 7-1. This was not the case for the cell that had been exposed to H_2S where Ni appeared to remain intact (Figure 7-7b). At higher magnification, the carbon formed in both cells was found to have a similar morphology with granular spherical grains (Figure 7-7c and Figure 7-7d).

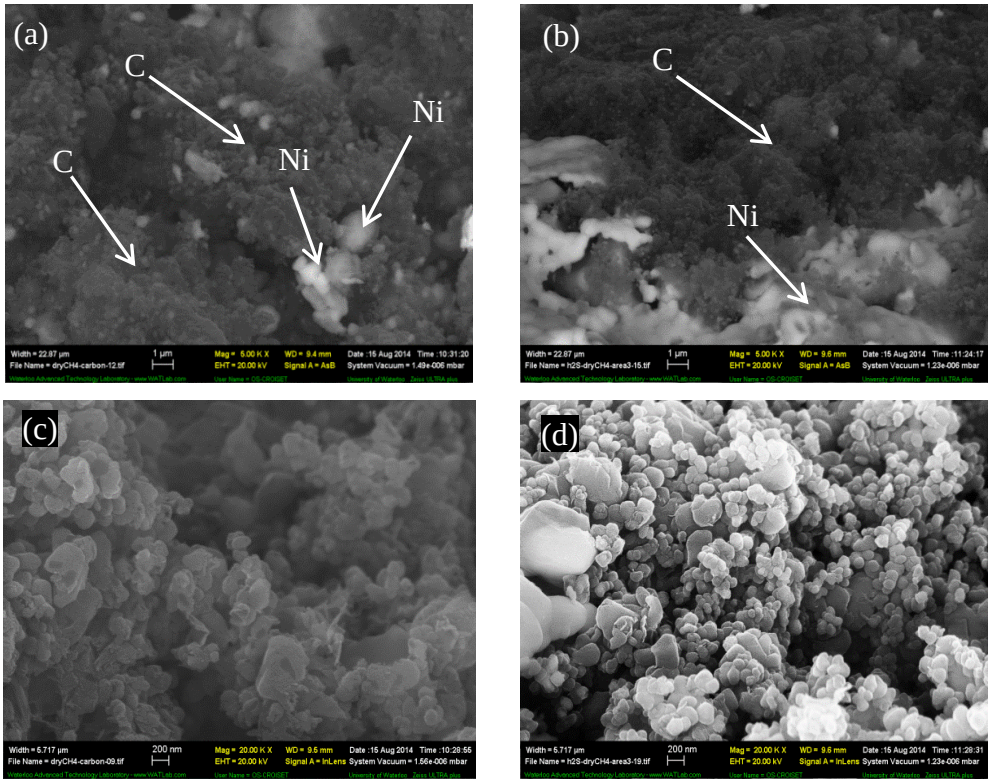

Figure 7-7 SEM micrographs of carbon deposited on Ni-SDC cells after galvanostatic operation with dry CH_4 and then humidified H_2 for the cells (a, c) without H_2S and (b, d) with H_2S pre-treatment. Top: 5.0 kx. Bottom: 20.0 kx

7.3.2 Carbon quantification

To further study the effect of H_2S on carbon deposition, quantitative determination of the amount of carbon formed in the cells was attempted. Two cells were operated with dry CH_4 for three consecutive runs (30, 40 and 15 hrs) at 0.35 A cm^{-2} and 700ºC. One cell was treated with a gas mixture containing 2 ppm H_2S in H_2 at 0.35 A cm^{-2} before dry CH_4 was introduced for each of these three runs. Another cell was not treated with the H_2S. Following each dry CH_4 operation, the gas through the cell was switched to Ar for 30 min and current turned off in order to remove any reactive gas within the outlet stream. The fuel was then switched to humidified H_2 (3% H_2O) and a current density of 0.35 A cm^{-2} quickly resumed

for 1 hr. The gas outlet composition while Ar and then humidified H_2 flowed through the cell was monitored using MS. No subsequent impedance or i-V curve measurements were taken. The next run was continued by directly supplying dry CH_4 for the cell never exposed to H_2S or incorporating H_2S for 30 min prior to the re-introduction of dry CH_4 to the other cell.

Since the galvanostatic operation under a flow of humidified H_2 also had the effect of serving as a carbon gasification procedure, the cell performance after the galvanostatic condition with humidified H_2 was also monitored. Figure 7-8 shows the variation of the cell voltage over the 30, 40 and 15 hrs of operation with dry CH_4 for the cells with and without H_2S pre-treatment. During the first 30 hrs of operation, both cells exhibited virtually identical voltages of ~0.75−0.76 V (Figure 7-8a and Figure 7-8b). In addition, stable performance was reached in both cases.

During the subsequent run, the cell that had not been exposed to H_2S exhibited a constant cell voltage of ~ 0.76 V throughout the 40 hrs of operation (Figure 7-8a). However, obvious degradation with large voltage fluctuations were observed for the cell that had been pre-treated with H_2S (Figure 7-8b). In the next run of 15 hrs, the cell without H_2S exposure was still able to maintain stable voltage with a small decline (Figure 7-8a). Meanwhile, the voltage of the cell with H_2S treatment worsened to a value of ~ 0.68 V by the end of 15 hrs (Figure 7-8b). This was surprising since it contradicted our previous finding that H_2S pre-treatment tended to improve cell performance. It is possible that the repeated introduction of H_2S before each run with dry CH_4 operations could have led to the accumulation of excessive amounts that poisoned the anode. On the other hand, the ability of the cell that had not been pre-treated with H_2S to maintain a more stable voltage may be due to the action of the humidified H_2 that was also added to remove some of the carbon under galvanostatic conditions.

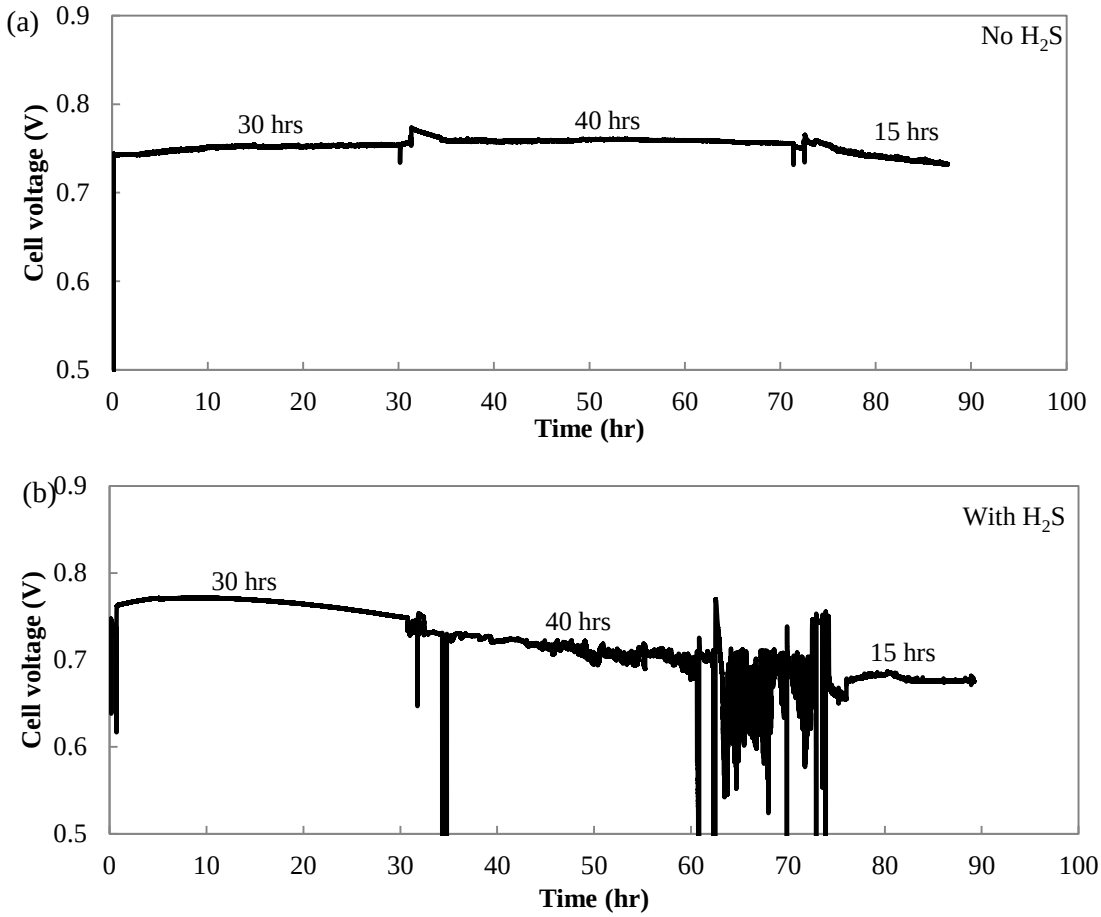

Figure 7-8 Variation of cell voltage with time during 30, 40 and 15 hrs of operation with dry CH_4 at 0.35 A cm^{-2} and 700ºC for the cells (a) without H_2S and (b) with H_2S pre-treatment

The CH_4 gas composition and conversion during these three consecutive runs are shown in Figure 7-9. In overall, Figure 7-9a and Figure 7-9b demonstrate that methane conversion in the cell treated with H_2S was lower than in the cell that had received no H_2S pre-treatment. It is believed that frequent introduction of H_2S has poisoned the cell and subsequently affecting the methane conversion. The decrease in methane conversion in Figure 7-9b was corresponding to the deterioration of cell voltage observed in Figure 7-8b.

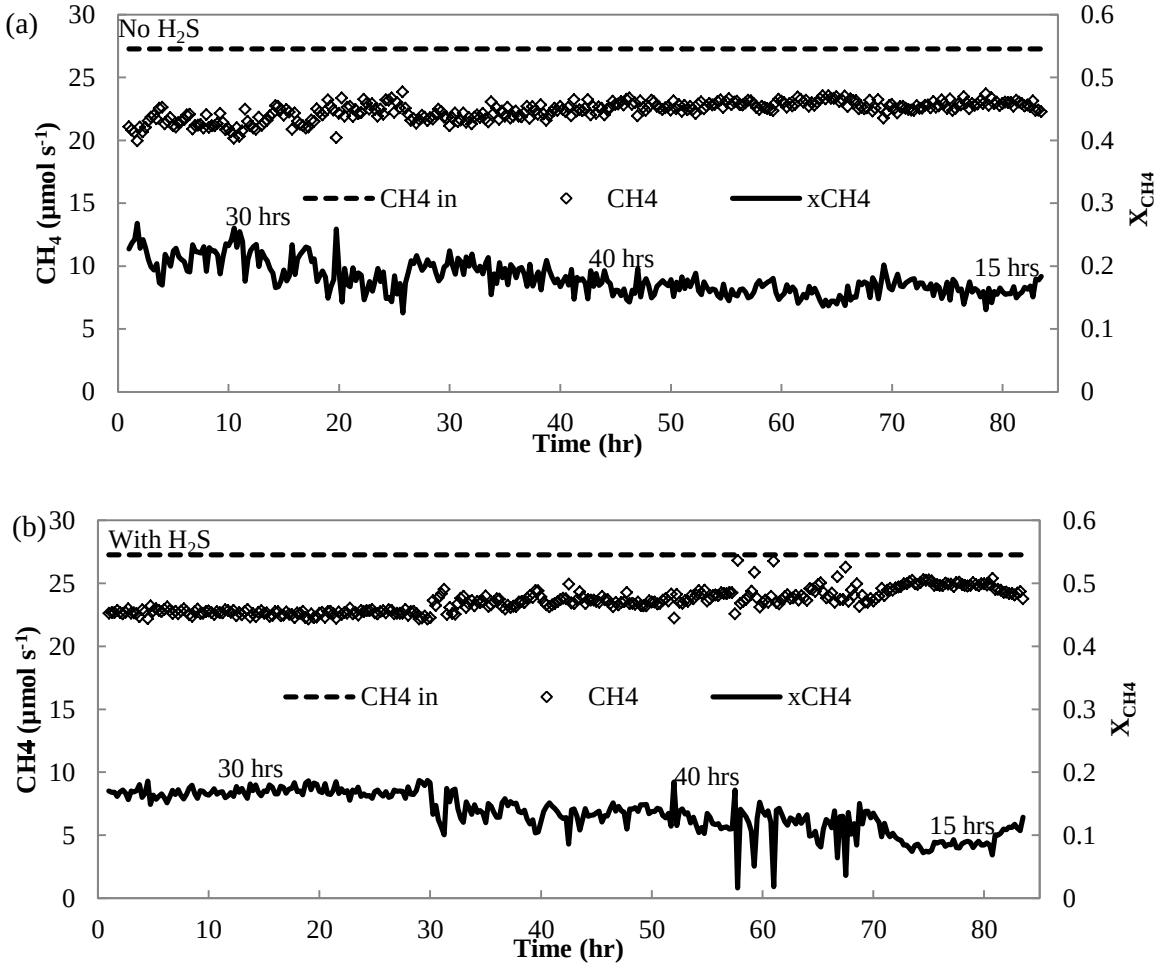

Figure 7-9 Variation of CH_4 composition and conversion during 30, 40 and 15 hrs of operation with dry CH_4 at 0.35 A cm^{-2} and 700ºC for the cell (a) without H_2S and (b) with H_2S pre-treatment

In this work, quantitative determination of the total amount of carbon remaining in the anode-supported cell at the end of a test run proved to be a challenge since this required that the cell remain intact after removing it from the SOFC setup. As an alternative, the approach attempted was to flow humidified H_2 under galvanostatic conditions to the cell in order to gasify all the deposited carbon and measure the amount of CO, CO_2 and CH_4 produced. The total number of carbonaceous gas moles would then be equal to the total number of moles of carbon deposited. However, previous SEM and EDX characterization revealed that carbon

accumulated on the anode surface was not completely removed by the introduction of humidified H_2. Therefore, the total number of carbon-containing gas moles produced will not exactly reflect the total amount of carbon deposited in the cell. Nevertheless, this analysis should still provide a reasonable measure of the relative quantity of carbon formed depending on whether or not the cell was exposed to H_2S.

To ensure that noise did not contribute to the MS peaks for the gases after the humidified H_2 was introduced into the cell, a blank test was performed. MS signals for CO, CO_2 and CH_4 were monitored when the gas composition was switched from Ar to humidified H_2 and back to Ar again. The signals produced from the blank test are presented in Appendix E.

CO, CO_2 and CH_4 generated after introducing humidified H_2 were monitored and their concentrations were measured to yield the results shown in Figure 7-10-7.12 over the three consecutive runs with dry CH_4 (lasting 30, 40 and 15 hrs, respectively). The cells were supplied with Ar with no current flowing before switching the fuel to humidified H_2 and applying 0.35 A cm^{-2} at t = 5 min. As shown, considerably more CO evolved than CH_4 and CO_2, suggesting that the removal of carbon from the anode surface occurred mostly due to the reaction of carbon with oxide ions and/or with H_2O available from H_2 oxidation or the humidified fuel. Further experimental work is needed in the future to identify which carbon removal reaction is dominant.

Based on the size of the gas peaks, the amount of carbon formed appeared to increase according to the operating time in dry CH_4 whether or not the cell was treated with H_2S. Overall, the CO, CO_2 and CH_4 peaks for the cell that had been treated with H_2S were smaller than those in the cell that had not been pre-treated with H_2S. This observation supports the conclusion that less carbon had deposited on the cell that had been exposed to H_2S than the one that had not. This also indicates the use of H_2S has effectively reduced carbon deposition on the anode.

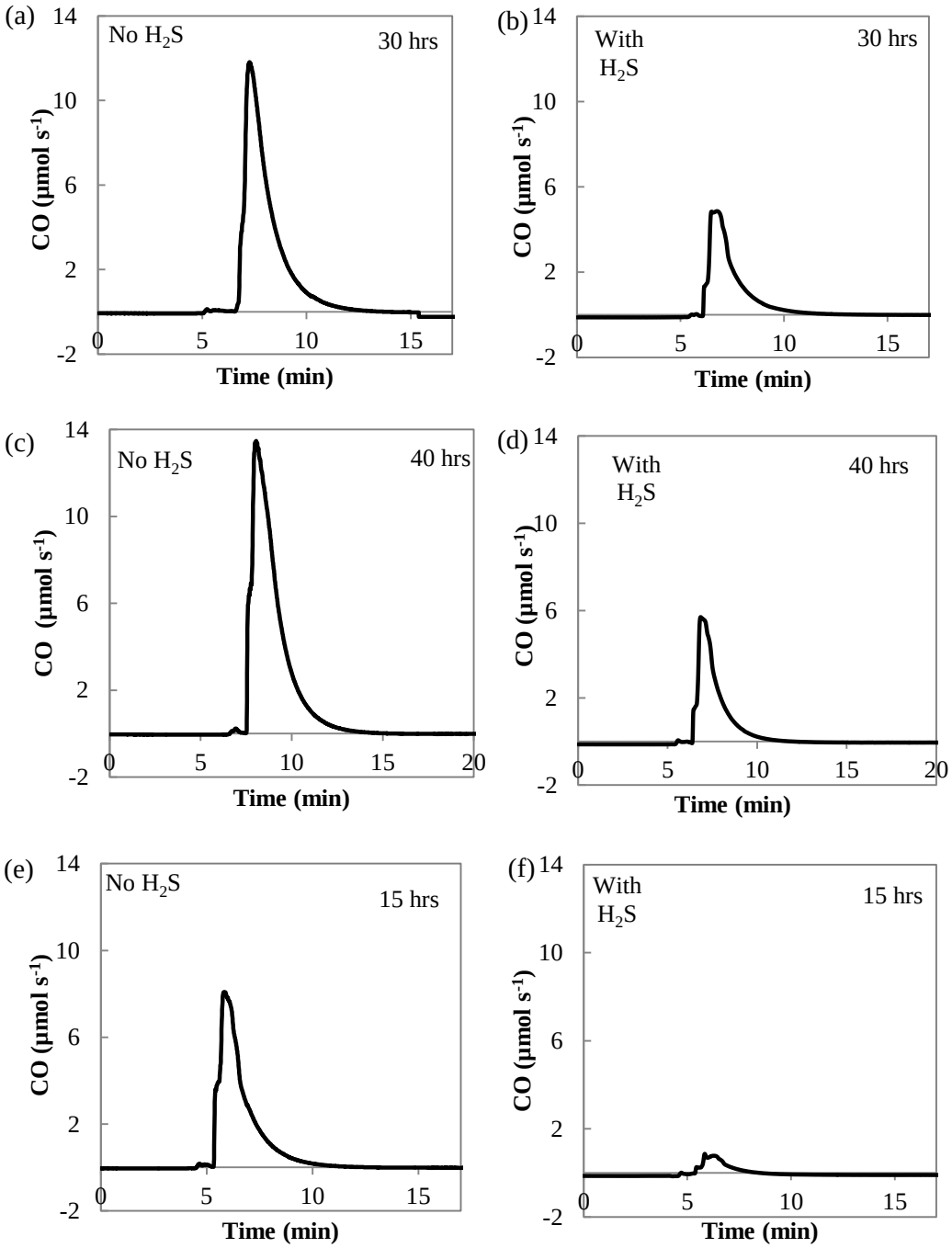

Figure 7-10 Variation of CO composition during galvanostatic operation with humidified H_2 after 30, 40 and 15 hrs operation in dry CH_4 at 0.35 A cm^{-2} and 700ºC in the cell (a, c, e) without H_2S and (b, d, f) with H_2S pre-treatment

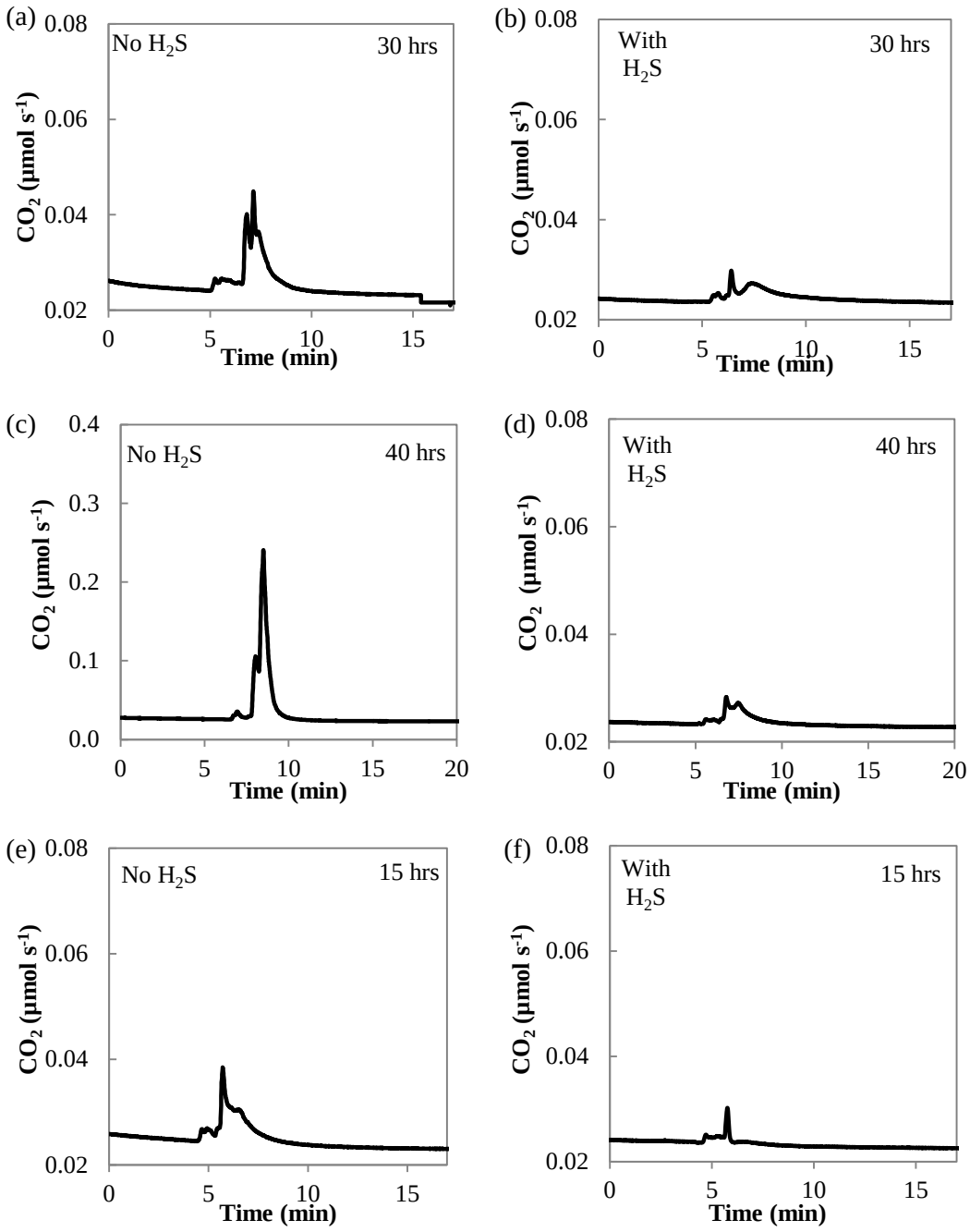

Figure 7-11 Variation of CO_2 composition during galvanostatic operation with humidified H_2 after 30, 40 and 15 hrs operation in dry CH_4 at 0.35 A cm^{-2} and 700ºC for the cell (a, c, e) without H_2S and (b, d, f) with H_2S pre-treatment

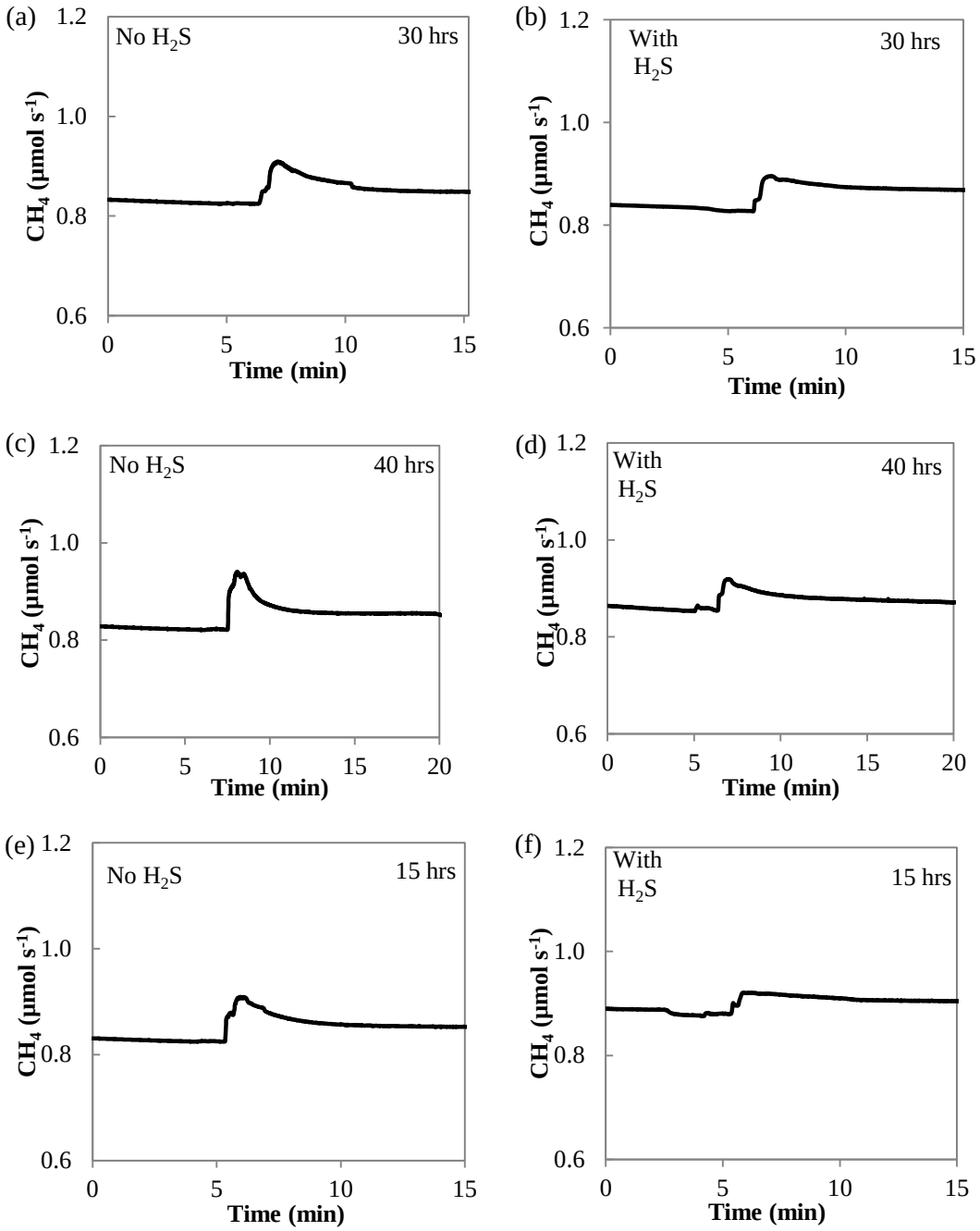

Figure 7-12 Variation of CH_4 composition during galvanostatic operation with humidified H_2 after 30, 40 and 15 hrs operation in dry CH_4 at 0.35 A cm^{-2} and 700ºC for the cell (a, c, e) without H_2S and (b, d, f) with H_2S pre-treatment

To further quantify the amount of carbon deposited on the anode (mmol) based on the gases produced, the area under the curves in Figure 7-10-7.12 were integrated using Origin 7.0 software (OriginLab Corporation, USA). Unfortunately, the quantification of the data for CH_4 was not possible due to the difficulty in selecting an appropriate baseline from the available peaks in Figure 7-12. Thus, only the areas under the curves for CO and CO_2 were computed and included in Table 7-1. The results clearly show that the amount carbon generated from CO_2 was insignificant compared to that produced from CO. Based on these total areas, it is concluded that the longer the operating time with dry CH_4, the more carbon was deposited in the cell. Most importantly, less carbon appeared to form in the cell pre-treated with H_2S than in the cell that had not been pre-treated.

Table 7-1 Area under the MS curves for gases generated in humidified H_2 after 30, 40 and 15 hrs of galvanostatic operation in dry CH_4

Compounds	Area (mmol)					
	30 hrs dry CH_4		40 hrs dry CH_4		15 hrs dry CH_4	
	Without H_2S	With H_2S	Without H_2S	With H_2S	Without H_2S	With H_2S
CO	1.033	0.478	1.361	0.507	0.737	0.118
CO_2	0.0012	0.0007	0.0080	0.0005	0.0009	0.0002
CH_4	N.A	N.A	N.A	N.A	N.A	N.A
Total	**1.034**	**0.479**	**1.369**	**0.508**	**0.738**	**0.118**

7.4 Summary

The effect of H_2S on SOFC performance and the extent of carbon deposition has been investigated. The findings in this chapter can be summarized as below:

- Cells pre-treated with a low concentration of H_2S were able to maintain a stable cell voltage over the subsequent 100 hrs of galvanostatic operation with dry CH_4, while cell

that had not been pre-treated with H_2S experienced continuous performance degradation over the same period.

- The introduction of H_2S has no significant effect on the methane conversion during galvanostatic operation with dry CH_4.
- Solid carbon formed in the anode whether or not the cell was pre-treated with H_2S. Some of the carbon deposited on the anode was removed when the fuel was switched to humidified H_2, resulting in the restoration of cell performance even to a level higher than that achieved in its initial state.
- The superior performance of the cell exposed to H_2S suggests that carbon formed was more reactive than the carbon deposited in the cell that had not been pre-treated with H_2S. This likely involved the various carbon removal reactions that also regenerate fuel and increase the cell performance. However, repetitive addition of H_2S has poisoned the cell, causing a decrease in methane conversion and subsequently deteriorated the cell performance.
- Galvanostatic operation under humidified H_2 operated in between dry CH_4 runs appeared to remove some carbon from the anode and allow the cell to operate with less degradation.
- Quantification of the carbon formed after the operation was attempted by flowing humidified H_2 under galvanostatic conditions into the cell. The amount of carbon-containing gases (CO, CO_2 and CH_4) produced supported the conclusion that less carbon was deposited in the cell pre-treated with H_2S than one without pretreatment. Also, regardless whether or not the cell was treated with H_2S, the amount of carbon deposited in the cell increased with the operating time in dry CH_4.

Chapter 8
Conclusions and Recommendations

8.1 Conclusions

The aims of this thesis were to investigate 1) the performance of Ni-samaria-doped-ceria (Ni-SDC) cell and its susceptibility to carbon deposition when directly fed with CH_4 and CO, 2) the effect of incorporating sulphur (i.e., H_2S) into the gas stream fed to the cell in order to improve its carbon tolerance when fuelled with CH_4.

In Chapter 4, anode-supported Ni-SDC cells were tested with various fuel compositions (H_2, CH_4, CO-CO_2 mixture) in the temperature range from 600 to 700ºC. At 700ºC, the highest maximum power density of 721 mW cm^{-2} was achieved using humidified CH_4 as fuel followed by dry CH_4 (697 mW cm^{-2}) and humidified H_2 (663 mW cm^{-2}). Better overall performance at both 700°C and 650°C was obtained with the cell using CH_4 fuel than H_2. On the other hand, the use of humidified H_2 yielded the best performance at 600ºC compared to CH_4 with 376 mW cm^{-2} maximum power density compared to 370 mW cm^{-2} and 356 mW cm^{-2} for humidified CH_4 and dry CH_4, respectively. Much lower power densities were observed with CO fuel than H_2 and CH_4 although it should be acknowledged that CO was added as mixtures with CO_2 at levels of only 40% and 20%. However, it should be noted that the cell performance achieved in CO-CO_2 was found to be better than that reported in previous studies.

Stability tests were performed at 600 and 700ºC whereby cell voltage was monitored over 10 hours with H_2 and CH_4 fuels and 6 hours with CO-CO_2. No significant drop was found in the cell voltage with each fuel over these time periods. The cell was found to exhibit higher voltage and be more stable using CH_4 at 700ºC than at 600ºC. The opposite trend was observed during the operation with CO-CO_2. These results confirmed temperature has a strong influence on the performance and stability of cells operating with CH_4 and CO-CO_2 fuels.

In Chapter 5, the tendency of carbon to deposit in the Ni-SDC cells under dry CH_4 and CO-CO_2 mixtures was investigated. Thermodynamic analysis of the system was first conducted to determine the conditions for carbon deposition and use these to set the experimental procedure. Stability tests were conducted galvanostatically (0.35 A cm^{-2} at 700ºC and 0.1 A cm^{-2} at 550ºC) for 100 hours using dry CH_4 fuel and 6 hours using a 40%CO-60%CO_2 mixture. The cell voltage during operation with dry CH_4 remained stable during the first 20 hrs before starting to gradually degrade at 1.33 mV hr^{-1}. A much higher degradation rate of 4.5 mV hr^{-1} was observed with the CO-CO_2 fuel. Cell degradation during long term operation in both fuels was attributed to carbon accumulation in the anode.

Carbon deposition in the Ni-SDC cell from dry CH_4 and CO-CO_2 fuels was found to occur primarily at the surface of the anode closest to the fuel entry point with insignificant amounts at the electrolyte-anode interface or the middle of the anode. Despite this build-up of carbon in the anode, the drop in cell performance with both fuels was relatively small. This may due to the fact that that carbon only deposited near the anode surface exposed to the fuel and an anode-supported cell was being used. Most of the anode including the electrolyte-anode interface remained free from carbon, thus allowing the electro-catalytic processes to continue.

The focus of Chapter 6 was on the effect of sulphur on inhibiting carbon deposition over long term operation with dry CH_4 fuel. When H_2S was continuously fed to the anode within the CH_4 fuel stream at levels of 2 ppm and 10 ppm, no significant degradation in performance was observed immediately after H_2S was first introduced. However, after ~20 hrs the performance of the Ni-based cell began to deteriorate rapidly and ultimately failed catastrophically, presumably due to the poisoning effect of H_2S.

A considerable amount of carbon still formed on the anode surface and carbon deposition was not deterred when H_2S was introduced within the dry CH_4. Although sulphur presumably has a high tendency to adsorb onto Ni step sites, the concentration of H_2S was so low relative to CH_4 when the two species were introduced together in the same stream that sulphur could

not effectively compete with the carbonaceous species for the Ni step sites and inhibit carbon formation.

Another feeding scheme of H_2S investigated involved the introduction of a mixture of 2 ppm H_2S in dry H_2 into the cell for 30 minutes before switching to dry CH_4 for 100 hrs. This method of H_2S introduction was found to be very successful in maintaining good SOFC performance and stability of the Ni-based cell for over 100 hours of operation under dry CH_4 alone. A degradation rate in the cell voltage of only 0.63 mV hr^{-1} was achieved, smaller than that obtained during 100 hours of operation in dry CH_4 if the anode was not contacted with H_2S prior to the operation (1.33 mV hr^{-1}).

TPO analysis showed that the presence of H_2S did influence the type of carbon formed by the reaction of CH_4 at the anode. Furthermore, the nature of the carbon formed also depended on the manner in which the H_2S was incorporated into the SOFC. Carbon deposits that formed during operation with dry CH_4 alone after the anode had been contacted with H_2S for 30 minutes were more weakly bound to the surface and more easily removed than the carbon formed if the cell was not pre-treated with H_2S or a fuel mixture of H_2S in CH_4 was fed continuously throughout the entire run. XPS analysis further revealed that the introduction of H_2S for only a short duration prior to shifting to dry CH_4 suppressed the formation of graphitic carbon on the anode. Thus, it appears that the best long-term performance of the cell through this H_2S inclusion was achieved due to the reduction of the amount of graphitic carbon formed on the anode. XPS showed no evidence for the formation of nickel sulphide on the anode surface.

Finally, the experiments described in Chapter 7 confirmed that the performance was superior in the cell which had been pre-treated with 2 ppm H_2S in H_2 suggested that carbon formed was easier to react over various carbon removal reactions compared to carbon deposited on the cell without H_2S. At the same time, the methane conversion during the galvanostatic operation with dry CH_4 was not affected by the introduction of H_2S prior to the operation.

A flow of humidified H_2 under galvanostatic conditions for ~ 1 hour at the end of the 100 hours of operation effectively removed carbon from the anode and allowed the cell to maintain cell voltage, especially in the cell that had operated with dry CH_4 alone. The amount of carbon that had accumulated in the anode after operation with dry CH_4 at 0.35 A cm^{-2} was estimated by analyzing the amount of carbon-containing gases produced while humidified H_2 was flowed through the anode and the same current density was left unchanged. This analysis showed that the cell which had been exposed to H_2S prior to operation with dry CH_4 contained less carbon than the cell that had not been pre-treated with H_2S.

8.2 Recommendations for future work

- Investigation of the effect of H_2S on systems operating with CO and higher hydrocarbons since only cell operating with dry CH_4 was considered in this work.
- Further experiments on gasification step to determine which reaction is dominant for the removal of carbon on the anode while flowing humidified H_2 under galvanostatic conditions.
- Development of a suitable method to ensure that all of the carbon accumulated on the anode can be measured. An approach attempted during this research involved the introduction of an O_2/He mixture into the cell, but this damaged the cell structure and caused the oxygen from the surrounding air to leak into the system.

Bibliography

Abild-Pedersen, F., Lytken, O., Engbæk, J., Nielsen, G., Chorkendorff, I., and Nørskov, J. K. (2005). Methane activation on Ni(1 1 1): Effects of poisons and step defects. *Surface Science, 590*(2–3), 127-137.

Aguiar, P., Adjiman, C. S., and Brandon, N. P. (2004). Anode-supported intermediate temperature direct internal reforming solid oxide fuel cell. I: Model-based steady-state performance. *Journal of Power Sources, 138*(1–2), 120-136.

Ai, N., Chen, K., Jiang, S. P., Lü, Z., and Su, W. (2011). Vacuum- assisted electroless copper plating on Ni/(Sm,Ce)O_2 anodes for intermediate temperature solid oxide fuel cells. *International Journal of Hydrogen Energy, 36*(13), 7661-7669.

Ai, N., Lü, Z., Chen, K., Huang, X., Wei, B. and Zhang, Y. (2006). Low temperature solid oxide fuel cells based on $Sm_{0.2}Ce_{0.8}O_{1.9}$ films fabricated by slurry spin coating. *Journal of Power Sources, 159*(1), 637-640.

Ai, N., Lü, Z., Tang, J., Chen, K., Huang, X., and Su, W. (2008). Improvement of output performance of solid oxide fuel cell by optimizing Ni/samaria-doped ceria anode functional layer. *Journal of Power Sources, 185*(1), 153-158.

Alzate-Restrepo, V. and Hill, J. M. (2008). Effect of anodic polarization on carbon deposition on Ni/YSZ anodes exposed to methane. *Applied Catalysis A: General, 342*(1–2), 49-55.

Asamoto, M., Miyake, S., Sugihara, K. and Yahiro, H. (2009). Improvement of Ni/SDC anode by alkaline earth metal oxide addition for direct methane–solid oxide fuel cells. *Electrochemistry Communications, 11*(7), 1508-1511.

Azad, A. K., and Irvine, J. T. S. (2011). Characterization of $YSr_2Fe_3O_{8-\delta}$ as electrode materials for SOFC. *Solid State Ionics, 192*(1), 225-228.

Basu, R. N., S., Basu, R. N., Sharma, A. D., Dutta, A., and Mukhopadhyay, J. (2008). Processing of high-performance anode-supported planar solid oxide fuel cell. *International Journal of Hydrogen Energy, 33*(20), 5748-5754.

Belyaev, V. D., Politova, T. I., Mar'ina, O. A., and Sobyanin, V. A. (1995). Internal steam reforming of methane over ni-based electrode in solid oxide fuel cells. *Applied Catalysis A: General, 133*(1), 47-57.

Bengaard, H. S., Nø, Bengaard, H. S., Nørskov, J. K., Sehested, J. and Clausen, B. S. (2002). Steam reforming and graphite formation on Ni catalysts. *Journal of Catalysis, 209*(2), 365-384.

Biesinger, M. C., Payne, B. P., Lau, L. W. M., Gerson, A. and Smart, R. S. C. (2008). X-ray photoelectron spectroscopic chemical state quantification of mixed nickel metal, oxide and hydroxide systems. *Surface and Interface Analysis, 41*(4), 324-332.

Bu, Y., Zhong, Q., Tan, W., Zhou, R., Song, Y., and Cai, W. (2013). Synthesis and properties of samaria-doped ceria electrolyte via ultrasound–microwave assisted sol–gel method. *Materials Science in Semiconductor Processing, 16*(6), 2058-2062.

Buccheri, M. A and Hill, J. M. (2012). Methane electrochemical oxidation pathway over a Ni/YSZ and $La_{0.3}Sr_{0.7}TiO_3$ bi-layer SOFC anode. *Journal of the Electrochemical Society, 159*(4), B361.

Buccheri, M. A., Singh, A., and Hill, J. M. (2011). Anode- versus electrolyte-supported Ni-YSZ/YSZ/Pt SOFCs: Effect of cell design on OCV, performance and carbon formation for the direct utilization of dry methane. *Journal of Power Sources,* 196(3), 968-976.

Chan, S. H., Khor, K. A., and Xia, Z. T. (2001). A complete polarization model of a solid oxide fuel cell and its sensitivity to the change of cell component thickness. *Journal of Power Sources, 93*(1–2), 130-140.

Chen, T., Wang, W. G., Miao, H., Li, T., and Xu, C. (2011). Evaluation of carbon deposition behavior on the nickel/yttrium-stabilized zirconia anode-supported fuel cell fueled with simulated syngas. *Journal of Power Sources, 196*(5), 2461-2468.

Cheng, Z., and Liu, M. (2007). Characterization of sulfur poisoning of Ni–YSZ anodes for solid oxide fuel cells using in situ raman microspectroscopy. *Solid State Ionics, 178*(13), 925-935.

Chick, L. A., Pederson, L. R., Maupin, G. D., Bates, J. L., Thomas, L. E., and Exarhos, G. J. (1990). Glycine-nitrate combustion synthesis of oxide ceramic powders. *Materials Letters, 10*(1–2), 6-12.

Christie, G. M., and van Berkel, F. P. F. (1996). Microstructure — ionic conductivity relationships in ceria-gadolinia electrolytes. *Solid State Ionics, 83*(1–2), 17-27.

Demirbas, A. (2009). Biohydrogen: For future engine fuel demands. *Springer-Verlag London Limited,* London.

Deng, X., and Petric, A. (2005). Geometrical modeling of the triple-phase-boundary in solid oxide fuel cells. *Journal of Power Sources, 140*(2), 297-303.

Dijkstra, J.W. and Jansen, D. (2002). Novel concepts for CO_2 capture with SOFC. *6th International Conference on Greenhouse Gas Control Technologies (GHGT-6)*, Kyoto, Japan.

Ding, D., Liu, B., Gong, M., Liu, X., and Xia, C. (2010). Electrical properties of samaria-doped ceria electrolytes from highly active powders. *Electrochimica Acta, 55*(15), 4529-4535.

Doshi, R., Richards, V.L., Carter, J.D., Wang, X., and Krumpelt, M. (1999). Development of solid-oxide fuel cells that operate at 500°C. *Journal of the Electrochemical Society, 146*, 1273.

Eguchi, K. (1997). Ceramic materials containing rare earth oxides for solid oxide fuel cell. *Journal of Alloys and Compounds, 250*(1–2), 486-491.

Eguchi, K., Setoguchi, T., Inoue, T., and Arai, H. (1992). Electrical properties of ceria-based oxides and their application to solid oxide fuel cells. *Solid State Ionics, 52*(1–3), 165-172.

Finnerty, C. M. and Ormerod, R. M. (2000). Internal reforming over nickel/ zirconia anodes in SOFCS oparating on methane: Influence of anode formulation, pre-treatment and operating conditions. *Journal of Power Sources, 86*(1), 390-394.

Finnerty, C. M., Coe, N. J., Cunningham, R. H. and Ormerod, R. M. (1998). Carbon formation on and deactivation of nickel-based/ zirconia anodes in solid oxide fuel cells running on methane. *Catalysis Today, 46*(2), 137-145.

Fuentes, R. O. and Baker, R. T. (2008). Synthesis and properties of gadolinium-doped ceria solid solutions for IT-SOFC electrolytes. *International Journal of Hydrogen Energy, 33*(13), 3480-3484.

Fukunaga, H., Ishino, M., and Yamada, K. (2007). Effective thickness of Ni–Sm- doped ceria cermet anode for solid oxide fuel cell. *Electrochemical and Solid-State Letters, 10*(1), B16.

Galea, N. M., Knapp, D., and Ziegler, T. (2007). Density functional theory studies of methane dissociation on anode catalysts in solid-oxide fuel cells: Suggestions for coke reduction. *Journal of Catalysis, 247*(1), 20-33.

Gavrielatos, I., Drakopoulos, V., and Neophytides, S. G. (2008). Carbon tolerant Ni–Au SOFC electrodes operating under internal steam reforming conditions. *Journal of Catalysis, 259*(1), 75-84.

Gorte, R. J. and Vohs, J. M. (2003). Novel SOFC anodes for the direct electrochemical oxidation of hydrocarbons. *Journal of Catalysis, 216*(1–2), 477-486.

Gorte, R. J., Kim, H., and Vohs, J. M. (2002). Novel SOFC anodes for the direct electrochemical oxidation of hydrocarbon. *Journal of Power Sources, 106*(1–2), 10-15.

Grgicak, C. M., Green, R. G., and Giorgi, J. B. (2008). SOFC anodes for direct oxidation of hydrogen and methane fuels containing H 2S. *Journal of Power Sources, 179*(1), 317-328.

Guo, J., Lou, H. and Zheng, X. (2007). The deposition of coke from methane on a Ni/$MgAl_2O_4$ catalyst. *Carbon, 45*(6), 1314-1321.

He, H. and Hill, J. M. (2007). Carbon deposition on Ni/YSZ composites exposed to humidified methane. *Applied Catalysis A, General, 317*(2), 284-292.

He, H., Huang, Y., Vohs, J. M., and Gorte, R. J. (2004). Characterization of YSZ– YST composites for SOFC anodes. *Solid State Ionics, 175*(1), 171-176.

http://www.xpsfitting.com (2003). X-ray Photoelectron Spectroscopy (XPS) Reference Pages.

Huang, Y. -. H., Dass, R. I., Xing, Z. -. L. and Goodenough, J. B.(2006) Double perovskites as anode materials for solid-oxide fuel cells. *Science, 312*(5771), 254.

Hui, S., Roller, J., Yick, S., Zhang, X., Decès-Petit, C., Xie, Y., Ghosh, D. (2007). A brief review of the ionic conductivity enhancement for selected oxide electrolytes. *Journal of Power Sources, 172*(2), 493-502.

Huijsmans, J. P. P. (2001). Ceramics in solid oxide fuel cells. *Current Opinion in Solid State and Materials Science, 5*(4), 317-323.

Huijsmans, J. P. P., van Berkel, F. P. F., and Christie, G. M. (1998). Intermediate temperature SOFC – a promise for the 21st century. *Journal of Power Sources, 71*(1–2), 107-110.

Iida, T., Kawano, M., Matsui, T., Kikuchi, R. and Eguchi, K. (2007). Internal reforming of SOFCs. *Journal of the Electrochemical Society, 154*(2), B234.

Inaba, H. and Tagawa, H. (1996). Ceria-based solid electrolytes. *Solid State Ionics, 83*(1–2), 1-16.

Ishikura, A., Sakuno, S., Komoyama, N., Sasatsu, H., Masuyama, N., Itoh, H. and Yasumoto, K. (2007). Influence of H_2S poisoning on anode layer of SOFC. *ECS Transactions*, 7 (1), 845-850.

Jasinski, P., Suzuki, T., Dogan, F., and Anderson, H. U. (2004). Impedance spectroscopy of single chamber SOFC. *Solid State Ionics, 175*(1–4), 35-38.

Jiang, S. P. and Chan, S. H. (2004). A review of anode materials development in solid oxide fuel cells. *Journal of Materials Science, 39*(14), 4405-4439.

Jung, C., Jalota, S., and Bhaduri, S. B. (2005). Quantitative effects of fuel on the synthesis of Ni/NiO particles using a microwave-induced solution combustion synthesis in air atmosphere. *Materials Letters, 59*(19–20), 2426-2432.

Kan, H. and Lee, H. (2010a). Enhanced stability of Ni–Fe/ GDC solid oxide fuel cell anodes for dry methane fuel. *Catalysis Communications, 12*(1), 36-39.

Kan, H. and Lee, H. (2010b) Sn-doped Ni/YSZ anode catalysts with enhanced carbon deposition resistance for an intermediate temperature SOFC. *Applied Catalysis B, Environmental, 97*(1), 108-114.

Kan, H., Hyun, S. H., Shul, Y., and Lee, H. (2009). Improved solid oxide fuel cell anodes for the direct utilization of methane using sn-doped Ni/YSZ catalysts. *Catalysis Communications, 11*(3), 180-183.

Kharton, V. V., Marques, F. M. B., and Atkinson, A. (2004). Transport properties of solid oxide electrolyte ceramics: A brief review. *Solid State Ionics, 174*(1), 135-149.

Kim, H., Lu, C., Worrell, W. L., Vohs, J. M. and Gorte, R. J. (2002). Cu-Ni cermet anodes for direct oxidation of methane in solid-oxide fuel cells. *Journal of the Electrochemical Society, 149*(3), A247-A250.

Kim, J., V., Kim, J. W., Virkar, A. V., Fung, K. Z. and Mehta, K., (1999). Polarization effects in intermediate temperature, anode-supported solid oxide fuel cells. *Journal of the Electrochemical Society, 146*(1), 69-78.

Kim, S., Hyun, S., Moon, J., Kim, J., and Song, R. (2005). Fabrication and characterization of anode-supported electrolyte thin films for intermediate temperature solid oxide fuel cells. *Journal of Power Sources, 139*(1-2), 67-72.

Kim, T., Liu, G., Boaro, M., Lee, S. -., Vohs, J. M. and Gorte, R. J. (2006). A study of carbon formation and prevention in hydrocarbon-fueled SOFC. *Journal of Power Sources, 155*(2), 231-238.

Kishimoto, H., Yamaji, K., Horita, T., Xiong, Y., Sakai, N. and Brito, M. E., (2006). Reaction process in the Ni–ScSZ anode for hydrocarbon fueled SOFCs. *Journal of the Electrochemical Society, 153*(6), A982.

Kuhn, J. N., Lakshminarayanan, N. and Ozkan, U. S. (2008). Effect of hydrogen sulfide on the catalytic activity of Ni-YSZ cermets. *Journal of Molecular Catalysis.A, Chemical, 282*(1), 9-21.

Laosiripojana, N. and Assabumrungrat, S. (2005). Methane steam reforming over Ni/Ce–ZrO2 catalyst: Influences of Ce–ZrO2 support on reactivity, resistance toward carbon formation, and intrinsic reaction kinetics. *Applied Catalysis A: General, 290*(1–2), 200-211.

Laosiripojana, N. and Assabumrungrat, S. (2006a). Hydrogen production from steam and autothermal reforming of LPG over high surface area ceria. *Journal of Power Sources, 158*(2), 1348-1357.

Laosiripojana, N., and Assabumrungrat, S. (2006b). Catalytic steam reforming of ethanol over high surface area CeO2: The role of CeO2 as an internal pre-reforming catalyst. *Applied Catalysis B: Environmental, 66*(1–2), 29-39.

Laosiripojana, N., Sangtongkitcharoen, W., and Assabumrungrat, S. (2006). Catalytic steam reforming of ethane and propane over CeO2-doped Ni/Al2O3 at SOFC temperature: Improvement of resistance toward carbon formation by the redox property of doping CeO2. *Fuel, 85*(3), 323-332.

Legrand, D. L., Nesbitt, H. W. and Bancroft, G. M. (1998). X-ray photoelectron spectroscopic study of a pristine millerite (NiS) surface and the effect of air and water oxidation. *American Mineralogist, 83*(11), 1256.

Li, X. (2006). Principles of fuel cells. *Taylor & Francis*, New York.

Lin, Y., Zhan, Z., Liu, J. and Barnett, S. A. (2005). Direct operation of solid oxide fuel cells with methane fuel. *Solid State Ionics, 176*(23), 1827-1835.

Liu, J. and Barnett, S. A. (2003). Operation of anode-supported solid oxide fuel cells on methane and natural gas. *Solid State Ionics, 158*(1–2), 11-16.

Liu, Z., Ding, D., Liu, M., Li, X., Sun, W. and Xia, C. (2013). Highly active Sm0.2Ce0.8O1.9 powders of very low apparent density derived from mixed cerium sources. *Journal of Power Sources, 229*(0), 277-284.

Lussier, A., S., Lussier, A., Sofie, S., Dvorak, J. and Idzerda, Y. U. (2008) Mechanism for SOFC anode degradation from hydrogen sulfide exposure. *International Journal of Hydrogen Energy, 33*(14), 3945-3951.

Maček, J., Novosel, B. and Marinšek, M. (2007). Ni–YSZ SOFC anodes—Minimization of carbon deposition. *Journal of the European Ceramic Society, 27*(2–3), 487-491.

Marrero-López, D., Peña-Martínez, J., Ruiz-Morales, J. C., Gabás, M., Núñez, P. and Aranda, M. A. G. (2010). Redox behaviour, chemical compatibility and electrochemical performance of Sr2MgMoO6 − δ as SOFC anode. *Solid State Ionics, 180*(40), 1672-1682.

Matsui, T., Inaba, M., Mineshige, A., Ogumi, Z., Matsui, T. and Inaba, M. (2005b). Electrochemical properties of ceria-based oxides for use in intermediate-temperature SOFCs. *Solid State Ionics, 176*(7), 647-654.

Matsui, T., Kosaka, T., Inaba, M., Mineshige, A., Ogumi, Z. and Matsui, T. (2005a) Effects of mixed conduction on the open-circuit voltage of intermediate-temperature SOFCs based on sm-doped ceria electrolytes. *Solid State Ionics, 176*(7), 663-668.

Matsuzaki, Y. and Yasuda, I. (2000). The poisoning effect of sulfur-containing impurity gas on a SOFC anode: Part I. dependence on temperature, time, and impurity concentration. *Solid State Ionics, 132*(3), 261-269.

McIntosh, S., and Gorte, R. J. (2004). Direct hydrocarbon solid oxide fuel cells. *Chemical Reviews, 104*(10), 4845.

McIntosh, S., Vohs, J. M., and Gorte, R. J. (2002). An examination of lanthanide additives on the performance of Cu–YSZ cermet anodes. *Electrochimica Acta, 47*(22–23), 3815-3821.

McIntosh, S., Vohs, J. M., and Gorte, R. J. (2003). Impedance spectroscopy for the characterization of cu-ceria-YSZ anodes for SOFCs. *Journal of the Electrochemical Society, 150*(10), 1305-12.

Minh N.Q and Takahashi, T. (1995) Science and Technology of Ceramic Fuel Cells. *Elsevier Science*, Netherland. 71-70.

Minh, N. Q. (1993). Ceramic fuel cells. *Journal of the American Ceramic Society*, *76*(3), 563-588.

Minh, N. Q. (2004). Solid oxide fuel cell technology - features and applications. *Solid State Ionics, 174*(1-4), 271-277.

Mogensen, M., and Kammer, K. (2003). Conversion of hydrocarbons in solid oxide fuel cells. *Annual Review of Materials Research, 33*(1), 321-331.

Mogensen, M., Sammes, N. M., and Tompsett, G. A. (2000). Physical, chemical and electrochemical properties of pure and doped ceria. *Solid State Ionics, 129*(1–4), 63-94.

Moon, H., Kim, S.D., Hyun, S.H., and Kim, H. S. (2008). Development of IT-SOFC unit cells with anode-supported thin electrolytes via tape casting and co-firing. *International Journal of Hydrogen Energy*, 33(6), 1758-1768.

Mukerjee, S., Jacob-Haltiner, J.K. and Wiessman, J.G. (2013). Method for adding sulphur to a fuel cell stack system for improves system cell stability. *US Patent* US20130302709 A1.

Murray, E., Sever, M. J., and Barnett, S. A. (2002). Electrochemical performance of (La,Sr)(Co,Fe)O_3–(Ce,Gd)O_3 composite cathodes. *Solid State Ionics, 148*(1–2), 27-34.

Murray, E., Tsai, T., and Barnett, S. A. (1999). A direct-methane fuel cell with a ceria-based anode. *Nature, 400*(6745), 649-651.

Nabae, Y., Yamanaka, I., Hatano, M. and Otsuka, K. (2006). Catalytic behavior of Pd–Ni/Composite anode for direct oxidation of methane in SOFCs. *Journal of the Electrochemical Society, 153*(1), A140-A145.

Niakolas, D. K., Ouweltjes, J. P., Rietveld, G., Dracopoulos, V. and Neophytides, S. G. (2010). Au-doped Ni/GDC as a new anode for SOFCs operating under rich CH_4 internal steam reforming. *International Journal of Hydrogen Energy, 35*(15), 7898-7904.

Nikolla, E., Schwank, J., and Linic, S. (2009a). Direct electrochemical oxidation of hydrocarbon fuels on SOFCs: Improved carbon tolerance of ni alloy anodes. *Journal of the Electrochemical Society, 156*(11), B1312-B1316.

Nikolla, E., Schwank, J., and Linic, S. (2009b). Comparative study of the kinetics of methane steam reforming on supported ni and Sn/Ni alloy catalysts: The impact of the formation of ni alloy on chemistry. *Journal of Catalysis, 263*(2), 220-227.

Nikooyeh, K., Clemmer, R., Alzate-Restrepo, V., Hill, J. M., (2008). Effect of hydrogen on carbon formation on Ni/YSZ composites exposed to methane. *Applied Catalysis A, General, 347*(1), 106-111.

O'Hayre, R. P., Cha, S. W., Colella ,W. and Prinz, F. B. (2006). Fuel Cell Fundamentals, *John Wiley & Sons*, New York.

Offer, G. J., Mermelstein, J., Brightman, E. and Brandon, N. P. (2009). Thermodynamics and kinetics of the interaction of carbon and sulfur with solid oxide fuel cell anodes. *Journal of the American Ceramic Society, 92*(4), 763.

Öksüzömer, M. A. F., Dönmez, G., Sariboğa, V., and Altinçekiç, T. G. (2013). Microstructure and ionic conductivity properties of gadolinia doped ceria ($Gd_xCe_{1-xO2-x/2}$) electrolytes for intermediate temperature SOFCs prepared by the polyol method. *Ceramics International, 39*(7), 7305-7315.

Oudghiri-Hassani, H., Rakass, S., Abatzoglou, N. and Rowntree, P. (2007). Inhibition of carbon formation during steam reforming of methane using thiol-coated nickel catalysts. *Journal of Power Sources, 171*(2), 850-855.

Pacific Gas and Electric Company (2014). Sulphur information. http://www.pge.com/pipeline/operations/sulfur/sulfur_info.shtml

Pajkossy, T. (2005). Impedance spectroscopy at interfaces of metals and aqueous solutions — surface roughness, CPE and related issues. *Solid State Ionics, 176*(25–28), 1997-2003.

Park, E. W., Moon, H., Park, M. and Hyun, S. H. (2009). Fabrication and characterization of Cu–Ni–YSZ SOFC anodes for direct use of methane via Cu-electroplating. *International Journal of Hydrogen Energy, 34*(13), 5537-5545.

Peng, R., Xia, C., Peng, D., and Meng, G. (2004). Effect of powder preparation on (CeO2)0.8(Sm2O3)0.1 thin film properties by screen-printing. *Materials Letters, 58*(5), 604-608.

Prasad, D. H., Jung, H. -., Jung, H. -., Kim, B. -., Lee, H. -., and Lee, J. -. (2008). Single step synthesis of nano-sized NiO–Ce0.75Zr0.25O2 composite powders by glycine nitrate process. *Materials Letters, 62*(4–5), 587-590.

Ralph, J. M., Schoeler, A. C., and Krumpelt, M. (2001). Materials for lower temperature solid oxide fuel cells. *Journal of Materials Science, 36*(5), 1161-1172.

Rasmussen, J. F. B., and Hagen, A. (2010). The effect of H2S on the performance of SOFCs using methane containing fuel. *Fuel Cells, 10*(6), 1135-1142.

Rembelski, D., Viricelle, J. P., Combemale, L., and Rieu, M. (2012). Characterization and comparison of different cathode materials for SC-SOFC: LSM, BSCF, SSC, and LSCF. *Fuel Cells, 12*(2), 256-264.

Resofszki, G., Muhler, M., Sprenger, S., Wild, U. and Paal, Z. (2003). Electron spectroscopy of sulfated zirconia, its activity in n-hexane conversion and possible reasons of its deactivation. *Applied Catalysis A, General, 240*(1), 71-81.

Rodriguez, N. M., A., Rodriguez, N. M., Anderson, P. E., Wootsch, A. and Wild, U. (2001). XPS, EM and catalytic studies of the accumulation of carbon on Pt-black. *Journal of Catalysis, 197*(2), 365-377.

Rostrup-Nielsen, J. (1984). Sulfur-passivated nickel catalysts for carbon-free steam reforming of methane. *Journal of Catalysis, 85*(1), 31-43.

Sahibzada, M., Steele, B. C. H., Hellgardt, K., Barth, D., Effendi, A. and Mantzavinos, D. (2000). Intermediate temperature solid oxide fuel cells operated with methanol fuels. *Chemical Engineering Science, 55*(16), 3077-3083.

Sammes, N., Bove, R. and Pusz, J. (2006) Solid oxide fuel cells in Fuel cell technology: Reaching towards Commercialization edited by Sammes, N. *Springer-Verlag London Limited*, London, 1-26.

Sasaki, K., Adachi, S., Haga, K., Uchikawa, M., Yamamoto, J., Iyoshi, A., Chou, J.T. Shiratori, Y. and Itoh, K. (2007). Fuel impurity tolerance of solid oxide fuel cells. *ECS Transactions*, 7 (1), 1675-1683.

Sasaki, K., and Teraoka, Y. (2003). Equilibria in fuel cell gases. *Journal of the Electrochemical Society, 150*(7), A878.

Sasaki, K., Susuki, K., Iyoshi, A., Uchimura, M., Imamura, N., Kusaba, H., Teraoka, Y., Fuchino, H., Tsujimoto, K., Uchida, Y. and Jingo, N. (2006). H2S poisoning of solid oxide fuel cells. *Journal of the Electrochemical Society, 153*(11), A2023-A2029.

Sehested, J. (2006). Four challenges for nickel steam-reforming catalysts. *Catalysis Today, 111*(1), 103-110.

Shah, R. (2007) Introduction to fuel cells in Recent Trend in Fuel Cell Science and Technology edited by Basu, S. *Anamaya Publishers*, New Delhi, 1-9.

Shao, Z., and Haile, S. M. (2004). A high-performance cathode for the next generation of solid-oxide fuel cells. *Nature*, 431(7005), 170.

Shiratori, Y., O., Shiratori, Y., Oshima, T., and Sasaki, K. (2008). Feasibility of direct-biogas SOFC. *International Journal of Hydrogen Energy, 33*(21), 6316-6321.

Singh, A. and Hill, J. M. (2012). Carbon tolerance, electrochemical performance and stability of solid oxide fuel cells with Ni/yttria stabilized zirconia anodes impregnated with sn and operated with methane. *Journal of Power Sources, 214*(0), 185-194.

Singhal, S. C. (2000). Advances in solid oxide fuel cell technology. *Solid State Ionics, Diffusion and Reactions, 135* (1-4), 305-313.

Skinner, S. J. and Kilner, J. A. (2003). Oxygen ion conductors. *Materials Today, 6*(3), 30-37.

Smith, J. M. (1996). In Van Hess H. C., Abbott M. M. (Eds.), *Introduction to chemical engineering thermodynamics*. New York: New York : McGraw-Hill.

Snoeck, J., Froment, G. F., and Fowles, M. (1997). Kinetic study of the carbon filament formation by methane cracking on a nickel catalyst. *Journal of Catalysis, 169*(1), 250-262.

Stambouli, A. B., and Traversa, E. (2002). Solid oxide fuel cells (SOFCs): a review of an environmentally clean and efficient source of energy. *Renewable and Sustainable Energy Reviews, 6*(5), 433-455.

Steele, B. C. H. (2000). Appraisal of $Ce_{1-y}GdyO_{2-y/2}$ electrolytes for IT-SOFC operation at 500°C. *Solid State Ionics, 129*(1–4), 95-110.

Struis, R. P. W. J., Schildhauer, T. J., Czekaj, I., Janousch, M., Biollaz, S. M. A. and Ludwig, C. (2009) Sulphur poisoning of Ni catalysts in the SNG production from biomass: A TPO/XPS/XAS study. *Applied Catalysis A, General, 362*(1), 121.

Sumi, H., Lee, Y., Muroyama, H., Matsui, T. and Eguchi, K., (2010). Comparison between internal steam and CO_2 reforming of methane for Ni-YSZ and Ni-ScSZ SOFC anodes. *Journal of the Electrochemical Society, 157*(8), B1118.

Sun, C., and Stimming, U. (2007). Recent anode advances in solid oxide fuel cells. *Journal of Power Sources, 171*(2), 247-260.

Sun, C., Hui, R., Roller, J., Sun, C., and Hui, R. (2009). Cathode materials for solid oxide fuel cells: A review. *Journal of Solid State Electrochemistry, 14*(7), 1125-1144.

Takeguchi, T., Kani, Y., Yano, T., Kikuchi, R., Eguchi, K., Tsujimoto, K. Uchida, Y., Ueno, K., Omoshiki, K. and Aizawa, M. (2002). Study on steam reforming of CH_4 and C_2 hydrocarbons and carbon deposition on Ni-YSZ cermets. *Journal of Power Sources, 112*(2), 588-595.

Takeguchi, T., Kikuchi, R., Yano, T., Eguchi, K., and Murata, K. (2003). Effect of precious metal addition to ni-YSZ cermet on reforming of CH4 and electrochemical activity as SOFC anode. *Catalysis Today, 84*(3–4), 217-222.

Tanner, C. W., Fung, K. Z., and Virkar, A. V. (1997). The effect of porous composite electrode structure on solid oxide fuel cell performance .1. theoretical analysis. *Journal of the Electrochemical Society, 144*(1), 21-30.

Tian, R., Zhao, F., Chen, F., and Xia, C. (2011). Sintering of samarium-doped ceria powders prepared by a glycine-nitrate process. *Solid State Ionics, 192*(1), 580-583.

Toh, C. H., Munroe, P. R., Young, D. J. and Foger, K. (2003). High temperature carbon corrosion in solid oxide fuel cells. *Materials at High Temperatures, 20*(2), 129-136.

Trembly, J. P., Marquez, A. I., Ohrn, T. R., Bayless, D. J., Trembly, J. P. and Marquez, A. I. (2006) Effects of coal syngas and H_2S on the performance of solid oxide fuel cells: Single-cell tests. *Journal of Power Sources, 158*(1), 263-273.

Trimm, D. L. (1999). Catalysts for the control of coking during steam reforming. *Catalysis Today, 49*(1–3), 3-10.

Trovarelli, A., de Leitenburg, C., Boaro, M., and Dolcetti, G. (1999). The utilization of ceria in industrial catalysis. *Catalysis Today, 50*(2), 353-367.

Varga, A. (2007). Introduction to Fuel Cell Technology in Fuel Cell Electronics Packaging edited by Kuang, K. and Easler, K. *Springer Science + Bussiness Media*, New York, 1-32.

Virkar, A. V., Chen, J., Tanner, C. W., and Kim, J. (2000). The role of electrode microstructure on activation and concentration polarizations in solid oxide fuel cells. *Solid State Ionics, 131*(1–2), 189-198.

Wang, J. and Liu, M. (2007) Computational study of sulfur–nickel interactions: A new S–Ni phase diagram. *Electrochemistry Communications, 9*(9), 2212-2217.

Wang, J. B., Jang, J., Huang, T., (2003) Study of ni-samaria- doped ceria anode for direct oxidation of methane in solid oxide fuel cells. *Journal of Power Sources, 122*(2), 122-131.

Wang, Z., Weng, W., Chen, K., Shen, G., Du, P. and Han, G. (2008a). Preparation and performance of nanostructured porous thin cathode for low-temperature solid oxide fuel cells by spin-coating method. *Journal of Power Sources, 175*(1), 430-435.

Wang, Z., Weng, W., Cheng, K., Du, P., Shen, G., and Han, G. (2008b). Catalytic modification of Ni–Sm-doped ceria anodes with copper for direct utilization of dry methane in low-temperature solid oxide fuel cells. *Journal of Power Sources, 179*(2), 541-546.

Watts, J. F. (2003). In Wolstenholme J. (Ed.), *An introduction to surface analysis by XPS and AES*. Chichester, England ; New York: Chichester, England ; New York : J. Wiley.

Xia, C., (2009) Electrolytes in Solid Oxide Fuel Cells: Material Properties and performance edited by Fergus, J.W., Hui, R., Li, X., Wilkinson, D. P. and Zhang, J. *CRC Press*, Boca Raton, 1-71.

Xia, C., (2009) Electrolytes in Solid Oxide Fuel Cells: Material Properties and performance edited by Fergus, J.W., Hui, R., Li, X., Wilkinson, D. P. and Zhang, J. *CRC Press*, Boca Raton, 1-71.

Xia, C., and Liu, M (2002). Novel cathodes for low-temperature solid oxide fuel cells. *Advanced Materials, 14*(7), 521.

Xia, C. and Liu, M. (2001). Low-temperature SOFCs based on $Gd_{0.1}Ce_{0.9}O_{1.95}$ fabricated by dry pressing. *Solid State Ionics, 144*(3-4, pp. 249-255), December.

Xia, C., Rauch, W., Chen, F., and Liu, M. (2002). $Sm_{0.5}Sr_{0.5}CoO_3$ cathodes for low-temperature SOFCs. *Solid State Ionics, 149*(1–2), 11-19.

Xia, C., Zhang, Y., Liu, M., Xia, C., Zhang, Y., and Liu, M. (2003). LSM-GDC composite cathodes derived from a sol-gel process. *Electrochemical and Solid-State Letters, 6*(12), A290.

Xu, C., Gansor, P., Zondlo, J. W., Sabolsky, K. and Sabolsky, E. M. (2011). An H_2S-tolerant Ni-GDC anode with a GDC barrier layer. *Journal of the Electrochemical Society, 158*(11), B1405-B1416.

Yahiro, H., Eguchi, Y., Eguchi, K., and Arai, H. (1988). Oxygen ion conductivity of the ceria-samarium oxide system with fluorite structure. *Journal of Applied Electrochemistry, 18*(4), 527-531.

Yamamoto, O. (2000). Solid oxide fuel cells: Fundamental aspects and prospects. *Electrochimica Acta, 45*(15–16), 2423-2435.

Yan, A., Phongaksorn, M., Nativel, D., and Croiset, E. (2012). Lanthanum promoted NiO–SDC anode for low temperature solid oxide fuel cells fueled with methane. *Journal of Power Sources, 210*, 374-380.

Yang L., Choi, Y., Qin, W., Chen, H., Blinn, K., and Liu, M. (2011). Promotion of water-mediated carbon removal by nanostructured barium oxide/nickel interfaces in solid oxide fuel cells. *Nature Communications, 2(357).*

Yang, R., Lee, M., Chang, J., Lin, T., Chang, Y. and Kao, W. (2012). Fabrication and characterization of a $Sm_{0.2}Ce_{0.8}O_{1.9}$ electrolyte film by the spin-coating method for a low-temperature anode-supported solid oxide fuel cells. *Journal of Power Sources, 206*(0), 111-118.

Ye, X., Huang, B., Wang, S. R., Wang, Z. R., Xiong, L., and Wen, T. L. (2007). Preparation and performance of a Cu–CeO_2–ScSZ composite anode for SOFCs running on ethanol fuel. *Journal of Power Sources, 164*(1), 203-209.

Yin, Y., Zhu, W., Xia, C., and Meng, G. (2004). Gel- cast NiO– SDC composites as anodes for solid oxide fuel cells. *Journal of Power Sources, 132*(1), 36-41.

You, H., Abuliti, A., Ding, X. and Zhou, Y. (2007). Reactions of low and middle concentration dry methane over Ni/YSZ anode of solid oxide fuel cell. *Journal of Power Sources, 165*(2), 722-727.

Yu, J. H., Park, G. W., Lee, S., and Woo, S. K. (2007). Microstructural effects on the electrical and mechanical properties of Ni–YSZ cermet for SOFC anode. *Journal of Power Sources, 163*(2), 926-932.

Yun, J. W., Yoon, S. P., Kim, H. S., Han, J. and Nam, S. W. (2012). Effect of $Sm_{0.2}Ce_{0.8}O_{1.9}$ on the carbon coking in Ni-based anodes for solid oxide fuel cells running on methane fuel. *International Journal of Hydrogen Energy, 37*(5), 4356-4366.

Zha S., Cheng, Z. and Liu, M. (2007) Sulfur poisoning and regeneration of Ni-based anodes in solid oxide fuel cells. *Journal of the Electrochemical Society, 154*, B201-B206.

Zha, S. W., Xia, C. R., and Meng, G. Y. (2001). Calculation of the e.m.f. of solid oxide fuel cells. *Journal of Applied Electrochemistry, 31*(1), 93-98.

Zha, S., Xia, C., and Meng, G. (2003). Effect of Gd (Sm) doping on properties of ceria electrolyte for solid oxide fuel cells. *Journal of Power Sources, 115*(1), 44-48.

Zhan, Z., Wen, T. L., Tu, H., and Lu, Z. Y. (2001). AC impedance investigation of samarium-doped ceria. *Journal of The Electrochemical Society, 148(5),* (A427-A432).

Zhang, L., Jiang, S. P., He, H. Q., Chen, X., Ma, J. and Song, X. C. (2010) A comparative study of H_2S poisoning on electrode behavior of Ni/YSZ and Ni/GDC anodes of solid oxide fuel cells. *International Journal of Hydrogen Energy, 35*(22), 12359-12368.

Zhang, X., Robertson, M., Deĉes-Petit, C., Qu, W., Kesler, O. and Maric, R., (2007). Internal shorting and fuel loss of a low temperature solid oxide fuel cell with SDC electrolyte. *Journal of Power Sources, 164*(2), 668-677.

Zhang, X., Robertson, M., Yick, S., Deĉes-Petit, C., Styles, E., Qu, W., Ghosh, D. (2006). $Sm_{0.5}Sr_{0.5}CoO_3$ + $Sm_{0.2}Ce_{0.8}O_{1.9}$ composite cathode for cermet supported thin $Sm_{0.2}Ce_{0.8}O_{1.9}$ electrolyte SOFC operating below 600 °C. *Journal of Power Sources, 160*(2), 1211-1216.

Zhang, Y., Gao, J., Peng, D., Guangyao, M., and Liu, X. (2004). Dip- coating thin yttria-stabilized zirconia films for solid oxide fuel cell applications. *Ceramics International, 30*(6), 1049-1053.

Zhao, S., and Gorte, R. J. (2004). A comparison of ceria and sm-doped ceria for hydrocarbon oxidation reactions. *Applied Catalysis A: General, 277*(1–2), 129-136.

Zhou, M., Ge, L., Chen, H., and Guo, L. (2012). Effect of transition metal oxides doping on $Ce_{0.9}Sm_{0.05}Nd_{0.05}O_{1.95}$ solid electrolyte materials. *Journal of Advanced Ceramics, 1(2),* 150-156.

Zhu, W. Z., and Deevi, S. C. (2003). A review on the status of anode materials for solid oxide fuel cells. *Materials Science & Engineering A, 362*(1), 228-239.

APPENDIX A

Temperature programs for sintering

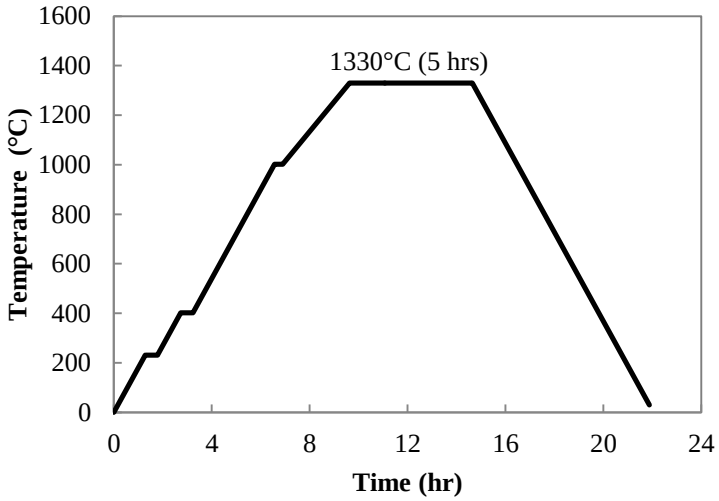

Figure A-1 Temperature program for NiO-SDC|SDC bi-layer sintering

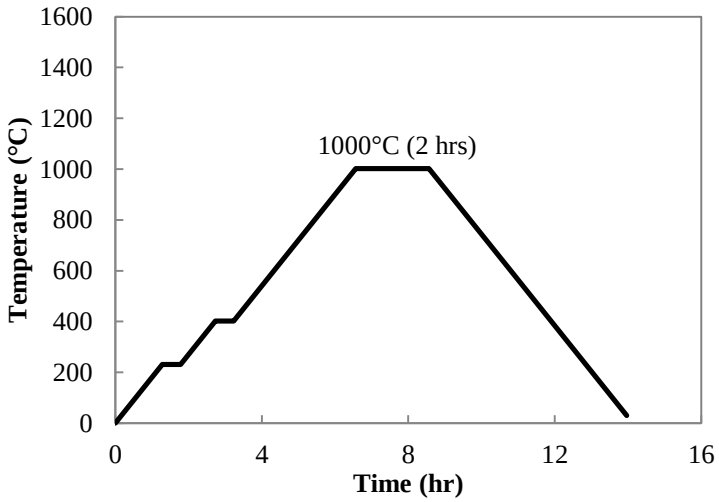

Figure A-2 Temperature program for SSC-SDC sintering

APPENDIX B

Calculating Nernst voltage E_r and theoretical OCV for SDC

Properties obtained from Smith's Introduction to Chemical Thermodynamics (5th edition) (Smith, 1996).

$H_2+0.5O_2 \rightarrow H_2O$	H_f 298 K (J mol)	S_f 298 (J $mol^{-1}K$)
H_2	0	130.60
O_2	0	205.04
H_2O	-241845	188.72

	Cp (K)			
	A	B	C	D
H_2	3.249	4.22×10^{-4}	0	8.30×10^{3}
O_2	3.639	5.06×10^{-4}	0	-2.27×10^{4}
H_2O	3.47	1.45×10^{-3}	0	1.21×10^{4}

T(ºC)	T (K)	ΔH(T) $H_2+0.5O_2 \rightarrow H_2O$	ΔS (T) $H_2+0.5O_2 \rightarrow H_2O$	ΔG° -= ΔH-TΔS (J/mol)
550	823	-246657	-54	-202294
600	873	-247039	-54	-199587
650	923	-247407	-55	-196859
700	973	-247759	-55	-194112

pH_2O	0.03 atm	pH_2	0.97 atm
pO_2 cathode	$p_{O_2,ca}$	0.21 atm	
R	8.3142	J $mol^{-1}K$	
F	96485	C mol^{-1}	

$$K_{eq} = exp\left(-\frac{\Delta G^{\circ}}{RT}\right)$$

$$p_{O_2,an} = \left(\frac{p_{H_2O}}{K_{eq}p_{H_2}}\right)^2$$

$$E_r = -\frac{RT}{4F} ln\left(\frac{p_{O_2,an}}{p_{O_2,ca}}\right)$$

T(C)	T (K)	ΔG°	K_{eq}	$p_{O_2,an}$	E_r
550	823	-2.02E+05	6.91E+12	2.00E-29	1.14
600	873	-2.00E+05	8.75E+11	1.25E-27	1.14
650	923	-1.97E+05	1.38E+11	5.00E-26	1.13
700	973	-1.94E+05	2.64E+10	1.38E-24	1.12

Calculating theoretical OCV for SDC

$$E_r = \frac{RT}{4F}\int_{\ln p_{O_2,an}}^{\ln p_{O_2,ca}} \frac{\sigma_i}{\sigma_i + \sigma_e^0 p_{O_2}^{\left(-\frac{1}{4}\right)}} d\ln p_{O_2}$$

T(C)	$p_{O_2,an}$	σ_i	σ_e^0	Integration	RT/4F	(OCV) SDC-theory
500	1.89743E-31	0.00532	2.51E-10	64.45	0.016652528	1.073
600	2.00334E-29	0.0176	1.780E-08	53.40	0.018806801	1.004
700	1.24849E-27	0.00471	5.010E-07	44.17	0.020961073	0.926

APPENDIX C

Equilibrium compositions for CO-CO_2 mixtures

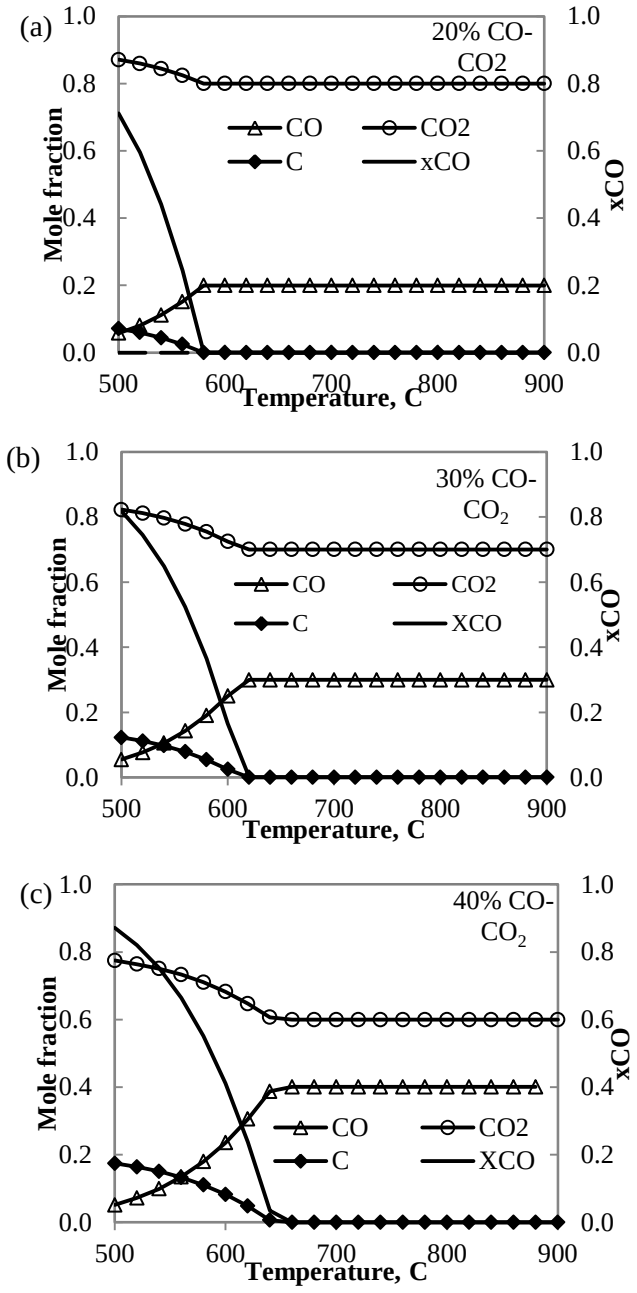

Figure A-3 Equilibrium compositions calculated for a) 20% b) 30% c) 40% CO-CO_2

APPENDIX D

i-V curves under humidified H_2 before and after 100 hrs dry CH_4 for the cells a) without and b) with H_2S

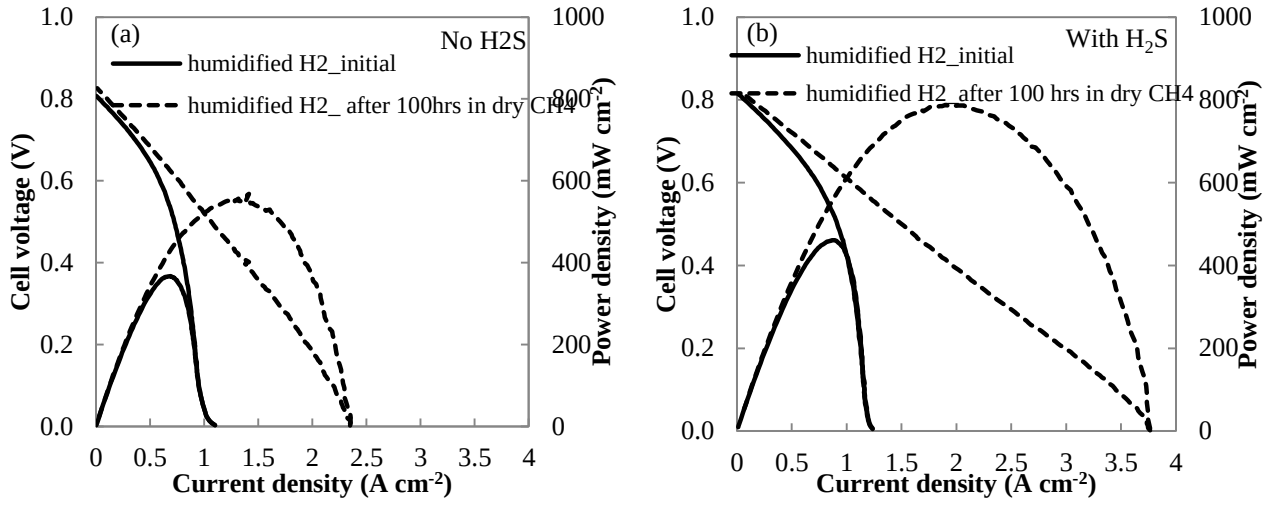

Figure A-4 IV curves under humidified H_2 before and after 100 hrs dry CH_4 for the cells a) without H_2S and b) with H_2S at 700ºC

APPENDIX E

Signals from a) CO b) CO_2 and c) CH_4 when switching gas composition

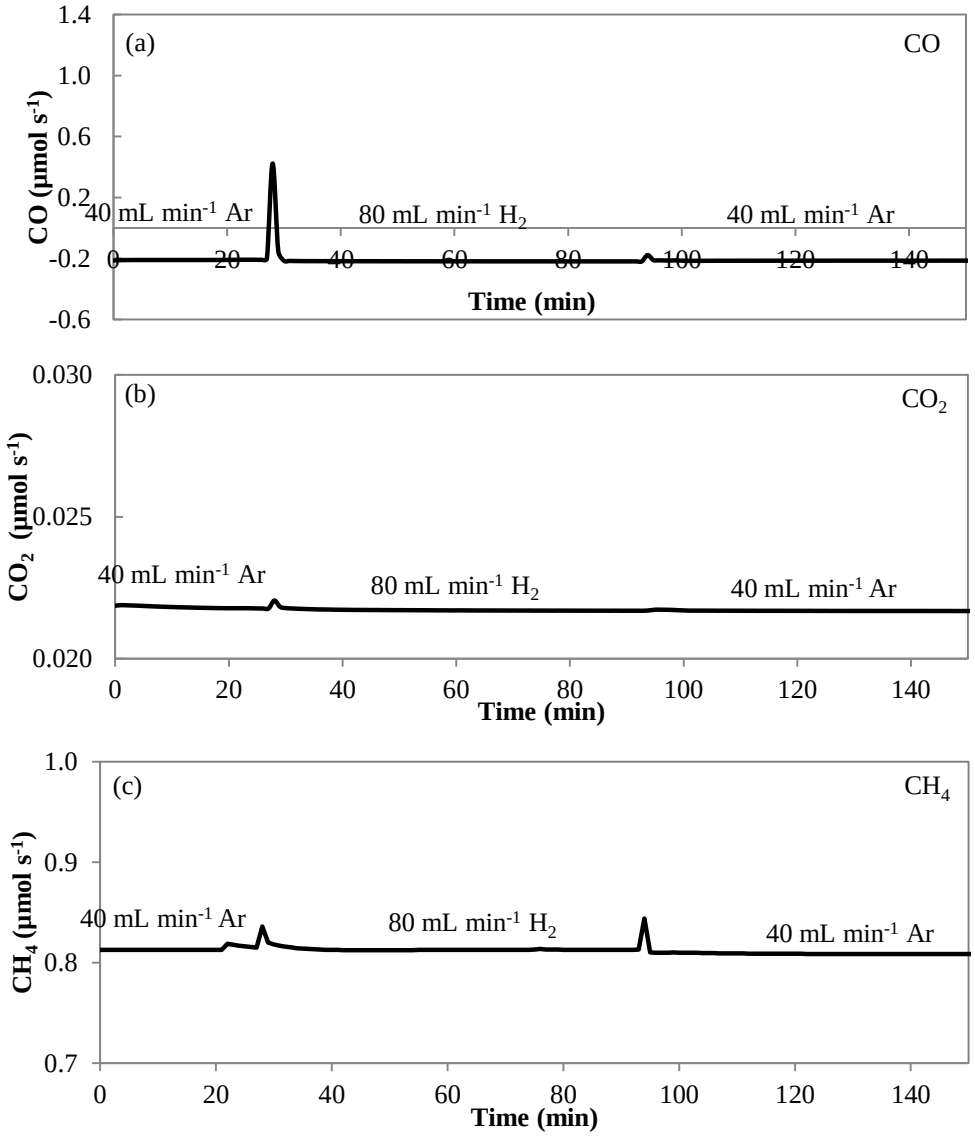

Figure A-5 Signals from a) CO b) CO_2 and c) CH_4 when switching gas composition from Ar to H_2 and to Ar again